Measurement of the $W^{\pm}Z$ production cross section and limits on anomalous triple gauge couplings at $\sqrt{s} = 7$ TeV using the ATLAS detector

A dissertation presented

by

Michael Aaron Kagan

to

The Department of Physics

in partial fulfillment of the requirements

for the degree of

Doctor of Philosophy

in the subject of

Physics

Harvard University

Cambridge, Massachusetts

May 2012

Thesis advisor

Masahiro Morii

Author

Michael Aaron Kagan

Measurement of the $W^{\pm}Z$ production cross section and limits on anomalous triple gauge couplings at $\sqrt{s} = 7$ TeV using the ATLAS detector

Abstract

This dissertation presents a measurement of the $W^{\pm}Z$ production cross section and limits on anomalous triple gauge couplings in proton-proton collisions at a center of mass energy of 7 TeV using data produced by LHC collisions and acquired by the ATLAS detector in 2011. The measurement and limits probe the electroweak sector of the Standard Model at high energies and allow for generic tests for new physics that could be present at high energy scales. This analysis is also useful for understanding the ATLAS detector response in the presence of multi-lepton signatures.

The dataset used corresponds to an integrated luminosity of 1.02 fb^{-1}. The measurement relies on the leptonic decay modes of the W and Z, resulting in final states with electrons, muons, and missing energy. Events are selected by requiring three high momentum leptons, a large missing transverse energy, a Z candidate (reconstructed from two of the leptons) with a mass consistent with the Z pole mass, and a W candidate (reconstructed from the third lepton and the missing energy) with a large transverse mass. The backgrounds to the $W^{\pm}Z$ process are estimated using Monte Carlo simulations and Data-Driven techniques.

A total of 71 $W^{\pm}Z$ candidate events are observed in data, with 50.3 signal and 12.1 background events expected. The production cross section is extracted from these events using a maximum likelihood method, and is found to be in good agreement with the Standard Model expectation. Limits at the 95% confidence interval on anomalous triple gauge couplings are extracted from the observed event yields using a frequentist limit setting approach.

Contents

List of Figures

List of Tables

Acknowledgments

There are many people to whom I am deeply indebted for all of their help and support:

My advisor, Masahiro Morii, thank you for all of your guidance; for teaching me particle physics while giving me the freedom to explore my ideas; and for always being willing to listen, no matter how crazy my ideas were.

George Brandenburg, Melissa Franklin, João Guimarães da Costa, and John Huth, I have had the great fortune to work closely with all of you and learn from your expertise. Thank you for all of your advice, feedback, and encouragement.

Matt Schwartz, thank you for giving me the opportunity to explore my interests in theoretical physics, and for taking the time to be a member of my thesis committee.

Gary Feldman, thank you for being on my thesis committee and for all of your comments, questions, and support.

Kevin Einsweiler and Ludo Pontecorvo, thank you for all of your guidance and support while I have been a graduate student on ATLAS.

My partner on team $W^{\pm}Z$, Laura Jeanty, thank you for all of your insight, dedication, and flexibility, and for making this analysis an enjoyable experience.

My fellow graduate students, Jason Gallicchio, Verena Martinez Outschoorn, Kevin

Mercurio, Srivas Prasad, Ben Smith, and Giovanni Zevi de la Porta; I have greatly enjoyed working with all of you, thank you for making graduate school incredibly fun and interesting.

The post-docs, Alberto Belloni, Kevin Black, Corrinne Mills, and Shulamit Moed; thank you for working closely with me and taking the time to help me learn.

Lynn, thank you for being there for me, for your unwavering support and amazing patience; most of all, for making me happy and always keeping me going.

My family, thank you for all of your love, encouragement, and support, and for always taking the time to listen. I couldn't have done this without you.

Chapter 1

Introduction

This thesis describes a measurement of the $W^{\pm}Z$ production cross section and limits on anomalous triple gauge couplings from proton-proton collisions at $\sqrt{s} = 7$ TeV using the ATLAS detector. Chapter 2 begins with a discussion of the theoretical background and previous experimental results that is needed to frame the measurement. Chapter 3 provides an introduction to the Large Hadron Collider design and recent performance. Chapter 4 provides an overview of the ATLAS detector. It also describes some of the nomenclature and terminology that is used in the analysis. Chapter 5 discusses the reconstruction of detector signals into the physics objects that are used for data analysis. Finally, Chapter 6 describes the full $W^{\pm}Z$ analysis in which a production cross section is measured and limits on anomalous triple gauge couplings are derived.

Chapter 2

Background

This chapter presents the theoretical background needed to frame the measurement of the $W^{\pm}Z$ diboson production cross section and the limits derived on anomalous triple gauge couplings presented in this thesis, as well as the previous experimental results pertaining to this measurement. The chapter begins with a brief and technical introduction to the Standard Model (SM) in Section 2.1. As Electroweak (EW) physics plays a fundamental role in the simultaneous production of a W and Z boson, further description of the EW sector of the SM is presented in Section 2.2 with particular emphasis on triple gauge interactions. The theoretical framework used to build models and derive limits on anomalous triple gauge couplings (aTGC) is described in Section 2.3. Further details of Quantum Chromodynamics (QCD) and its role in hadron collider physics is discussed in Section 2.4 in order to provide the necessary background for discussing collider signatures of $W^{\pm}Z$ diboson production in Section 2.5. The chapter concludes with a review of the existing experimental knowledge of the $W^{\pm}Z$ process with a presentation of previous measurements of the

$W^{\pm}Z$ diboson production cross section and limits on aTGCs in Section 2.6.

It should be noted that the notations and conventions used for defining and manipulating equations within the framework of quantum field theory follow closely from reference [99]. In addition, unless explicitly noted, this analysis will work in units where $\hbar = c = 1$, where $\hbar$ is Planck's constant and c is the speed of light. With these units, length, time, energy and mass can all be expresses in terms of energy. Specifically, length and time are expressed in units of inverse energy, while mass is expressed in units of energy.

2.1 The Standard Model

The Standard Model (SM) [80, 113, 102, 99] is the theoretical foundation of the current understanding of fundamental particles and their interactions. It describes the known and directly observed particle content of the universe and how these particles behave under the influence of Quantum Chromodynamics (QCD), the theory of the strong force, and the Electroweak (EW) force, a single force which unifies the Quantum Electrodynamics (QED) description of electromagnetism with the weak force. This theory has seen unprecedented success in accurately predicting the behavior of nature at the smallest scales. For example, theoretical predictions of the QED fine structure constant are in agreement with experimental measurements to less than one part-per-billion [85]. Testing the SM and searching for deviations from its predictions has been a primary goal of modern high energy physics experiments. Given the vast scope of the SM, this thesis will only be able to provide a brief introduction to some

aspects of the theory.

The SM is a relativistic quantum field theory built from the principles of gauge invariance, i.e. the idea that physics should be invariant under local symmetry transformations. Within this framework of gauge invariance, each gauge symmetry gives rise to a force which is mediated by particles known as gauge bosons. The matter particles then live in representations of the symmetry group, and the representation determines the charge of the particle under the symmetry.

In the SM, the EW interactions are described by an $SU(2)_L \times U(1)_Y$ gauge group and are mediated by the $W^{\pm}$, Z, and γ gauge bosons, while the QCD interactions are described by an $SU(3)$ gauge group and are mediated by gluons. Both the EW and QCD gauge symmetries are non-abelian, thus giving rise to multi-gauge-boson point-like interactions.

The matter content of the SM comprises spin-1/2 fermions which are organized into two categories based on how they interact via the strong force: quarks and leptons. The quarks are organized into $SU(3)$ triplets which describes their color charge, while the leptons are singlets of $SU(3)$ and do no interact via the strong force. Further, the left-handed and right-handed quarks and leptons are categorized separately because the $SU(2)_L$ gauge bosons of the EW gauge group only couple to left-handed particles (and right-handed anti-particles). The left-handed fermions form $SU(2)_L$ doublets, known as generations (or families), while the right handed fermions are singlets of $SU(2)_L$. There are three generations of quarks and leptons, which comprise a total of six flavors of quarks and six flavors of leptons. The particles of the SM, along with

their masses, EM charges, and spin, are shown in Figure 2.1.

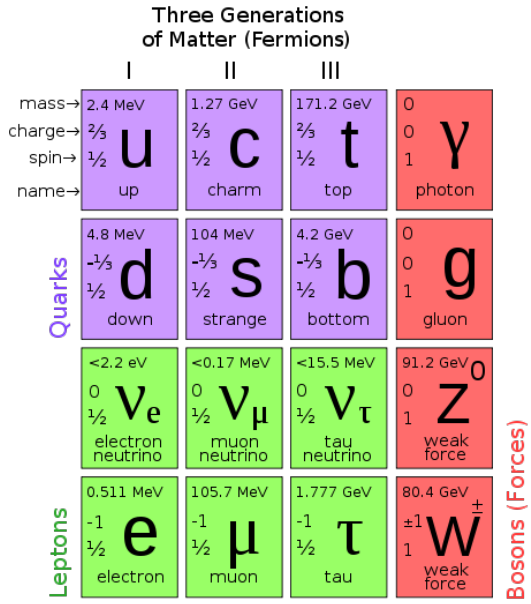

Figure 2.1: The Standard Model particles and their properties [115].

2.2 The Electroweak Sector

The Electroweak theory is a unified theory of Quantum Electrodynamics (QED) [103, 74, 75], which describes the electromagnetic force in terms of the exchange of a photon, and the weak force, which is described in terms of the exchange of the W and Z bosons and is responsible for weak nuclear decay. First described by Glashow, Weinberg, and Salam (GSW) [80, 113, 102, 83, 99], EW theory unifies the weak and EM interactions under an $SU(2)_L \times U(1)_Y$ gauge symmetry which is spontaneously broken down to the observable $U(1)_{EM}$ symmetry by the Higgs mechanism.

The EW gauge bosons mediate the effect of the weak and EM forces amongst the matter content of the SM, as well as between gauge bosons. The fundamental couplings between the EW gauge bosons and the SM matter content can be found in Figure 2.2. All quarks and charged leptons interact electromagnetically via the exchange of a photon, while all SM matter particles interact weakly via the exchange of a W or Z. However, only left-handed particles and right-handed anti-particles couple to the W, while left-handed and right-handed particles couple with different strengths to the Z. Unlike the interactions of the photon and Z, the interactions of the W are not flavor conserving. Up type and down type quarks can be mixed via the W couplings to quarks in the Cabibbo-Kobayashi-Maskawa (CKM) matrix [83]. In addition, unlike EM interactions, the weak interactions of the W and Z can violate the parity (P), charge conjugation (C), and the combined CP symmetries [83].

The coupling strength and the mass of the gauge bosons determines the characteristic lifetime of a decaying particle. EM decays proceed at $\sim 10^{-16}$ seconds while weak decays proceed at $\sim 10^{-13}$ seconds. The longer lifetime of weakly decaying particles is related to the large masses of the W and Z which suppress the decay of light particles. Heavy particles with masses larger than the W and Z do not experience this mass suppression and can decay at a much faster rate. For example, the top quark with mass ~ 172 GeV has a lifetime of approximately $\sim 10^{-25}$ seconds [95].

2.2.1 The Electroweak Lagrangian

Before symmetry breaking, the EW Lagrangian contains four massless gauge bosons A^a_μ, where $a = 1...3$, and B_μ which are, respectively, the $SU(2)$ and $U(1)$ gauge bosons.

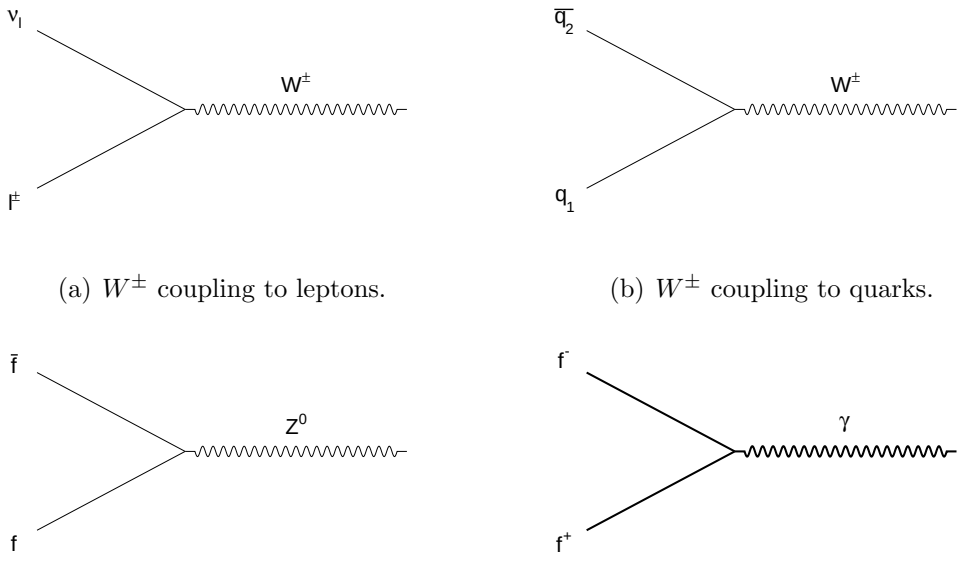

(a) $W^{\pm}$ coupling to leptons.

(b) $W^{\pm}$ coupling to quarks.

(c) Z coupling to fermions.

(d) γ coupling to fermions.

Figure 2.2: Fundamental couplings of electroweak gauge bosons to the SM matter content.

Since the $SU(2)$ and $U(1)$ gauge groups in this theory commute, the A^a_μ and B_μ can couple with different strengths. Therefore, the $SU(2)$ coupling will be denoted g and the $U(1)$ gauge coupling will be denoted g'. The covariant derivative needed to maintain local gauge invariance is

$$D_\mu = \left(\partial_\mu + igA^a_\mu \tau^a - i\frac{1}{2}g'B_\mu\right) \tag{2.1}$$

where τ^a are the generators of the $SU(2)$ gauge group in the adjoint representation. These generators follow the commutation relation $\left[\tau^a, \tau^b\right] = if^{abc}\tau^c$, where $f^{abc} = \epsilon^{abc}$ are called the structure constants and for $SU(2)$ are equal to the totally anti-symmetric tensor, ϵ^{abc}. In the adjoint representation, $(\tau^b)_{ac} = if^{abc}$.

The EW Lagrangian can be organized as,

$$\mathcal{L}_{EW} = \mathcal{L}_g + \mathcal{L}_f + \mathcal{L}_h + \mathcal{L}_y. \tag{2.2}$$

The gauge boson kinetic energy term is

$$\mathcal{L}_g = -\frac{1}{4}\left(A^a_{\mu\nu}\right)^2 - \frac{1}{4}\left(B_{\mu\nu}\right)^2 \tag{2.3}$$

where

$$X^a_{\mu\nu} = \partial_\mu X^a_\nu - \partial_\nu X^a_\mu + g f^{abc} X^b_\mu X^c_\nu \tag{2.4}$$

is the gauge boson field strength. The last term in the field strength, the self-coupling term, vanishes for abelian gauge theories, such as $U(1)$, but arises in non-abelian gauge theories because the generators of the gauge group do not commute. Thus, the self-interaction term is necessary to maintain gauge invariance for non-abelian groups. These terms give rise to the multi-gauge-boson interactions and are the source of EW diboson production. Further discussion of the self-interaction terms can be found in section 2.2.2.

The fermion kinetic energy term is,

$$\mathcal{L}_f = \bar{E}_L(i\not{D})E_L + \bar{e}_R(i\not{D})e_R + \bar{Q}_L(i\not{D})Q_L + \bar{u}_R(i\not{D})u_R + \bar{d}_R(i\not{D})d_R \tag{2.5}$$

In this equation, $\not{D} = \gamma^\mu D_\mu$ and γ^μ are the Dirac matrices. In addition, E_L denotes the left-handed lepton doublets, e_R denotes the right handed leptons (right handed neutrinos are not included in this term because they are not charged under any SM gauge group), Q_L denotes the left-handed quark doublets, u_R denotes the up-type right-handed quarks, and d_R denotes the down-type right-handed quarks. Due to

the presence of the covariant derivative, these terms contain all of the interactions between the gauge bosons and the matter content of the SM.

The Higgs term is,

$$\mathcal{L}_h = |D_\mu \phi|^2 + \mu^2 \phi^\dagger \phi - \lambda(\phi^\dagger \phi)^2 \tag{2.6}$$

where the Higgs field ϕ is a complex scalar $SU(2)$ doublet. This Higgs term contains the Higgs kinetic and potential energy. In order for this potential to have a minimum which allows for spontaneous symmetry breaking, it must be that $\mu^2 > 0$.

Finally, the Yukawa interaction terms between the fermions and the Higgs are,

$$\mathcal{L}_y = -Y_d \bar{Q}_L \cdot \phi d_R - Y_u \epsilon^{ab} \bar{Q}_{La} \cdot \phi_b^\dagger u_R - Y_e \bar{E}_L \cdot \phi e_R + \ h.c. \tag{2.7}$$

where the matrices Y_u, Y_d, and Y_e, are the Yukawa coupling constants, ϵ^{ab} is the totally antisymmetric tensor, and $h.c.$ denotes the hermitian conjugate.

The primary concern of this analysis is the gauge bosons and multi-gauge-boson interaction terms. While the terms $\mathcal{L}_f$ and $\mathcal{L}_y$ have been included for completeness, they will not be considered further as they do not directly contribute to the understanding of multi-gauge-boson interactions.

The Lagrangian in equation 2.2 does not represent the interactions of physically observable fields. To understand the physical interactions of the Lagrangian, EW symmetry must be broken. Electroweak symmetry is spontaneously broken by the Higgs mechanism, whereby the Higgs field settles to a minimum of the quartic potential, found in equation 2.6, and acquires a vacuum expectation value (vev). When

this occurs, the Higgs field can be written as

$$\langle\phi\rangle = \frac{1}{\sqrt{2}}\begin{pmatrix}0\\ \\ v\end{pmatrix} \tag{2.8}$$

where $v = \sqrt{\frac{\mu^2}{\lambda}}$ is the minimum of the potential energy.

Once the Higgs acquires a vev, the gauge bosons gain mass through their interactions with the Higgs in the covariant derivative term $|D_\mu\phi|^2$. At the potential minimum, this term becomes

$$\begin{aligned} |D_\mu\phi|^2 &\rightarrow \frac{1}{2}\begin{pmatrix}0 & v\end{pmatrix}\left(gA^a_\mu\tau^a + \frac{1}{2}g'B_\mu\right)\left(gA^{b\mu}\tau^b + \frac{1}{2}g'B^\mu\right)\begin{pmatrix}0\\ \\ v\end{pmatrix} \\ &= \frac{v^2}{8}[g^2(A^1_\mu)^2 + g^2(A^2_\mu)^2 + (-gA^3_\mu + g'B_\mu)^2]. \end{aligned} \tag{2.9}$$

The terms with squared vector fields are exactly the form of a vector boson mass. In other words, one result of the Higgs acquiring a vev is that mass terms are generated for the vector bosons. Specifically, there are now three massive vector bosons, $W^\pm$ and Z, and a fourth massless vector boson, A, which is orthogonal to Z and represents the physical photon field. In terms of the original gauge fields, the new fields are

$$\begin{aligned} W^\pm_\mu &= \frac{1}{\sqrt{2}}(A^1_\mu \mp iA^2_\mu) \\ Z_\mu &= \frac{1}{\sqrt{g^2+g'^2}}(gA^3_\mu - g'B_\mu) \\ A_\mu &= \frac{1}{\sqrt{g^2+g'^2}}(gA^3_\mu + g'B_\mu) \end{aligned} \tag{2.10}$$

with masses

$$\begin{aligned} m_W &= g\frac{v}{2} \\ m_Z &= \sqrt{g^2+g'^2}\frac{v}{2} \\ m_A &= 0. \end{aligned} \tag{2.11}$$

It is easy to see that the two neutral fields, A and Z, are linear combinations of the original A^3 and B fields. This can be understood as a change of basis where the weak mixing angle, θ_W, is defined as the angle of rotation between the two bases, such that

$$\begin{aligned} Z &= \cos(\theta_W)A^3 - \sin(\theta_W)B \\ A &= \cos(\theta_W)A^3 + \sin(\theta_W)B \end{aligned} \tag{2.12}$$

where

$$\cos(\theta_W) = \frac{g}{\sqrt{g^2+g'^2}}, \qquad \sin(\theta_W) = \frac{g'}{\sqrt{g^2+g'^2}}. \tag{2.13}$$

From equations 2.13 and 2.11, one can see that the W and Z masses are not independent, but are related by $m_W = m_Z\cos(\theta_W)$. In addition, by analyzing the covariant derivative in this new basis after symmetry breaking, the coupling associated to the electromagnetic interactions of the photon field can be identified with the well known electron charge e,

$$e = \frac{gg'}{\sqrt{g^2+g'^2}}. \tag{2.14}$$

It is clear that there are many relations amongst the couplings and masses of particles in the EW sector. These relations arise from the underlying gauge symmetry and are fundamental predictions of the theory that can be, and have been, tested in order to determine the symmetries of nature.

2.2.2 Gauge Boson Self-Couplings

Multi-gauge-boson couplings arise from the non-abelian nature of the EW gauge group and take the form of boson self-interaction terms in the Lagrangian, as in equation 2.4. These terms exists only in theories with non-abelian symmetries and the allowed gauge boson self-interactions are determined by the representation of the group generators in the self-interaction term (which in the SM is the totally anti-symmetric tensor). Thus the gauge boson self interactions and couplings are completely fixed by the structure of the non-abelian symmetry.

In the SM before symmetry breaking, when the field strength is squared in equation 2.4, the presence of the antisymmetric tensor implies that the only allowed triple gauge coupling (TGC) vertex combinations are of the form $A^1A^2A^3$, while the only allowed quartic gauge coupling (QGC) vertex combinations are of the form $A^iA^jA^iA^j$, where $i, j \in \{1, 2, 3\}$ and $i \neq j$. To understand why these are the only allowed TGC and QGC combinations, one can appeal to the analogy with the SU(2) symmetry of spin. The A^i fields live in the adjoint representation, which is essentially the spin-1 representation. Thus the A^i's, each with a different SU(2) charge, are essentially the different spin states. The Lagrangian must be invariant under this SU(2) rotation, and thus the terms of the Lagrangian must form spin-0 singlets[1]. Considering the analogy with spin, it is easy to see that the allowed TGC and QGC vertices conserve the total SU(2) charge at each vertex and their combinations form the singlet states.

[1]It should be noted that each individual term does not have to be completely symmetric under rotations, but combinations of terms must. In analogy again with spin, two spin-1/2 particles can form a spin-0 state with the anti-symmetric combination $|\uparrow\downarrow\rangle - |\downarrow\uparrow\rangle$. In this case two terms are needed to form the singlet state.

After symmetry breaking, the original gauge fields must be transformed according to equation 2.10. Since combinations of the A^1 and A^2 fields form the W^+ and W^-, whereas the A^3 fields becomes a γ or Z, the only allowed TGC vertices will be W^+W^-Z and $W^+W^-\gamma$ while all other TGC's are forbidden by the SM. Applying the same logic to the QGC vertices, the only QGC vertices allowed in the SM after symmetry breaking are $W^+W^-W^+W^-$, W^+W^-ZZ, $W^+W^-\gamma\gamma$, and $W^+W^-Z\gamma$.

The transformation from the original gauge fields to the physical fields after symmetry breaking can now be applied to the gauge boson kinetic term of the Lagrangian, found in equation 2.3, in order to compute the exact coupling strength of each of the TGC and QGC vertices. After applying this transformation, and including the vector boson mass terms (discussed earlier), the gauge boson kinetic term is transformed to,

$$\Delta\mathcal{L} = -\frac{1}{2}W^+_{\mu\nu}W^{-\mu\nu} + m_W^2 W^+_\mu W^{-\mu} - \frac{1}{4}Z_{\mu\nu}Z^{\mu\nu} + \frac{1}{2}m_Z^2 Z_\mu Z^\mu + \mathcal{L}_{WWV} + \mathcal{L}_{WWVV} \quad (2.15)$$

where the new field strength tensors, without group indices, are defined as $X_{\mu\nu} = \partial_\mu X_\nu - \partial_\nu X_\mu$. The terms $\mathcal{L}_{WWV}$ and $\mathcal{L}_{WWVV}$ contain the TGC and QGC interactions, respectively, and take the form,

$$\begin{aligned}\mathcal{L}_{WWV} = \; & -ig[(W^+_{\mu\nu}W^{-\mu} - W^{+\mu}W^-_{\mu\nu})(A^\nu \sin(\theta_W) - Z^\nu \cos(\theta_W)) \\ & + W^-_\nu W^+_\mu (A^{\mu\nu}\sin(\theta_W) - Z^{\mu\nu}\cos(\theta_W))] \end{aligned} \quad (2.16)$$

and

$$\mathcal{L}_{WWVV} = -\frac{g^2}{4}\Big\{ \quad [2W^+_\mu W^{-\mu} + (A^\mu \sin(\theta_W) - Z^\mu \cos(\theta_W))^2]^2 \\ -[W^+_\mu W^-_\nu + W^+_\nu W^-_\mu \\ +(A^\mu \sin(\theta_W) - Z^\mu \cos(\theta_W))(A^\nu \sin(\theta_W) - Z^\nu \cos(\theta_W))]^2\Big\}. \tag{2.17}$$

The fundamental TGC interactions of the SM can be found in Figure 2.3. The two possible vertices are $WW\gamma$ and WWZ with coupling constants of $g_{WW\gamma} = -e$ and $g_{WWZ} = -e\cot(\theta_W)$ respectively. In addition, the coupling strength of these interactions have a momentum dependence coming from the derivative in each term of the Lagrangian, as seen in equation 2.16. The momentum dependence implies that the coupling strength of the TGC vertices will have a non-trivial dependence on the gauge-boson momentum.

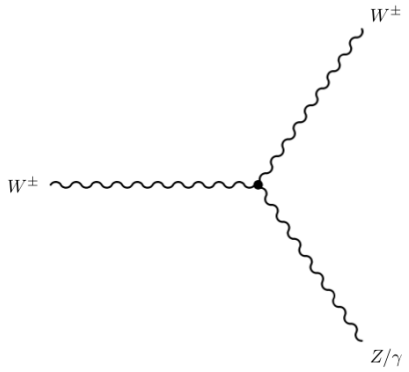

Figure 2.3: Fundamental triple gauge coupling vertex of electroweak gauge bosons.

The fundamental QGC interactions, as predicted by equation 2.17, can be found in Figure 2.4. The four possible vertices are $WWWW$, $WWZZ$, $WW\gamma\gamma$, and $WWZ\gamma$

with coupling constants of $g_{WWWW} = -\frac{e^2}{\sin^2(\theta_W)}$, $g_{WWZZ} = e^2\cot^2(\theta_W)$, $g_{WW\gamma\gamma} = e^2$, and $g_{WWZ\gamma} = e^2\cot(\theta_W)$ respectively.

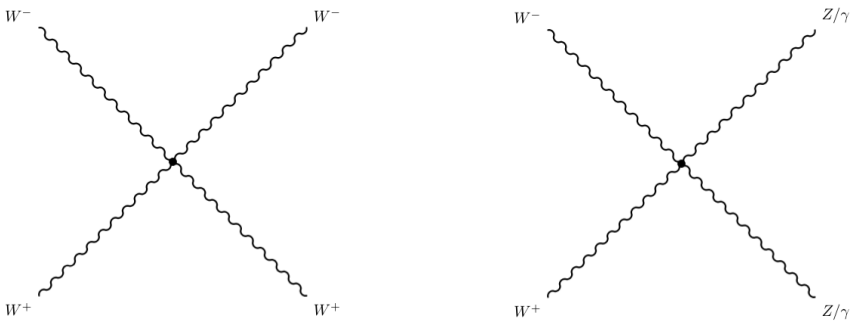

(a) QGC interactions involving only W bosons.

(b) QGC interactions involving W, Z, and γ.

Figure 2.4: Fundamental quartic gauge coupling vertices of electroweak gauge bosons.

As this analysis focuses on WZ diboson production and the study of the WWZ triple gauge couplings, the $WW\gamma$ and QGC vertices will not be described further here. Additional information on the $WW\gamma$ and QGC vertices can be found in references [99, 83, 79].

2.3 Anomalous Triple Gauge Couplings

In much the same way that Newtonian Mechanics is a large distance limit of quantum mechanics, one possibility is that the SM is a low energy limit of a more fundamental higher energy theory [112]. A great deal of work has been done on building theoretical models of high energy physics that reproduce the SM at low energies and do not violate existing experimental constraints, such as Super Symmetry

(SUSY) [101, 96, 81, 111, 114], Technicolor [72], Sequential Z' and W' [87, 95], and many others. At the same time, experiments push farther into the energy frontier and continue to search for and constrain models of new high energy physics. Currently, no signs of new physics have been observed and thus there is no way to determine which high energy models should be studied. However, generic approaches to model building can be followed based on the guiding principle that models of new physics should not violate any existing experimental constraints [70].

Given that no new physics signals have been directly observed, it is reasonable to assume that the scale of the high energy new physics, Λ, must be above the energies accessible by experiments. Much like Fermi's original theory of weak interactions [83], wherein the relatively high energy degree of freedom of the W boson gave rise to low energy observable consequences such as the point-like beta decay of the neutron, high energy new physics could give rise to observable deviations from the expected behavior of the SM at low energies. The method of effective Lagrangians provides a generic and model independent approach to parameterizing and studying these low energy deviations. Specifically, an effective Lagrangian is used to build a generic model of triple gauge couplings in $W^{\pm}Z$ production. The new couplings of the effective Lagrangian are termed anomalous triple gauge couplings (aTGC) as they describe couplings not predicted by the SM gauge theory.

2.3.1 Effective Lagrangian Approach

A model-independent effective Lagrangian approach is used to parameterize the non-SM physics contributing to $W^{\pm}Z$ production. The approach assumes Λ is above

the energy accessible by current experiments, and the low energy particle spectrum (i.e. the SM particle spectrum) is not changed. In this case, the high energy particles can affect the measured observables of SM particles at low energy through virtual effects. As the scale Λ is assumed to be much larger than the interaction energies and SM particle masses, the virtual effects can be summarized by a series expansion in powers of $1/\Lambda$ of effective vertices [70, 6]. These effective vertices express the deviations at low energy caused by the high energy physics in terms of local operators involving only the SM particles and form the effective Lagrangian, $\mathcal{L}_{eff}$, which can be written as

$$\mathcal{L}_{eff} = \sum_{n} \frac{1}{\Lambda^n} \sum_{i} \alpha_i^{(n)} \mathcal{O}_i^{(n)}. \tag{2.18}$$

where the operators $\mathcal{O}_i^{(n)}$ have dimension $[\text{mass}]^{n-4}$ and are local functions of the SM particle. The coupling coefficients, $\alpha_i^{(n)}$, are derived from the parameters of the original theory and parameterize all possible effects at low energies [70].

The expansion in equation 2.18 can be approximated using a finite number of terms because, by assumption, all particle momentum and masses lie significantly below the scale Λ and thus high order terms in the expansion become extremely small. However, at energies close to Λ all terms of the Lagrangian expansion become important and this approach will fail. At this limit close to Λ, the true underlying high energy theory must be used to build the Lagrangian and to make predictions. A more complete description of the effective Lagrangian method can be found in references [116, 6].

2.3.2 Model of WWZ Anomalous Triple Gauge Coupling

The effective Lagrangian for the WWZ triple gauge boson vertex is [84]

$$\begin{aligned}
\mathcal{L}_{WWZ}/g_{WWZ} &= ig_1^Z(W^\dagger_{\mu\nu}W^\mu Z^\mu - W^\dagger_\mu Z_\nu W^{\mu\nu}) + i\kappa_Z W^\dagger_\mu W_\nu Z^{\mu\nu} \\
&+ i\frac{\lambda_Z}{m_W^2}W^\dagger_{\lambda\mu}W^\mu{}_\nu Z^{\nu\lambda} - g_4^Z W^\dagger_{mu}W_\nu(\partial^\mu Z^\nu + \partial^\nu Z^\mu) \\
&+ g_5^Z\epsilon^{\mu\nu\lambda\rho}(W^\dagger_{mu}\partial_\lambda W_\nu - \partial_\lambda W^\dagger_{mu}W_\nu)Z_\rho \\
&+ i\tilde{\kappa}_Z W^\dagger_{mu}W_\nu\tilde{Z}^{\mu\nu} + i\frac{\tilde{\lambda}_Z}{m_W^2}W^\dagger_{\lambda\mu}W^\mu{}_\nu\tilde{Z}^{\nu\lambda}, \qquad (2.19)
\end{aligned}$$

where $g_{WWZ} = -e\cot(\theta_W)$, and $\tilde{X}_{\mu\nu} = \frac{1}{2}\epsilon_{\mu\nu\lambda\rho}X^{\lambda\rho}$. All operators of dimension 8 and higher have been cut off in this expansion, which is justified if Λ is large and thus the effect of aTGCs is small. More precisely, the expected size of the aTGCs is $\mathcal{O}(\frac{m_W^2}{\Lambda^2})$ and thus aTGCs of $\mathcal{O}(10^{-2})$ are expected for $\Lambda = 1$ TeV with deviations decease with increasing Λ [70, 6][2]. It should be noted that if large aTGCs are observed, this would indicate the presence of new physics at a low energy scale. In this case the effective Lagrangian would not describe the proper degrees of freedom of the underlying physics, but the break-down of this approach at low energies would be an important and identifiable signal of the presence of new physics within the energy reach of experiments.

In the SM at tree level, all of the anomalous couplings in equation 2.19 are zero except $g_1^Z = \kappa_Z = 1$. In order to isolate the anomalous components of g_1^Z and κ_Z, one can define the couplings $\Delta g_1^Z \equiv g_1^Z - 1$ and $\Delta\kappa_Z \equiv \kappa_Z - 1$. All of the anomalous couplings, except g_1^Z, κ_Z, and λ_Z, violate one of the discrete symmetries P or C, and

[2]This assumes that EW symmetry is broken by a scalar such as the Higgs. In the case of symmetry breaking from strong dynamics, this relation does not hold and aTGCs can be as large as $\mathcal{O}(10^{-2})$ for $\Lambda = 3$ TeV [70].

possibly the combined symmetry CP. The summary of the properties under discrete transformation can be found in Table 2.1.

Coupling	$\{\Delta g_1^Z, \Delta\kappa_Z, \lambda_Z\}$	Δg_4^Z	Δg_5^Z	$\{\Delta\tilde{\kappa}_Z, \tilde{\lambda}_Z\}$
P	+	+	-	-
C	+	-	-	+
CP	+	-	+	-

Table 2.1: Behavior of anomalous coupling under discrete transformations [84, 70].

To simplify the analysis, and to avoid injecting new sources of C,P, or CP violation into physical observables, all of the terms in the effective Lagrangian which violate C or P can be discarded. In this case, the most general C and P conserving effective Lagrangian is,

$$\frac{\mathcal{L}_{WWZ}}{g_{WWZ}} = ig_1^Z(W^\dagger_{\mu\nu}W^\mu Z^\mu - W^\dagger_\mu Z_\nu W^{\mu\nu}) + i\kappa_Z W^\dagger_\mu W_\nu Z^{\mu\nu} + i\frac{\lambda_Z}{m_W^2}W^\dagger_{\lambda\mu}W^\mu{}_\nu Z^{\nu\lambda}. \tag{2.20}$$

Only one dimension-6 operator is left in the effective Lagrangian, with all others being of dimension-4. The anomalous interaction amplitudes have a non-trivial dependence on the total energy at the TGC vertex, $\hat{s}$ (equivalent to the diboson invariant mass). To give a rough estimate, the dependence on $\hat{s}$ of the terms in the Lagrangian associated to the different anomalous couplings can be found in Table 2.2. The fact that the anomalous contributions for the $\Delta\kappa_Z$ terms grow as $\sqrt{\hat{s}}$, while the other contributions grow as $\hat{s}$, implies that the limits on coupling's sizes will be least stringent on $\Delta\kappa_Z$ at a fixed energy.

Coupling	Proportionality
Δg_1^Z	$\hat{s}$
$\Delta\kappa_Z$	$\sqrt{\hat{s}}$
λ_Z	$\hat{s}$

Table 2.2: Dependence of anomalous couplings on the energy at the TGC vertex [24].

The remainder of this analysis will concentrate on this model of C and P conserving aTGCs. Further information on the effects of C and P violating terms can be found in references [84, 70, 67].

2.3.3 Unitarity Violation

As noted earlier, the effective interactions are not adequate for properly describing interactions at energies close to Λ. One important consequence is that at high enough energies, tree-level unitarity will be violated by the effective interactions. For example, interactions involving the λ_Z coupling will violate unitarity at energies above $\sim m_W/\sqrt{\lambda_Z}$ [70]. Of course, as is well known for the case of gauge theories, individual interactions may violate unitarity but the sum of all interactions contributing to the amplitude will behave properly at high energies [99]. However, the effective Lagrangian in equation 2.20 is not guaranteed to be invariant under the SM gauge group[3], nor is it renormalizable due to the presence of the dimension 6 operator, and thus tree level unitarity is not ensured.

[3]It should be noted that the SM gauge symmetry can be enforced on the effective Lagrangion, and will give rise to relations between the various couplings of the WWZ and $WW\gamma$ vertices. For maximum generality, this approach is not used in this analysis, but more information can be found in [70].

In order to avoid this unitarity violation near and above Λ, either the correct high-energy particle spectrum must be known and used to define the Lagrangian, or form-factors can be added to the effective couplings. Both of these approaches are model-dependent, and thus contradict the general model-independent approach of the effective Lagrangian. However, introducing form factors requires relatively fewer assumptions about the high energy physics. Therefore, the anomalous couplings can be modified with a form-factor, as in reference [70], such that,

$$\alpha \to \alpha(\hat{s}) \equiv \frac{\alpha}{(1 + \hat{s}/\Lambda_{FF}^2)^n} \tag{2.21}$$

where $\alpha \in \{\Delta g_1^Z,\ \Delta\kappa_Z,\ \lambda_Z\}$, and n is the exponent chosen to ensure unitarity (i.e. to ensure that the effects of the anomalous couplings vanish as $\hat{s} \to \infty$). In this context, Λ_{FF} serves as the cut-off scale, above which the effect of aTGCs is negligible. Λ_{FF} is not known *a priori* because it is a function of the new physics scale Λ and the couplings of the high energy theory. However, given a complete high energy theory, the values of Λ_{FF} and n could be computed.

The purpose of the form factor is to dampen the effect of the anomalous couplings at high energies. In a theory where all high energy degrees of freedom are known, a form factor would arise naturally from the high energy particle interactions and could be computed explicitly. While this high energy theory is not specified, the choice of the form factor parameters n and Λ_{FF} are not general as only a subset of high energy theories could have generated a form-factor with these parameters. The choice of this form-factor will thus have a major effect on experimental searches and limits on anomalous couplings. For example, in the case of the WWZ vertex typically $n = 2$

is used and Λ_{FF} is chosen to be 2 or 3 TeV [70, 44, 62]. If new physics happens to be present near 2 TeV, the anomalous coupling search may miss this signal because the form factor will have essentially completely damped anomalous coupling contributions near the new physics.

The proper approach to using form-factors has been discussed in the LHC EW working group meetings [89], and there has been no clear consensus on whether experimental searches should use form-factors. One option is to avoid using form factors altogether, which has the benefit of model-independence but allows for unitarity violation. Of course, nature does not violate unitarity, as long as Quantum Mechanics is correct, and the center-of-mass energies of experiments are finite. Thus unitarity violations are not expected to be realized in experiments. One could restrict searches to regimes of physical observables below the unitarity violating energy scale, but this approach does not test the highest energy regimes where the effects of aTGCs are most predominant. The approach of this analysis when setting limits on aTGCs is to quote two limits, one with no form factor and one with the typical form factor used by experiments ($n = 2$, $\Lambda_{FF} = 2$ TeV).

2.3.4 Impact on Physical Observables

One important impact of aTGCs is to modify the expected behavior of measured observables. Due to the $\hat{s}$ dependence of the aTGCs, seen in Table 2.2, observables that are sensitive to $\hat{s}$ will be sensitive to aTGCs, such as the total cross section, mass or transverse mass of the $W^{\pm}Z$ system, or the p_T of the hardest lepton in the case when the W and Z bosons decay leptonically. In addition, the presence of the

derivative in the couplings, seen the effective Lagrangian of equation 2.20, translates to a gauge boson momentum dependence. Thus, the p_T of the Z boson is particularly sensitive to aTGCs. Further, the spin structure of aTGCs will change the shapes of spin-dependent observables, such as the Z leptons' rapidities, or the lepton decay angles.

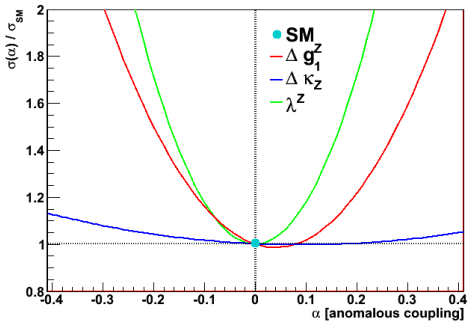

(a) Cross section

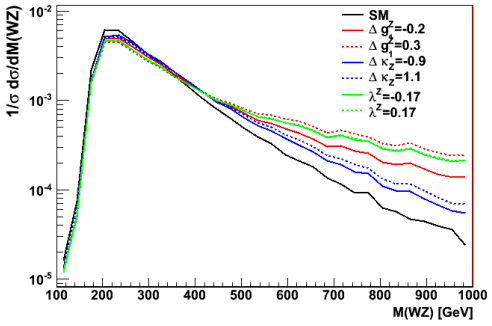

(b) m_{WZ}

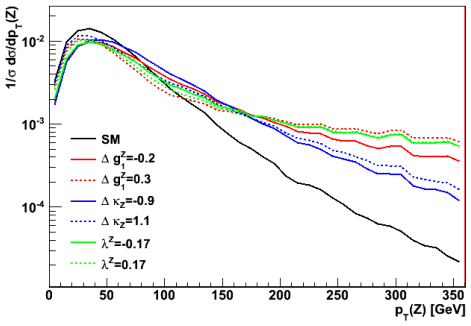

(c) $p_T(Z)$

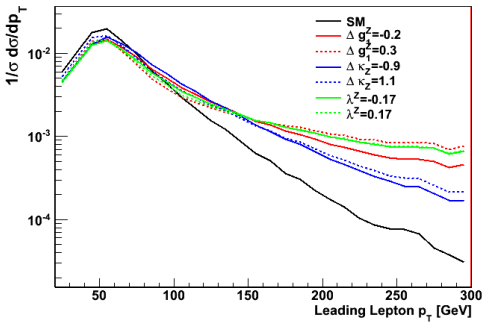

(d) Leading lepton p_T.

Figure 2.5: Impact of anomalous couplings on physical observables. A form factor with $n = 2$ and $\Lambda_{FF} = 2$ TeV is used in these distributions.

The dependence on aTGCs of the inclusive $W^{\pm}Z$ cross section, as well as the distributions of several observables, can be found in Figure 2.5. These distributions are

produced with the MC@NLO event generator [76], using the CTEQ6.6 parton distribution functions [100], for proton-proton collisions at center of mass energy $E_{CM} = 7$ TeV[4]. The black line in all distributions of Figure 2.5 shows the SM prediction, while the colored lines show the expected distributions with anomalous couplings (only the anomalous coupling mentioned in the legend for each color is altered from the SM value). As seen in Figure 2.5(a), the cross section has a strong and quadratic dependence on aTGCs. This quadratic dependence comes from the fact that the matrix elements are linear in anomalous couplings, and thus the cross section, which depends on the square matrix elements, must be quadratic. The mass of the $W^{\pm}Z$ system can be found in Figure 2.5(b), the transverse momentum of the Z in Figure 2.5(c), and the transverse momentum of the highest p_T lepton in Figure 2.5(d).

While all of these distributions show large deviations at high mass or momentum, the Z transverse momentum is particularly sensitive. In addition, the peak of the Z transverse momentum at low energies is shifted depending on the choice and sign of the aTGC. For these reasons, the Z transverse momentum distribution is a particularly good choice for aTGC searches if there is adequate experimental data. If the statistics are small for an experimental search, the cross section, or similarly the expected event yield, is a good choice for searches due to the high sensitivity to aTGCs.

[4]The relevant details of QCD, hadron collider physics, parton distribution functions, and $W^{\pm}Z$ production at colliders can be found in sections 2.4 and 2.5.

2.4 QCD and Physics at Hadron Colliders

Underlying the physics of proton-proton (or proton-anti-proton) collisions occurring at hadron colliders, like the LHC, is the theory of Quantum Chromo Dynamics (QCD) [68]. The proton is a hadron composed of quarks and gluons and QCD describes the strong interactions of these quarks and gluons. The fundamental interaction vertices of QCD can be found in Figure 2.6. Notice that QCD contains multi-gauge boson self-interactions of gluons, as seen in the vertices 2.6(b) and 2.6(c), which arise from the non-abelian nature of the $SU(3)$ symmetry of QCD. These are the QCD analogues to the EW TGC and QGC vertices.

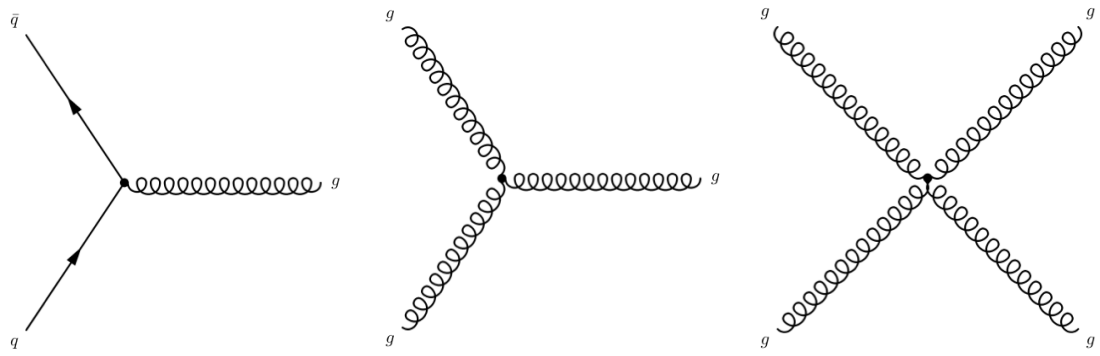

(a) QCD interaction between quarks and gluons

(b) QCD triple gluon self-interaction

(c) QCD quartic gluon self-interaction

Figure 2.6: Fundamental interaction vertices of QCD.

Perhaps the most important feature of QCD is *asymptotic freedom*, which refers to the fact that the QCD coupling strength, α_s, decreases with increasing energy. Specifically,

$$\alpha_s(Q) = \frac{6\pi}{(11n_c - 2n_f)\log(Q/\Lambda_{QCD})} \tag{2.22}$$

where $n_c = 3$ is the number of color charges, $n_f = 6$ is the number of quark flavors, $\Lambda_{QCD} \sim 200$ MeV is the QCD scale, and Q is the energy transfer of the interaction.

At high enough energies, or short enough distances, α_s becomes small enough that colored particles can effectively be treated as free, and thus perturbative QCD (pQCD) calculations can be performed as expansions in α_s. Conversely, at low energies, or large distances, α_s becomes increasingly large, negating the possibility for perturbative expansions in α_s. In this non-perturbative low energy regime, the increasing strength of α_s as distance increases implies that the QCD potential energy between color-charged quarks increases as they are separated. When enough potential energy becomes available, a quark-anti-quark pair can be produced in order to bind and neutralize the color charge of the original separated quarks. As a result, only color neutral hadrons such as the proton, rather than isolated color charges, can be observed in nature. This property of QCD is known as *confinement*.

In high energy proton collisions QCD plays a fundamental role. The proton is a bound state of strongly interacting quarks and gluons, or *partons*, confined within the proton. When colliding two protons at high energies, interactions take place between the partons of the two protons giving rise to hard scatterings. As noted earlier, when considering the high energy hard scattering of two free partons, pQCD can be used to calculate scattering amplitudes. However, inside of the proton the physics governing the interactions amongst partons is low energy non-perturbative, or soft, QCD. The question then arises of how to separate the soft physics inside of the proton from the physics of the hard scattering between protons. Fortunately, the *factorization*

theorem, first proposed by Drell and Yan [65], offers guidance.

The factorization theorem suggests that the hard and soft aspects of hadron collisions can be split, whereby the perturbative and process-dependent hard scattering can be separated from the non-perturbative but universal (i.e. process-independent) structure inside of the proton. Essentially, the physics inside of the proton can be summarized with a set of probability distributions of quarks and gluons, or *parton distribution functions* (PDF), which are independent of what particle is used to probe the proton and thus independent of the details of the hard scattering. These PDFs encapsulate all of the non-perturbative QCD that determines the probability of finding a parton of a given flavor and momentum inside of the proton. To calculate full interaction cross sections starting from the proton, the amplitudes for hard scattering between partons should be convolved with the PDFs in order to incorporate the probability of finding the necessary partons for the hard interaction.

Qualitatively, this approach of separating the low energy and high energy physics is sensible. The hard scattering physics taking place with a momentum transfer Q^2 has a typical interaction timescale of $\sim 1/Q$. The soft interactions inside of the proton have an energy typically close to the QCD scale Λ_{QCD}, and thus have a typical interaction timescale of $\sim 1/\Lambda_{QCD}$. Since typical hard scattering processes like vector boson production have a $Q >> \Lambda_{QCD}$, the timescale of the hard interaction is much shorter than the timescale of the soft physics inside the proton. This implies that during the time at which the hard interaction occurs, the internal structure of the proton can not be changing significantly and thus must have been determined before the hard

interaction took place. It then becomes quite natural to separate these two processes and calculate their contributions to the scattering process independently.

This picture of separating the hard and soft process can be summarized by Figure 2.7 for a pp collision giving rise to a $W^{\pm}Z$ pair. In this diagram, a quark from one proton and an anti-quark from the other are selected out of the proton PDF, represented by the grey circles, and then interact on the right hand side inside through the hard scattering process, represented by the red circle, which then leads to the production of the W and Z bosons. The physics of the hard interaction giving rise to the $W^{\pm}Z$ pair will be discussed further in section 2.5.

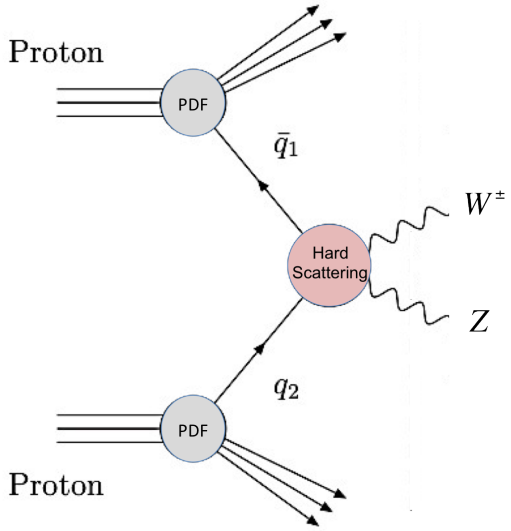

Figure 2.7: $W^{\pm}Z$ production at p-p colliders [2].

One additional feature of the hard scattering process is that high energy quarks and gluons can be produced in the interaction. The contribution of these high energy quarks/gluons can be calculated pertubatively as a part of the scattering amplitude.

These high energy quarks/gluons are effectively free from the interactions inside the proton, and thus are are not contained in the PDF. However, free color-charged particles can not be observed in nature. Instead, the high energy quark/gluon pulls addition quarks and gluons from the vacuum and radiates gluons as is travels, a process known as fragmentation. These quarks and gluons quickly hadronize and neutralize any free color charge. The end product is a collimated spray of hadrons, known as a *Jet*, proceeding in approximately the original direction of the quark/gluon. This is an extremely simplified explanation of jet production and more complete descriptions can be found in References [69, 68].

2.4.1 Proton Structure

A detailed discussion of the proton structure can be found in references [68, 99] and only a few important points are summarized here. The proton comprises two u and one d *valence* quarks which are confined within the proton and whose charge sum yields the overall charge of the proton. The quarks interact by the exchange of gluons and subsequently the gluons can also pair produce additional quark-anti-quark pairs, called *sea* quarks, or self-interact to produce more gluons. The momentum of the proton is distributed amongst these partons, i.e. valence quarks, sea quarks, and gluons. The PDFs mentioned earlier describe the probability to find a parton with a given fraction of the proton momentum, i.e. $p_i = xP$ where p_i is the momentum of parton i carrying a fraction x of the proton momentum P.

When probed at low energies, the three valence quarks essentially carry all of the proton's momentum. However, when the energy transfer Q^2 is large, $Q^2 \gtrsim 1$ GeV,

the complex sub-structure of valence quarks, sea quarks, and gluons can be resolved. As the proton is probed with larger and larger energies, and thus finer scales, the substructure evolves and the total momentum is shared amongst a larger and larger number of constituents (although the valence quarks always tend to carry significant fractions of the proton momentum). The proton substructure depends on Q because partons at high x tend to radiate and drop down to lower values of x, while at the same time additional new partons at low x arise from the radiation [99]. Thus, as the energy Q^2 increases, the probability to find partons with large x tends to decrease while the probability at low x tends to increase more rapidly.

The fundamental source of this Q dependence is gluon radiation, specifically the effects of soft and collinear gluon emission. Soft and collinear gluons emissions lead to divergences which, when incorporated into the PDF, lead to a logarithmic scale dependence of the PDF on Q^2. Incorporating all of this information, the PDFs take the form $f_i(x, Q^2)$, where i is the parton type, x is the momentum fraction, and Q^2 is scale. These PDFs can not be calculated from first principles, due to the presence of non-perturbative effects, but the evolution of the PDFs with Q^2 can be calculated [68, 99]. Thus, the PDFs can be fit to experimental data at one scale and evolved to different scales. An example of the PDFs at $Q = 100$ GeV from the CTEQ group [100] can be found in Figure 2.8.

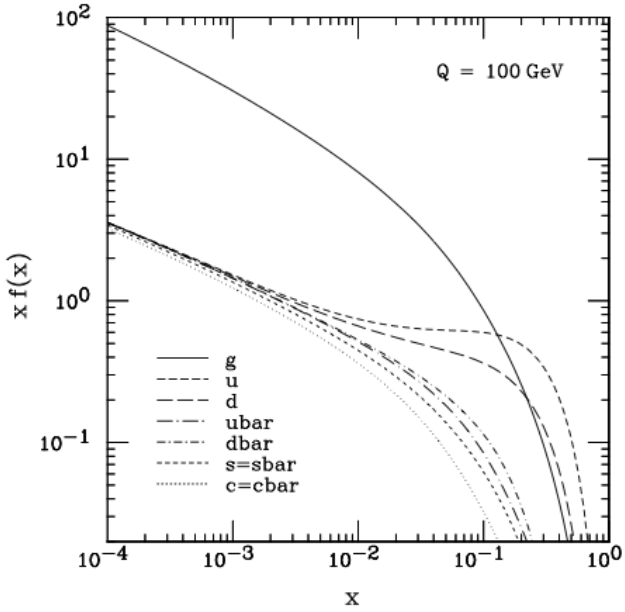

Figure 2.8: Parton distribution functions as calculated by the CTEQ group [100].

2.5 $W^{\pm}Z$ Production at Colliders

The primary production mechanism for $W^{\pm}Z$ events at hadron colliders is from quark-anti-quark annihilation, as seen in Figure 2.9. In order conserve charge, for $W^{+}Z$ production the quark must be an up-type quark and the anti-quark must be a down-type quark, and conversely for $W^{-}Z$. The quark and anti-quark are not required to be from the same generation, although cross-generation $W^{\pm}Z$ production is highly suppressed due to the small off-diagonal elements of the CKM matrix [83].

At leading order (LO) there are three Feynman diagrams contributing to the $q\bar{q} \rightarrow W^{\pm}Z$ process, as shown in Figure 2.9. In the t-channel and u-channel diagrams, the W and Z are emitted from quark lines. The s-channel diagram is the only LO diagram which contains the TGC vertex, whereby a $q\bar{q}$ pair annihilate to an off-shell W which

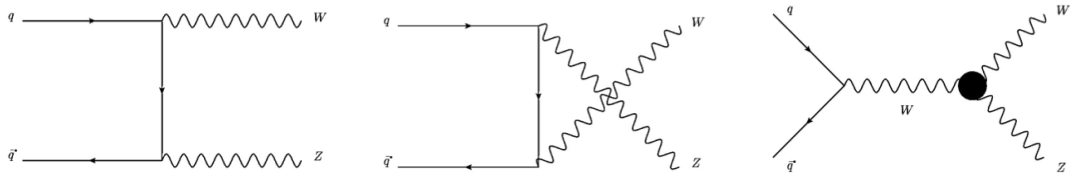

(a) t-channel (b) u-channel (c) s-channel

Figure 2.9: LO diagrams for $W^{\pm}Z$ production.

then decays to the $W^{\pm}Z$ pair via the triple gauge coupling vertex. When next-to-leading order (NLO) corrections from QCD are included, the $W^{\pm}Z$ process can also be induced by gluon-quark or gluon-anti-quark interactions, as seen in the Feynman diagrams of Figures 2.10(a), 2.10(b), 2.10(c), 2.10(f), and 2.10(g). These $gq(\bar{q})$ processes result in an additional quark being present in the final state. Additional NLO corrections include $q\bar{q}$ initiated interactions with gluon bremsstrahlung in the final state (diagrams 2.10(d), and 2.10(e)), as well as $q\bar{q}$ interactions with virtual corrections (diagrams 2.10(h) - 2.10(k)).

The processes in Figures 2.9 and 2.10 represent the interactions of free quarks, i.e. the hard interaction partons selected from each proton. These diagrams must be convolved with the proton PDFs in order to calculate the full cross section for $W^{\pm}Z$ production. Notice that some of the NLO diagrams include gluon bremsstrahlung. The gluons included in the hard scattering diagram are emitted with enough energy that their contribution to the scattering amplitude can be calculated perturbatively, while soft gluons contributions are contained in the PDFs.

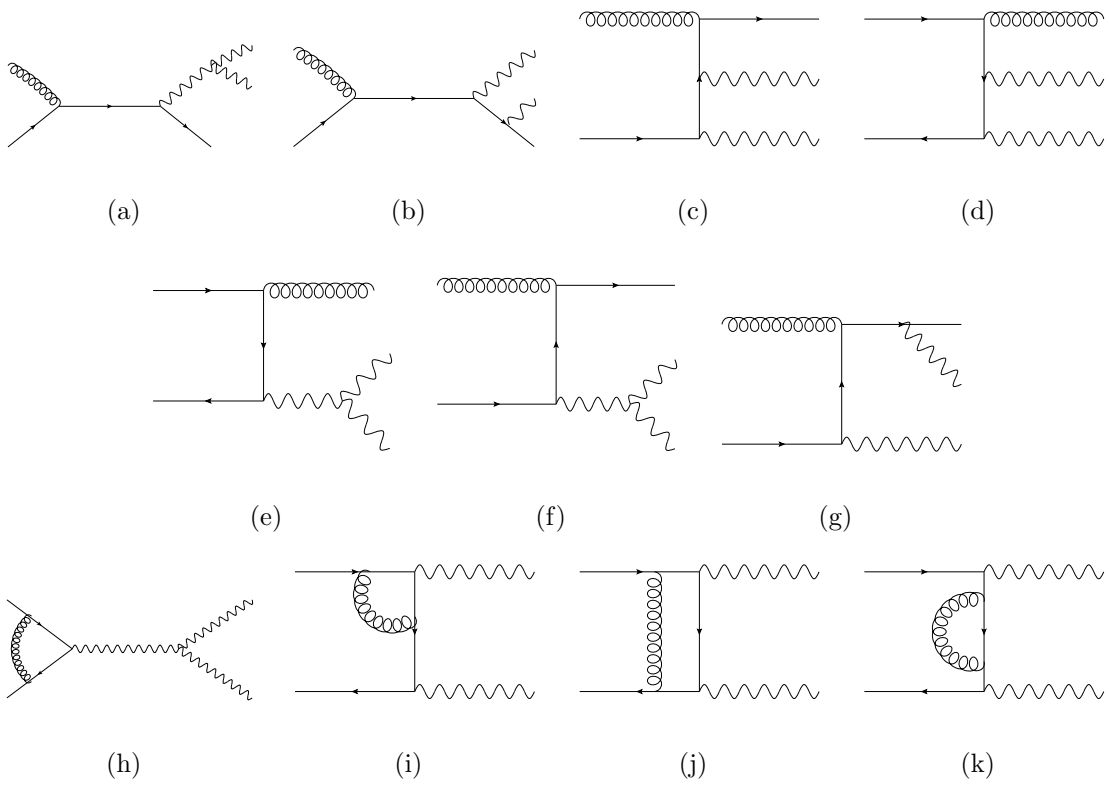

Figure 2.10: QCD NLO corrections to $W^{\pm}Z$ production. Figures 2.10(a) - 2.10(g) are the real contributions with additional quarks or gluons in the final state. Figures 2.10(h) - 2.10(k) are the virtual contributions with internal gluon loops.

The predicted cross section for the W^+Z, W^-Z, and $W^\pm Z$ processes are shown in Table 2.3. The calculations are done using MCFM [55] and PDF CTEQ6.6 [100]. In the MCFM calculation full spin correlations, the Z and W widths, and Z/γ^* interference have been included. Due to the Z/γ^* interference, the $W^\pm Z$ cross section diverges at very low m_{Z/γ^*} and an appropriate phase space must be defined for the cross section calculation. As the contributions from the Z become extremely small far from the Z mass-pole, a window around the Z mass-pole is used. Calculations for two different mass windows are shown. These calculations show that the QCD NLO contributions to the $W^\pm Z$ production cross section are quite large, on the order of 75% of the LO cross section, and can not be ignored. Further, MCFM estimates that 85-87% of the cross section comes from $q\bar{q}$ annihilation with the remainder coming from qg interactions (contributions from $\bar{q}g$ were found to be negligible, which is consistent with much larger availability of quarks than anti-quarks in the proton PDFs).

Process	σ [pb] LO $m_Z \in \{66-116\}$ GeV	σ [pb] NLO in QCD $m_Z \in \{66-116\}$	σ [pb] NLO in QCD $m_Z \in \{81-101\}$
W^+Z	6.70	11.50	11.17
W^-Z	3.65	6.47	6.03
$W^\pm Z$	10.35	17.97	17.20

Table 2.3: Cross sections for the $pp \to W^\pm Z$ process at $\sqrt{s} = 7$ TeV at LO and NLO in QCD, as calculated in references [35, 10] using MCFM [55] and pdf CTEQ6.6 [100]. Results with different cuts on the Z mass window are also shown.

The analysis presented in this thesis uses the fully leptonic decays of the W and Z to measure the cross section. These leptonic decay channels produce striking 3-lepton signatures in detectors and have relatively small backgrounds in experimental

searches (as opposed to the hadronic decays of W and Z which have large experimental backgrounds from QCD multi-jet production). However, the leptonic decays only represent a small fraction of possible W and Z decays, as can be seen in Tables 2.4 and 2.5 for the W and Z respectively and for the $W^{\pm}Z$ pair in Table 2.6. The branching ratio for the $W^{\pm}Z \to l\nu ll$ process is approximately 0.365% for each leptonic decay channel. Including all four combinations with electrons and muons in the final state, the total branching fraction is approximately 1.5%.

Decay	Branching Fraction [%]
$l^{\pm}\nu$ (per flavor)	10.80±0.09
Hadrons	67.60±0.27

Table 2.4: W branching Fractions [95].

Decay	Branching Fraction [%]
$l^{+}l^{-}$ (per flavor)	3.3658±0.0023
Invisible ($\nu\bar{\nu}$ all flavors)	20.00±0.06
Hadrons	69.91±0.06

Table 2.5: Z branching Fractions [95].

Decay	Branching Fraction [%]
$l^{\pm}\nu l'^{+}l'^{-}$ (per flavor)	0.364±0.003
$l^{\pm}$ + Invisible (per flavor)	2.16±0.02
Hadrons (+anything)	90.25±0.07

Table 2.6: WZ branching Fractions, derived from Tables 2.4 and 2.5.

2.6 Previous Measurements

Measurements of the $W^{\pm}Z$ production cross section and limits on aTGCs have previously been performed by the DØ and CDF experiments at the Tevatron $p\bar{p}$ collider at $\sqrt{s} = 1.96$ TeV [63, 62, 56, 57]. These were the first experiments to observe $W^{\pm}Z$ production and set direct limits on aTGCs in $W^{\pm}Z$ production. Prior to the Tevatron, indirect limits on anomalous couplings in the WWZ vertex were measured using the WW final state by the LEP collaborations [106]. Direct limits on WWZ anomalous couplings using the $W^{\pm}Z$ final state were not possible at LEP as the $W^{\pm}Z$ final state is charged and LEP could only produce charge neutral final states.

For the measurement of the $W^{\pm}Z$ production cross section, the DØ experiment used 8.6 fb^{-1} of integrated luminosity in which 75 candidate events were observed in the fully leptonic $W^{\pm}Z \to l\nu ll$ decay channel (where $l \in \{e, \mu\}$). The production cross section was measured to be $\sigma(p\bar{p} \to W^{\pm}Z) = 4.50 \pm 0.61\ (stat.)\ ^{+.16}_{-0.25}(syst.)$ pb, in agreement with the NLO prediction from MCFM [55] of 3.21 ± 0.12 pb. Limits on aTGCs were derived using 4.1 fb^{-1} of integrated luminosity in which 34 candidate events were observed. The Z boson transverse momentum spectrum was used to search for the presence of aTGCs and calculate limits. Limits on aTGCs were derived using a form factor with $n = 2$ and $\Lambda_{FF} = 2$ TeV and can be found in Table 2.7.

The CDF experiment used 7.1 fb^{-1} of integrated luminosity for the measurement of the $W^{\pm}Z$ production cross section and to derive limits on aTGCs. A total of 64 candidate events were observed in the fully leptonic decay channel with electrons and muons in the final state, leading to a measured cross section of $\sigma(p\bar{p} \to W^{\pm}Z) =$

$3.9^{+.6}_{-0.5}(stat.)\ ^{+.6}_{-0.4}(syst.)$ pb, in agreement with the NLO prediction of 3.46 ± 0.21 pb. The Z boson transverse momentum spectrum was used to search for the presence of aTGCs and calculate limits. Limits on aTGCs were derived using a form factor with $n = 2$ and $\Lambda_{FF} = 2$ TeV and can be found in Table 2.7.

Experiment	Cross Section [pb]	Δg_1^Z	$\Delta\kappa_Z$	λ_Z
DØ	$4.50^{+0.63}_{-0.66}$	[-0.053, 0.156]	[-0.376, 0.686]	[-0.075, 0.093]
CDF	$3.9^{+0.8}_{-0.7}$	[-0.08, 0.20]	[-0.39, 0.90]	[-0.09, 0.11]

Table 2.7: Measurements of $W^{\pm}Z$ production cross section and limits on aTGCs at the 95% confidence interval, obtained from direct measurement of the WWZ vertex, from the DØ and CDF collaborations [63, 62, 56, 57]. Limits were derived using a form factor with $n = 2$ and $\Lambda_{FF} = 2$ TeV.

Chapter 3

The Large Hadron Collider

The Large Hadron Collider (LHC) is a circular superconducting hadron accelerator and collider located at CERN in Geneva, Switzerland. The accelerator is designed to provide 14 TeV proton-proton collisions at an instantaneous luminosity of 10^{34} cm^{-2} s^{-1}, making it the world's highest energy and highest luminosity proton collider. The LHC combines cutting edge accelerator technology with the existing infrastructure in place at CERN from the LEP experiment in order to provide the energy and luminosity needed to fully explore the rarest physics processes at the TeV scale. In addition, the LHC is designed to provide lead ion collisions at 2.76 TeV/nucleon at an instantaneous luminosity of 10^{27} cm^{-2} s^{-1} in order to probe the landscape of high energy nuclear physics.

The layout of the LHC can be seen in Figure 3.1. There are eight straight sections and eight arcs in the LHC ring. Counter rotating beams of protons are injected into the LHC around Point 1, and are accelerated at Point 4 using radio frequency (RF)

superconducting cavities. Collisions occur at Points 1, 2, 5, and 8 and major detector experiments have been built at each of these points in order extract the physics from the LHC collisions. The experiments are:

- ATLAS ("**A** **T**oroidal **L**HC **A**pparatu**S**") [39] and CMS ("**C**ompact **M**uon **S**olenoid") [58] are general purpose detectors designed to be sensitive to a broad scope of possible new physics signatures produced at the highest energy proton-proton collisions. The goal of these experiments is to provide precision measurements of the Standard Model up to the TeV scale, understand electroweak symmetry breaking and search for the Higgs boson, and to search for new physics beyond the Standard Model.

- ALICE ("**A** **L**arge **I**on **C**ollider **E**xperiment") [7] is designed to study the lead-lead collisions of the LHC and as such uses detector technologies that are able to function properly in the presence of extremely high track multiplicities. One of the major physics goals of ALICE is to understand the properties of a new state of matter known as the *quark-gluon plasma*.

- LHCb ("**LHC** **B**eauty") [90] is designed to study the physics of b-quarks and B-hadrons and is instrumented in the forward regions of collisions. One of the major goals of LHCb is to search for signs of CP violation in B decays in order to understand the particle/anti-particle asymmetry of the universe.

In addition, several smaller experiments, such as TOTEM [109], LHCf [91], and MoEDAL [94], have been installed on the LHC with much more specific physics goals.

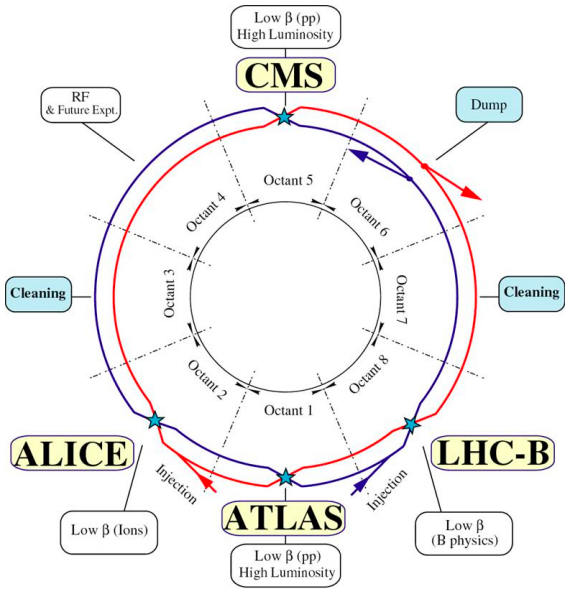

Figure 3.1: The layout of the detectors at the LHC [71].

This remainder of this chapter provides a brief introduction to the LHC technical design in Section 3.1 and some aspects of the achieved accelerator performance in 2011 in Section 3.2. It should be noted that many of the LHC design parameters discussed in Section 3.1 have not yet been reached (such as full 7 TeV beam energy, or bending magnetic field strength needed for such beam energies) and the attained LHC parameters are discussed in Section 3.2. An in-depth overview of the LHC can be found in reference [71], and the full details of the technical design can be found in references [52, 53, 50].

3.1 Design

The LHC is installed in the existing 26.7 km long tunnel originally created for the LEP machine at CERN. The tunnel lies between 45 m and 170 m below the surface of

the earth on a plane with slope of ∼1.4%. While an accelerator of this energy would ideally be built with a larger circumference, it was significantly cheaper to place the LHC in the already excavated LEP tunnel rather than to bore a new tunnel.

The existing CERN accelerator complex acts as the injector into the LHC ring, though the injector accelerators were upgraded for operations with the LHC. The layout for the LHC and injector chain can be found in Figure 3.2. The protons are produced at the LINAC 2 linear accelerator with an energy of 50 MeV, accelerated to 1.4 GeV in the Proton Synchrotron Booster (PSB), further accelerated to 25 GeV in the Proton Synchrotron (PS), and finally accelerated to 450 GeV by the Super Proton Synchrotron (SPS) and injected into the LHC ring.

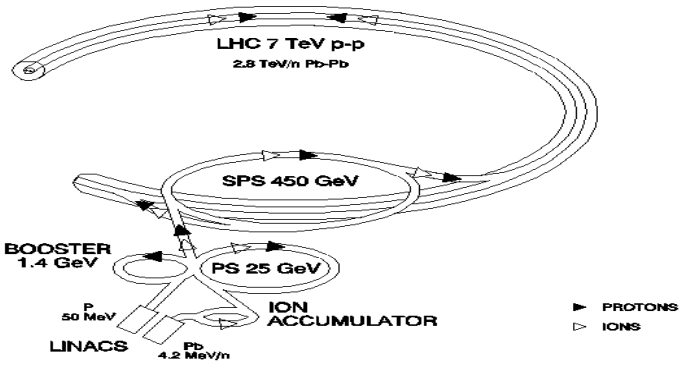

Figure 3.2: The layout of the LHC and the CERN accelerator complex acting as the injector chain for the LHC [71].

Once inside the LHC ring, the protons are accelerated by electric fields in superconducting RF cavities operating at 400 MHz with an accelerating gradient of 5 MV/m and are located around Point 4. Once the nominal beam energy is reached, the RF cavities also provide energy corrections to the beams in order to account for the ∼7

keV of synchrotron radiation loss per turn. The protons are steered through the LHC using superconducting NbTi magnets cooled to 2 K. In order to bend the 7 TeV beams of protons around the 27 km ring, dipole bending magnets are used and operated with fields of approximately 8.3 T. In addition, superconducting quadrupole and higher order magnets are used for focusing, for beam corrections, and for steering the beams into the collisions. Ideally, completely separate proton rings and magnets would be used for each of the two beams, but this was not feasible or cost effective due to space limitations inside of the LEP tunnel. Thus, the LHC uses a *two-in-one* or *twin-bore* design [51] whereby both proton rings are contained within the same cryostat. One of the LHC twin-bore dipole magnets can be seen in Figure 3.3. The major disadvantage of this design is that the distance between the two proton rings is small enough that they are coupled both magnetically and mechanically, making the design of the magnets extremely complicated [71].

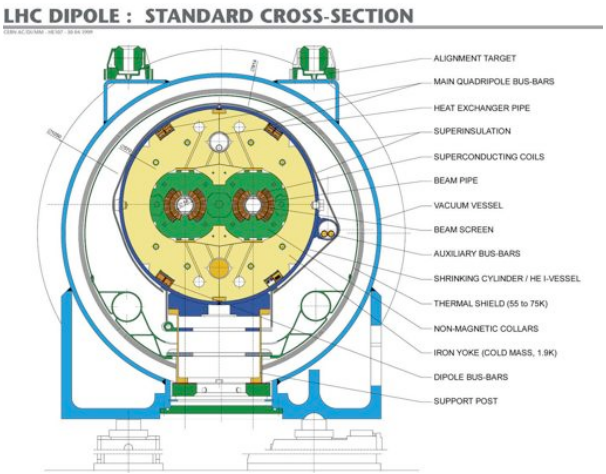

Figure 3.3: An example of an LHC dipole magnet with the twin bore design [48].

The protons are provided to the LHC in *bunches* of $\sim 10^{11}$ protons placed in RF *buckets* of 2.5 ns length. The beam is divided into a total of 35640 RF-buckets for which approximately every tenth bucket can be filled with a bunch. The LHC is designed to have 2808 proton bunches circulating in each ring, while the rest of the available buckets are reserved for injection and abort gaps. The proton bunches come in *trains* of 72 bunches, each separated by 25 ns, followed by a gap of 12 empty buckets between bunch trains. The trains are produced by injecting six bunches (produced in the LINAC2) from the PSB into the PS, at which point each bunch in split into three and injected into the SPS where each bunch is further split in two. Thus, the original six bunches are split into a total of 72 bunches.

The large bunch intensity and number of bunches in the LHC are needed in order to attain the design instantaneous luminosity. In addition, the particle flux must be as high as possible to increase the likelihood of interactions when the beams cross. Thus the cross sectional area of the beam must be squeezed to as small as possible, with a design radius of ~ 17 μm. However, there are several limitations to the LHC performance. Non-linear beam-beam interactions as well as the geometric aperture of the LHC arc limit the bunch intensity to approximately 10^{11} protons per bunch. Furthermore, the high field in the magnets operating near quenching points and the heating of the magnets due to radiation loss and beam clouds limits the maximum intensity of the beam. In addition, the large number of bunches in each train implies that up to 34 parasitic interactions could occur between bunches away from interaction point, and thus a crossing angle between beams of 286 μrad is imposed.

3.2 Performance

In 2010, the LHC provided the world's highest energy collisions of 2.36 TeV and quickly increased the collision energy to 7 TeV. Instantaneous luminosities of 2.1×10^{32} cm^{-2} s^{-1} were reached, allowing for the accumulation of an integrated luminosity of approximately 50 pb^{-1}. In 2011, instantaneous luminosities of 3.6×10^{33} cm^{-2} s^{-1} were reached, allowing for the accumulation of an integrated luminosity of approximately 5 fb^{-1}. To attain such high luminosity, a total of 1380 bunches per beam were used (each bunch separated by 50 ns) with a bunch intensity of $\sim 10^{11}$ protons per bunch and a transverse beam width of ~ 30 μm. The integrated luminosity accumulated by the ATLAS experiment from LHC collisions in 2010 and 2011 as a function of day can be seen in Figure 3.4.

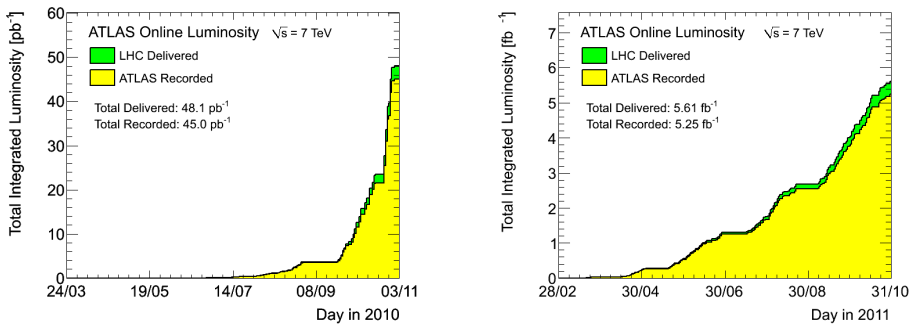

(a) 2010 (b) 2011

Figure 3.4: Integrated luminosity per day in 2010 (left) and 2011 (right) as acquired by the ATLAS experiment [20].

One of the major challenges of 2011 is *in-time* and *out-of-time* pileup. In-time pileup refers to the fact that at such high beam intensities there will be multiple protons from each bunch interacting in a given bunch crossing. Out-of-time pileup

refers to the fact that the read-out window for many of the detector elements is larger than the bunch spacing of 25 ns, and thus energy from multiple bunch crossings can be present in the read-out of a single bunch crossing. The maximum average number of interactions per bunch crossing per luminosity block (∼2 minutes) as a function of day in 2011 can be seen in in Figure 3.5(a) as well as the recorded luminosity as a function of the average number of interactions per bunch crossing in 2011 can be seen in Figure 3.5(b). The average number of interactions per bunch crossing was approximately 6 in early 2011 running and increased to approximately 12, with tails up to nearly 24, when the beam cross section was squeezed to a smaller size.

Some of the major effects of pileup are to increase the number of interaction vertices, number of tracks, and energy in a given bunch crossing. These effects make the reconstruction of object like tracks, vertices, calorimeter energy from the primary collision, and jets challenging and can introduce systematic errors into physics measurements. Thus, a precise modeling and understanding of the effects of pileup is necessary for a successful physics analysis program from the experiments.

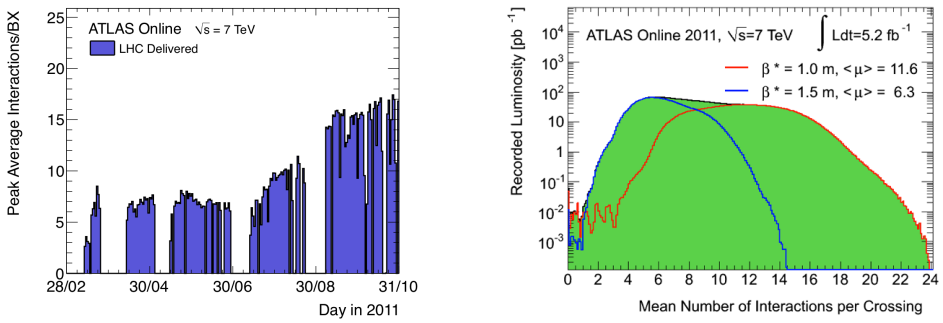

Figure 3.5: (Left) The average number of interactions per bunch crossing as a function of the day in 2011. (Right) The distribution of the average number of interactions per bunch crossing in 2011 [20].

Chapter 4

The ATLAS Detector

ATLAS ("**A** **T**oroidal **L**HC **A**pparatu**S**") [39] is a general purpose detector experiment located at one of the collisions points of the LHC, in Geneva, Switzerland. From low-energy diffractive QCD to exploring the TeV scale in search of signs of new phenomena, ATLAS is designed to study the wide variety of physics produced by the proton-proton collisions of the LHC. To achieve this measurement versatility, ATLAS combines several different technologies with complimentary detection capabilities in a cylindrical geometry with nearly hermetic azimuthal coverage over a large acceptance. The inner most detector layers are built of silicon pixels, silicon strips, and small drift tubes, all designed to measure the trajectory and momentum of charged particles as they travel through a 2 T solenoidal magnetic field. Outside of the inner detector sits the calorimeter system, making use of liquid argon and tile scintillator technologies, designed to measure the energy and direction of electrons, photons, and hadrons, and infer the transverse energy carried out of the detector by neutrinos. At the outer most layers is the Muon Spectrometer, which combines precision tracking

from monitored drift tubes and cathode strip chambers with the triggering capabilities of resistive plate and thin gap chambers in order to measure the trajectory and momentum of muons as they pass through a toroidal magnetic field. The layout of the ATLAS detector can be found in Figure 4.1.

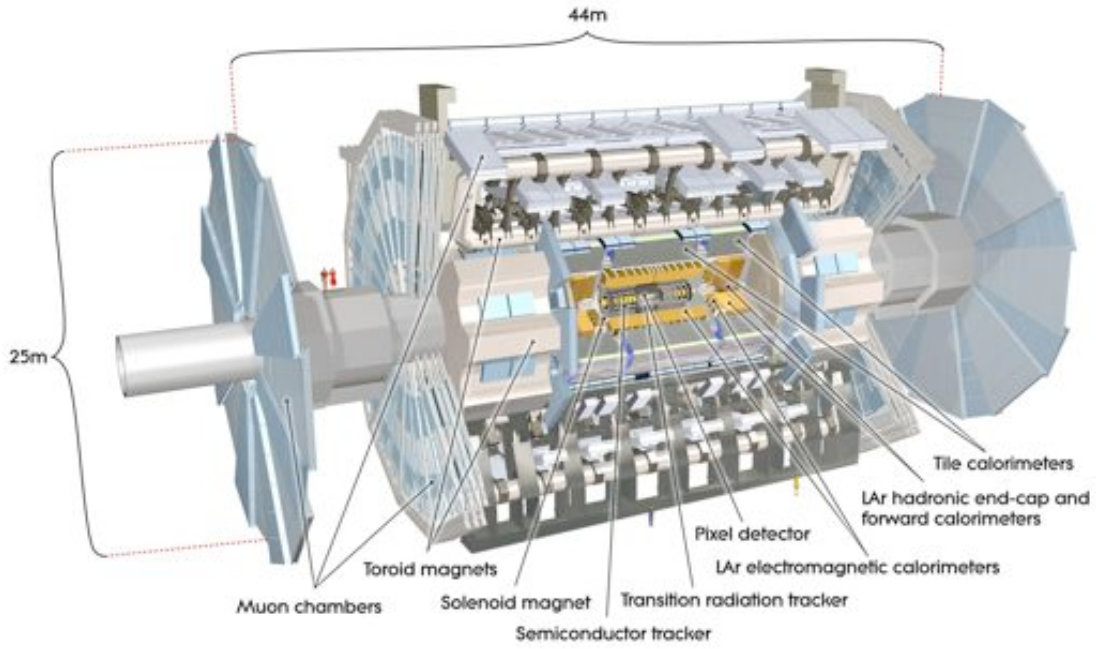

Figure 4.1: A schematic of the ATLAS detector [39].

The design of the ATLAS detector is driven by the necessary performance goals dictated by benchmark physics measurement needs. For instance, the various decays of the Higgs boson, as well as the W and Z bosons, require high resolution measurements of momentum, direction, and charge of leptons, photons, taus, and b-jets, in the $\mathcal{O}(1-100)$ GeV range. Furthermore, high resolution lepton measurements are needed up to the TeV range for ensuring the possibility of studying a new heavy Z'

or W' boson with masses up to $\sim$ 7 TeV. Studies of high energy QCD interactions require accurate jet measurements for jet energies up to the TeV range. Various new physics and SM physics signatures containing neutrinos in the final state, such as SUSY, require accurate measurements of missing transverse energy. These physics goals require large detector acceptance coverage and efficient triggering. The performance goals of the ATLAS detector, as dictated by these physics processes, and many others not mentioned here, can be found in Table 4.1.

Detector	Resolution	Measurement Coverage	Trigger Coverage
Tracking	$\sigma_{p_T}/p_T = 0.05\% p_T \oplus 1\%$	$\|\eta\| < 2.5$	
Electromagnetic Calorimeter (electrons, photons)	$\sigma_E/E = 10\%/\sqrt{E} \oplus 0.7\%$	$\|\eta\| < 3.2$	$\|\eta\| < 2.5$
Hadronic Calorimeter (jets)			
Barrel / End-Cap	$\sigma_E/E = 50\%/\sqrt{E} \oplus 3\%$	$\|\eta\| < 3.2$	$\|\eta\| < 3.2$
Forward	$\sigma_E/E = 100\%/\sqrt{E} \oplus 10\%$	$3.1 < \|\eta\| < 4.9$	$3.1 < \|\eta\| < 4.9$
Muon Spectrometer	$\sigma_{p_T}/p_T = 10\%$ at 1 TeV	$\|\eta\| < 2.7$	$\|\eta\| < 2.4$

Table 4.1: Performance goals of the ATLAS detector [39]. Energy and momentum are listed in GeV and $\oplus$ indicates a sum in quadrature.

This chapter serves as an introduction to the ATLAS detector systems. Before reviewing the ATLAS technologies, the ATLAS coordinate system is defined in Section 4.1. The description of the magnetic field, which provides the bending needed for momentum measurements in the inner detector and in the muon spectrometer, is discussed in Section 4.2. The inner detector technologies are discussed in Section 4.3, the calorimeter technologies are discussed in Section 4.4, and the detectors of the muon spectrometer are discussed in Section 4.5. Finally, the measurement of luminosity

and the determination of the luminosity uncertainty are discussed in Section 4.7. This thesis will provide a brief overview of ATLAS, while detailed descriptions can be found in References [39, 12, 24].

4.1 Coordinate System

The origin of ATLAS is located at the center of the detector. The z-axis points along the beam line, while the $x-y$ plane is transverse to the beam line with the positive x-axis pointing into the center of the LHC ring and the positive y-axis pointing up. The positive z side of the detector is known as the A-side while the negative side is known as the C-side. ϕ is the azimuthal angle in the $x-y$ plane with $\phi = 0$ on the positive x-axis , and θ is the polar angle with $\theta = 0$ on the positive z-axis. One frequently used variable transformation is $\eta \equiv -\ln\tan(\theta/2)$ where η is known as the pseudo-rapidity and is the high energy or zero mass limit of the rapidity $y = \frac{1}{2}\ln\left(\frac{E+p_z}{E-p_z}\right)$. The angular distance between objects is defined as $\Delta R \equiv \sqrt{\Delta\eta^2 + \Delta\phi^2}$.

The projection of variables onto the transverse plane is frequently used in ATLAS because collisions occur with essentially no energy transverse to the beam line and thus momentum in the transverse plane must sum to zero. In addition, the overall energy in the z-direction is not known *a priori* because the collisions occur between partons of unknown energy. The transverse momentum vector is defined as $\mathbf{p}_T = (p_x, p_y)$ with magnitude $p_T = \sqrt{p_x^2 + p_y^2}$. The transverse energy is defined as $E_T = E\sin(\theta)$. When a particle decays to two *daughter* particles with 4-vectors $(E^1, \mathbf{p^1})$ and $(E^2, \mathbf{p^2})$, the transverse mass of the parent can be defined using the two daughter

4-vectors as $m_T \equiv \sqrt{E_T^1 E_T^2 - \mathbf{p}_T^1 \cdot \mathbf{p}_T^2}$. For massless daughters, this can be written as $m_T = \sqrt{2 \times E_T^1 \times E_T^2 \times (1 - \cos(\phi_1 - \phi_2))}$. The transverse mass is especially useful when the p_z component of one of the daughter 4-vectors is unknown, for instance when the daughter is a neutrino and only the transverse momentum can be measured.

The physics analysis in this thesis uses electrons and muons reconstructed by ATLAS. Both muons and electrons rely on the tracking system to measure momentum and angular information, and thus it is useful to discuss tracking variables. In the cylindrical geometry common to most collider experiments, tracks are described by a 5-component *state* vector which can be computed at each point along the track. The 5-components are $(r,\ z,\ \phi,\ \theta,\ q/p)$, where r is the radial distance from the beam line, z is the longitudinal distance from the origin, ϕ and θ are the angular variables described earlier, p is the momentum, and q is the charge of the track. It is also frequent to use to cotangent of θ instead of simply θ because $\cot(\theta) = z/r$ is linear in z for fixed radius and is thus geometrically convenient in cylindrical space. The inverse of the track momentum is used because track momenta are measured from the sagitta of the track helix which is proportional to B/p, where B is the magnetic field strength. These variables allow the determination of the track position, pointing angle, and momentum. When the track is extrapolated to the point of closest approach to the beam line, the transverse and longitudinal distances between the track and the beam line are denoted d_0 and z_0, respectively.

4.2 Magnetic Field

The ATLAS magnetic field [39, 117], used for bending the trajectory of charged tracks to allow for momentum measurements, is provided by four large superconducting magnets. A solenoid, aligned with the beam axis, surrounds the inner detector and produces a 2 T magnetic field in the z-direction. Three air-core toroid magnets, one in the barrel and one on each end-cap, provide magnetic fields for the muon spectrometer of approximately 0.5 T and 1 T in the barrel and end-cap, respectively, with peak fields up to $\sim$4 T. Each of the toroid magnets are composed of 8 coils, with the end-cap coils rotated by 22 degrees with respect to the barrel coils in order to provide better magnetic field coverage in the transition region between magnets. The magnetic field of the solenoid and toroid are approximately in the z and ϕ directions, respectively, and thus bending occurs in the ϕ and η directions, respectively.

The solenoid magnet is made of 1154 windings of Al-stabilized NbTi cooled to 4.5 K and run with a current of 7.7 kA. The solenoid is approximately 5.8 m long with a diameter of approximately 2.5 m. In order to minimize the energy loss of particles upstream of the calorimeter, the solenoid layout was optimized to keep the material thickness as small as possible. Thus, the solenoid was kept to $\sim$0.66 radiation lengths at normal incidence [117] and is housed in the same cryostat vacuum system as the EM calorimeter (thus eliminating additional vacuum walls).

The toroid magnets are made of 8 air-core coils, each with approximately 120 windings of Al-stabilized NbTi cooled to 4.6 K and run at a current of 20.5 kA. Each barrel coil is housed in its own vacuum chamber, while all of the coils of each

end-cap toroid are housed together in a single vacuum chamber. The barrel toroid is 25.3 m long, with inner diameter of 9.4 m and outer diameter of 20.1 m, thus setting the overall scale of the ATLAS detector. An air-core design of the coils is used to minimize the material crossed by muons and reduce the effects of multiple scattering. The large magnetic field over the large bending volume is designed to allow muon momentum measurements with excellent resolutions over a large coverage, with the aim of a 10% resolution on momentum measurements for muons with a momentum of 1 TeV.

The layout of the magnet system and a cross sectional view of the field strength is shown in Figure 4.2. In Figure 4.2(a), the magnets are colored red, while all other colors show the different layers of the barrel calorimeter. The solenoid is inside of the calorimeter system and the coils of the barrel and end-cap toroids are outside of the calorimeter. A cross sectional view of the ATLAS B-field strength in the barrel is displayed in Figure 4.2(b). In this figure, both the very homogeneous solenoid field at the center and the 8-fold symmetry of the barrel toroid at the outer regions can be seen. It can easily be seen that the toroid field is very inhomogeneous, resulting in different bending strengths at different ϕ.

The ability to accurately measure the momentum of charged particles depends on the ability to detect deviations of charged particle trajectories from straight lines, i.e. the sagitta resolution. The sagitta resolution depends heavily on the B-field strength and the particle's path length in the B-field. The larger the field and the longer a particle stays in a magnetic field, the more it will depart from a straight line. One way

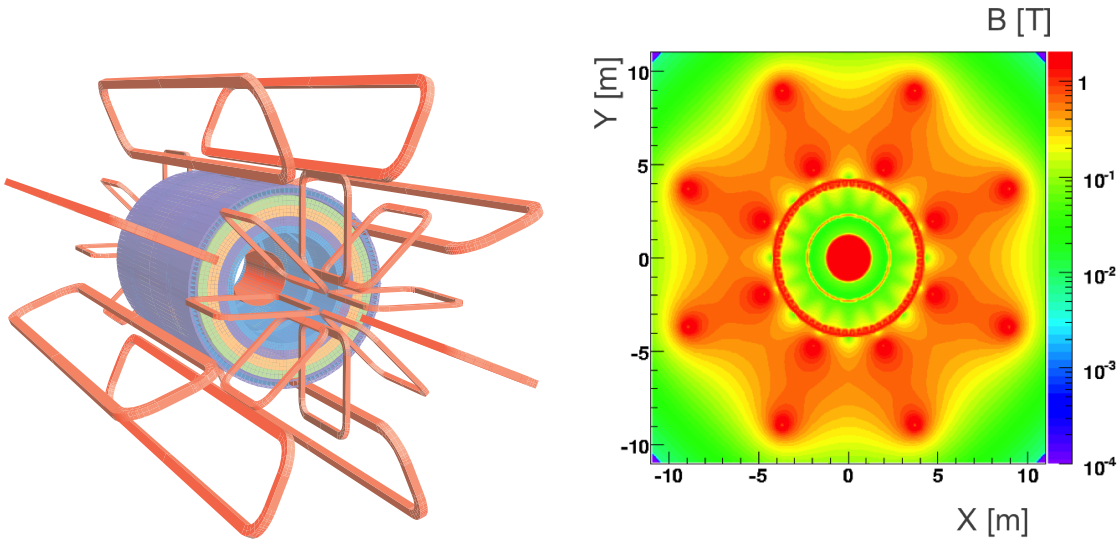

(a) (b)

Figure 4.2: (Left) Layout of ATLAS Magnet System. (Right) Cross section view of the ATLAS magnetic field strength [39].

to understand the B-field performance is to consider the total integrated magnetic field seen by a particle on a given trajectory, or $\int B \cdot \mathrm{d}l$, which is denoted the bending power. Strictly speaking, the sagitta resolution has a more complex dependence on B and l, but bending power is a reasonable proxy for performance for the purposes of this discussion. The bending power of the ATLAS toroids can be see as a function of $|\eta|$ for two different trajectories in ϕ in Figure 4.3. At $\phi = 0$ the muon is pointing between two coils in the barrel and into a coil in the end-cap, while the converse is true at $\phi = \pi/8$. Thus the bending power is stronger at $\phi = \pi/8$ in the barrel and stronger at $\phi = 0$ in the end-cap. It can also be seen that the confluence of the barrel and end-cap magnets creates an incredibly complex field in the transition region, which can result in negative bending power, i.e. bending of the tracks in the wrong direction.

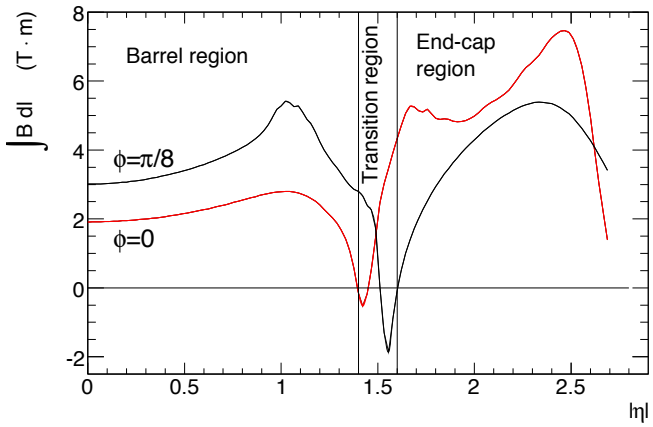

Figure 4.3: Toroid magnet bending power in the ATLAS Muon Spectrometer [39].

4.3 Inner Detector

The ATLAS inner detector (ID) is the primary charged particle tracking and vertexing system. The ID is built in a cylindrical geometry directly surrounding the beam-pipe in an envelope with a radius of 1150 mm and length 3512 mm in both the positive and negative z directions. The ID is immersed in a 2 T solenoidal magnetic field that provides the bending necessary for momentum measurements. Three detector technologies are used in the ID. The closest detector to the beam-pipe is the semiconductor Pixel Detector which is composed of silicon pixels and typically provides three high precision space-point measurements. Surrounding the pixels is the SCT which is a silicon strip detector that typically provides eight high precision measurements along a particle's trajectory. Outside of the SCT is the TRT which is built from a large number of small drift tubes, called *straw* tubes, and typically provides 36 measurements along a particle's trajectory. The layout of the ID can be found in Figure 4.4 and a schematic of the detector envelopes can be found in

Figure 4.5.

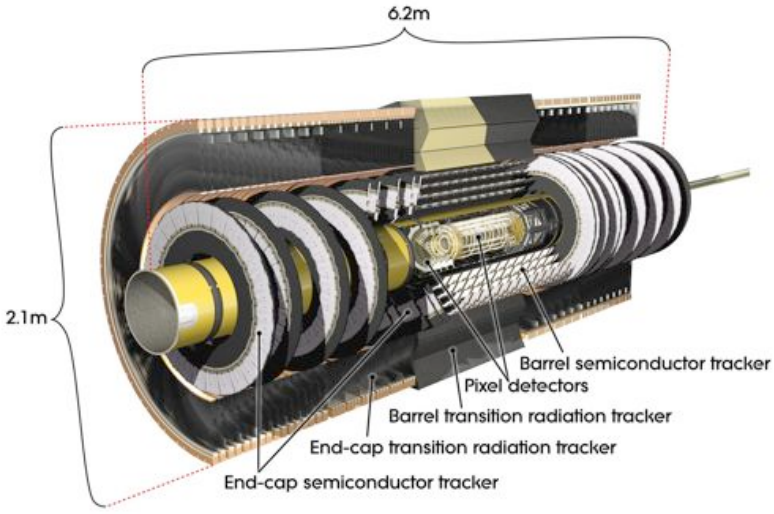

Figure 4.4: The layout of the ATLAS inner detector [39].

The purpose of the ID is to provide accurate and efficient charged particle tracking for tracks with $p_T > 0.5$ GeV with nearly hermetic coverage out to $|\eta| < 2.5$ and robust pattern recognition in the dense environments of high luminosity LHC collisions ($\sim$1000 particles in the $|\eta| < 2.5$ range emerging from each collision) [39]. The ID is also designed to allow for the reconstruction of primary vertices from pp collisions and secondary vertices from the decay of long-lived particles (such as K_S, Λ_0, τ, and heavy flavor quarks in jets). In order to achieve this performance, the ID must be built from highly granular detectors with adequate redundancy for tracking which can survive in the high radiation environment of the LHC. However, the ID must maintain as low as possible material budget so as not to deteriorate tracking resolution from multiple scattering or cause significant energy loss before the energy measurements of the ATLAS calorimeters. These consideration drive the design of the ID, whereby

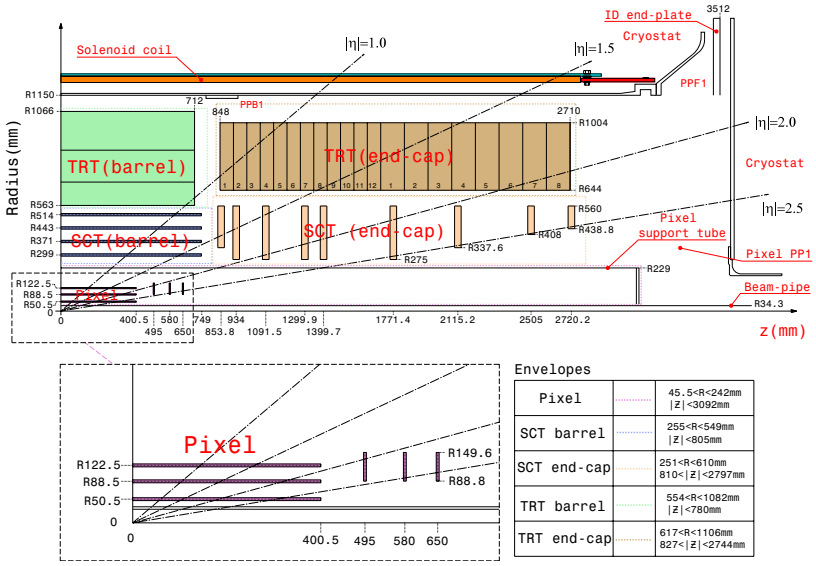

Figure 4.5: A schematic of the envelopes of the sub-detectors in the ATLAS inner detector [39].

the dense pixel and SCT detectors provide precision η and ϕ measurements to allow for accurate determination of the location and angle with which tracks emerged from the collision, while the low material-budget TRT provides a large number of hits over a large bending radius to facilitate pattern recognition and reduce momentum resolution [39]. Even with the current design, the ID has a significant material budget, seen in Figure 4.6, that must be accounted for during track reconstruction.

4.3.1 Pixel Detector

The ATLAS silicon pixel detector [38] is the first sub-detector traversed by particles emerging from the LHC collisions and provides high resolution space-point measurements needed for tracking in high multiplicity environments and for the identification of displaced vertices from long-lived particles such as B-hadrons. The detector is organized into three barrel and three end-cap layers which allow for adequate tracking

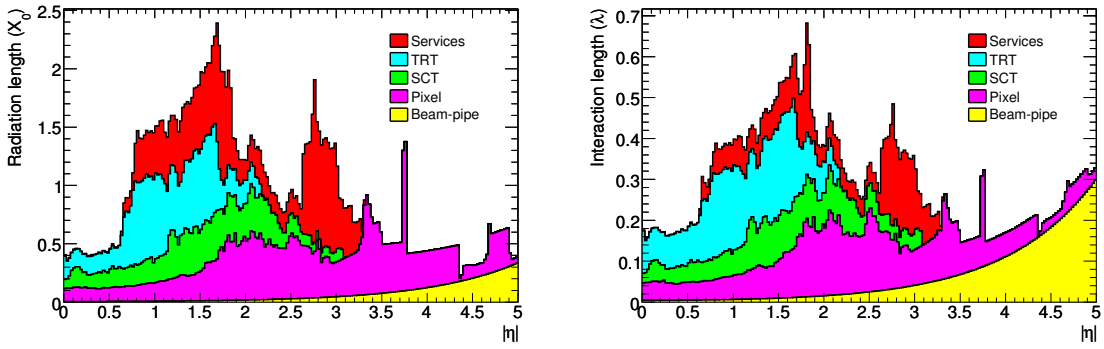

Figure 4.6: ATLAS inner detector material budget crossed by a straight track as measured at the exit of the ID envelope in terms of radiation lengths X_0 (left) interaction lengths λ (right) [39].

and vertexing capabilities while keeping costs and material budgets reasonable. The barrel layers are arranged in a cylindrical geometry around the beam-pipe located at a radius of R = 50.5 mm, 88.5 mm, and 122.5 mm from the IP and extending to $\pm$400.5 mm in the z direction. The closest barrel pixel layer is denoted the B-layer, and is vital for secondary vertex reconstruction. The end-cap layers are arranged as disks transverse to the beam-pipe each extending from 88.8 mm$< R <$149.6 mm and located at $|z|$ = 495 mm, 580 mm, and 650 mm.

Each layer of the pixel detector is built from identical detector modules with a thickness of 250 μm and approximate dimensions 20$\times$60 mm^2. The individual pixels have a nominal size of 50 μm (around the beam-pipe in the ϕ direction) and 400 μm (along the beam-pipe in the z direction), allowing for an intrinsic resolution of 10 μm (ϕ) and 115 μm (z) for the barrel and 10 μm (ϕ) and 115 μm (R) for the end-cap disks. Each pixel is bump-bonded to a read-out element on the front-end electronics of the module. The module electronics perform amplification, shaping, and discrimination

of pixel signals which can then be used as binary hit measurements or time-over-threshold measurements. There are 1744 modules in the pixel system with each module containing ∼46000 pixel channels. Thus the pixel system contains ∼80 million pixel read-out channels in total. The pixels are cooled to -7 C, to minimize the impact of radiation damage, and operated with a bias voltage of 150 V initially and up to 600 V after several years of operation.

4.3.2 Semiconductor Tracker

The ATLAS semiconductor tracker [5] is a silicon strip detector located outside of the pixel detector that provides high resolution space-point measurements that are vital for precision tracking and play a crucial role in the performance of track momentum measurements. The SCT detectors are used to extend the precision tracking past the pixels rather than addition pixel layers due to their lower cost of production and reliability. The SCT is organized into four cylindrical layers in the barrel and nine disks, extending radially away from the beam-pipe, on each end-cap side. The barrel layers are located between 299 mm$< R <$563 mm extending out to $\pm$749 mm in z while the end-cap disks have varying radial length and are located between 853 mm$< |z| <$2720 mm. The layout was designed to allow for at least eight SCT hits per track.

The SCT modules use micro-strip sensors containing 768 strips with an 80 μm pitch. Each sensor is 6.36×6.40 cm^2 and two of the sensors are daisy chained together. Two of these 12cm sensor chains are combined back-to-back with a relative rotation angle of $\pm$20 mrad. The strips are oriented along the beam-pipe in the barrel and radially

outward in the end-caps. The strip pitch was chosen to allow for adequate digitization precision and granularity while keeping in mind the expected occupancy and noise performance. The rotation angle is used to allow for more precise determination of the second coordinate (z in the barrel and R in the end-cap) and thus the back-to-back design allows for accurate space-point measurements in both directions. The intrinsic resolution of SCT hit measurements are 17 μm in ϕ and 580 μm in z (R) for the barrel (end-cap). There are a total of 6.2 million read-out channel which operate in a binary read-out mode. The system is cooled to -7 C and operated with a bias voltage of 150 V initially and up to 350 V after several years of operation.

4.3.3 Transition Radiation Tracker

The transition radiation tracker [1] sits outside of the SCT system and is composed of a large number of gaseous drift tube detectors (or straw tubes) with interleaving transition radiation material. The TRT is a low density and cost effective detector that provides approximately 36 measurements for each track over a large bending radius. Thus the TRT provides vital information for particle trajectory tracking over a large volume. The transition radiation photons produced by high-β particles (like electrons and positrons) traversing the radiator material cause large signals in the tubes, called high threshold hits, that can be use for electron/pion separation. In the barrel, the tubes are parallel to the beam-pipe and organized into a cylindrical geometry for 563 mm $< R <$ 1066 mm, with a length of 72 cm. There are two barrel sections of this type, separated at $\eta \sim 0$. On each side of the end-cap, the tubes extend radially outward from R =644 mm to R =1004 mm for 848mm$< |z| <$2710 mm. Due

to the long length of the tubes, the TRT only gives accurate position measurements in the bending ϕ direction and relatively little information about the z (R) coordinate in the barrel (end-cap).

The TRT tubes are 4 mm in diameter with 32 μm tungsten anode wires plated with gold. The tube walls function as the cathode and are primarily made with polymide wrapped in kapton film and reinforced with aluminum and carbon fiber. The cathode is operated at -1530 V giving a gas gain of 2.5×10^4 using the gas mixture of 70% Xe, 27% CO_2 and 3% O_2 with 5 to 10 mbar over-pressure. In total, there are approximately 351,000 tubes in the TRT system which operate at room temperature. As particles traverse the tube, they ionize the gas and the electric field causes the ionized electrons to drifts towards the anode wire. The signal collection time is approximately 48 ns. The time of arrival of electrons is converted to a drift radius measurement (radius of closest approach to the anode) using an R-T calibration function. Once converted to the drift radius measurement, the intrinsic tube resolution is $\sim$130 μm. Although each hit is much less precise than the silicon trackers, the large number of hits over the large track length allows the TRT to contribute significantly to the momentum resolution.

4.4 Calorimeter

The ATLAS calorimeter is composed of electromagnetic (EM) and hadronic sampling detectors designed to provide accurate energy and direction measurements of electrons, photons, taus, hadrons, and jets. The measurements of the calorimeter

energy depositions are also used in the calculation of the transverse missing energy caused by non-interacting particles escaping detection, such as neutrinos. The EM calorimeter is designed for high momentum and pointing resolution measurements of electrons and photons utilizing a high granularity of read-out elements. This high granularity allows for the shower shape analysis that is necessary for electron and photon identification. The EM calorimeter, sitting outside of the ID and solenoid magnet, is split into a barrel and end-cap and is composed of liquid Argon (LAr) with lead absorber plates. The EM calorimeter provides essentially hermetic coverage in ϕ with a projective geometry in η covering $|\eta| < 3.2$. The hadronic calorimeter, sitting outside of the EM calorimeter, measures the energy and direction of charged and neutral hadrons in jets. The hadronic calorimeter utilizes tile scintillators with steel absorbers for $|\eta| < 1.7$ while the end-cap uses LAr with copper absorbers for $1.5 < |\eta| < 3.2$. Finally, the coverage is extended from $3.1 < |\eta| < 4.9$ with the forward calorimeter which uses LAr with tungsten absorbers. The layout of the calorimeter system can be found in Figure 4.7.

The segmentation and depth of the calorimeter system reflect the performance goals for electrons, photons, jets, and missing energy. The parameters of the calorimeter subsystems can be found in Table 4.2. The EM presampler detects showers induced before the calorimeter entrance. The fine granularity of the EM first layer is vital for electron and photon direction measurements, for detecting photon conversions, and for pion/photon discrimination. The granularity of the EM second and third layers allow for the detection and analysis of electromagnetic shower shape development. The EM calorimeter cells are typically larger in ϕ than η to account for electron

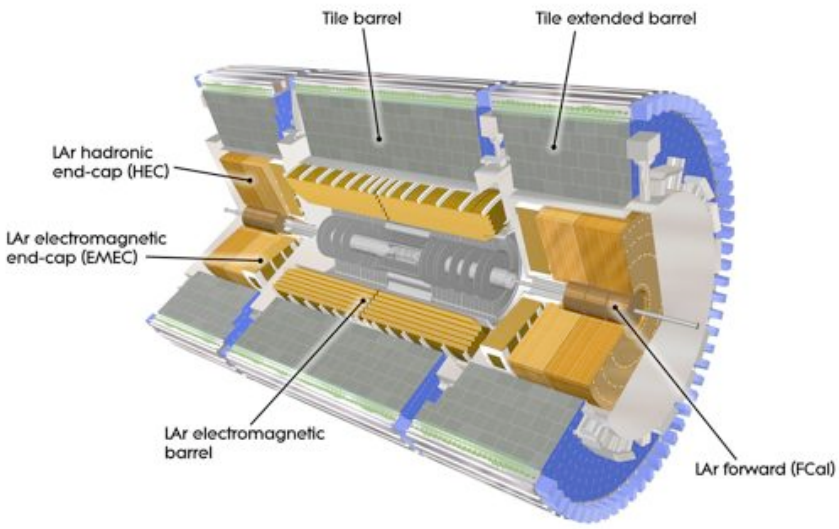

Figure 4.7: A schematic of the ATLAS calorimeter [39].

bremsstrahlung (which follows a straight trajectory while the electron continues to bend in the solenoid field). The hadronic calorimeter has a coarser granularity than the EM calorimeter, but is still adequate for accurate jet energy and shower shape measurements[1]. The hadronic calorimeter is also deep enough to contain hadronic showers in order to avoid punch-through to the muon spectrometer.

4.4.1 Electromagnetic Calorimeter

The EM calorimeter [27] sits outside of the ID and shares a cryostat with the solenoid in order to reduce the amount of material in front of the calorimeter and reach the desired performance for electron and photon reconstruction. The barrel is split with a small gap of 4 mm at $z = 0$ and each half section is 3.2 m in length

[1]Given that ∼80 (50)% of the energy of p_T =30 (400) GeV jets are deposited in the EM calorimeter [26], a coarser Hadronic Calorimeter granularity can be used.

EM Calorimeter			
Barrel			
Num. Readout Channels		7808 (Presampler) + 101760 (Calo)	
Component	Layers	Coverage	Granularity ($\Delta\eta \times \Delta\phi$)
Presampler	1	$\lvert\eta\rvert < 1.52$	0.025×0.1
Layer 1	1	$\lvert\eta\rvert < 1.475$	$\sim 0.003 \times 0.1$
Layer 2	1	$\lvert\eta\rvert < 1.475$	$\sim 0.025 \times 0.025$
Layer 3	1	$\lvert\eta\rvert < 1.475$	0.05×0.025
End-Cap			
Num. Readout Channels		1563 (Presampler) + 62208 (Calo)	
Component	Layers	Coverage	Granularity($\Delta\eta \times \Delta\phi$)
Presampler	1	$1.5 < \lvert\eta\rvert < 1.8$	0.025×0.1
Layer 1	1	$1.375 < \lvert\eta\rvert < 3.2$	$\sim 0.003 \times 0.1$
Layer 2	1	$1.375 < \lvert\eta\rvert < 3.2$	$\sim 0.025 \times 0.025$
Layer 3	1	$1.5 < \lvert\eta\rvert < 2.5$	0.05×0.025
Hadronic Tile Calorimeter			
Num. Readout Channels		9852	
Component	Layers	Coverage	Granularity($\Delta\eta \times \Delta\phi$)
Layer 1,2	2	$\lvert\eta\rvert < 1.7$	0.1×0.1
Layer 3	1	$\lvert\eta\rvert < 1.7$	0.2×0.1
LAr Hadronic End-Cap Calorimeter			
Num. Readout Channels		5632	
Component	Layers	Coverage	Granularity($\Delta\eta \times \Delta\phi$)
Low η Layers	4	$1.5 < \lvert\eta\rvert < 2.5$	0.1×0.1
High η Layers	4	$2.5 < \lvert\eta\rvert < 3.2$	0.2×0.2
Forward Calorimeter			
Num. Readout Channels		3524	
Component	Layers	Coverage	Granularity($\Delta\eta \times \Delta\phi$)
FCAL Layers	3	$3.1 < \lvert\eta\rvert < 4.9$	$\sim 0.2 \times 0.2$

Table 4.2: Calorimeter Parameters.

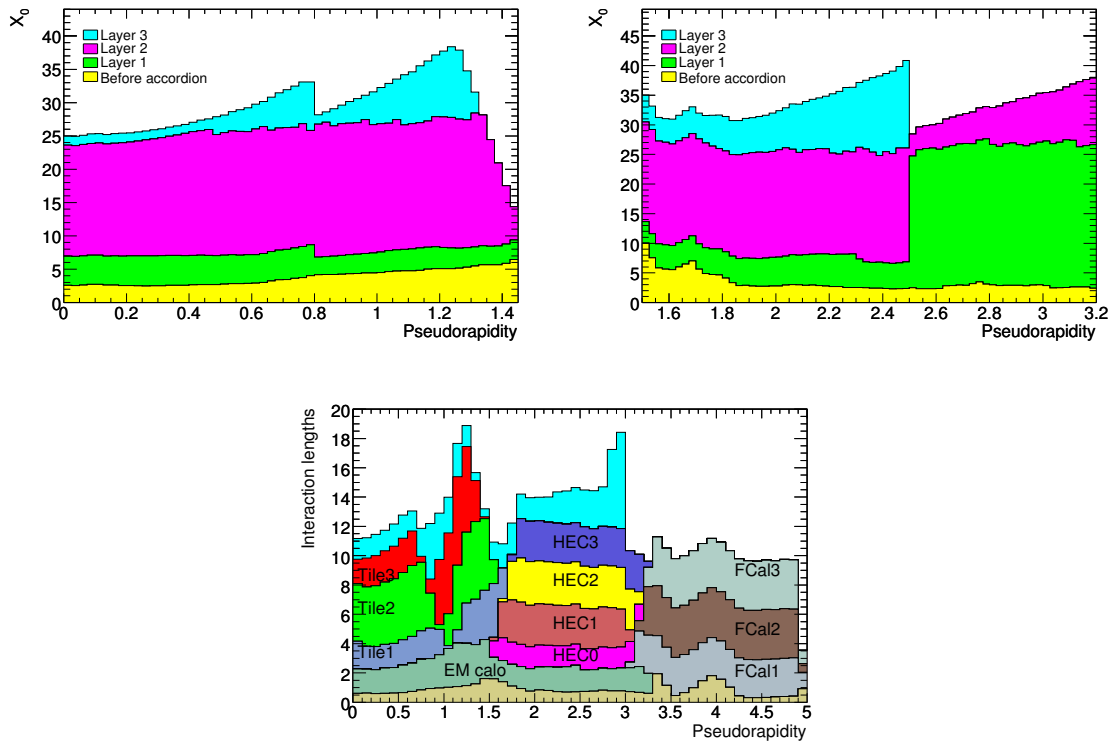

Figure 4.8: Cumulative amount of material in the calorimeter systems [39]. The amount of material in terms of radiation lengths X_0 for the EM barrel (top left) and EM end-cap (top right) . The amount of material in terms of nuclear interaction lengths for the different hadronic calorimeter layers, as well as the total EM calorimeter, and the material before the calorimeter (bottom center).

with inner and outer radii of 2.8 m and 4 m respectively. The end-cap sections are 63 cm in length, with inner and outer radii of 330 mm and 2098 mm, respectively. The barrel and each end-cap section are contained in their own cryostat system.

The calorimeter uses liquid argon as the sensitive material with accordion shaped lead absorber plates and kapton electrodes (sitting between the lead absorber plates) over the full coverage. The electrodes are surrounded by thin copper plates held at ∼2000 V (but varies in η) and thus readout is performed via capacitive coupling. The gaps between electrodes and absorber plates are ∼2.1 mm which implies a drift time of 450 ns. The accordion design, seen in Figure 4.9, allows for complete ϕ coverage with signal read-out at the front and back of the calorimeter and thus no azimuthal cracks.

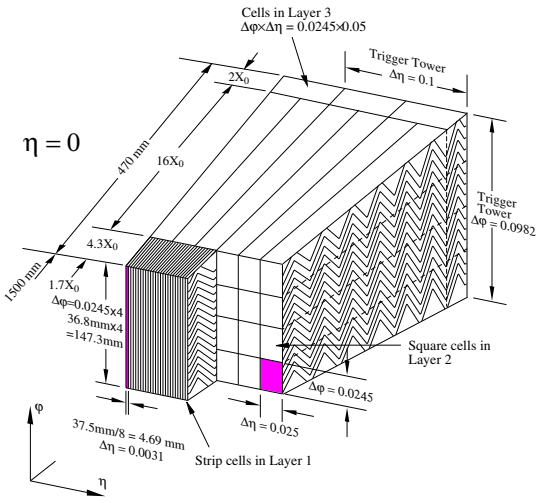

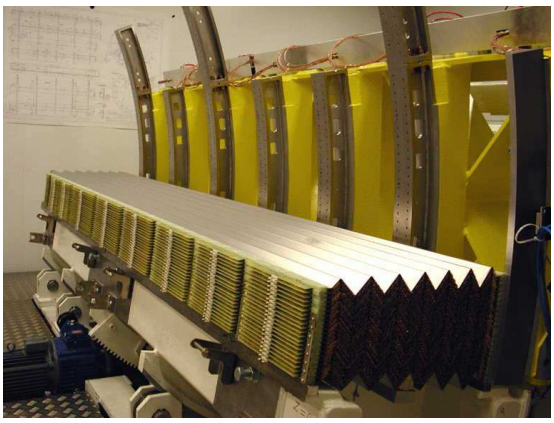

Figure 4.9: A sketch of the EM calorimeter accordion geometry and readout granularity (left) and a photo of a partially stacked barrel module showing the accordion design (right) [39].

As charged particles are incident on the lead absorber plates, they produce electromagnetic showers of electrons and photons (which further pair produce electrons). The EM showers ionize the LAr, and the ionized electrons drift to the kapton electrodes. The energy measurement is determined by the size of the signal on the electrodes, which is approximately linear in the number of electrons reaching the electrode. The resolution is determined in large part by the total number of ionization electrons reaching the electrodes. Thus it is vital to effectively shower the incident particle and contain the shower in the longitudinal direction.

The thickness of the lead absorber plates and folding angle of the accordion shape have been optimized as a function of η in order to reach the desired energy resolution performance. In the region of $|\eta| < 2.5$ devoted to precision physics, the calorimeter has three layers of segmentation with high granularity while the high $1.5 < |\eta| < 3.2$ region has two layers with lower granularity. The first layer is optimized to allow precision direction determination and particle discrimination, while the second layer is optimized in material depth to contain the largest fraction of the shower energy. The third layer is used to measure the tails of the shower. The total thickness of the calorimeter is > 22 radiation lengths (X_0). In addition, the region of $|\eta| < 1.8$ is instrumented with a single layer of active LAr of 0.5-1.1 cm in thickness, called the presampler, in order to identify EM showers and correct for energy loss in material upstream of the calorimeter.

4.4.2 Hadronic Calorimeter

The hadronic calorimeter is built from two different sampling detector technologies with approximate pointing geometries. The tile calorimeter (TileCal) [36] uses steel and scintillator (polystyrene) in the barrel while the end-cap calorimeter (HEC) [27] is built with copper and LAr. The TileCal sits outside of the EM calorimeter and is divided into the barrel ($|\eta| < 1.0$) and extended-barrel ($0.8 < |\eta| < 1.7$), where the crack between barrel and extended-barrel is used for services. The TileCal has an inner radius of 2.28 m and an outer radius of 4.25 m. Scintillating tiles are used as the active material and steel plates are used as the absorber. The scintillating tiles are oriented radially, i.e. perpendicular to the beam direction, and are read out via wavelength shifting fibers that route the signal into photo-multiplier tubes. The radial thickness of the TileCal is approximately 7.4 interaction lengths. To cope with the higher particle flux in the forward region, the HEC detector uses copper absorber plates with LAr as the active material. The detectors are built in a cylindrical wheel geometry with an inner radius of 372 mm and outer radius of 2030 mm. The HEC material thickness is approximately 10 radiation lengths. The thickness of the hadronic calorimeter layers are optimized to contain the hadronic showers and provide adequate longitudinal sampling for shower shape development analysis. The granularity of the layers are optimized to allow jet direction measurements and to provide adequate measurements of the shower profile in η and ϕ.

4.4.3 Forward Calorimeter

The forward calorimeter [27] is designed to cope with the high particle flux and energy densities in the forward direction and is located 4.7 m from the interaction point covering $3.1 < |\eta| < 4.9$. The detector is built from a metal matrix with regularly spaced holes, oriented along the beam direction, which are filled with high voltage rods surrounded by tubes. The small gaps between the rods and tubes are filled with LAr. In the first layer of the FCAL, the metal matrix is made of copper and is used for EM measurement. The second and third layer metal matrices are made of tungsten and are primarily for hadronic measurements. The total thickness of the FCAL is approximately 10 interaction lengths. The primary purpose of this detector is to aid in the calculation of the missing transverse energy and measure the properties of forward jets. For most precision measurements, FCAL is typically not used but some dedicated studies aiming to extend measurement acceptances have incorporated FCAL measurements.

4.5 Muon Spectrometer

The ATLAS muon spectrometer (MS) [37] is composed of four detector technologies and is designed to provide accurate muon direction and momentum measurements as well as efficient triggering on muons with momenta from ∼4 GeV up to several TeV. The MS sits outside of the calorimeter system and defines the overall envelope of ATLAS, covering an area of approximately 5,500 m^2. The tracking of muons in the MS relies on the bending of muon trajectories in the toroidal magnetic field and

the subsequent measurement of the track curvatures. The high-field of the toroid over large bending distances with low material density allows precision stand-alone momentum measurements up to the TeV range, where the ID resolution is significantly degraded. The layout of the MS and toroid magnets can be found in Figure 4.10

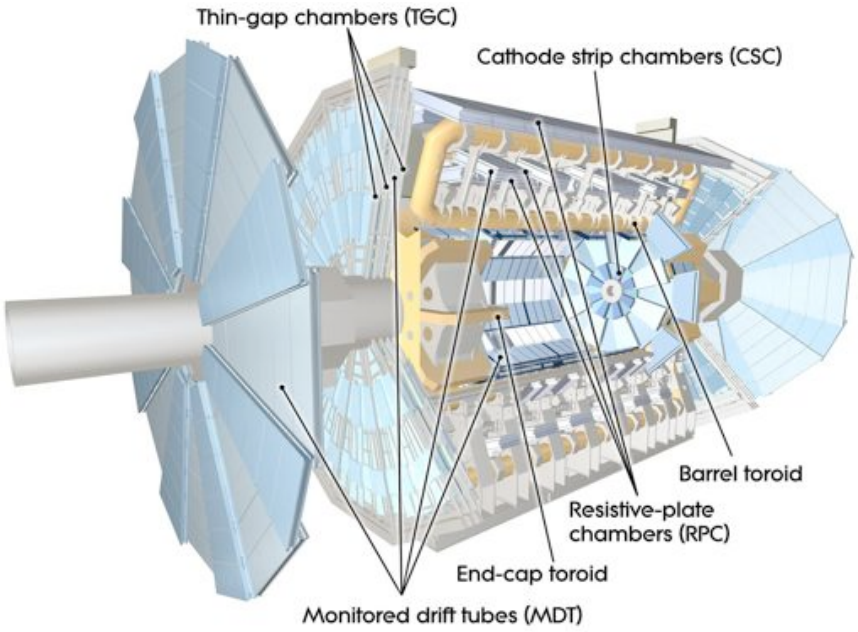

Figure 4.10: A schematic of the ATLAS muon spectrometer [39].

The primary precision tracking measurements in the bending direction are provided by Monitored Drift Tubes (MDT) over most of the detector acceptance. Given the direction of bending of the toroidal field, the MDTs are oriented such that the long tube length extends in the ϕ direction, thus allowing precision measurements of the track coordinates in the bending direction (η). In the forward region, where the particle flux is too high for MDT chambers, Cathode Strip Chambers (CSC) are used. Triggering and the second coordinate (ϕ) measurements are provided by Resistive

Plate Chambers (RPC) and Thin Gap Chambers (TGC). Both the RPC and TGC are fast tracking detectors with excellent time resolution capable of identifying the bunch crossing from which a muon originated, and thus are used to provide the first level of muon triggering. The coverage, number of chambers, and number of readout channels for each MS detector technology can be found in Table 4.3.

	Coverage	Num. Chambers	Num. Channels
MDT	$\|\eta\| < 2.7$ (2.0 inner layer)	1088	339,000
CSC	$2.0 < \|\eta\| < 2.7$	32	31,000
RPC	$\|\eta\| < 1.05$	544	359,000
TGC	$1.05 < \|\eta\| < 2.7$ (2.4 for trigger)	3588	318,000

Table 4.3: MS detector parameters as installed [39].

The MS is built into sixteen sectors[2] in ϕ, based on the eight-fold symmetry of the toroids. The sectors alternate between large (in between toroid coils) and small (around toroid coils) chambers, with overlaps between sectors to minimize azimuthal gaps and to aid in the relative alignment of chambers. In the barrel ($|\eta| < 1.05$), the chambers are arranged into three cylindrical layers around the beam axis and are located at approximately R =5 m, 7.5 m and 10 m. There is a small gap at $z = 0$ for services. In the end-cap ($1.05 < |\eta| < 2.7$), the chambers are arranged in three planes, called wheels, that are perpendicular to the beam axis and located at approximately z =7.4 m, 14 m and 21.5 m. The first two end-cap layers are built on movable wheels, while the outer most layer is built into the cavern support structure

[2]Except the TGC chambers, which are organized into 12 sectors.

and is fixed in place. The three layers are denoted the inner (I), middle (M), and outer layers (O), both in the barrel and end-cap, and the layers of a given sector build a projective tower. In the barrel, the inner layer sits inside the toroid, the middle layer sits in between the toroid coils, and the outer layer sits outside of the toroid. In the end-cap, the toroid sits in between the inner and middle wheels. Each of the layers contain MDT chambers, except for the far forward region of the inner end-cap layer ($|\eta| > 2.0$) where the CSCs are located. The RPC chambers are used in the barrel and are located on the outer layer and both sides of the middle layer MDT chamber. The TGC chambers are located in the end-cap with three chambers surrounding the middle layer allowing for triggering up to $|\eta| = 2.4$. The inner layer of the end-cap is also instrumented with TGCs, but these chambers are only used for second coordinate (ϕ) measurements. Finally, there are a number of additional MDT chambers in the feet region, surrounding the end-cap toroids, and in the transition region. These additional chambers help to minimize gaps in the tracking acceptance.

The benchmark goal of the MS is to have 10% resolution on 1 TeV muon tracks. Given that a 1 TeV muon has a sagitta of approximately 500 μm, the design sagitta resolution is 50 μm. To reach this goal, not only are precision hit measurements with accurate calibrations and accurate modeling of energy loss in materials needed, but also accurate detector alignment and B-field modeling are essential. The chambers are aligned to the required 30 μm precision using mechanical assembly techniques and optical alignment systems within and between muon chambers. The alignment system allows for chamber alignment both within a projective tower and in adjacent

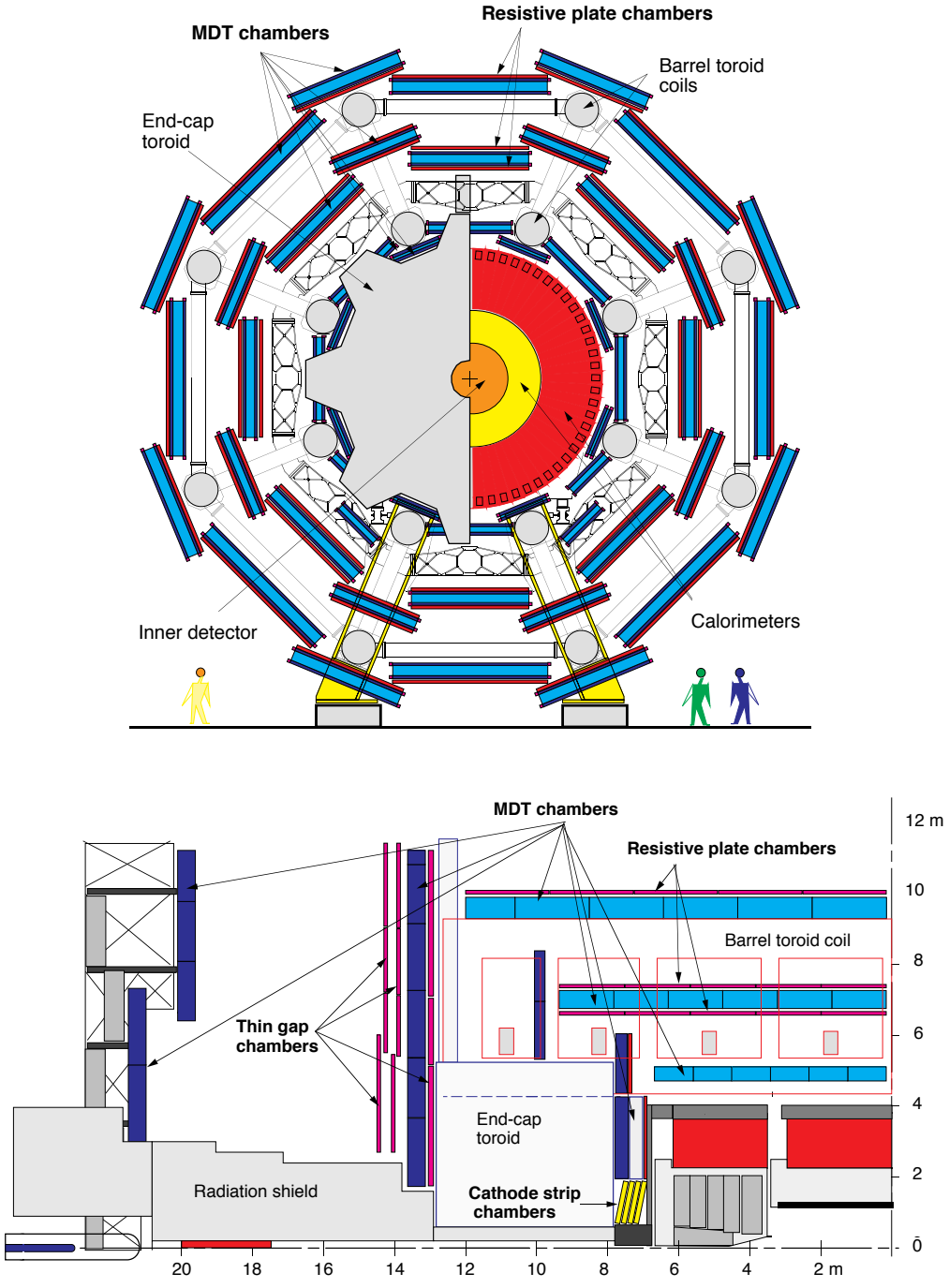

Figure 4.11: The layout of the muon spectrometer [37]. A cross-sectional view is shown on top, and a cut-away side view is shown on bottom.

sectors. The magnetic field is monitored by nearly 1800 Hall probes throughout the MS and are used to compare and improve the B-field modeling software used for tracking. Incorporating all the design parameters, the main contributions to the MS stand-alone tracking resolution can be found in Figure 4.12. The momentum resolution is dominated by energy loss in material before the MS at low energies, by multiple scattering at medium energies, and chamber alignment and intrinsic detector resolution at high energies.

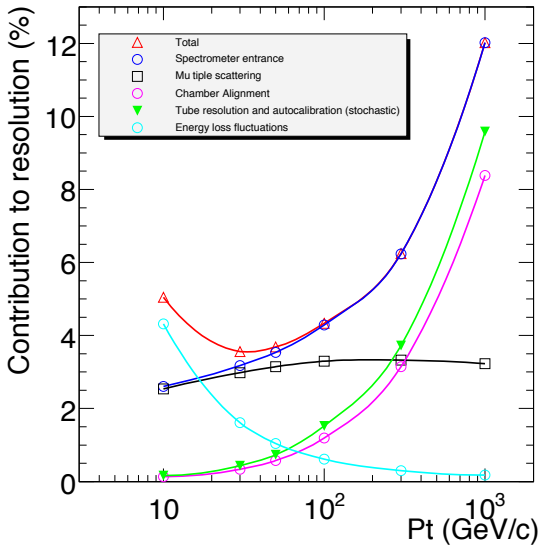

Figure 4.12: Primary contributions to muon stand-alone tracking resolution [24].

4.5.1 Monitored Drift Tubes

A schematic of a typical MDT chamber can be found in Figure 4.13. Each chamber is built with two multi-layers of three tube layers, except in the inner most layers where four tube layers are used in order to aid pattern recognition in the face of high particle

flux. There are 30-72 tubes in each layer, depending on the chamber location, and the tubes of adjacent layers are staggered by half a tube. The chambers in the barrel are rectangular while those in the end-cap are trapezoidal. Because of the differing chamber shapes and sizes, the tube lengths vary depending on location from ∼1 m to ∼6 m in the largest radius chambers of the end-cap wheels. The chambers are held together with a support structure which contains an optical alignment system that is used to monitor the chambers for deformations and to monitor the inter-chamber alignment. In addition, each chamber is outfitted with sensors to monitor the local magnetic field and temperature.

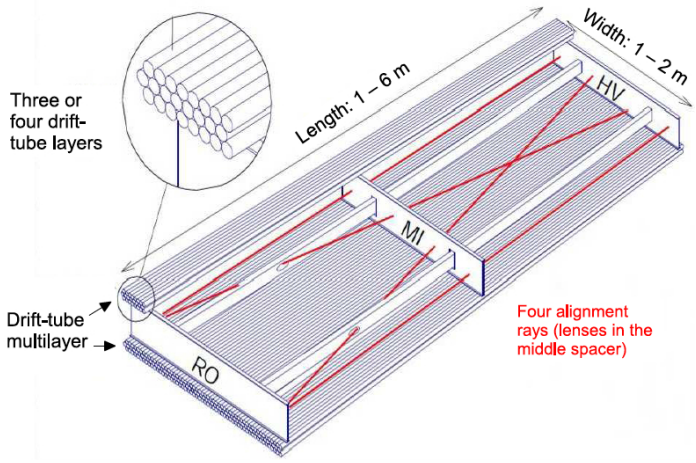

Figure 4.13: Layout of an MDT chamber [37]. The two multilayers containing three layers of tube are shown, along with the support structure and the optical alignment system.

Each tube is built from aluminum with a 30 mm diameter and has a 50 μm thick gold-plated tungsten anode wire at the center. The anode wire is held at 3080 V while the cathode tube is held at ground, thus generating a radial electric field. The tubes are filled with a constantly circulating gas mixture of 93% argon, 7% CO_2, and

1 part per million H_2O, held at pressure of 3 bars. The maximum drift time of the tubes is approximately 700 ns.

As a muon passes through an MDT tube, it ionizes the gas, as seen in Figure 4.14. The ionized electrons drift in the electric field towards the anode wire and create an avalanche in the high field region near the wire. The avalanche causes a voltage drop on the wire and is the primary signal of the MDT tube, called a *hit*. The time of arrival of the hit and the integrated charge in the leading edge of the signal pulse are read out and digitized. The charge measurement allows for noise suppression and time slewing corrections. The hit time is a measure of the time of arrival of electrons produced at the distance of closest approach to the wire. Thus, the drift time can be converted into a drift radius measurement with a calibrated R-T relation. Using this method, each tube has a single hit resolution of approximately 80 μm on the hit radius. Since the tubes are oriented along the ϕ direction, each tube gives essentially no information on this second coordinate.

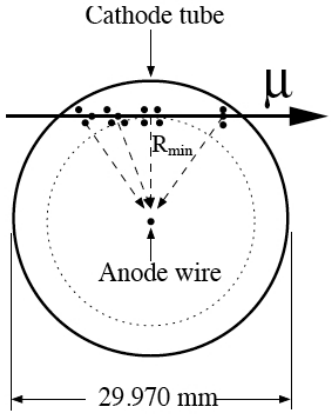

Figure 4.14: A schematic of an MDT tube with a muon traversing the gas. The muon ionizes the gas mixture, and the ionized electrons at the distance of closest approach to the wire, or R_{min}, create the leading edge of the hit signal [37].

4.5.2 Cathode Strip Chambers

The CSC chambers are used in the forward region of the end-cap inner layer ($2.0 < |\eta| < 2.7$) where the particle flux is too high for MDT chambers. The chambers are located approximately 7 m from the IP, with a sixteen chamber wheel (one chamber for each sector, alternating large and small chambers) on each end-cap. The chambers are tilted with respect to vertical as the chamber resolution is optimal for particles traversing at a normal incidence.

Each CSC chamber acts as a multi-wire proportional chamber with anode wires oriented in the radial direction and held at 1900 V and cathode strips run along both sides of the anode wire, as seen in Figure 4.15(a). The chambers are filled with a gas mixture of 80% Argon and 20% CO_2. One set of strips runs perpendicular to the anode wire with a strip spacing of $\sim$5 mm and provides the precision (η) measurement. The other set of strips runs parallel to the anode wires with a coarser strip spacing of $\sim$16 mm and provides the second coordinate (ϕ) information. The cathode-to-wire distance is 2.54 mm (as is the wire-to-wire distance) and this short drift distance leads short maximum drift times of $\sim$30 ns and a hit time resolution of 7 ns. A single chamber combines four such anode/cathode layers, thus providing four precision and four second-coordinate measurements per track.

When a muon traverses the chamber, the gas is ionized and an electron avalanche is formed on the anode wire. The avalanche induces a charge on the strips, which is read out as the signal. A single avalanche can induce signals on multiple strips, and interpolating the charge on neighboring strips allows for a hit resolution of ap-

proximately 60 μm in η and 5 mm in ϕ. An example of the charge sharing between neighboring strips can be found in Figure 4.15(b).

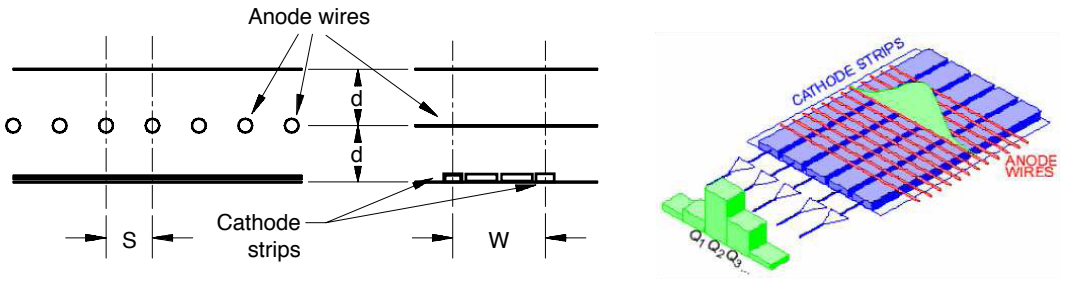

(a) (b)

Figure 4.15: (Left) The layout of a CSC chamber. (Right) An example of the charge sharing amongst neighboring CSC strips [37].

4.5.3 Resistive Plate Chambers

The RPC chambers provide the triggering and second-coordinate measurements in the barrel region ($|\eta| < 1.05$). The chambers are located on both sides of the MDT middle layer chambers, and on the outer (inner) side of the MDT outer layer chambers in the odd (even) sectors. Alternating the chambers between the outside and inside of the outer layer allows for more complete RPC coverage. The geometrical coverage of the RPC chambers is approximately 80% due to spatial constraints from support structures, services, and the feet of the detector.

Each RPC chamber contains two gas volumes imbedded in a paper honeycomb matrix, as seen in Figure 4.16. Each gas volume is surrounded by parallel resistive plates (made of phenolic-melaminic plastic laminate) kept 2 mm apart using insulating spacers and filled with a $C_2H_2F_4$ (93%)/ isobutane (5%)/ SF_6(0.3%) gas mixture. A

strong electric field (4.6-4.8 kV/mm) is applied in the gap. Signals are generated when a muon traverses the gaps and ionizes the gas. The primary ionization causes an avalanche that is read out capacitively by metallic strips mounted on the plates. The strips on either side of the gap are perpendicular, thus allowing for measurements of both the η and ϕ coordinate. The strip pitch is approximately 30 mm, thus giving a spacial resolution of approximately 10 mm. The time resolution of hits is approximately 7 ns, which allows for accurate bunch crossing identification.

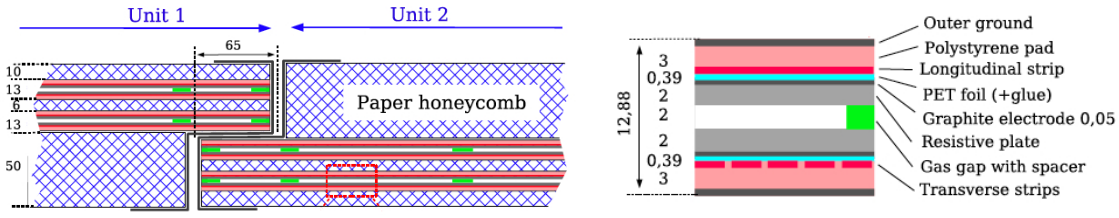

Figure 4.16: The RPC chamber layout (left) and the material layers of a gas gap (right) are shown [37].

4.5.4 Thin Gap Chambers

The TGC chambers provide the triggering and second-coordinate measurements in the end-cap region ($1.05 < |\eta| < 2.7$ with triggering out to $|\eta| = 2.4$). TGC chambers are used because of their higher granularity and higher rate capabilities than RPCs, both of which are vital for performance in the high flux environment in the end-caps. The chambers used for triggering are located around the end-cap middle wheel, with two layers of chambers on the inside of the wheel and one on the outside. Additional chambers used for second coordinate measurements are located on the end-cap inner layer. Each TGC layer is constructed as a wheel with 12 sectors in ϕ and multiple

chambers extending radially. The geometric coverage of this chamber configuration is nearly 99% in the end-cap.

TGC chambers are built from multi-wire proportional chambers, with two layers of graphite cathodes separated by 2.8 mm and a series of 50 μm anode wires running in the middle of the gap between cathodes. One side of the cathodes is segmented into read-out strips. The wire-to-wire distance is 1.8 mm and is thus larger than the wire-to-cathode distance. The wires are held at 2.9 kV and the gaps are filled with a gas mixture of n-pentane (45%) and CO_2 (55%). The wires are oriented in the ϕ direction to measure the η coordinate, while the strips are oriented radially and measure ϕ. The spatial resolution is 2-6 mm in η and 3-7 mm in ϕ. When a muon traverses the gap, the ionized electrons drift to the anode wires and produce a signal. The small gap size allows for very fast signal response and a hit time resolution of 4 ns. Each TGC chamber contains two or three gas gaps held together with a honeycomb structure, called doublet and triplet chambers respectively. Each chamber gives two strip measurements and two or three wire measurements, for doublets and triplets respectively, as seen in Figure 4.17.

4.6 Trigger and Data Acquisition

The ATLAS trigger system [39] is built in three levels: the Level-1 trigger (L1), the Level-2 trigger (L2), and the event filter (EF). The L1 trigger is hardware based,

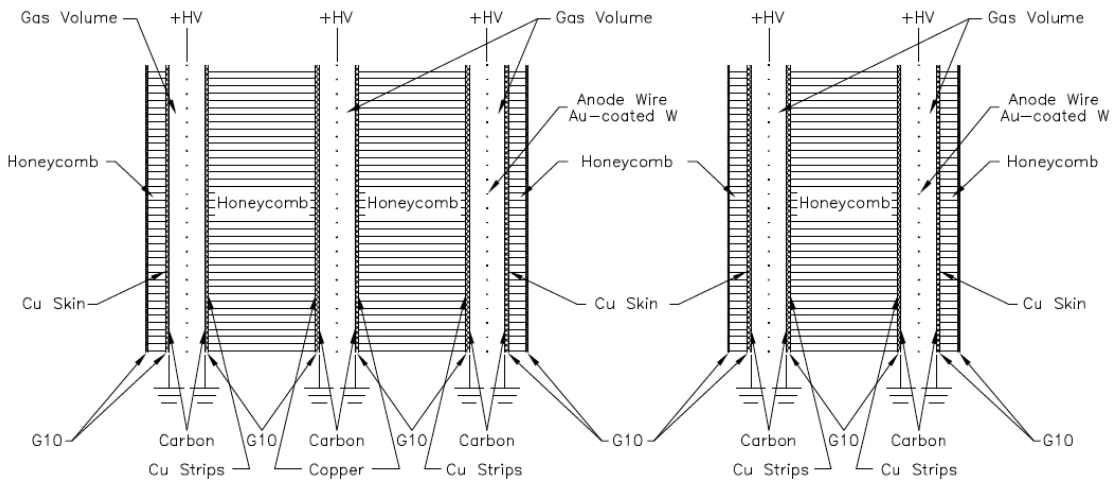

Figure 4.17: The layout out the TGC triplet (left) and doublet (right) chambers [37].

relying on the RPC and TGC for muon triggers and the calorimeter for triggering on EM clusters, jets, taus, and missing energy. The L1 system uses custom electronics to provide low granularity but fast triggering. The L1 trigger decision is designed to occur within 2.5 μs and have a L1 output rate of $\sim$100 kHz. The L2 trigger and event filter together form the High-Level-Trigger (HLT), which is primarily based on commercially available computers and network hardware. The L2 trigger uses Regions-of-Interest (RoI) identified by the L1 trigger, which corresponds to only a subset of the detector information, and thus only a small fraction of the total event data must be transferred to the L2 trigger. Fast reconstruction algorithms are performed on the data in the RoI to allow for more precise trigger decisions. The L2 trigger decision is designed to occur within 40 ms and have a L2 output rate of $\sim$4 kHz. The EF uses the full detector granularity and is based on the analysis of fully reconstructed events. The 2011 output rate of the EF was approximately 400 Hz (about a factor of two above the design output rate).

The ATLAS data acquisition (DAQ) system is designed to control the movement of the data, configure and control the hardware operations, and monitor the detectors. The DAQ moves the L1 selected event data from the detectors into readout buffers. It then provides the necessary RoI data to the L2 trigger. Finally, the DAQ performs the event building (reconstruction) for L2 selected events, and provides the built events to the EF. Monitoring occurs at various levels of this chain, including monitoring the raw detector readouts after the L1 decision to test low level detector operations, rough monitoring of detector performance using fast reconstructed data after the L2 decision, and monitoring physics processes and correlations between detectors using fully reconstructed events after the EF decision.

The primary triggers used in this analysis are high p_T muon and electron triggers. In order to maximize acceptance, the lowest p_T un-prescaled trigger is chosen. As the L2 and EF trigger algorithms are based on reconstruction algorithms used in the offline reconstruction algorithms[3] which are described in Chapter 5, they will not be discussed here. However, the L1 detector trigger algorithms are described briefly in the next sections. A more complete description of the trigger and DAQ system can be found in Reference [39].

4.6.1 Level-1 Muon Trigger

The L1 Muon trigger is based on hit patterns in the RPC and TGC detectors. The hit patterns are computed using fast on-chamber look-up tables defining the necessary

[3]It should be noted that the L2 algorithms are based on simplified and faster reconstruction algorithms, which will not be discussed in detail here.

hit coincidences of the different layers of the trigger chambers. The coincidences are designed to find deviations of tracks from straight lines, and correlate these deviations with trigger momentum thresholds.

The L1 muon trigger algorithm is described pictorially in Figure 4.18. The triggering begins on a reference layer, known as the *pivot plane*, which is the second (middle) layer of the RPCs and the third (outer most) layer of the TGCs. The slope of the line from the interaction point to the hit on the pivot plane is computed, thus defining the straight line hypothesis. Given the location of the pivot-layer hit, predefined search windows, or *roads*, are used to search for hits on the other layers. Once the hits are found, the slope of the straight line from the IP to the new trigger hits is compared to the slope from the pivot layer hits in order to determine the momentum. A predefined number of hits must be found in these roads (typically 3-out-of-4 coincidence of hits, summing over several layers) to ensure a muon has been found. For low $p_T < 10$ GeV triggers, only hits on the inner (middle) layer for the RPC (TGC) are required in addition to the pivot layer hits. For high momentum triggers, hits on all three layers are required.

4.6.2 Level-1 Electron Trigger

The L1 electron trigger is a part of the L1 calorimeter (L1Calo) trigger menu, which also includes photon, tau, jet, missing energy, and total calorimeter energy triggers. The L1Calo system uses 7000 calorimeter trigger towers of size $\Delta\eta \times \Delta\phi = 0.1 \times 0.1$ (except in the forward region which uses lower granularity towers) in both the EM and hadronic calorimeters. The L1Calo system is located off detector in the service cavern

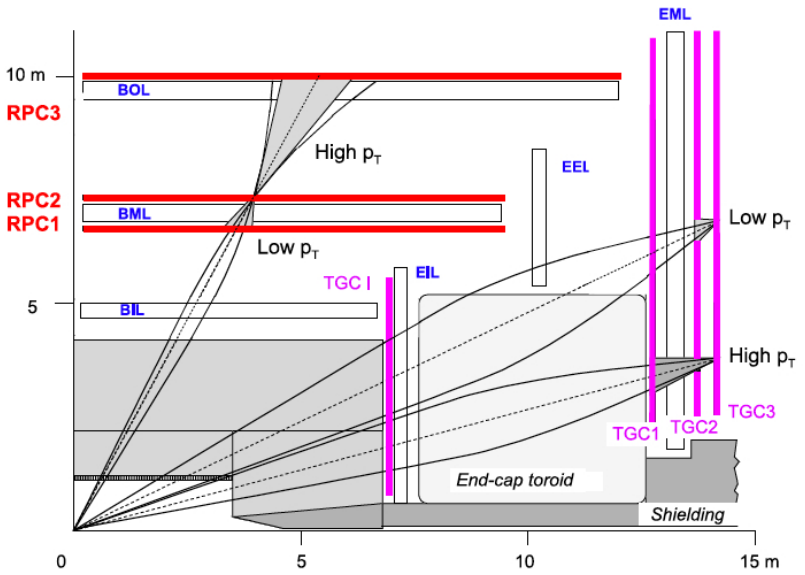

Figure 4.18: Muon L1 trigger logic [39].

and receives the analogue signals from the calorimeter for each trigger tower. These signal are then digitized, and used for bunch crossing identification. A lookup table is used to convert the digitized signals into transverse energy estimates at high speed. A cluster-processor (CP) is then used to identify electron like clusters, determine if the candidate passes a programmable energy and, if required, determine if the candidate passes an isolation threshold. The CP is also capable of identifying photon and tau candidates. A separate processor, called the Jet/Energy processor, is used to identify jets, calculate total calorimeter energy, and calculate the missing energy.

A diagram describing the identification of L1 trigger electron candidates by the CP can be found in Figure 4.19. A sliding window of size 4×4 trigger towers is used to search for candidates. In the central 2×2 group of towers, the EM calorimeter energy in at least one of the possible two tower sums (2×1 or 1×2) must pass a

pre-defined energy threshold. The 12 surrounding EM towers and the 2×2 window of hadronic towers are used to estimate the cluster isolation. Since the sliding window could identify the same electron candidate in multiple windows, the local maximum of energy in the 2×2 window is identified as the candidate.

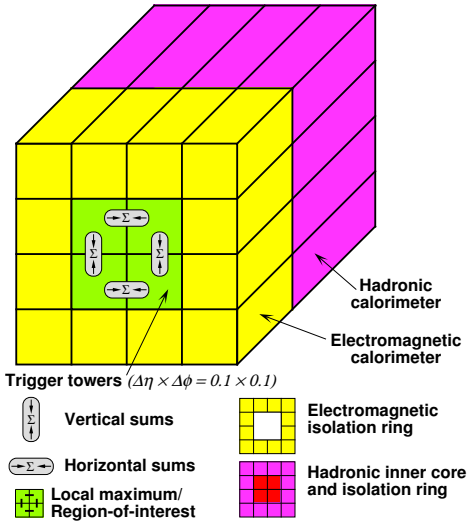

Figure 4.19: Electron L1 trigger logic [39].

4.7 Luminosity Determination

Accurate determination of the LHC luminosity is vital for understanding the performance of the LHC, for determining the proper runtime setting of the ATLAS detector and data acquisition system, and for measuring or limiting the cross sections of SM and BSM processes. Since the luminosity serves as the scaling between the number of observed events and the cross section for a given process, any uncertainties in the luminosity will degrade the precision with which the cross section can be measured. As such, the luminosity is independently determined at ATLAS using several algo-

rithms and detectors, and the agreement between different methods can be used to reduce systematic uncertainties.

The general strategy for luminosity determination in ATLAS is to calibrate the luminosity detectors using a luminosity determined from beam parameter measurements. Once calibrated, the event rates on the detectors can be turned into estimates of the average number of inelastic *pp* collisions per bunch crossing (BC) and then used to measure the luminosity. The luminosity measurements can be performed online, for LHC and detector monitoring, and offline for physics analysis. Only a brief introduction to this strategy is discussed here, while a detailed description of the luminosity determination methods, as well as the performance in 2010, can be found in Reference [41]. The luminosity determination in 2011 can be found in Reference [28].

4.7.1 Detectors for Luminosity Determination

The primary detectors used for luminosity determination in ATLAS in 2011 are LUCID and BCM. LUCID is a Cerenkov detector surrounding the beam-pipe located at a distance of 17 m on each side of the IP and covering the range $5.6 < |\eta| < 6.0$. The detector comprises sixteen aluminum tubes filled with C_4F_{10} gas and the Cerenkov light produced in the gas when traversed by charged particles is reflected down the tubes into photomultiplier tubes (PMT). The beam condition monitor (BCM) is built from 4 diamond sensors arranged in horizontal and vertical pairs on each side of the IP at $z = \pm 184$ cm and $r = 5.5$ cm. The BCM is designed to measure hit rates with fast electronics for beam background monitoring and for sending beam-abort requests. Both LUCID and BCM are capable of providing measurements for each

LHC bunch, thus allowing for bunch-by-bunch luminosity measurements.

4.7.2 Methodology

The luminosity of a pp collider can be expressed as

$$\mathcal{L} = \frac{R_{inel}}{\sigma_{inel}} = \frac{\mu n_b f_r}{\sigma_{inel}} \tag{4.1}$$

where R_{inel} is the rate of inelastic collisions and σ_{inel} is the inelastic scattering cross section. In the second equality, the rate of inelastic collision is expressed in terms of the more fundamental quantities n_b, the number of colliding bunches, f_r, the revolution frequency of the bunches, and μ, the average number of inelastic interactions per bunch crossing (BC). Since n_b and f_r are known LHC parameters, the instantaneous luminosity can be determined by measuring μ and σ_{inel} (or their ratio, if posible).

The luminosity is monitored in ATLAS by measuring the observed number of inelastic interactions per BC, μ_{vis}, using several detectors and algorithms. This observed quantity $\mu_{vis} \equiv \mu\epsilon$ takes into account the efficiency, ϵ, for one inelastic collision to be detected and satisfy selection criteria. The luminosity equation 4.1 can be rewritten as,

$$\mathcal{L} = \frac{\mu_{vis} n_b f_r}{\epsilon \sigma_{inel}} = \frac{\mu_{vis} n_b f_r}{\sigma_{vis}} \tag{4.2}$$

where $\sigma_{vis} \equiv \epsilon\sigma_{inel}$ is denoted the visible cross section. Since μ_{vis} is a measured quantity, σ_{vis} serves as the calibration scale that relates the detector measurements to the luminosity. It should be noted that the luminosity can vary between bunches, which would result in different μ_{vis} values for each bunch. If each bunch is identified

with an integer label, called BCID, equation 4.2 can be written as a sum over BCIDs,

$$\mathcal{L} = \sum_{i \in BCID} \mathcal{L}_i = \sum_{i \in BCID} \mu^i_{vis} \frac{f_r}{\sigma_{vis}} \tag{4.3}$$

where $\mathcal{L}_i$ is the luminosity of bunch i and μ^i_{vis} is the observed average number of interactions per BC of bunch i.

The parameter μ_{vis} is determined in ATLAS using the *Event Counting* method [41] whereby the fraction of bunch crossings passing some selection criteria in a specific detector is determined[4]. More specifically, the detectors used for selection are instrumented on both the A-side and C-side and a bunch crossing is selected as having an event (i.e. at least one pp interaction) if the detector registers at least one hit on either side (the OR algorithm) or at least one hit on both sides of the detector (the AND algorithm). At very small values of μ_{vis}, the average number of visible interactions per BC is given simply by $\mu_{vis} \approx N/N_{BC}$ where N is the number of events passing the selection in a given time interval and N_{BC} is the number of bunch crossings in that interval. As μ_{vis} increases and the probability to observe multiple interactions per BC becomes non-negligible, Poisson statistics must be used to relate μ_{vis} to the event count N. Details of the conversion of counting rates to μ_{vis} measurements incorporating Poisson statistics for both the OR and AND algorithms can be found in Reference [41].

[4]More detailed techniques can also be used to determine μ_{vis}, such as counting the number of hits in a detector per BC or the number of particles produced per BC. However, converting the hit or particle rates into luminosity requires complex Monte Carlo modeling of inelastic pp collisions and modeling of the detector response. This modeling introduces systematic uncertainties into the luminosity calculation. Extensive study of the conversion methods and the systematic errors are needed to reliable use these methods and are not yet available for ATLAS.

The calibration of the luminosity scale, i.e the measurement of σ_{vis}, is performed by inferring the absolute luminosity from measured beam parameters,

$$\mathcal{L} = \frac{n_b f_r n_1 n_2}{2\pi \Sigma_x \Sigma_y} \tag{4.4}$$

where n_1 and n_2 are the number of particles in the two colliding bunches and Σ_x and Σ_y are related to the horizontal and vertical widths of the beam overlap profiles. The beam currents n_1 and n_2 are measured using two complementary LHC systems, the DCCT which measures the total beam current and the FBCT which measures the bunch-to-bunch current variations [49]. The values of Σ_x and Σ_y can be measured using a technique called *van der Meer* (vdM) scans[5] [110], whereby the observed event rate R, as measured by the ATLAS detectors, is recorded as the separation between the two colliding beams, δ, is scanned first horizontally and then vertically. The resulting event rates as a function of separation in the x direction, $R_x(\delta)$, can be used to extract the values of Σ_x using the relation

$$\Sigma_x = \frac{1}{\sqrt{2\pi}} \frac{\int R_x(\delta) \mathrm{d}\delta}{R_x(0)} \tag{4.5}$$

where $R_x(0)$ is the observed event rate at zero separation, i.e. the maximum rate [41]. The same procedure is applied in the y direction to extract Σ_y. The absolute luminosity at zero separation can then be computed from beam parameters, and σ_{vis} can be extracted by relating equations 4.1 and 4.4,

$$\sigma_{vis} = \frac{R^{MAX}}{\mathcal{L}^{MAX}} = \mu_{vis}^{MAX} \frac{2\pi \Sigma_x \Sigma_y}{(n_1 n_2)^{MAX}} \tag{4.6}$$

where R^{MAX}, $\mathcal{L}^{MAX}$, $(n_1 n_2)^{MAX}$, and μ_{vis}^{MAX} are the maximum event rate, luminosity, beam currents, and observed average number of interaction per BC, respectively, as

[5] vdM scans are also called luminosity or beam-separation scans

measured at zero separation. Thus σ_{vis} can be determined with this *vdM* technique without *a priori* knowledge of the inelastic *pp* cross section or detector efficiencies, both of which are prone to systematic uncertainties.

4.7.3 Calibration Using Beam Scans

Dedicated *vdM* scans for luminosity calibration took place on May 15, 2011, and results presented here are from the analysis of this scan data in Reference [28]. Several horizontal and vertical scans were performed while the LHC was operating with 14 bunches and an average $\mu \approx 2.3$. An example measurement of the horizontal beam profile from LHC fill 1783 can be seen in Figure 4.20, where the specific interaction rate, $\mu_{vis}/(n_1 n_2)$, is measured as a function of beam separation. The specific interaction rate is used so that the results are not sensitive to changes in beam current over the course of the fill. This profile was fit with a Gaussian and used to extract the beam widths. Between bunches, the beam width was seen to vary up to ± 3 μm, as seen in Figure 4.21, and the beam currents were seen to vary by 10-20%. Thus bunch-by-bunch measurements are vital for precision luminosity determination. The results for the measurement of σ_{vis} can be seen in Figure 4.22 as a function of the BCID for one of the *vdM* scans. Variations between bunches were seen to be approximately 0.6%. The deviation in values of μ_{vis} from the measurement of the BCM horizontal detectors using the OR algorithm for other detectors and algorithms can be found in Figure 4.23, showing a consistency between detectors and algorithms of less than 1% over a large range of μ_{vis} values.

The total uncertainty on σ_{vis} was determined to be 3.4% and the total luminosity uncertainty was determined to be 3.7%. The primary source of uncertainty, with a contribution 3.0%, was from the beam current measurements. Specifically, the calibration of the DCCT (which determines the total current normalization) had a 2.7% uncertainty due to variations over time. The bunch-to-bunch current fraction, as determined by the FBCT, had an uncertainty of 1.3% determined by comparing measurements with the ATLAS beam pickup system. Some of the other sources of uncertainties came from beam centering, beam separation length scale calibrations, fit modeling, beam position jitter, bunch to bunch variations in σ_{vis}, as well as several other sources all documented in [28].

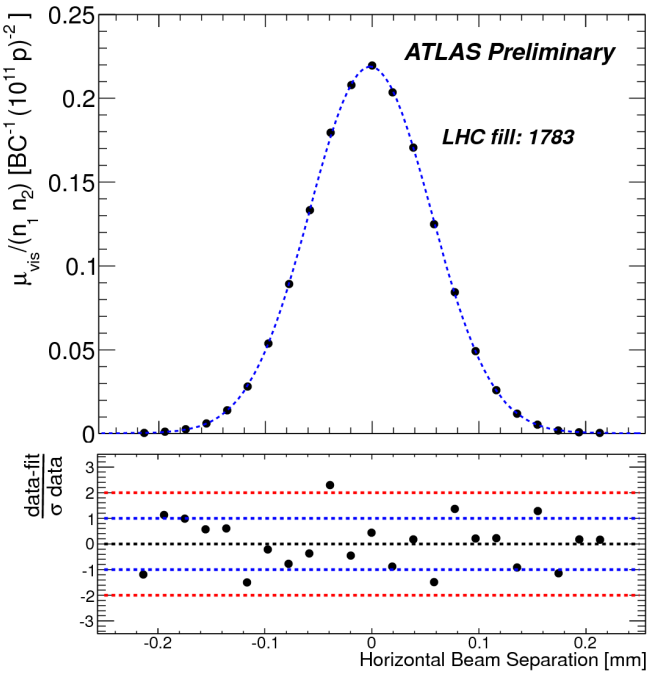

Figure 4.20: Specific interaction rate versus beam separation, which allows for the measurement of the beam profile and the determination of Σ_x and Σ_y. This measurement is from a single BCID using data from a horizontal scan [28].

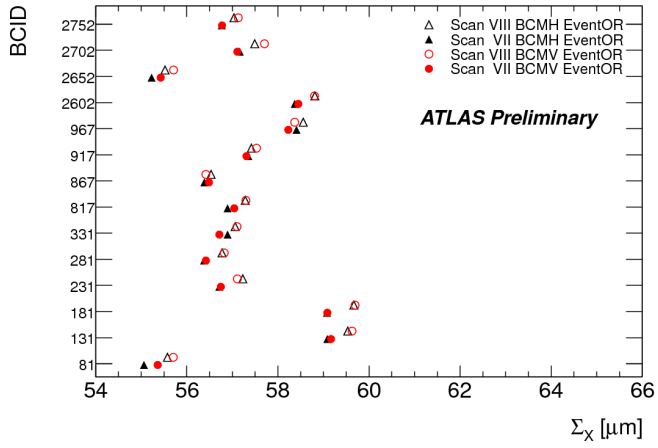

Figure 4.21: Σ_x measurements from different scans for different BCIDs as measured by the BCM detector using the OR algorithm [28].

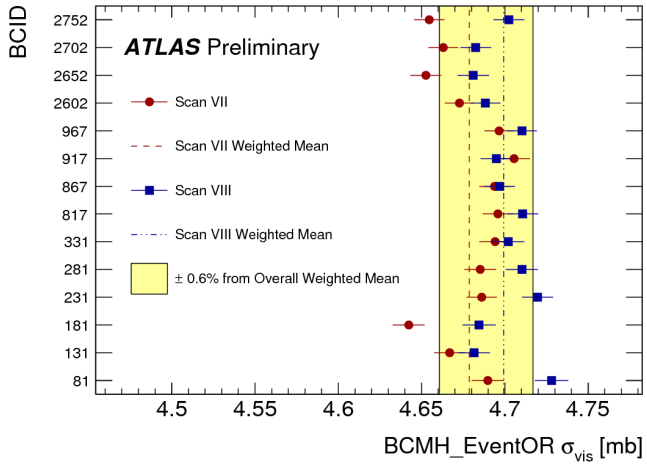

Figure 4.22: Visible cross section, σ_{vis}, measurements from different scans for different BCIDs as measured by the BCM horizontal detectors using the OR algorithm [28].

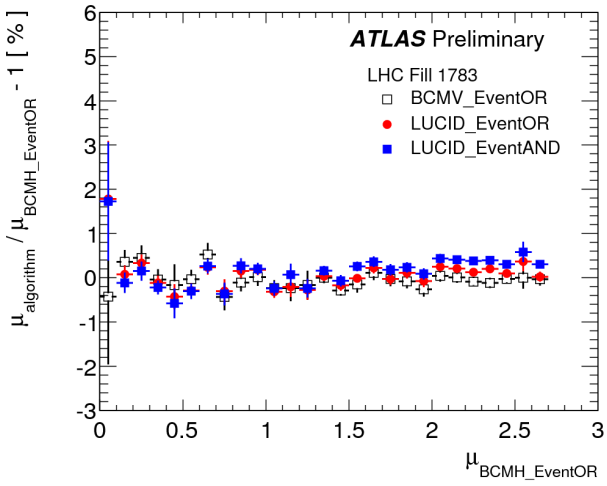

Figure 4.23: Deviations in the measured number of observed interactions per BC μ_{vis} from the measurement of the BCM horizontal detectors using the OR algorithm as a function of μ_{vis} [28].

Chapter 5

Physics Object Reconstruction

This chapter provides an introduction to the reconstruction of physics objects from the detector signals. Only the reconstruction of physics objects used in this analysis are discussed here. Charged particles are reconstructed as tracks in the ID, described in Section 5.1. The ID tracks are also used for primary vertex reconstruction, described in Section 5.2. The reconstruction of electrons and muons, used extensively in this analysis, is described in Section 5.3 and Section 5.4 for electrons and muons, respectively. The reconstruction of jets, used in event cleaning and missing energy reconstruction, is discussed in Section 5.5. Finally, the reconstruction of the transverse missing energy associated to particles escaping detection (i.e. neutrinos) is described in Section 5.6.

It should be noted that the performance of the muon and electron reconstruction, as it pertains to this analysis, will be discussed in Chapter 6.

5.1 Inner Detector Tracks

The ATLAS inner detector track reconstruction algorithm, known as *New Tracking* (NEWT) [60], relies on several pattern recognition and track fitting methods. Due to the complex material structure and magnetic field of ATLAS, a simple helical model of a particle's trajectory in a B-field can not be used. Instead, track finding (i.e. associating hits to track candidates) and track fitting (i.e. estimating the track parameters and covariance matrix) must be done simultaneously whilst also extrapolating the track though the B-field and estimating the energy loss in material.

The first step of the ID track reconstruction is to build tracks with the *inside-out* method, which starts from the inner most detector elements and works outward. After converting silicon and SCT hits to space-point measurements, hits in the pixel detector are used to seed the tracks. Track segments are then formed by extrapolating outward through the remaining pixel layers and through the SCT using the *Kalman Filter* [77]. The Kalman filter is an iterative procedure whereby the track is described by a state vector and error matrix at each point along the track. Starting from the seed, the state vector and error matrix are extrapolated to the next detection layer. The extrapolation takes into account the bending in the magnetic field, expected energy loss, multiple scattering, and the associated uncertainties. A search window on the next detection layer is defined based on the extrapolated state vector and error matrix. If a new hit is found on the next detection layer, the state-vector and error matrix are updated to include the new hit information and its uncertainty. If no hit is found, the method can continue search further detection layers to account for the

possibility of a hole, or detector element which failed to register a hit even though it was crossed by the particle. Mathematically, the Kalman filter is equivalent to an iterative least-squares fit of the track that accounts for energy loss and inhomogeneous magnetic fields [105]. The algorithm also scales linearly with the number of hits found at each layer (in the case where multiple are found) and thus multiple track candidates can be examined with relatively low time consumption [60]. During this whole procedure, the quality of the track is monitored by examining the track χ^2. Hits which significantly degrade the track quality are removed from the track fit, and treated as outliers. To resolve ambiguities caused by shared hits, track candidates are scored and the hit is typically associated to the track with the higher score. Once the ambiguities are resolved, only tracks with sufficiently high quality are kept, thus helping to remove poorly reconstructed or fake tracks. The tracks are then extended to the TRT, whereby the parameters of the fitted silicon track are used to search for a compatible set of measurements in the TRT. Once TRT hits have been associated, the full track is refit.

There are several circumstances that can cause the inside-out method to fail. Silicon tracks may fail their extension into the TRT because of bremsstrahlung (causing a kink in the track and thus track extrapolation may miss the correct TRT measurements), the track can originate from a decay in flight or photon conversion (meaning the track may not have the necessary hits in the inner pixel layers needed for seeding), or the silicon track may be thrown away or never formed at all due to the track quality cuts and ambiguity resolution methods. Thus, the second step of the ID track reconstruction, after the inside-out algorithm has finished to look for tracks, is to

build tracks with the *outside-in* algorithm. In this method, TRT hits are globally transformed into track parameter space using a Hough transform [66] where tracks appear as peaks in the parameter space distribution of the hits. The hits associated to the Hough maximum are then refit with the Kalman filter and extended backward into the silicon.

5.2 Primary Vertices

Primary vertex (PV) reconstruction is performed by first running a vertex finding algorithm to identify vertex candidates, followed by fitting each of the vertices to determine the position and error matrix. The vertex finding algorithm is an iterative procedure based on the *adaptive vertex finding* algorithm, described in detail in Referene [78]. Once vertices have been found, the tracks associated to the vertex are used to fit for the vertex position and error matrix whilst using the beam spot as a constraint[1]. The vertex with the highest $\sum p_T^2$ of tracks is considered the primary vertex of the bunch crossing.

A brief description of vertex finding follows, while a complete description can be found in Reference [32]. Tracks consistent with having originated from the interaction region (determined based on track d_0 and z_0 cuts defined such that tracks are consistent with the beam spot) and having $p_T > 400$ MeV are selected. The initial PV seed is taken as the z value corresponding to the maximum in the distribution of track z values at the point of closest approach to the beam spot center. The adaptive vertex

[1]The beam spot is formed by a fit to the distribution of primary vertices without any beam-spot constraints

finder, which is essentially an iterative χ^2 fit, takes this seed and the nearby tracks to fit the vertex. Outlier tracks are weighted lower in the fit during each iteration, and tracks that are incompatible with the vertex by more than 7σ are removed and used to fit a new vertex. This procedure is repeated until all tracks are associated to vertices, or no more vertices can be found.

Results on vertex reconstruction using $\sim$24 pb^{-1} of 2011 minimum bias triggered data can be found in Figures 5.1 and 5.2. The distribution of primary vertices in the $x-y$ plane and $x-z$ plane can be found in Figure 5.1. The RMS of of the vertex location are 15.7 μm, 13.5 μm, and 56.8 mm, in the x, y, and z directions, respectively, giving a rough estimate of the beam spot volume during this period of running. The vertex resolution, as determined by the error matrix of the fit of associated tracks, in the x and z directions can be found in Figure 5.2. For hard collisions giving PVs with $\sqrt{\sum p_T^2} > 10$ GeV, the resolution is roughly 15 μm in the x and y directions and roughly 30 μm in the z direction.

5.3 Electrons

This section describes the reconstruction of high p_T electrons in the central region $|\eta| < 2.47$, excluding the crack region of $1.37 < |\eta| < 1.52$ which contains large amounts of material and is used for services between the barrel and end-cap. Electron reconstruction and identification are described in detail in Reference [22], and this section follows this description closely. The process begins with calorimeter cluster finding, then proceeds to electron candidate reconstruction, after which the candi-

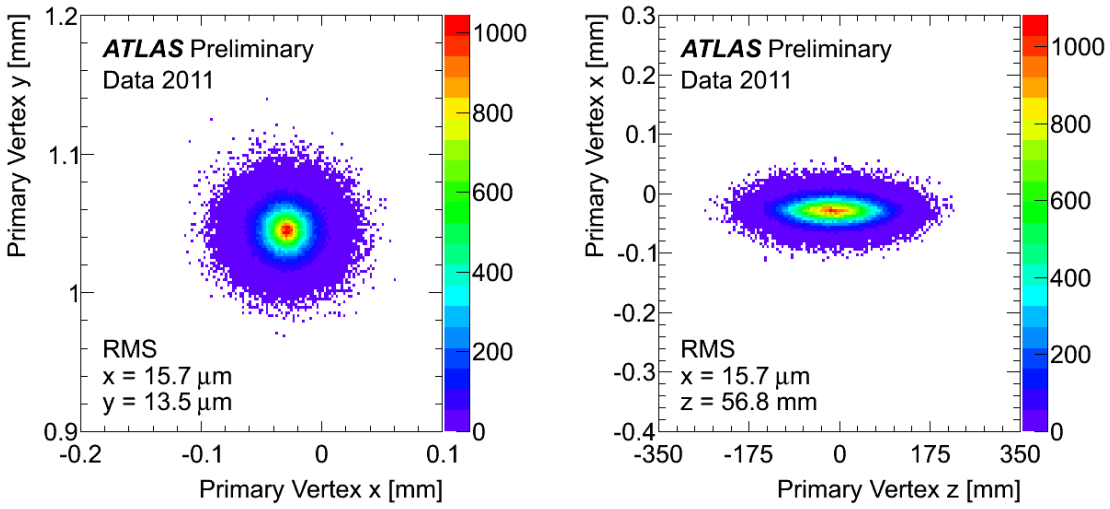

Figure 5.1: The distribution of the fitted location of primary vertices with at least 3 tracks in the $x-y$ plane (left) and $x-z$ plane(right) . The figures are made with $\sim$24 pb^{-1} of 2011 minimum bias triggered data [19].

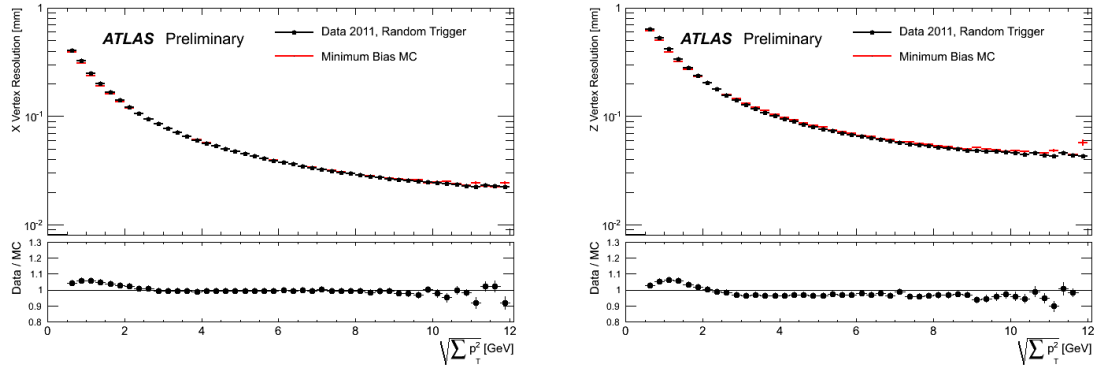

Figure 5.2: The primary vertex x resolution (left) and z resolution (right). The resolution is plotted as a function of the $\sqrt{\sum p_T^2}$ of tracks fitted to the vertex (at least 3 tracks are required to originate from the vertex). The figures are made with $\sim$24 pb^{-1} of 2011 minimum bias triggered data [19].

date is required to pass identification criteria, and finally the electron candidate is calibrated.

Electron cluster seeds, or pre-clusters, are found using a sliding window over the full acceptance of the EM calorimeter. The pre-cluster sliding window size is 3×5 cells in terms of the EM calorimeter middle layer granularity (i.e. single cells have a size of $\Delta\eta \times \Delta\phi = 0.025.025$). The calorimeter cell signals are converted to energies based on the observed electron response from test beam data. The energy in the window is calculated by summing the energy in the longitudinal layers of the window and if the energy satisfies $E_T > 2.5$ GeV then the pre-cluster is kept.

Electron candidate clusters are then reconstructed with an optimized fixed size around the center of the pre-clusters. The optimal size for electron clusters is 3×7 cells in the barrel and 5×5 cells in the end-cap, where again cells correspond to EM middle layer granularity. To be further considered as a candidate electron, the cluster must be loosely matched to an ID track. The track must have $p_T > 0.5$ GeV and must point within $\Delta\eta < 0.2$ and $\Delta\phi < 0.1$ to the cluster position when using the track parameters expressed at the origin. The best track is chosen by extrapolating the track to the EM calorimeter middle layer and finding the track pointing closest to the cluster barycenter.

The electron candidate is then required to pass identification criteria designed to select electrons with high and uniform efficiency over the detector acceptance. There are three levels of criteria, labeled *loose*, *medium*, and *tight*. The selection criteria rely on rectangular cuts on calorimeter and track variables that allow for good dis-

crimination between electrons, photons, and QCD fakes (such as π^0s). The tighter criteria correspond to more stringent requirements on the electron candidate and thus have better background rejection but lower efficiency. The loose criteria includes cuts on the shower shape in the EM calorimeter middle layer and the fraction of energy deposited into the hadronic calorimeter. The medium selection criteria includes all the loose criteria as well as cuts on the shower shape in the strips of the first EM calorimeter layer, cuts on the ID track quality (i.e. cuts on the number of hits in the pixel and SCT detectors, and cuts on the track parameters), and cuts on the track matching to the cluster. The tight selection criteria includes all of the medium selection criteria as well as more stringent track matching, cuts on the ratio of the cluster energy to the track momentum (E/p), cuts on the number of required TRT regular and high-threshold hits, and a requirement that the track must have a hit in the first pixel layer (if the pixel was known to be functioning).

The electron candidate energy is then calibrated, taking into account energy lost before the calorimeter, lateral and longitudinal leakage outside the cluster, and the energy contained in the cluster itself. The first step includes η and ϕ dependent corrections for small variations in the local energy response due to hardware effects (like the accordion structure). Then the calibration is performed as a function of η using the equation,

$$E = s(\eta)[c(\eta) + w_0(\eta) \cdot E_{PS} + E_{strips} + E_{middle} + w_3(\eta) \cdot E_{back}] \tag{5.1}$$

where $s(\eta)$ is the overall scale, $c(\eta)$ is a constant offset term, $w_0(\eta)$ accounts for energy lost upstream of the detector, and $w_3(\eta)$ accounts for longitudinal leakage outside the

EM calorimeter. The energy terms come from the calorimeter layer measurements, where E_{PS} is the energy measured in the presampler, E_{strips} is the energy measured in the first layer strips, E_{middle} is the energy measured in the middle layer, and E_{back} is the energy measured in the third back layer. The different weights are determined using Monte Carlo simulations which have been refined used test beam and collision data. In addition, the overall energy scale is refined using the Z mass peak position in data.

if the track associated to the electron is observed to have sufficient quality, then the electron direction is taken from the track η and ϕ because the ID tracking has a high precision angle determination than the calorimeter. However, if the ID track does not meet the quality criteria, the electron direction is taken from the cluster direction defined by the energy barycenter in the EM calorimeter middle layer.

5.4 Muons

The reconstruction of muons in ATLAS relies on the Muon Spectrometer, the Inner Detector, and the Calorimeter, and is performed with several identification and tracking algorithms. The MS is capable of stand-alone tracking out to $|\eta| < 2.7$, for which the tracks are referred to as *MS tracks* or *Stand-Alone (SA) muons*. In regions with ID coverage ($|\eta| < 2.5$), the ID provides an independent measurement of the muon track. The ID track can be identified as a muon candidate by matching the track with calorimeter energy depositions consistent with minimum ionizing particles (called *Calo muons*), matching the track with hits in the MS (called *Segment-Tagged*

muons or *Segment-Tagged tracks*), or matching and combining with MS tracks (called *Combined muons* or *Combined tracks*). The Calo muons are most useful for very low p_T muon reconstruction and will not be discussed further here. The Segment-Tagged muon reconstruction is useful when it is not possible to identify hits on all layers of the MS, either because the track is low momentum and is bent out of the acceptance by the toroid field or because all layers of the MS are not instrumented (i.e. in regions used to allow for services or support structures).

The Combined muons have the lowest fake rates and the best resolution of the reconstruction algorithms. In the $p_T \lesssim 40$ GeV regime, the ID track resolution is excellent because the solenoid field is strong enough to significantly bend the track and there is relatively little material causing energy loss of muons in the ID. In the high momentum $p_T \gtrsim 100$ GeV regime, the MS tracking resolution is excellent because of the long MS lever arm and energy loss is not a primary contribution to resolution. Thus, the Combined tracking performance relies on the ID resolution in the low p_T regime, on the MS resolution in the high p_T regime, and on a balance between both ID and MS track resolutions in the intermediate p_T regime.

There are two primary MS tracking algorithms known as `MOORE` [3] and `MUONBOY` [98], and the combined tracks making use of these MS tracks are known as `MuID` and `STACO`, respectively. Both the MS track reconstruction and the matching procedure differ between these two algorithms, but the two algorithms have been shown to have equivalent performance in terms of reconstruction efficiency and resolution. This analysis makes use of the `MUONBOY`/`STACO` algorithm, collectively known as `STACO` and thus the

`MOORE/MuID` algorithm will not be discussed further. A brief description of only the `STACO` algorithm will be provided here, and thus it unambiguous to refer to the track types as MS tracks, Segment-Tagged tracks, or Combined tracks, without explicitly stating the algorithm name.

The first step of reconstruction is to find hits on the trigger chambers (RPC and TGC) and define a region of activity (ROA) of $\sim 0.4 \times 0.4$ in $\eta \times \phi$ around the trigger hits. All chambers in the ROA are then used for pattern recognition. The next step is to form straight line *segments* in the MS layers (a straight line approximation is used since bending is negligible over the length scale of a single chamber). The segments are formed from the drift radius measurements of the MDTs, where the lowest χ^2 line segment formed from the hits and their errors are kept. Hits significantly degrading χ^2 are removed. The highest quality, or *tight* segments, are required to have at least one ϕ hit from a trigger chamber and thus can only be formed on the middle and outer layers of the barrel and on the inner and middle layers of the end-cap. Lower quality, or *loose*, segments do not require the ϕ hit.

Tight segments are used to seed the track finding. Using a rough momentum estimate from the track segment, the track is extrapolated to the nearest MS layer and a search is performed for addition loose segments which are consistent with the rough momentum estimate within a momentum window. If a loose segment is found, a the track containing both segments is simultaneously fit, and then additional segments are searched for in the same manner. After segment searching is finished, track candidates with at least two segments are kept, and the hits contained in all the

segments are refit to form the final MS track candidate. The track is then extrapolated to the IP. It should be noted that track extrapolation takes into account bending in the magnetic field, parameterized energy loss in material, and multiple scattering.

Combined muons are formed with a statistical combination of MS tracks and ID tracks. The combination is performed with a χ^2 which accounts for the track parameters and covariance matrices of both the MS and ID tracks. Combinations with low enough χ^2 are kept, and a covariance weighted combination of the MS and ID track parameters is used as the Combined track parameters.

Segments not used by the MS stand-alone or Combined muon tracking are used for Segment-Tagged muon reconstruction. These segments are matched in η and ϕ to ID tracks, yielding the Segment-Tagged muon candidate. The track parameters are taken only from the ID track measurement.

Finally, a completely separate tracking algorithm outside of the `STACO` package called `MuGirl` [88] is used for reconstruction in the trigger. This algorithm extrapolates ID tracks outward into the MS using a neural network to identify hits. The ID track and the identified MS hits are refit to form the best track parameter measurements.

5.5 Jets

Jets are not used heavily in this analysis, except in missing energy reconstruction and for vetoing events with poorly reconstructed jets that signify poor calorimeter

performance. Thus jet reconstruction will only be discussed briefly here, and a more complete description can be found in Reference [40].

The input to jet reconstruction is *topo-clusters*, or clusters of calorimeter cells. The topo-clusters are an attempt to perform 3D reconstruction of energy depositions of hadron showers in the calorimeter. Topo-clusters are seeded with calorimeter cells satisfying $|E_{cell}| > 4\sigma$, where E_{cell} is the pedestal subtracted EM scale calibrated cell energy and σ is the cell noise from electronics and pileup. All cells neighboring the seed with $|E_{cell}| > 2\sigma$ are added to the topo-cluster. Neighbors of the secondary cells with $|E_{cell}| > 2\sigma$ are added to the cluster, and this process is repeated until no neighboring cells with $|E_{cell}| > 2\sigma$ are found. At this point, all cells neighboring the topo-cluster are added to the cluster. The energy of the topo-cluster is the sum of the energy of the cells in the cluster, and the direction is the energy weight sum of the directions of the constituent cells.

Jet reconstruction is preformed by combining topo-clusters with the anti-k_T algorithm [54] with distance parameter $R = 0.4$. As the clusters are calibrated only to the EM scale, the jet is said to be calibrated at the EM scale. The jet is then calibrated to the hadron scale using the jet response observed in MC simulations. A variety of data-driven techniques are used to improve the accuracy of the jet energy scale, improve the jet energy resolution, and derive systematic uncertainties.

5.6 Missing Transverse Energy

Missing transverse energy [46], or E_T^{miss}, is calculated from energy depositions in calorimeter cells and from reconstructed muons using the equation,

$$E_{x(y)}^{miss} = E_{x(y)}^{miss,\ calo} + E_{x(y)}^{miss,\ \mu} \tag{5.2}$$

$$E_T^{miss} = \sqrt{(E_x^{miss})^2 + (E_y^{miss})^2} \tag{5.3}$$

$$\phi^{miss} = \arctan(E_y^{miss},\ E_x^{miss}). \tag{5.4}$$

The calorimeter cells are first associated to reconstructed physics objects and calibrated as a part of these physics objects. Specifically, the calorimeter cells are associated to electrons, photons, hadronically decaying taus, hard jets with $p_T > 20$ GeV, soft jets with 7 GeV$< p_T <$20 GeV, and muon energy depositions in the calorimeter. Cells not associated to one of these objects are summed together and called the *CellOut* term. Once calibrated to the appropriate physics object, the missing energy contribution is calculated by summing over the cells using the equation

$$\begin{aligned} E_x^{miss,\ object} &= -\sum_{i \in cells} E_i \sin(\theta_i)\cos(\phi_i) \\ E_y^{miss,\ object} &= -\sum_{i \in cells} E_i \sin(\theta_i)\sin(\phi_i) \end{aligned} \tag{5.5}$$

where E_i, θ_i, and ϕ_i are the cell calibrated energy, polar angle, and azimuthal angle, respectively. Physics objects can be included up to $|\eta| < 4.5$.

The muon term is calculated for muons with $|\eta| < 2.7$ using the equation

$$E_{x(y)}^{miss,\ \mu} = -\sum_{muons} p_{x(y)}^{\mu} \tag{5.6}$$

The summation includes Combined muons, Segment-Tagged muons with $p_T > 12$ GeV, and MS Stand-Alone muons for $2.4 < |\eta| < 2.7$. The muon momentum is expressed at the IP and thus has been extrapolated though the calorimeter taking into account energy loss. Since muon energy depositions in the calorimeter are included as a part of the calorimeter cell summation, the cells associated to isolated[2] muons and a parameterized energy loss in the calorimeter for non-isolated muons (where muon specific cells can't be identified) are subtracted off the cell summation to avoid double counting.

[2]Isolation is a measure of how much energy is near the muon as measured by tracks in the inner detector and/or energy depositions in the calorimeter. Isolation will be discussed further in Chapter 6.

Chapter 6

$W^{\pm}Z$ Analysis

This chapter describes the measurement of the $W^{\pm}Z$ production cross section in events containing electrons, muons, and missing energy in the final state. Thus there are four final states considered in the analysis: $\mu\mu\mu$, $e\mu\mu$, $ee\mu$, and eee, where the presence of a neutrino from the W decay is assumed in the channel naming scheme. The analysis uses 1.02 fb^{-1} of data produced by LHC collisions and accumulated by the ATLAS detector in 2011. This chapter is adapted from the ATLAS internal note describing the analysis [10], but provides more detail than the note when appropriate. This analysis has been published in an abbreviated form [44].

The $W^{\pm}Z$ production cross section measurement is a probe of the electroweak sector of the Standard Model at high energies. Given that the EW sector of the SM is known to have problems at the TeV scale, this measurement helps to frame the performance of EW predictions and the ATLAS detector in the presence of high energy multi-lepton signatures. As such, cross section measurements of SM processes

are the first step towards understanding the EW sector, thus allowing for clearer interpretations of searches for new physics like the Higgs Boson. In addition to cross section measurements, the data set can be used to test for anomalous triple gauge couplings. The anomalous triple gauge couplings model a generic contribution to $W^{\pm}Z$ production from new high energy physics processes, and thus the aTGC analysis provides a generic test of the high energy behavior of the EW sector.

Events are required to have three high momentum electrons or muons, as well as large missing transverse energy. Additional selection criteria on the dilepton mass of the Z candidate and the transverse mass of the W candidate are required in order to ensure the presence of the Z and W bosons. Even with this selection criteria, several background processes can mimic this signature. The backgrounds can roughly be categorized into two types.

The first category of backgrounds includes processes with three or more prompt leptons from the hard scattering, and is predominantly ZZ events with four leptons in the final state. If one of the leptons falls outside of the detector acceptance and is observed as missing energy, the event will have the $W^{\pm}Z$ signature. However, the detector acceptance and the ZZ kinematics are well described in simulation and thus this background is modeled using MC predictions.

The second category of backgrounds is events containing at least one *fake* lepton, where fake leptons can be non-prompt leptons from heavy flavor decay, pion/kaon decay in flight, or jets misidentified as leptons (particularly in the case of electrons). The primary backgrounds which fall into this category are Z+jets and $t\bar{t}$. Thus these

events contain two prompt leptons and one fake lepton. While the vast majority of these events are rejected by the selection criteria, these process have large inclusive production cross sections at the LHC and thus contribute a non-negligible background to $W^{\pm}Z$ events. Since the properties of fake leptons depend greatly on the jet production and fragmentation process, which are not well modeled by MC simulations, these backgrounds are modeled using control regions in data.

The cross section is extracted using a maximum likelihood (ML) fit to the observed number of events in each of the four decays channels in data. For this extraction, the selection acceptance and efficiency are modeled using MC simulations of the signal. Several corrections are applied to this simulation in order to account for several observed discrepancies between the MC simulations and the data.

The selected $W^{\pm}Z$ sample is also interpreted in terms of anomalous triple gauge couplings by setting limits on contributions from aTGCs at the 95% confidence interval using a frequentist limits setting procedure. The limits are calculated using the observed number of events per decay channel. In order to set limits, the same likelihood function from the cross section analysis is used, except that it is modified to predict the number of signal events as a function of aTGCs rather than as a function of production cross section. This modification of the likelihood function allows for the inclusion of deviations of the acceptance from the SM predictions.

6.1 Data Samples

The data used in this analysis was acquired by ATLAS between April and June of 2011 from 7 TeV collisions of the LHC. The data is subjected to a set of data quality criteria, which requires proper functioning of the inner detector, calorimeter, muon spectrometer, magnets, luminosity detectors, trigger and data acquisition system (including the reconstruction software for the event filter), and require that the colliding bucket of both beams contains protons (i.e. collisions were possible). The quality of the data per luminosity block is stored in a *Good Run List* (GRL)[1] [14]. This high quality dataset corresponds to an integrated luminosity of 1.02 fb^{-1} with an uncertainty of 3.7% [28]. The calculation of the total luminosity and the luminosity uncertainty is described in Section 4.7. The data is recorded in two streams, depending on the event trigger: physics_Muons (muon triggered) and physics_Egamma (electron or photon triggered). If an event is observed to be both muon and electron triggered (and thus in both streams), the event is removed from the electron stream. Offline reconstruction is performed with Athena [11] release 16.6. It should be noted that during approximately 95% of this data taking period, six LAr calorimeter front-end boards were not functioning and the associated drop in acceptance is taken into account by scaling the MC samples. The samples are post-processed by the SM W/Z physics group into the D3PD format, which are essentially ROOT [107] ntuples.

[1]Specifically, the GRL is
`data11_7TeV.periodAllYear_DetStatus-v18-pro08-04_WZjets_allchannels.xml`
made using the `StandardModel.WZjets_allchannels_v4` configuration.

6.2 MC Samples

The $W^{\pm}Z$ production matrix elements, including the vector boson leptonic decays, are modeled by the MC@NLO4.0 [76] MC generator with PDF set CTEQ6.6 [100], which incorporates the NLO QCD matrix elements into the parton shower by interfacing to the HERWIG/Jimmy [59] programs. Full spin correlations and the W and Z-boson width are included in the matrix elements, but Z/γ^* interference is not. Gauge-boson decays into τ leptons are included in the matrix elements, while the decays of τ leptons to all known final states are performed with the TAUOLA [64] program. Hard gluon emission is contained in the matrix element NLO computation, while the soft/collinear emission of QCD initial state radiation (ISR) and final state radiation (FSR) is treated with the HERWIG parton shower. Smooth matching between these two regions is performed in order to avoid double-counting or undercounting. The fragmentation of quarks and gluons and the subsequent hadronization process is performed by HERWIG. The PHOTOS [82] program is used for QED FSR. Table 6.1 lists the $W^{\pm}Z$ MC signal samples and corresponding cross sections as predicted by MC@NLO. Three sets of signal samples are listed, the primary set with SM couplings, one set with anomalous coupling $\lambda^Z = 0.13$, and one set with anomalous couplings $\Delta g_1^Z = -0.3$, $\Delta\kappa^Z = 1.0$, and $\lambda^Z = 0.3$. The SM samples are used in the cross section analysis to calculate the acceptance and efficiency of the selection, while the samples including anomalous couplings are used in the aTGC analysis. It should be noted that the signal cross sections noted in the table are not used for the final cross section prediction and subsequent MC normalization, rather the signal expectation is scaled to the cross section calculated with MCFM [55] because this calculation

includes Z/γ^* interference. The MCFM theoretical cross section calculation can be found in Section 6.3.

Major backgrounds in the $W^{\pm}Z$ sample come from W or Z bosons produced in association with jets (V+jets), diboson production of ZZ pairs, diboson production of a W or Z in association with a photon, and top events. MC@NLO is used to model the $t\bar{t}$ and single top events and ALPGEN [92] to model the V+jets background. Due to difficulties modeling the τ polarization with ALPGEN, PYTHIA [108], a leading order (LO) MC generator, is used to model V+jets background with τ final states. The ZZ process is modeled with PYTHIA, while $W/Z + \gamma$ is modeled with MADGRAPH [8]. Additional backgrounds which are expected to be extremely small or are expected to contribute only to control regions (and not the signal region) include WW (modeled with HERWIG), events with dileptons from low-mass Drell-Yan (10 GeV$< m_{ll} <$40 GeV) production (modeled with ALPGEN or PYTHIA, depending on the presence of τ leptons in the final state), and events with heavy flavor dijets (modeled with PYTHIAB [104]).

The cross sections for the different background processes, the generator names, the generator level filter efficiencies (the efficiency of the MC generated events to pass a truth level filter[2]) and the total number of MC events produced are shown in Table 6.2 for Z+jets, Table 6.3 for W+jets, Table 6.4 for top and dijets, and Table 6.5 for diboson backgrounds. In the case a filter efficiency is listed in the table, the listed cross section is the unfiltered cross section, and the final filtered cross section

[2]For instance a Z+jets sample could have a filter that only selects events with at least one lepton with $p_T > 20$ GeV.

is the product of the filter efficiency and the unfiltered cross section. Whenever LO event generators are used, the cross sections are corrected by linearly scaling the LO cross section to NLO or NNLO (if available) matrix element calculations [35]. The scaling factors are denoted *k-factors*, and are listed in the tables. The background MC samples generally correspond to ∼1-10 fb^{-1} of integrated luminosity.

All of the MC samples are interfaced to a GEANT4 [4] simulation of the ATLAS detector response. The simulated signals are then digitized and reconstructed using the Athena release 16.6 offline reconstruction software. The simulation includes detector, trigger, and reconstruction efficiencies and resolutions. While this simulation is seen to perform very well, small differences between the data and MC simulations have been observed. These differences come primarily in three forms: pileup modeling, efficiency modeling, and resolution modeling.

The pileup conditions of the MC are not identical to those of the data. This is not surprising as the MC was produced prior to the data taking and thus the exact LHC collision conditions were not known. The difference in pileup conditions primarily causes discrepancies in the modeling of the energy in the calorimeter, which translates into discrepancies of the modeling of physics objects such as the missing energy. Underlying this problem is the fact that the distribution of μ (the average number of inelastic scatterings per BC) is different between data and MC. Thus, the MC μ distribution is corrected to that of the data using a reweighing procedure described in Section 6.2.1.

The simulation modeling of the reconstruction and trigger efficiency for electrons and muons are not identical to the data efficiencies. These efficiency differences can cause incorrect predictions for the number and kinematics distributions of expected $W^{\pm}Z$ events, and thus must be corrected in order to accurately measure cross sections and set limits on aTGCs. As such, the efficiencies in both data and MC are measured using Z decays, and the efficiencies of the MC are corrected to that of the data using *scale factors* (i.e. the data/MC ratio). Trigger efficiencies corrections are described in further detail in Section 6.4, while reconstruction efficiency corrections are described in more detail in Section 6.5 for muons and Section 6.6 for electrons.

The electron E_T and muon p_T resolutions in the simulation are not the same as the resolutions in the data. These resolution differences imply that the MC does not properly model the $W^{\pm}Z$ event selection efficiency, and thus must be corrected. The MC resolution is corrected by adding additional resolution smearing to the electrons and muons using the Z mass as a constraint, as described in more detail in Section 6.5 for muons and Section 6.6 for electrons.

6.2.1 Pileup Reweighting

In order to account for the effect of multiple inelastic collisions in a given bunch crossing, additional events, or pileup events, are overlaid with the hard scattering collision for each MC event. All the MC samples are simulated with an average of 8 inelastic collisions per bunch crossing (i.e. the distribution of μ values in the MC samples has an average value of 8) and a bunch spacing of 50 ns. The μ distribution was chosen based on the expected pileup distribution of the collisions and the same

MCID	Process	Generator	Events	k-factor	ϵ_{filter}	cross section [pb]
126053	$W^+Z \to e\nu ee$	MC@NLO	49990	1.0	1.0	0.04060
126054	$W^-Z \to e\nu ee$	MC@NLO	49988	1.0	1.0	0.02191
126055	$W^+Z \to e\nu\mu\mu$	MC@NLO	49991	1.0	1.0	0.04060
126056	$W^-Z \to e\nu\mu\mu$	MC@NLO	49983	1.0	1.0	0.02191
126057	$W^+Z \to e\nu\tau\tau$	MC@NLO	49983	1.0	1.0	0.04060
126058	$W^-Z \to e\nu\tau\tau$	MC@NLO	49989	1.0	1.0	0.02191
126059	$W^+Z \to \mu\nu ee$	MC@NLO	49984	1.0	1.0	0.04060
126060	$W^-Z \to \mu\nu ee$	MC@NLO	49989	1.0	1.0	0.02191
126061	$W^+Z \to \mu\nu\mu\mu$	MC@NLO	49992	1.0	1.0	0.04060
126062	$W^-Z \to \mu\nu\mu\mu$	MC@NLO	49995	1.0	1.0	0.02191
126063	$W^+Z \to \mu\nu\tau\tau$	MC@NLO	49984	1.0	1.0	0.04060
126064	$W^-Z \to \mu\nu\tau\tau$	MC@NLO	49989	1.0	1.0	0.02191
126065	$W^+Z \to \tau\nu ee$	MC@NLO	49992	1.0	1.0	0.04060
126066	$W^-Z \to \tau\nu ee$	MC@NLO	49989	1.0	1.0	0.02191
126067	$W^+Z \to \tau\nu\mu\mu$	MC@NLO	49983	1.0	1.0	0.04060
126068	$W^-Z \to \tau\nu\mu\mu$	MC@NLO	49988	1.0	1.0	0.02191
126069	$W^+Z \to \tau\nu\tau\tau$	MC@NLO	49989	1.0	1.0	0.04060
126070	$W^-Z \to \tau\nu\tau\tau$	MC@NLO	49981	1.0	1.0	0.02191
126071-9	$W^+Z \to \ell\nu\ell\ell$	MC@NLO	$\approx$ 49995	1.0	1.0	0.14097
126080-8	$W^-Z \to \ell\nu\ell\ell$	MC@NLO	$\approx$ 49995	1.0	1.0	0.06772
126089-97	$W^+Z \to \ell\nu\ell\ell$	MC@NLO	$\approx$ 49995	1.0	1.0	0.05129
126098-106	$W^-Z \to \ell\nu\ell\ell$	MC@NLO	$\approx$ 49995	1.0	1.0	0.02669

Table 6.1: The $W^{\pm}Z$ signal production processes, cross sections and numbers of fully simulated MC events. The MC simulation "filter" is an event selection at the generator level. The corresponding filter efficiencies are given in the table. The MC generators used to produce the MC events and the MC run number (used for sample identification) are listed. ℓ denotes e, μ and τ. Samples 126071-126088 are produced at aTGC values $\Delta g = 0$, $\Delta\kappa = 0$, $\lambda = 0.13$, and samples 126089-126106 at $\Delta g = -0.3$, $\Delta\kappa = 1.0$, $\lambda = 0.3$.

MCID	Process	Generator	Events	k-factor	ϵ_{filter}	cross section [pb]
107650	ZeeNp0	ALPGEN	6582268	1.26	1.0	664.100
107651	ZeeNp1	ALPGEN	1323746	1.26	1.0	132.462
107652	ZeeNp2	ALPGEN	404873	1.26	1.0	40.226
107653	ZeeNp3	ALPGEN	109942	1.26	1.0	11.138
107654	ZeeNp4	ALPGEN	29992	1.26	1.0	3.12818
107655	ZeeNp5	ALPGEN	8992	1.26	1.0	0.753425
107660	Z$\mu\mu$Np0	ALPGEN	6619010	1.26	1.0	663.79
107661	Z$\mu\mu$Np1	ALPGEN	1334723	1.26	1.0	132.95
107662	Z$\mu\mu$Np2	ALPGEN	403886	1.26	1.0	40.375
107663	Z$\mu\mu$Np3	ALPGEN	109954	1.26	1.0	11.161
107664	Z$\mu\mu$Np4	ALPGEN	29978	1.26	1.0	2.8987
107665	Z$\mu\mu$Np5	ALPGEN	9993	1.26	1.0	0.75662
106052	Z$\tau\tau$	PYTHIA	1988042	1.15	1.0	856.967
109300	ZeebbNp0_nofilter	ALPGEN/JIMMY	149971	1.25	1.0	6.57
109301	ZeebbNp1_nofilter	ALPGEN/JIMMY	99977	1.25	1.0	2.48
109302	ZeebbNp2_nofilter	ALPGEN/JIMMY	38985	1.25	1.0	0.89
109303	ZeebbNp3_nofilter	ALPGEN/JIMMY	9990	1.25	1.0	0.39
109305	Z$\mu\mu$bbNp0_nofilter	ALPGEN/JIMMY	149971	1.25	1.0	6.56
109306	Z$\mu\mu$bbNp1_nofilter	ALPGEN/JIMMY	109962	1.25	1.0	2.47
109307	Z$\mu\mu$bbNp2_nofilter	ALPGEN/JIMMY	39980	1.25	1.0	0.89
109308	Z$\mu\mu$bbNp3_nofilter	ALPGEN/JIMMY	9994	1.25	1.0	0.39
116250	ZeeNp0 M10to40 pt20	ALPGEN/JIMMY	999859	1.22	1.0	3051.62
116251	ZeeNp1 M10to40 pt20	ALPGEN/JIMMY	299940	1.22	1.0	87.87
116252	ZeeNp2 M10to40 pt20	ALPGEN/JIMMY	499880	1.22	1.0	41.10
116253	ZeeNp3 M10to40 pt20	ALPGEN/JIMMY	149940	1.22	1.0	8.46
116254	ZeeNp4 M10to40 pt20	ALPGEN/JIMMY	39973	1.22	1.0	1.84
116255	ZeeNp5 M10to40 pt20	ALPGEN/JIMMY	9995	1.22	1.0	0.46
116260	Z$\mu\mu$Np0 M10to40 pt20	ALPGEN/JIMMY	999869	1.22	1.0	3051.62
116261	Z$\mu\mu$Np1 M10to40 pt20	ALPGEN/JIMMY	299890	1.22	1.0	87.87
116262	Z$\mu\mu$Np2 M10to40 pt20	ALPGEN/JIMMY	499864	1.22	1.0	40.95
116263	Z$\mu\mu$Np3 M10to40 pt20	ALPGEN/JIMMY	149939	1.22	1.0	8.41
116264	Z$\mu\mu$Np4 M10to40 pt20	ALPGEN/JIMMY	39988	1.22	1.0	1.85
116265	Z$\mu\mu$Np5 M10to40 pt20	ALPGEN/JIMMY	9996	1.22	1.0	0.46

Table 6.2: MC samples/processes used to model Z+X, including Z+jets, Zbb+jets and Drell-Yan samples. The corresponding cross sections, generator names, generator level filter efficiencies, and total numbers of simulated events are shown. NpX (X = $0 \ldots 5$) in the process name refers to the number of additional partons in the matrix element final state.

MCID	Process	Generator	Events	k-factor	ϵ_{filter}	cross section [pb]
107680	W$e\nu$Np0	ALPGEN	2072731	1.21	1.0	6870.5
107681	W$e\nu$Np1	ALPGEN	641361	1.21	1.0	1293.0
107682	W$e\nu$Np2	ALPGEN	4521053	1.21	1.0	376.60
107683	W$e\nu$Np3	ALPGEN	1211068	1.21	1.0	101.29
107684	W$e\nu$Np4	ALPGEN	301832	1.21	1.0	25.246
107685	W$e\nu$Np5	ALPGEN	83447	1.21	1.0	7.1239
107690	W$\mu\nu$Np0	ALPGEN	3466523	1.21	1.0	6871.1
107691	W$\mu\nu$Np1	ALPGEN	641867	1.21	1.0	1294.7
107692	W$\mu\nu$Np2	ALPGEN	4519611	1.21	1.0	376.08
107693	W$\mu\nu$Np3	ALPGEN	1213499	1.21	1.0	100.72
107694	W$\mu\nu$Np4	ALPGEN	306848	1.21	1.0	25.993
107695	W$\mu\nu$Np5	ALPGEN	83452	1.21	1.0	7.1300
106022	W$\tau\nu$	PYTHIA	999868	1.17	0.8765778	8916.33

Table 6.3: MC samples/processes used to model W+jets. The corresponding cross sections, generator names, generator level filter efficiencies, and total numbers of simulated events are shown. NpX (X = 0...5) in the process name refers to the number of additional partons in the matrix element final state.

MCID	Process	Generator	events	k-factor	ϵ_{filter}	cross section [pb]
105200	$t\bar{t}$	MC@NLO	999332	1.0	0.5562	164.57
108340	t-channel→e	MC@NLO	9996	1.0	1.0	7.1522
108341	t-channel→ μ	MC@NLO	9994	1.0	1.0	7.1767
108342	t-channel→ τ	MC@NLO	9995	1.0	1.0	7.1277
108343	s-channel→e	MC@NLO	9992	1.0	1.0	0.46856
108344	s-channel→ μ	MC@NLO	9991	1.0	1.0	0.46837
108345	s-channel→ τ	MC@NLO	9997	1.0	1.0	0.46978
108346	Wt	MC@NLO	59960	1.0	1.0	13.102
105757	bbcc mu10mu10X	PYTHIAB	297118	1.0	1.0	2830.3
105758	bbcc mu10e10X	PYTHIAB	796391	1.0	1.0	4017.1
105759	bbcc e10e10X	PYTHIAB	290326	1.0	0.0031913	530580

Table 6.4: MC samples/processes used to model top (including $t\bar{t}$ and single top) and dijet backgrounds. The corresponding cross sections, generator names, generator level filter efficiencies, and total numbers of simulated events are shown.

MCID	Process	Generator	Events	k-factor	ϵ_{filter}	cross section [pb]
105985	WW	HERWIG	249915	1.48	1.0	11.5
109292	ZZ	PYTHIA	149969	1.41	1.0	0.0749
126013	W$e\nu\gamma$_1jet	Sherpa	398935	1.0	1.0	75.5
126014	W$\mu\nu\gamma$_1jet	Sherpa	399936	1.0	1.0	75.5
106003	W$^+(\tau)$ γ	PYTHIA,MADGRAPH	46996	1.0	1.0	25.4
108290	W$^-(\tau)$ γ	PYTHIA,MADGRAPH	49996	1.0	1.0	16.8
126015	Z$ee\gamma$_1jet	Sherpa	199974	1.0	1.0	14.7
126016	Z$\mu\mu\gamma$_1jet	Sherpa	174975	1.0	1.0	14.7
108325	Z($\tau\tau$) γ	PYTHIA,MADGRAPH	49997	1.41	0.15	9.41

Table 6.5: MC samples/processes used to model diboson backgrounds, including WW, ZZ, $W\gamma$ and $Z\gamma$. The corresponding cross sections, generator names, generator level filter efficiencies, and total numbers of simulated events are shown.

distribution is used in all MC samples. However, since this distribution was chosen in advance of data taking, the MC distribution is not exactly the same as the distribution observed in data. In order to account for this difference, the distribution of μ values in MC is weighted to reproduce the μ distribution in data whilst keeping the total sum of weights equal to one (thus keeping the total MC normalization equal to the original number of MC events). This procedure is known as *pileup reweighting*. The weight $w_{\mu'}$ of an MC event with $\mu = \mu'$ is calculated as,

$$w_{\mu'} = (\mathcal{L}^{Data}_{\mu'}/\mathcal{L}^{Data})/(N^{MC}_{\mu'}/N^{MC}) \tag{6.1}$$

where $\mathcal{L}^{Data}_{\mu'}$ is the recorded data luminosity with $\mu = \mu'$, $\mathcal{L}^{Data}$ is the total luminosity of the data sample, $N^{MC}_{\mu'}$ is the number of MC events simulated with $\mu = \mu'$, and N^{MC} is the total number of simulated MC events. Thus, the procedure reweights the fraction of the MC sample with a given μ value to be the same fraction observed in data.

The normalized μ distributions in data and MC can be found in Figure 6.1. The MC distribution, in red, is wider than the data distribution because it is necessary that

the MC covers the full phase space of possible data μ values. The μ values simulated in MC that are not observed in data are reweighted to zero. Thus the large fraction of MC events simulated with μ values unrepresented in data does not contribute to the final MC predictions, and therefore reweighting decreases the statistical power of the MC sample. In addition, the MC distribution is simulated with only integer μ values, while the data distribution has a much higher granularity. To handle this in the reweighting, the integral of the data over the corresponding MC bins is used.

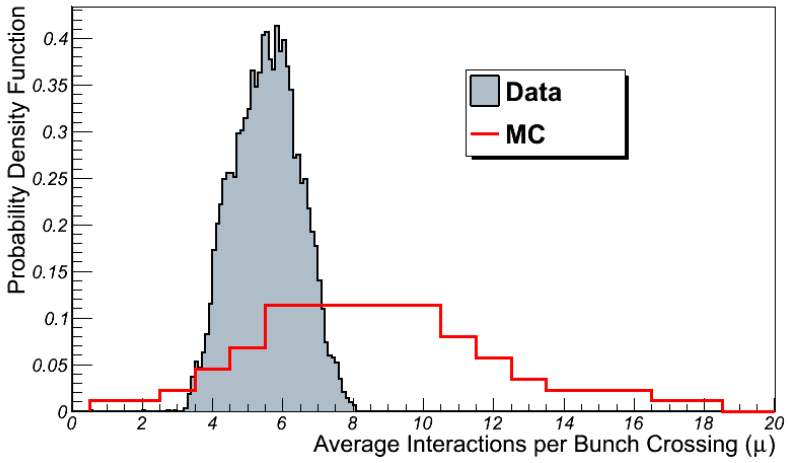

Figure 6.1: The normalized distribution of μ values in data (grey) and in MC (red).

The effect of pileup reweighting on the distribution of the number of reconstructed primary vertices per event, n_{PV}, for events passing a Z boson selection can be seen in Figure 6.2. These events are selected by requiring two muons (combined or tag) or two medium electrons whose invariant mass is within 10 GeV of the Z boson pole mass of 91.1876 GeV [95]. More details on the exact lepton requirements can be found in Section 6.5. The top two plots show the $Z \to ee$ candidate events, while

the bottom two plots show the $Z \to \mu\mu$ candidate events. The data is shown in black, while the MC distribution is shown in blue (backgrounds in this sample are not visible, contributing $< 1\%$ [42]). The left plots show the MC distributions before reweighting, and the right plots show the distributions after reweighting. It can easily be seen that the pileup reweighting greatly improves the data/MC agreement of the n_{PV} distribution.

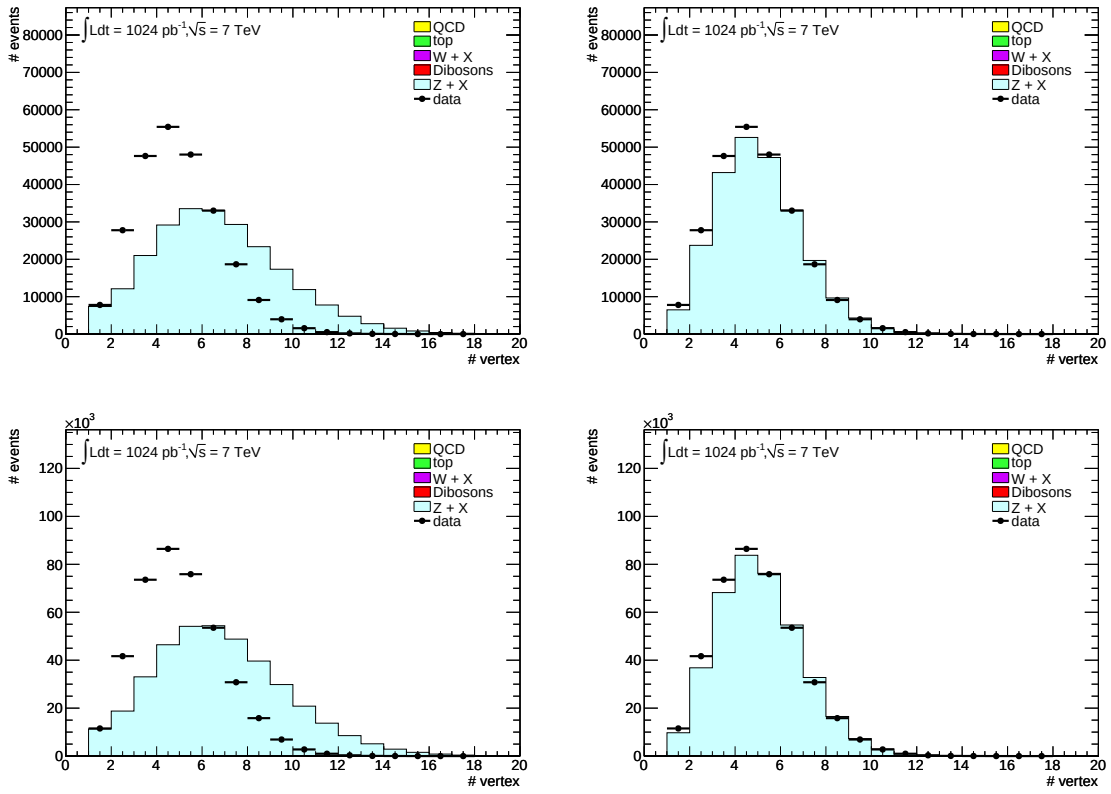

Figure 6.2: The number of reconstructed vertices is shown for $Z \to ee$ (top) and $Z \to \mu\mu$ (bottom) candidate events, where MC is in blue and the data is the black points. The left plots show the MC distributions before pileup reweighting, while the right plots show the MC after reweighting.

6.3 $W^{\pm}Z$ Theoretical Cross Section

The total cross section for the $W^{\pm}Z$ process is calculated using MCFM [55]. Given the presence of Z/γ^* interference, the total cross section diverges (at low mass) without a suitably defined mass window around the Z pole mass. An earlier ATLAS study [35] used a mass window of 66 GeV$< m_{ll} <$116 GeV and reported a total cross section of $\sigma_{W^{\pm}Z} = 17.3$ pb. This mass window choice of 66 GeV$< m_{ll} <$116 GeV is kept for the total cross section calculation in this analysis.

The total cross section calculation in MCFM is compared to MC@NLO in Table 6.6 for various PDF sets. The PDF used in this analysis is CTEQ6.6. It is important to note that MC@NLO does not have Z/γ^* interference. Therefore, the cross section of the two generators are also compared in the absence of Z/γ^* interference by setting $\Gamma_Z = 0$ in MCFM and using no mass window in MC@NLO. The difference between MCFM and MC@NLO, averaged over the PDF sets, is 2.0%. The impact of the mass window on the cross section calculation using various PDF sets for both MCFM and MC@NLO can be seen in Figure 6.3(a), and the difference between the two predictions can be found in Figure 6.3(b). The x-axis in these plots is the half width of the mass window, and thus the 66 GeV$< m_{ll} <$116 GeV window chosen for this analysis corresponds to 25 GeV on the x-axis.

The uncertainties on the total cross section are,

- The $\pm$0.03 pb statistical uncertainty of the MC calculations, which is negligible.
- The difference between CTEQ 6.6 and MSTW 2008 PDF sets of +0.62 pb

	MCFM		MC@NLO	
PDF	66−−116 GeV	$\Gamma_Z = 0$	66−−116 GeV	No Mass Window
CTEQ6.6	17.31 ± 0.03	17.89	17.07	17.41
CT10	17.56 ± 0.03	18.11	17.28	17.63
MSTW 2008	17.93 ± 0.03	18.52	17.69	18.05
NNPDF2.0	17.63 ± 0.03	18.23	17.42	17.77
NNPDF2.1	18.06 ± 0.03	18.66	17.82	18.18

Table 6.6: SM cross section (pb) for $pp \to WZ$ at $\sqrt{s} = 7\,\text{TeV}$ computed with MCFM and MC@NLO.

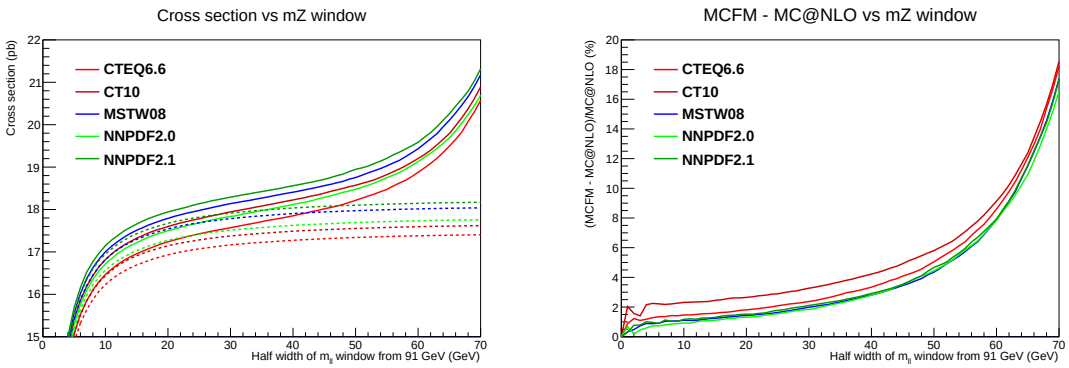

Figure 6.3: The SM WZ cross section (pb) computed with MCFM (solid curves) and MC@NLO (dashed curves) is shown on the left and their fractional difference (in %) on the right, both as functions of the half width of the allowed range of m_{ll} centered at 91 GeV.

(+3.6%), is take as the systematic uncertainty due to different PDF implementations.

- The differences between the nominal calculation and the 44 eigenvectors of the CTEQ 6.6 PDF set are added in quadrature to estimate the uncertainty of the PDF. The uncertainties are calculated separately for positive and negative errors using the equation,

$$\sigma_{+} = \sum_{i=1}^{44} \left(\max\{\sigma^{i}_{W^{\pm}Z} - \sigma^{default}_{W^{\pm}Z},\ 0\} \right)^2 \tag{6.2}$$

$$\sigma_{-} = \sum_{i=1}^{44} \left(\min\{\sigma^{i}_{W^{\pm}Z} - \sigma^{default}_{W^{\pm}Z},\ 0\} \right)^2 \tag{6.3}$$

  The resulting uncertainty is +0.65/-0.47 pb, or +3.8%/-2.7%.

- The QCD scale and factorization scale are varied up by a factor of 2 and down by a factor of 0.5 in order to estimate the uncertainty of the NLO calculation. The resulting difference in predicted cross section is taken as the uncertainty, and is determined to be +0.96/-0.67 pb (+5.5%/-3.9%).

In summary, the total cross section is calculated using MCFM and the CTEQ 6.6 PDF set in the mass window 66 GeV$< m_{ll} <$116 GeV , resulting in an estimate of,

$$\begin{aligned} \sigma^{\mathrm{MCFM}}_{W^{\pm}Z} &= 17.31\ ^{+0.62}_{-0}\ (\mathrm{MSTW08})\ ^{+0.65}_{-0.47}\ (\mathrm{PDF})\ ^{+0.96}_{-0.67}\ (\mathrm{scale})\ \mathrm{pb} \\ &= 17.3^{+1.3}_{-0.8}\ \mathrm{pb}. \end{aligned} \tag{6.4}$$

The MC@NLO samples are scaled to this total cross section when calculating the expected number of signal events.

6.4 Trigger

During 2011 running, the p_T thresholds of the lowest unprescaled single lepton triggers were low enough that the single lepton triggers could be used without significant acceptance loss for the $W^{\pm}Z$ signal. Considering that the $W^{\pm}Z$ analysis contains three leptons in the final state, each of which have a high probability of passing the trigger threshold, the probability that at least one of the leptons triggered is high. Therefore, the primary triggers used in this analysis are a 20 GeV electron trigger (called `EF_e20_medium`) and an 18 GeV combined muon trigger (called `EF_mu18_MG`) OR'd with a 40 GeV stand-alone muon barrel trigger (called `EF_mu40_MSonly_barrel`). The muon trigger includes the `EF_mu40_MSonly_barrel` because an efficiency loss of high p_T muons in the barrel is observed in the simulation samples (though not in the data) and using this trigger regains the efficiency and shows better data/MC agreement.

The trigger chains (i.e. the set of triggers at each level) for the electron and muon triggers can be found in Table 6.7. The electron trigger is seeded by a 14 GeV L1 trigger, followed by a 20 GeV medium electron trigger at L2. Both muon triggers are seeded by a 10 GeV L1 trigger, followed by an 18 GeV combined trigger and a 40 GeV stand-alone barrel trigger at L2 for `EF_mu18_MG` and `EF_mu40_MSonly_barrel`, repsectively.

An unbiased estimate of the electron and muon trigger efficiencies is measured using the Z tag-and-probe technique, as described in detail in References [31, 33]. The technique uses the Z resonance to select a pure sample of high momentum and isolated

Object	L1	L2	EF
electron	L1_EM14	L2_e20_medium	EF_e20_medium
muon	L1_MU10	L2_mu18_MG	EF_mu18_MG
	L1_MU10	L2_mu40_MSonly_barrel	EF_mu40_MSonly_barrel

Table 6.7: Single lepton trigger chains used in the analysis

leptons. Because two leptons are found in each Z event, a first lepton, called the *tag*, can be selected and required to match a trigger object[3], while the second lepton, called the *probe*, can be selected based only on if the invariant mass of the lepton pair is consistent with the Z mass. Since the second lepton should have triggered but is not required to have triggered (since the first lepton successfully triggered), the fraction of probes matched to a trigger object gives an unbiased estimate of the trigger efficiency.

Events for the tag-and-probe study are required to have a primary vertex with at least three tracks, and a pair of oppositely charged, same flavor leptons with an invariant mass within 10 GeV of the Z mass. Muons are required to pass the Combined muon selection described in Section 6.5, and satisfy $d_0/\sigma(d_0) < 10$, where d_0 is the transverse impact parameter and $\sigma(d_0)$ is its error. Electrons tags are required to pass the tight selection criteria and have $E_T > 20$ GeV. The tag muon (electron) is required to match to the trigger object within $\Delta R < 0.2$ (0.15). Additionally, for muon events, the tag and probe must have differences in d_0 less than 2 mm, z_0 less than 3 mm, and ϕ greater than 0.2.

[3]A trigger object is the physics object reconstructed online that is seen to pass the threshold of a given trigger. While there are trigger objects at each level of the trigger, EF trigger objects are the primary concern of this analysis since they correspond to the final trigger decision.

Trigger efficiencies measured using the Z tag-and-probe method can be found in Figure 6.4. The top three plots show the efficiency of the muon trigger combination (`EF_mu18_MG || EF_mu40_MSonly`) as a function of the muon p_T (left), η (middle), and ϕ (right) for data and MC [31], along with the data/MC ratio. The muon trigger has a sharp turn on curve and a plateau above ∼20 GeV of around 80%. The primary cause of efficiency loss is a lower trigger efficiency in the barrel than the end-cap (as seen in the η efficiency) due to the lack of full RPC coverage. The bottom two plots show the efficiency of the electron trigger as a function of the electron p_T (left) and η (right) in data at the three levels of the trigger chain [13]. At the EF level, the electron trigger has a sharp turn on curve and a plateau above ∼25 GeV at around 97%. In order to guarantee optimal trigger performance, muons (electrons) in the analysis are required to be matched to the trigger candidate within ΔR <0.1 (0.15) and be well onto the trigger plateau with a p_T >20 (25) GeV.

6.4.1 Single Lepton Trigger Efficiency Corrections for MC

Although the MC simulations model the trigger efficiencies fairly well, small discrepancies between data and MC are observed. To account for this, a scale factor is calculated as the ratio of the data to MC trigger efficiency and is applied to the MC for each reconstructed, selected, and trigger matched lepton satisfying the p_T requirement. Thus the relative weight of each MC event is raised or lowered in order to match the overall observed data efficiency. The scale factors are derived as functions of the kinematic variables showing the largest discrepancies between data and MC. The muon scale factors [31] are calculated as a function muon η and ϕ in

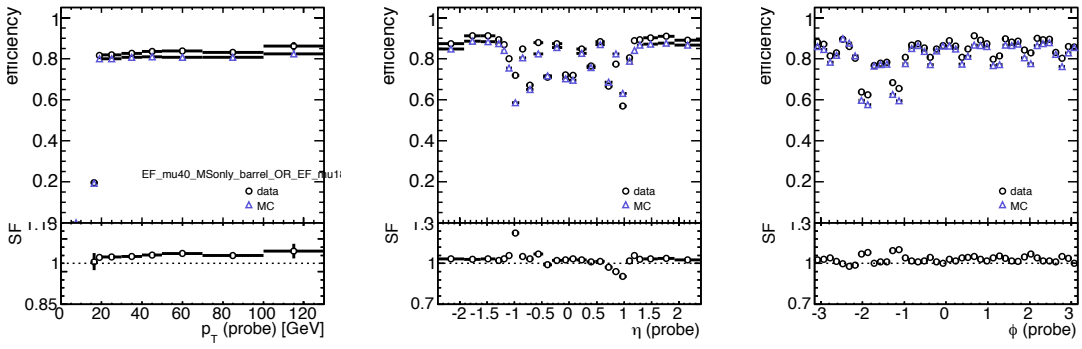

(a) Muon trigger efficiency as a function of p_T (b) Muon trigger efficiency as a function of η (c) Muon trigger efficiency as a function of ϕ

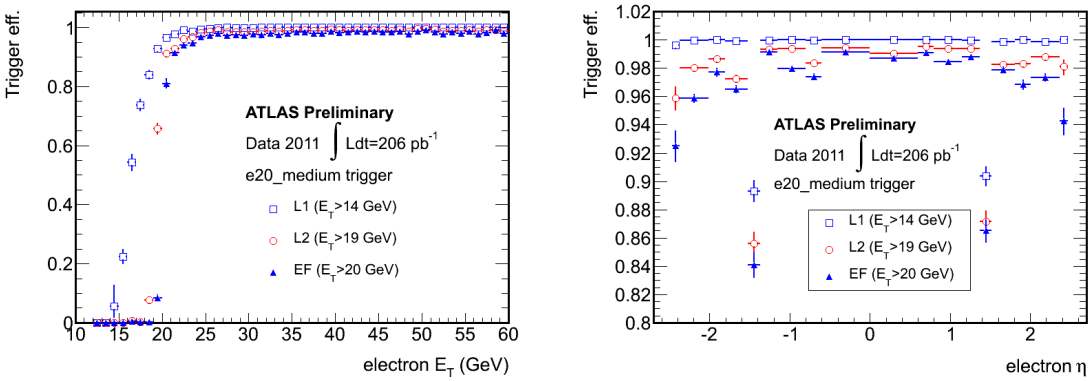

(d) Electron trigger efficiency as a function of p_T (e) Electron trigger efficiency as a function of η

Figure 6.4: Single lepton trigger efficiencies [31, 13].

the barrel, shown in Figure 6.5(a), and as a function of muon p_T in the end-cap, shown in Figure 6.5(b). The electron scale factors [23] are calculated as a function of electron η, as seen in Figure 6.5(c). The uncertainty on the single lepton scale factors is approximately 2% for electrons and 1% for muons, determined by slightly altering the lepton selection, considering differing pileup conditions, and examining multiple reconstruction algorithms.

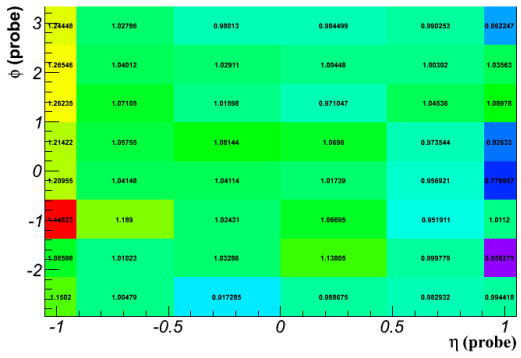

(a) Muon barrel scale factor vs. η and ϕ

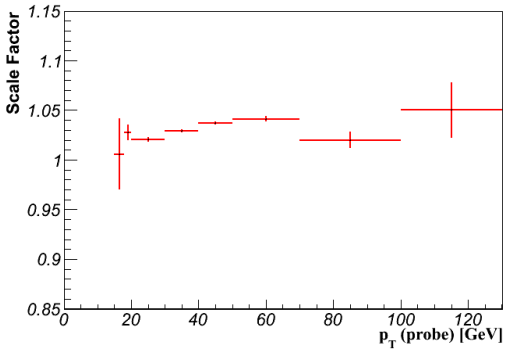

(b) Muon end-cap scale factor vs. p_T

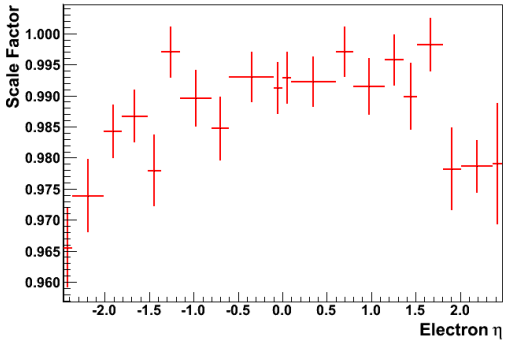

(c) Electron scale factor vs. η

Figure 6.5: Muon and electron trigger scale factors [31, 23].

6.4.2 $W^{\pm}Z$ Event Level Trigger Efficiency

The trigger efficiency for $W^{\pm}Z$ events is derived using the $W^{\pm}Z$ MC samples and modified with the scale factors. As there are three leptons in $W^{\pm}Z$ events, and only one of the leptons is required to trigger an event, the total $W^{\pm}Z$ event trigger scale factor must take into account the combinatorics of the possible triggering lepton combinations. The per event scale factor depends on lepton flavor and kinematics, and is calculated with the single leptons scale factors as

$$SF_{Trig}^{Event} = \frac{1 - \prod_{n=1}^{N_l}[1 - \epsilon_{MC}(l_n) \times SF_{Trig}^{Lepton}(l_n)]}{1 - \prod_{n=1}^{N_l}[1 - \epsilon_{MC}(l_n)]} \tag{6.5}$$

where N_l is the number of trigger matched leptons passing the p_T requirement, $\epsilon_{MC}(l_n)$ is the MC single lepton trigger efficiency for lepton l_n, and $SF_{Trig}^{Lepton}(l_n)$ is the single lepton scale factor for lepton l_n.

The trigger efficiency for $W^{\pm}Z$ events can be found before and after the application of the event level scale factor for each of the four $W^{\pm}Z$ decay channels in Table 6.8. The errors in the first two columns are statistical only. The third column shows the systematic uncertainty on the event level trigger efficiency derived by shifting the underlying single lepton scale factors within their systematic uncertainties and observing the change in the event level trigger efficiency. The single lepton scale factor uncertainty variation is performed simultaneously for muons and electrons, and is thus conservative. After scale factor application, the overall $W^{\pm}Z$ event level trigger efficiency is $\gtrsim 99\%$ in all channels.

Channel	Trigger Efficiency before SF [%]	Trigger Efficiency after SF [%]	Systematic Uncertainty [%]
eee	$99.92^{+0.02}_{-0.03}$	$99.91^{+0.02}_{-0.03}$	1.00
$ee\mu$	$99.78^{+0.03}_{-0.03}$	$99.75^{+0.03}_{-0.03}$	1.00
$e\mu\mu$	$98.15^{+0.13}_{-0.14}$	$98.98^{+0.13}_{-0.14}$	1.01
$\mu\mu\mu$	$96.54^{+0.10}_{-0.10}$	$98.62^{+0.10}_{-0.10}$	1.002

Table 6.8: $W^{\pm}Z$ event trigger efficiencies before and after applying the scale factor, shown with statistical errors. The systematic error is shown in the third column.

6.5 Muon Selection

Reconstructed muons used in this analysis can be either Combined or Segment-Tagged muons, as described in Section 5.4, and track parameters are extrapolated to the primary vertex taking into account parameterized energy loss in material. The muon track is required to have $p_T > 15$ GeV and $|\eta| < 2.5$. To ensure the muon originated from the PV, the absolute distance in z between the muon longitudinal impact parameter, z_0, and the primary vertex z-position must be less than 10 mm.

Additional quality criteria are required for the ID track in order to assure the accurate reconstruction of the ID track and to reject algorithmic or decay in flight backgrounds. This is vital as the ID track plays an important role in the track parameter calculation for Combined tracks and solely determines the track parameters for the Segment-Tagged muons. The ID track criteria are,

- At least 1 pixel B-layer hit, unless the pixel crossed by the track (as determined by extrapolation) is known to be a dead channel.

- At least 2 hits in the pixels (this can include the B-layer hit). If the track crosses

a known pixel dead channel then it is counted as containing a hit.

- At least 6 hits in the SCT system. If the track crosses a known SCT dead channel then it is counted as containing a hit.

- At most 2 silicon holes on the track, where a hole is an expected but missing hit on a silicon layer crossed by the track.

- If the track $|\eta| < 1.9$, then the track must have at least 6 TRT hits or outliers AND the outlier fraction must satisfy $N_{outlier}/(N_{hit} + N_{outlier}) < 0.9$.

- If the track $|\eta| \geq 1.9$ AND the track has at least 6 TRT hits or outliers, then the outlier fraction must satisfy $N_{outlier}/(N_{hit} + N_{outlier}) < 0.9$.

Finally, the muons are required to be isolated from other tracks in order to reject secondary muons from hadronic jets and heavy flavor decays. The muon isolation, called $ptCone20pt$, is calculated by summing the p_T of ID tracks within $\Delta R < 0.2$ of the muon track (excluding the muon track) and dividing by the muon track momentum. The isolation is required to be less than 0.1. That is,

$$ptCone20pt \equiv \sum_{i \in \{\Delta R < 0.2\}} p_T^{ID,i} \; / \; p_T^{\mu} < 0.1 \tag{6.6}$$

The ID tracks are required to originate from the primary vertex, which greatly reduces the contribution to, and uncertainty of, the isolation from pileup.

6.5.1 Muon Efficiency Corrections for MC

The muon reconstruction efficiency is measured using the Z tag-and-probe method, as described in detail in Reference [30]. Opposite charged, isolated, back-to-back

($\Delta\phi > 2.0$), and high $p_T > 20$ GeV muons originating from the same PV and with a dimuon mass within 10 GeV of the Z pole mass are selected. ID tracks are required to pass the ID quality criteria (described in Section 6.5). The tag muon is required to be combined, and to be matched to a trigger object. For Combined and Segment-Tagged track efficiency studies, the probe muon is required to be an ID track and the fraction of probes matched to a Combined or Segment-Tagged track with $\Delta R < 0.01$ gives the unbiased efficiency measurement. For ID track efficiency measurements, the probe muon is required to be an MS track and the fraction of MS tracks matched to an ID track with $\Delta R < 0.01$ gives the unbiased efficiency measurement.

The muon reconstruction efficiency as a function of η can be seen in Figure 6.6(a) for Combined muons and in Figure 6.6(b) for muons selected as being Combined OR Segment-Tagged [17]. The muons in these figures are required to pass the aforementioned ID track and isolation selection. The scale factors (data/MC ratio) are calculated only as a function of muon η, and can also be seen in both figures. The scale factors are used for correcting the MC reconstruction efficiency to that of the observed data. The effect of allowing Segment-Tagged muons in the selection is quite large; the Segment-Tagged muons improve the efficiency greatly in the barrel, especially in the transition regions near $|\eta| \sim 1.2$, and greatly improve the scale factors to the point where the $SF \sim 1$ over the full η range. Since every desired lepton must be reconstructed for an event to be selected, the event level reconstruction scale factor is simply the product of single lepton scale factors.

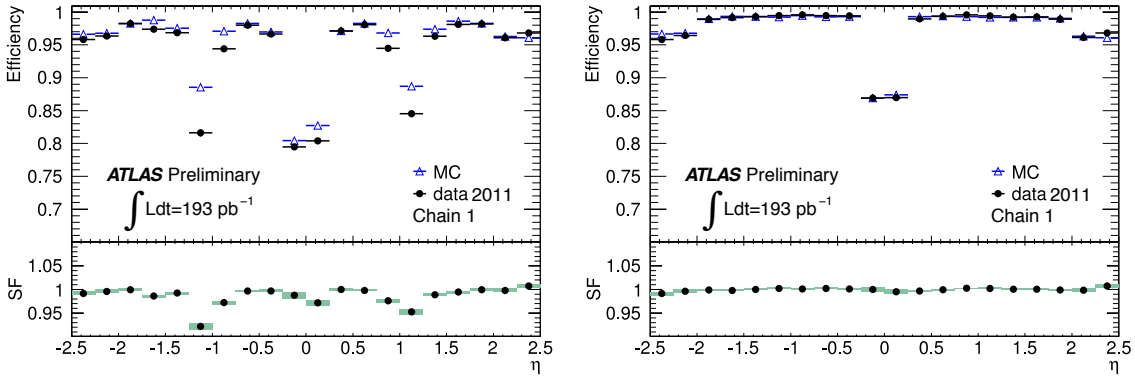

(a) Combined Muons

(b) Combined or tag muons

Figure 6.6: Muon reconstruction efficiency and scale factors as a function of η [17].

6.5.2 Muon Resolution and Scale Corrections for MC

The muon momentum resolution and momentum scale are measured using $Z \to \mu\mu$ decays in data and MC with the Z mass line shape as a constraint, as described in detail in Reference [29]. The width of the peak gives information about the momentum resolution, while the location of the peak gives information about the momentum scale. The primary causes of resolution smearing are mis-calibration and mis-alignment (between muon chambers and between the MS and ID), as well as the material distribution and magnetic field modeling for low momentum muons. The muon resolution and scale can impact the acceptance determination, which is a direct input to the cross section measurement. Since the acceptance must be determined from MC, it is vital to accurately model the muon resolution in the MC in order to accurately measure the cross section. As such, differences in the resolution between data and MC are corrected.

The resolution correction technique compares the $Z \to \mu\mu$ mass peak in the observed data to the peak in MC. Events are selected if they have opposite charge muons with $p_T > 20$ GeV in the same η region and have a dimuon invariant mass within 20 GeV of the Z pole mass. In addition, the ID tracks associated to the muons are required to pass the ID track quality criteria (described in Section 6.5). The muon momenta in the MC are then smeared and scaled, and a Z mass template is created that is compared to the data distribution using a χ^2. The procedure is iterated by adjusting the smearing and scaling parameters until the χ^2 is minimized. This procedure is performed separately in different η regions, as the resolution is known to differ by region. In addition, as the ID and MS resolution are impacted by different resolution effects, the two momentum measurements are smeared separately and then recombined. The corrections to the momentum derived using the smearing method for the different η regions can be found in Table 6.9.

Correction	$\lvert\eta\rvert < 1.05$	$1.05 < \lvert\eta\rvert < 1.7$	$1.7 < \lvert\eta\rvert < 2.0$	$2.0 < \lvert\eta\rvert < 2.7$
S	0.9997±0.0002	0.9999±0.0006	0.9990±0.0012	1.0013±0.0007
Δp_1^{ID}	0.00624±0.00102	0.00006±0.00438	0.00087±0.00443	0.00087±0.00415
Δp_2^{ID}	0.000299±0.000015	0.000721±0.000049	0.000845±0.000016	0.000048±0.000003
Δp_1^{MS}	0.02035±0.00016	0.04994±0.00198	0.02643±0.00045	0.01705±0.00383
Δp_2^{MS}	0.000129±0.000023	0.000335±0.000012	0.000163±0.000041	0.000443±0.000053

Table 6.9: Muon scale and resolution corrections [15, 18].

The muon spectrometer momentum measurement is smeared according to the equation,

$$p_T^{MS} \rightarrow p_T^{MS} \times (1 + \Delta(MS)) \tag{6.7}$$

$$\Delta(MS) = f(0,1) \times \Delta p_1^{MS} + f(0,1) \times \Delta p_2^{MS} \times p_T \tag{6.8}$$

where Δp_1^{MS} is the correction related to the effects of multiple scattering, while Δp_2^{MS} is the correction related to the effects of the intrinsic detector accuracies. The terms $f(0,1)$ are gaussian random variables with zero mean and unit width. Notice that there is no correction term for energy loss, as this effect is not seen to be a major contributor to the resolution of high p_T muons [29].

The ID track momentum measurements are smeared according to the equation,

$$p_T^{ID} \rightarrow p_T^{ID} \times (1 + \Delta(ID)) \tag{6.9}$$

$$\Delta(ID) = f(0,1) \times \Delta p_1^{ID} + f(0,1) \times \Delta p_2^{ID} \times \left\{ \begin{array}{ll} p_T & \text{if } |\eta| < 2.0 \\ \frac{p_T}{\tan^2\theta} & \text{if } |\eta| \geq 2.0 \end{array} \right\} \tag{6.10}$$

where Δp_1^{ID} and Δp_2^{ID} are corrections related to multiple scattering and intrinsic detector resolution, respectively, and the $f(0,1)$ terms are gaussian random variables with zero mean and unit width. As with the MS measurements, the energy loss is not seen to be a primary contribution to the resolution of high momentum tracks.

Once the ID and MS measurements are smeared, the Combined momentum measurement is formed with a resolution weighted average of the two measurements and then scaled, using the equation,

$$p_T^{CB} \rightarrow S \times p_T^{CB} \times \left(1 + \frac{\frac{\Delta(MS)}{\sigma^2(MS)} + \frac{\Delta(ID)}{\sigma^2(ID)}}{\frac{1}{\sigma^2(MS)} + \frac{1}{\sigma^2(ID)}}\right) \tag{6.11}$$

where the $\sigma^i(MS, ID)$ are the overall track resolutions, including the additional smearing corrections calculated by comparing the data and MC, and S is the momentum scale correction.

The observed resolution for 2011 data and MC (before corrections are applied) for the muon MS tracks, ID tracks, and Combined tracks can be found in Figure 6.7. The resolution variations as a function of η can be seen for the different tracks. The Combined tracks show the best performance, benefitting from the both the ID and MS measurements. The MC and data disagree for all track types and in essentially every η region, and thus the additional smearing is needed to match the MC resolution to that of the data.

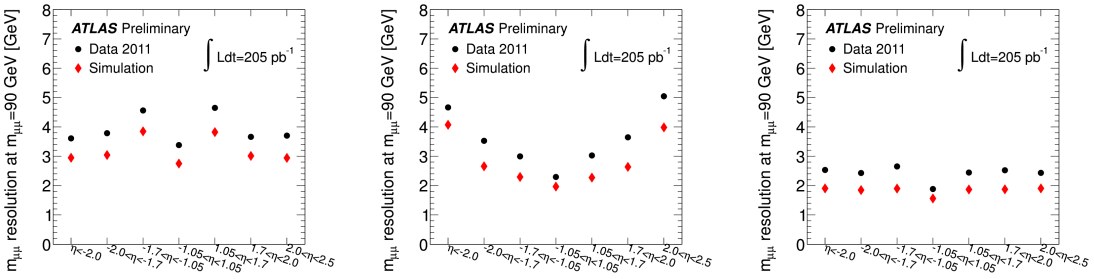

(a) MS track (b) ID track (c) Combined track

Figure 6.7: Observed muon resolution in data (black) and MC before additional corrections have been applied (red) for MS tracks (left), ID tracks (middle), and combined tracks (right) [16].

6.6 Electron Selection

Reconstructed electrons are required to pass the medium selection criteria, as described in Section 5.3. Each electron is also required to pass an object quality (OQ)

cut that tests if the electron cluster is affected by at least one of the following problems: the presence of a dead front-end board in the first or second EM calorimeter sampling layer, a dead region affecting the three EM calorimeter samplings, or a masked cell in the calorimeter. In addition, the electron cluster must not be in the transition crack region, and thus the cluster must satisfy $|\eta| < 1.37$ or $1.52 < |\eta| < 2.47$. To ensure the electron originated from the PV, the absolute distance in z between the electron track longitudinal impact parameter z_0 and the primary vertex z-position must be less than 10 mm.

The energy of the electron candidate is taken from the cluster measurement. If the electron candidate has ≥ 4 Pixel+SCT hits, then the electron candidate η and ϕ are taken from the track measurements. If the candidate does not satisfy the hit requirement, then η and ϕ are taken from the cluster. Using this definition of the energy and direction, the electron candidate must have $E_T > 15$ GeV.

Finally, the electron candidates are required to be isolated, as measured using an absolute calorimeter isolation variable called *etCone30*. That is, the total calorimeter energy in a cone of $\Delta R = 0.3$ around the electron, not including the electron candidate energy, must be less than 4 GeV. It should be noted that the calorimeter energy in the cone is corrected for leakage of the electron energy outside the cluster, and accounts for the number of primary vertices in the event. The number of primary vertices is a measure of the pileup contributions to the event, and this pileup correction, derived using $W \to e\nu$ events in data and MC, is linear in the number of primary vertices.

6.6.1 Electron Efficiency Corrections for MC

The electron reconstruction and identification efficiencies are measured using the Z tag-and-probe method, as described in detail in Reference [45]. The efficiency to reconstruct electron cluster candidates and match them to ID tracks passing quality criteria is denoted the reconstruction efficiency, while the efficiency for the reconstructed electron to pass the identification criteria is denoted the identification efficiency. In both cases, events with opposite charged electrons, matched to the same vertex, and with a dielectron invariant mass within 10 GeV of the Z pole mass are selected. Tag electrons are required to pass the tight identification criteria, have $E_T > 20$ GeV, and be matched to a trigger object. For reconstruction efficiency studies, the probe electron is an EM sliding window cluster with $E_T > 15$ GeV, and the fraction of the probes matched to a reconstructed electron cluster matched with a high quality ID track gives the unbiased measurement of the efficiency. For the identification efficiency studies, the probe electron is a reconstructed electron cluster candidate, matched with a high quality ID track with $E_T > 15$ GeV, and the fraction of the probes matched to an electron passing the identification criteria gives the unbiased efficiency measurement. It should be noted that background contamination in the probe samples is subtracted, and is a primary source of systematic uncertainty.

The electron reconstruction and medium and tight identification efficiencies, measured in 2010 data[4], can be found in Figure 6.8 [45]. While the 2011 efficiencies differ slightly from 2010, the collision conditions were not dramatically different in the early

[4]Efficiency plots from early 2011 data are not available publicly, and plots for the full 2011 use an updated identification criteria which was not available at the time of this analysis.

2011 data and thus this 2010 data gives a reasonable estimate for the reader's insight. The reconstruction efficiency is measured as a function of cluster η and is seen to suffer from large errors due to background subtraction uncertainties. The identification efficiency is shown as a function of η and E_T, and is higher for medium identification than for tight (as expected).

The difference in the measured efficiencies in MC from that of the data are corrected using scale factors, as described previously. The scale factors for the reconstruction efficiency as a function of cluster η are found in Table 6.10. The identification efficiency scale factors for medium and tight criteria are measured as a function of η (integrated over E_T), as seen in Figure 6.9. However, some E_T dependence of the scale factors is observed, and thus an E_T correction is applied. This correction is calculated as the ratio of the E_T dependent scale factor (integrated over η) to the average scale factor, and is multiplied by the η dependent scale factor. The E_T corrections can also be found in Figure 6.9 for medium and tight identification criteria. Since every desired lepton must be reconstructed for an event to be selected, the event level reconstruction scale factor is simply the product of single lepton scale factors.

An additional correction to the MC is needed to account for the dead LAr front end boards during much of the data taking. To account for this, the efficiency of electrons in the MC pointing to the dead LAr boards is scaled by fraction of luminosity for which the front-end boards were dead.

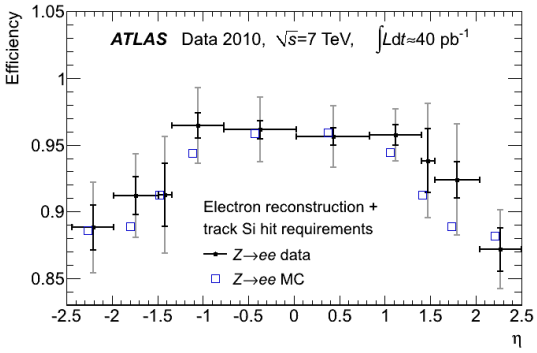

(a) Reconstruction efficiency

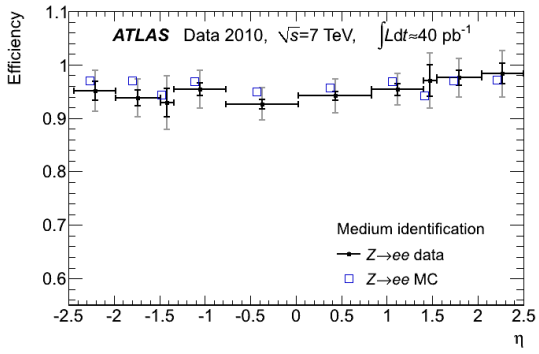

(b) Medium identification efficiency vs. η

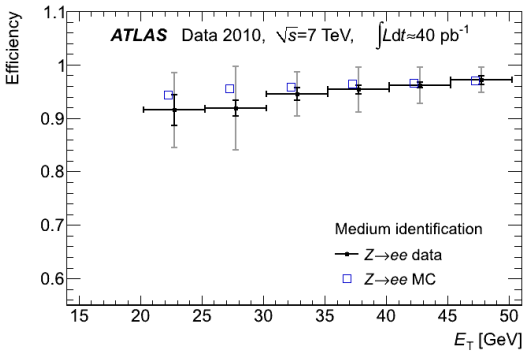

(c) Medium identification efficiency vs. E_T

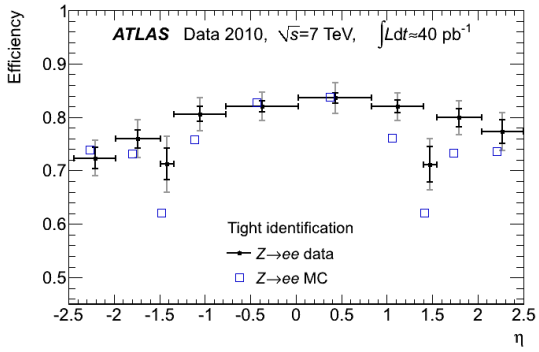

(d) Tight identification efficiency vs. η

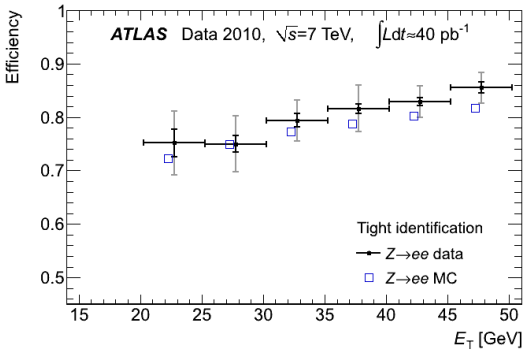

(e) Tight identification efficiency vs. E_T

Figure 6.8: Electron reconstruction and identification efficiencies from 2010 data [45].

η Bin	$\lvert\eta\rvert < 0.8$	$0.8 < \lvert\eta\rvert < 2.37$	$2.37 < \lvert\eta\rvert < 2.47$
SF	0.9984±0.0066	1.0091±0.0070	0.9759±0.0184

Table 6.10: Electron reconstruction efficiency scale factors [23].

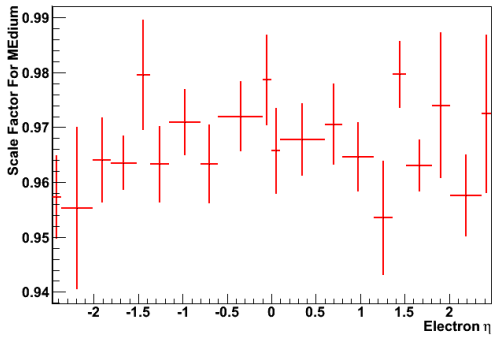

(a) Medium identification SF vs. η

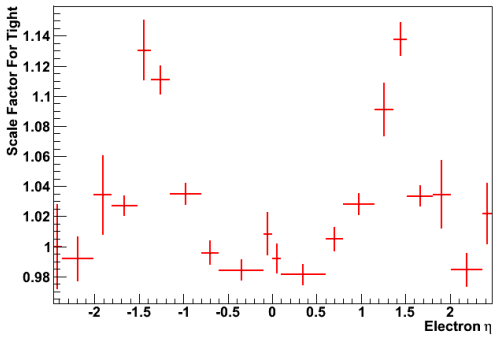

(b) Tight identification SF vs. η

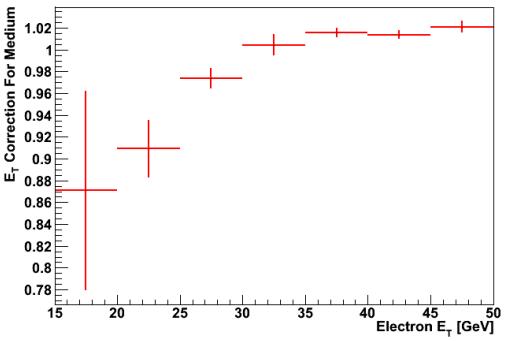

(c) Medium identification E_T Correction

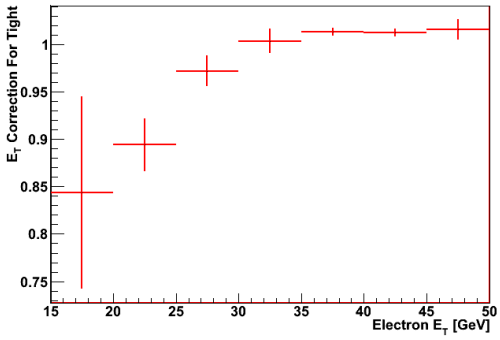

(d) Tight identification E_T Correction

Figure 6.9: Electron identification efficiencies scale factors and E_T corrections [23].

6.6.2 Electron Resolution Corrections for MC

The resolution fof high energy electrons is measured using the $Z \to ee$ mass distributions, as described in detail in Reference [45]. Events with opposite charged electrons passing the medium identification with $E_T > 25$ GeV and dielectron mass within 10 GeV of the Z pole mass are selected. The mass distributions are then fit with a Breit-Wigner distribution convolved with a Gaussian, and the Gaussian σ determines the experimental resolution. As the sampling and noise contributions to the energy resolution are small for high energy electrons [45], the Gaussian σ is used to determine only the constant resolution term related to detector non-uniformity and intrinsic accuracy. The fit is performed in several η bins in order to account for resolution variations. The $Z \to ee$ mass distribution, integrated over η, for data and MC along with the fitted resolutions can be seen in Figure 6.10 for 2010 data. While this analysis uses 1 fb^{-1} of 2011 data, the resolution is similar to the 2010 dataset, as the LHC running conditions were similar.

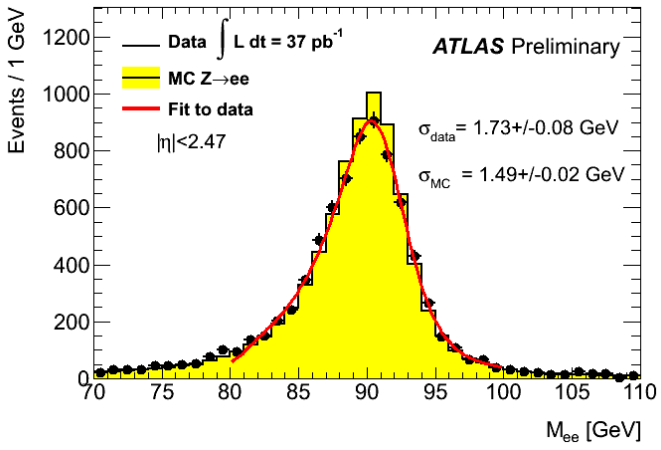

Figure 6.10: $Z \to ee$ mass distribution, in 2010 data, used for fitting the electron resolution[21].

The electrons in MC are then corrected using the equation,

$$E \to E + f(0,1)\sqrt{(C_{data}E)^2 - (C_{MC}E)^2} \tag{6.12}$$

where $C_{data(MC)}$ is the constant term measured in data (MC) and $f(0,1)$ is a zero mean, unit width normal distribution. The values of C in data and MC can be found in Table 6.11. Note that no error is listed on the C term in MC, as its uncertainty is much smaller than the data term and thus does not contribute significantly to the overall uncertainty of the resolution smearing correction.

Correction	$\|\eta\| < 1.37$	$1.37 < \|\eta\| < 2.47$
C_{MC}	0.007	0.007
C_{data}	0.011±0.005	0.018±0.006

Table 6.11: Electron resolution corrections [15, 18].

6.7 Event Selection

The primary physics objects used in the $W^{\pm}Z$ selection are muons, electrons, missing energy, primary vertices, and jets (only for bad event cleaning). The muon and electron selections are described in Sections 6.5 and 6.6 respectively. The primary vertex of each event is selected as the primary vertex with the largest sum of track p_T^2, for tracks associated to the vertex, and is required to have ≥3 tracks. Jets are reconstructed at the EM scale with topo-clusters and then calibrated to the hadronic scale, and are built with the anti-k_T algorithm using radius parameter is $R = 0.4$, as described in Section 5.5. Selected jets must have $p_T > 20$ GeV. The missing transverse energy is built from reconstructed objects, as described in Section 5.6.

$W^{\pm}Z$ final states with electrons and muons are considered: $\mu^+\mu^-\mu^{\pm}$, $\mu^+\mu^-e^{\pm}$, $e^+e^-\mu^{\pm}$, and $e^+e^-e^{\pm}$. The same cutflow is applied in those four cases, except for the last cut (trigger-matched high-p_T lepton). Event cleaning cuts apply only to data samples and only remove a small fraction of the data events (less than 1%). The event selection criteria for this cut-based analysis, in the order the cuts are applied, are:

1. ***Good Run List***: Keep events in the Good Runs List only.

2. ***Trigger***: Either `EF_e20_medium` (electrons) or `EF_mu18_MG` ||`EF_mu40_MSonly_barrel` (muons) must have fired.

3. ***Primary vertex***: The event must have at least one primary vertex with at least 3 good tracks.

4. ***Overlap removal***: Objects are removed from the event using a ΔR overlap criteria:

   - Remove electrons within $\Delta R < 0.1$ of any selected muon;
   - If two selected electrons overlap within $\Delta R < 0.1$, remove lower-p_T electron;
   - Remove jets within $\Delta R < 0.3$ of any selected muon or electron.

   No events are removed at this stage, only objects.

5. ***Event cleaning- Bad Jet cleaning***: Jets which do not overlap ($\Delta R > 0.3$) with a selected lepton are tested for the "loose" bad jet criteria [25]. This criteria assesses the quality of jets' energy depositions in the calorimeter in order to test

for noise spikes, coherent noise, non-collision backgrounds, and cosmics. If any jet is tagged as "bad", the entire event is rejected.

6. ***Event cleaning- LAr noise***: Events flagged as having noise in the LAr Calorimeter are removed.

7. ***Z candidate***: The event must have a pair of same flavor, opposite charge, leptons with a dilepton invariant mass that is consistent with the Z mass: $|M_{ll} - 91.1876| < 10$ GeV.

8. ***3 leptons***: The event must have at least 3 leptons passing the selection criteria, and coming from the primary vertex.

9. $\mathbf{E_T^{miss}}$: Missing transverse energy in the event must be greater than 25 GeV.

10. ***W transverse mass,*** $\mathbf{M_T(W^{\pm})}$: The transverse mass of the W candidate system, formed from the third lepton identified as coming from W and from the E_T^{miss}, must be greater than 20 GeV[5]. If this lepton is a muon (electron), it must be a combined muon (tight electron). The third lepton must have $p_T > 20$ GeV.

11. ***Trigger match***: One of the muons (electrons) in the event associated to the W or Z boson, with $p_T > 20$ (25) GeV, must match a triggered muon (electron).

6.8 Signal Acceptance

The expected number of events in $\mathcal{L} = 1.02$ fb^{-1} after each cut for the $W^{\pm}Z$ MC with all corrections applied are summarized in Table 6.12. The signal has been

[5]That is, $m_T(W) = \sqrt{2 \times p_T^l \times E_T^{miss} \times (1 - \cos(\phi^l - \phi^{miss}))} > 20$ GeV.

normalized using the MCFM cross section calculation, described in Section 6.3. In addition the relative acceptance of each cut is listed in Table 6.13. The absolute acceptance increases with the number of muons in the final state as expected because the reconstruction efficiency is higher muons than electrons. Finally, the contribution from $W^{\pm}Z \to \tau + X$, which includes three lepton final states where at least one of the leptons is a tau and where the tau decays into an electron or a muon, is added to the signal for the cross section extraction; the cutflow for this MC sample is shown in Table 6.14.

Cutflow	Events			
	$\mu\mu\mu$	$e\mu\mu$	μee	eee
All	261.4			
Muon or Electron Trigger	247.1			
Primary Vertex	246.4			
Z Cut	70.1		43.4	
Three Leptons	25.0	17.2	15.5	10.6
E_T^{miss} Cut	20.5	13.9	12.7	8.5
$M_T(W^{\pm})$ Cut	18.0	12.1	11.2	7.5
Trigger Match	17.9	12.0	11.1	7.5

Table 6.12: Expected number of MC events after each cut for $W^{\pm}Z \to l\nu ll$ events for $\mathcal{L}$ =1.02 fb^{-1}.

Cutflow	Acceptance (%)			
	$\mu\mu\mu$	$e\mu\mu$	μee	eee
All	100			
Muon or Electron Trigger	94.5			
Primary Vertex	99.8			
Z Cut	28.4		17.6	
Three Leptons	35.7	24.6	35.7	24.3
E_T^{miss} Cut	82.0	80.4	82.1	79.9
$M_T(W^{\pm})$ Cut	87.5	87.4	87.9	88.5
Trigger Match	99.4	99.2	99.1	100

Table 6.13: Relative acceptance of MC events after each cut for $W^{\pm}Z \to l\nu ll$ events.

Cutflow	Events			
	$\mu\mu\mu$	$e\mu\mu$	μee	eee
All	327.1			
Muon or Electron Trigger	216.4			
Primary Vertex	215.9			
Z Cut	33.8		21.1	
Three Leptons	2.00	1.09	1.16	0.69
E_T^{miss} Cut	1.58	0.88	0.91	0.58
$M_T(W^{\pm})$ Cut	0.75	0.44	0.43	0.28
Trigger Match	0.75	0.42	0.43	0.28

Table 6.14: Expected number of MC events after each cut for $W^{\pm}Z \to \tau + X$ for $\mathcal{L}$ =1.02 fb^{-1}. This sample contains three lepton final states where at least one of the leptons is a tau and where the tau decays into an electron or a muon

6.9 Background Estimation

The major backgrounds to the $W^{\pm}Z \to l\nu ll$ signal after the event selection are ZZ, Z+jets, $t\bar{t}$, and $W/Z + \gamma$. The ZZ background is modeled using the MC simulation because it contains prompt leptons from vector boson decays, for which the simulation of the acceptance and efficiency is known to perform well, as discussed in Section 6.9.1. The $W/Z + \gamma$ background contains prompt leptons from the vector boson decay as well as leptons from photon conversions or photons misidentified as electrons. This background is expected to be small, and is thus modeled using MC simulations, as discussed in Section 6.9.4.

Both Z+jets and $t\bar{t}$ events contain two prompt leptons from vector boson decay, as well as a third *fake* lepton. The fake leptons can come from a jet faking a lepton, from a heavy flavor quark decay, or from an in-flight decay of a pion or kaon. These fake leptons are produced in the the fragmentation process and thus will be spatially correlated with jets such that the majority will fail the isolation criteria. As the

process of producing fake leptons is extremely difficult to model and is not expected to be simulated well by MC, the Z+jets and $t\bar{t}$ backgrounds have been estimated using *Data-Driven* (DD) techniques, whereupon control regions in data are used to model the backgrounds and to extrapolate from the control regions into the signal region as discussed in Sections 6.9.2 and 6.9.3. It should be noted that the probability of producing fake leptons depends greatly on the composition of the jets in the sample, especially the amount of heavy flavor production. As the jet composition differs between Z+jets and $t\bar{t}$, these backgrounds must be estimated separately.

In principle, WW events fall into this category of background with two prompt leptons and one fake. However, the total WW cross section is much smaller than Z+jets and $t\bar{t}$, and folding in the probability for producing a fake lepton makes this background negligible. This is confirmed by MC simulation whereby no events pass our selection criteria and thus WW is not included in our final background estimate.

Finally, there could be additional backgrounds which contain two or more fake leptons, such as W+jets, single top production, or QCD dijet production. These backgrounds are expected to be very small since the probability of producing a fake lepton is extremely small. The size of these backgrounds have been checked in MC simulation, and no MC events in any of these samples pass our selection criteria. For completeness, the small contribution of these "double fake" backgrounds are accounted for in the Z+jets DD estimate.

6.9.1 ZZ

In all four channels, ZZ events in which both Z bosons decay leptonically are a major background to the $W^{\pm}Z$ signal. For a ZZ event to pass the $W^{\pm}Z$ event selection, the event must have E_T^{miss} greater than 25 GeV. The source of this E_T^{miss} can come from mismeasured jets, from the tail of the E_T^{miss} distribution, or from a lepton from a Z decay outside the fiducial acceptance of the detector (which is the primary source).

In order to check the modeling of this background, the kinematics of leptons falling outside of the detector acceptance are analyzed using the MC truth information. Figure 6.11 shows the η distributions of truth muons and electrons which fail a $\Delta R < 0.1$ match with a reconstructed muon or electron in $ZZ \rightarrow 4l$ MC events that pass the full $W^{\pm}Z$ selection. In these events, three of the four leptons have been reconstructed in the detector. The fourth lepton is considered "missing" and is a source of E_T^{miss} in particular for muons whose momentum is not measured fully by the calorimeter. The η distribution of "missing" muons confirms this, as the largest contribution of ZZ events to our signal region comes from events which have a muon near $\eta = 0$, where the muon spectrometer has a gap in coverage to allow services to enter, or which have a muon with $|\eta| > 2.7$, where spectrometer coverage ends. In the transition regions $|\eta| \sim 1.4$ and in the region $2.5 < |\eta| < 2.7$, the E_T^{miss} calculation uses Stand-Alone or Segment-Tagged muon tracks to correct for the lack or depletion of Combined tracks, and therefore muons in these regions have a small contribution to ZZ events which pass the signal selection. The electron η distribution shows peaks

at $|\eta| \sim 1.4$, which corresponds to the transition region between the calorimeters. Otherwise, the calorimeter coverage is hermetic, and therefore there are no obvious features in the η distribution of "missing" electrons.

The detector acceptance is known to be well modeled by simulation and the modeling of the ZZ process has relatively small theoretical uncertainties. Thus the shape of this background is estimated from MC simulation by applying the appropriate selection criteria and applying the pileup reweighting, trigger and lepton efficiency, and smearing corrections. The total number of events is determined by scaling the ZZ sample according to its theoretical cross section and the measured luminosity. The estimated background contributions from the ZZ process are shown in Table 6.18.

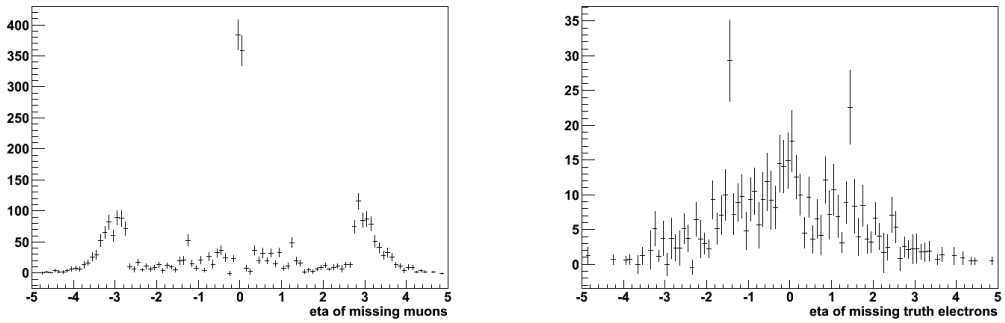

(a) (b)

Figure 6.11: The η distribution of truth muons (a) and electrons (b) without a reconstructed muon or electron with $\Delta R < 0.1$ in $ZZ \to 4l$ MC events that pass the full $W^{\pm}Z$ selection.

6.9.2 Z+Jets

The Z+jets process contains two prompt leptons from the Z decay, and a third fake lepton from a mis-identified jet, heavy quark decay, or pion/kaon decay in flight. If one of the jets in the event is mis-measured, or there is a hard neutrino from the heavy quark decay, the event can also contain missing energy. Although the additional requirement of a fake lepton and missing energy are only satisfied by a small fraction of Z+jets events, the cross section is large compared to $W^{\pm}Z$ and some of the Z+jets events pass the selection criteria. Given that the MC simulation does not model this fake lepton process well, a Data-Driven estimation is used to model this background whereby a Z+jets enriched control region is identified and an extrapolation is performed from the control region into the signal region. The control region is defined by events that pass all selection criteria except one of the leptons fails some of the lepton selection criteria. The extrapolation is performed using a linear scaling of the observed number of events in the control region. This scaling factor, called the *fake-factor*, is measured in a Z+jets enriched data sample using events which fail the missing energy cut. The method can be seen schematically in Figure 6.12, where leptons failing the selection criteria are denoted *fake-able* and leptons passing the selection criteria are denoted *good*. In the high missing energy *fake-able* sample, any of the leptons can be *fake-able*. In the low missing energy sample, the non-Z lepton must be fake-able while the Z leptons must be *good* so that the sample is known to be dominated by only Z+jets events. In the *good* samples, all leptons must be *good*. The final step, which is not seen in the figure, is that a *missing energy scaling* factor is applied to the fake-factor in order to account for the

difference in the fake factor between the low missing energy and high missing energy regions. The missing energy scaling is calculated in MC and cross checked in data.

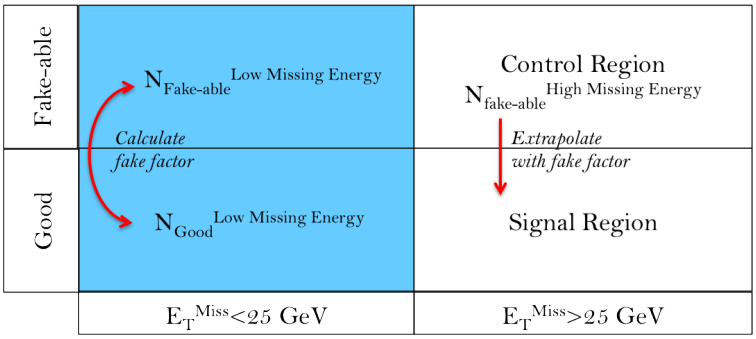

Figure 6.12: A schematic of the Z+jets data-driven estimation technique.

The Z+jets enriched control region is found by using events which pass all selection criteria, except one of the leptons is required to pass a *fake-able* lepton definition. The *fake-able* definition is orthogonal to the normal lepton selection criteria as it requires the lepton to have failed some of the usual lepton selection criteria, and is designed to identify leptons which originate from the same source as the fake leptons which pass all selection criteria. More specifically, the electron identification criteria cuts are specifically designed to reject mis-identified jets by making requirements on variables like the shower shape, track quality, and hadronic energy fraction, and thus the *fake-able* electrons are defined as electrons which fail the medium identification criteria but pass all other selection. For muons, isolation is one of the most powerful variables for rejecting muons from jets and thus *fake-able* muons are defined as muons which fail isolation but pass all selection criteria.

The fake-factor is used in order to extrapolated from the Z+jets enriched control region into the signal region. Since this extrapolation is done linearly, the fake factor, f, is simply the ratio of the number of *good* lepton events to the number of *fake-able* lepton events,

$$f = \frac{N^{good}}{N^{fake-able}} \tag{6.13}$$

where N^{good} and $N^{fake-able}$ are the number of Z+jets events passing all selection and containing *good* and *fake-able* leptons, respectively. Of course, the number of Z+jets events passing all selection and containing a *good* lepton is the number of Z+jets events in the signal region and thus is exactly the quantity which needs to be estimated. Since the fake factor is not expected to be well modeled in MC simulation, a data-based estimation is needed. In addition, the fake factor strongly depends on the composition of *fake-able* leptons (i.e. what fraction comes from mis-identified jets, from heavy flavor, etc.) and thus must be estimated in a data sample with a composition as close as possible to the signal and control regions. Therefore, the fake factor is estimated in a Z+additional lepton sample, where both Z leptons are *good* and the additional lepton can be either *good* or *fake-able*. These Z+additional lepton events are required to have a low missing energy failing the cut, i.e. $E_T^{miss} < 25$ GeV. The fake factor can then be calculated as the number of Z+*good* lepton events to the number of Z+*fake-able* lepton events in the low missing energy sample.

It should be noted that the MC expected contributions from non-Z+jets event in the Z+additional lepton samples are subtracted before the fake factor is calculated. This is less than a 1% correction in the Z+*fake-able* low E_T^{miss} sample and a 20% correction in the Z+*good* low E_T^{miss} sample for both muons and electrons as the third

lepton. In addition, due to statistical limitations the fake-factor is not measured as a function of muon p_T or electron E_T but is measured as a single quantity integrated over kinematic variables. The only exception is for muons with p_T >40 GeV, for which the fake-factor is calculated separately because this region is dominated by $W^{\pm}Z$ events failing the E_T^{miss} cut rather than Z+jets.

The distributions of the third lepton p_T in Z+additional lepton events with low missing energy can be found for electrons in Figure 6.13 and muons in Figure 6.13. The electron is required to pass the fake-able definition, medium electron identification criteria, and tight electron identification criteria, in Figures 6.13(a), 6.13(b), and 6.13(c) respectively. The muon is required to be non-isolated (*fake-able*) in Figure 6.14(a) and isolated in Figure 6.14(b).

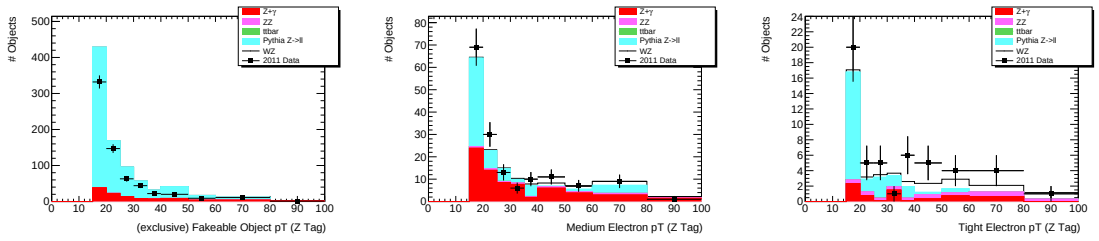

(a) (b) (c)

Figure 6.13: Number of electron candidates of various quality as a function of p_T in events with a Z and an extra object: (a) fake-able, (b) passing medium electron identification criteria, and (c) passing tight electron identification criteria.

Since the fake-factor is calculated in a low E_T^{miss} region, and applied to a high E_T^{miss} region, a correction is applied to extrapolate the fake-factor from low to high missing energy. This correction is expected for muon events due to the fact that many non-

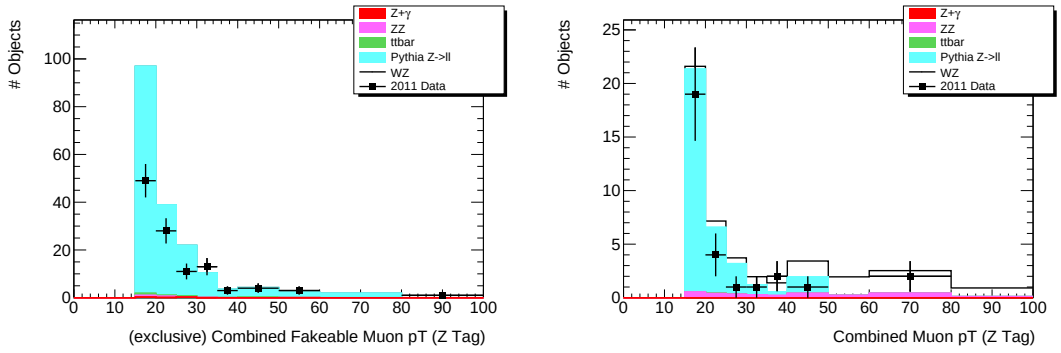

(a) (b)

Figure 6.14: Number of non-isolated (a) and isolated (b) muon candidates as a function of p_T in events with a Z and an extra object

isolated muons originate from heavy flavor decays in jets, and the presence of E_T^{miss} from the mis-measurement of the jet or from a hard neutrino in the jet is correlated with the isolation of the muon. The dependence of muon isolation efficiency on E_T^{miss} can be seen in Z MC and dijet-enriched data in Figure 6.15. To extrapolate from the low E_T^{miss} region to the high E_T^{miss} region, a scale factor of 0.65, measured from MC, is applied to the measured muon fake-factor. This scale factor is the ratio of fake factors in the high E_T^{miss} region to the low E_T^{miss} region. It is difficult to measure this E_T^{miss} dependence in Z plus extra object data because the high E_T^{miss} region is populated mainly by our signal $W^{\pm}Z$ events. The ability of the MC to simulate the E_T^{miss} dependence of the isolation efficiency is tested in dijet data. The difference in the muon E_T^{miss} scale factor between dijet data and dijet MC is 20%, which is used as the systematic uncertainty on the $Z+$ jet E_T^{miss} scale factor for muon fakes. In the case of electrons, this missing energy scale factor is observed to be consistent with unity in Z plus extra object MC, dijet MC, and dijet data. A 15% uncertainty is applied to the electron E_T^{miss} scale factor from the uncertainty of the E_T^{miss} scaling

observed in dijet data.

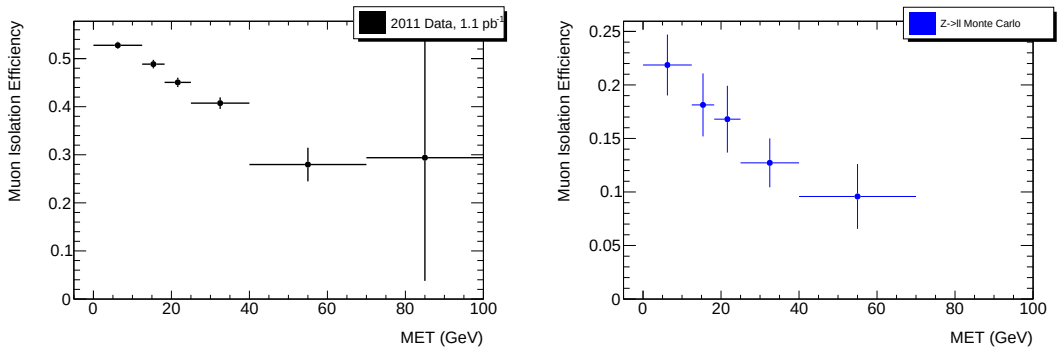

(a) (b)

Figure 6.15: Muon isolation efficiency as a function of missing energy in Z+jets MC (left) and dijet data (right) .

Additional shape systematic uncertainties on the fake-factor come from checking the consistency of the p_T dependence of the fake-factor between the high and low missing energy regions using the Z+jets MC. This systematic is 2% for electrons and 4% for muons. Finally, the fake-factor is measured using the third lepton in Z+additional lepton events, but the control region at high E_T^{miss} allows for any of the leptons to fake, including the leptons forming the Z. Such fakes could come from W+jets events, and thus the p_T shape consistentcy systematic on the fake-factor is checked by comparing Z+jets MC and W+Jets MC. The systematic is 12% for electrons and 4% for muons.

The final estimates of the electron and muon fake factors, including the statistical and systematic uncertainties, are presented in Table 6.15. The table includes two possible tight sample definitions for electrons (passing medium identification

Channel	p_T (GeV)	Fake Factor	Statistics	E_T^{miss} Scale	p_T Shape
Medium electron	> 15	0.220	± 0.021	± 0.033	± 0.026
	> 20	0.251	± 0.032	± 0.037	± 0.030
Tight electron	> 15	0.070	± 0.012	± 0.012	± 0.008
	> 20	0.087	± 0.020	± 0.010	± 0.013
Tag or combined μ	> 15	0.131	± 0.033	± 0.041	± 0.008
	20-40	0.081	± 0.038	± 0.025	± 0.005
	> 40	0	± 0.227	± 0.070	± 0.014
Combined μ	> 15	0.127	± 0.029	± 0.039	± 0.008
	20-40	0.060	± 0.036	± 0.019	± 0.004
	> 40	0	± 0.161	± 0.050	± 0.010

Table 6.15: List of fake factors, with errors from limited statistics, E_T^{miss} scale uncertainty, and p_T shape uncertainty for the different lepton types used in the analysis. The region with $p_T > 40$ GeV bins is dominated by the $W^{\pm}Z$ signal events.

or tight identification criteria) and two for muons (Combined muons only or Combined+Segment Tagged muons). The fake factor is also shown for different p_T lower bounds, which is needed as the p_T cut for the W lepton and the Z leptons are different in the analysis event selection.

The fake-factors are applied to the high missing energy control region to extrapolate into the signal region. MC expected contributions from non-Z+jets samples in the control region are subtracted before this extrapolation. The estimate allows for the W or Z leptons to be *fake-able*. In addition, the possibility that two of the leptons are fakes are included in the calculation . Since these double fakes contribute to the high E_T^{miss} control region, they are first subtracted in the control region to avoid double counting (although this contribution is only a few percent of the control region). Thus

the final estimate is calculated using the equation

$$\begin{aligned} N_{ggg} &= f \times (N_{ggf} - 2 \times f \times N_{gff}) + f^2 \times N_{gff} \\ &= f \times N_{ggf} - f^2 \times N_{gff} \end{aligned} \tag{6.14}$$

where N_{ggg} is the predicted number of events in the signal region with three *good* leptons, N_{ggf} is the number of events in the control region with two *good* and one *fake-able* lepton, N_{ttl} is the number of events in the control region with one *good* and two *fake-able* leptons, and f is the fake factor.

The final Z+jets estimates using this data driven technique can be found in Table 6.16. The asymmetric uncertainties on the muon estimates are a consequence of the fact that the muon fake-factor has a zero central value for $p_T > 40$ GeV while the uncertainty is non-zero. As the fake-factor is required to be positive, this results in an asymmetric error.

Channel	$\mu\mu\mu$	$e\mu\mu$	$ee\mu$	eee
Expected Events	$0.4 \pm 0.3^{+1.6}_{-0.3}$	$1.7 \pm 0.5^{+0.6}_{-0.6}$	$0.7 \pm 0.3^{+1.1}_{-0.4}$	$2.0 \pm 0.5^{+0.7}_{-0.7}$

Table 6.16: Z+jets background predictions using the data driven method. The first uncertainty is statistical; the second is from systematic sources.

6.9.3 $t\bar{t}$

The $t\bar{t}$ process has the potential to produce multiple leptons through the dilepton decay chain $t\bar{t} \rightarrow W^+bW^-\bar{b} \rightarrow l^+\nu bl^-\nu\bar{b}$ where the b-quarks further decay semi-leptonically. Even if the b-quarks do not decay semi-leptonically, fake leptons from mis-identified jets could contribute additional electrons (though the primary source of

fake leptons in $t\bar{t}$ is the b-quarks). Because of the presence of neutrinos, the $t\bar{t}$ process can result in events with three leptons and missing energy, which is very similar to the $W^{\pm}Z$ selection. However, there is no Z boson in the $t\bar{t}$ decay chain and thus there should be no resonance in the $t\bar{t}$ dilepton mass spectrum around the Z pole. $t\bar{t}$ is the only background without a Z resonance, and this fact greatly helps isolate $t\bar{t}$ dominated control regions for Data-Driven estimation. Specifically, the side-bands of the dilepton mass spectrum are dominated by $t\bar{t}$ and can be used as the $t\bar{t}$ control region. The final $t\bar{t}$ estimation is determined by extrapolating from the side-bands to under the Z peak.

Events are required to pass all selection criteria except the mass window cut around the Z pole mass. The leptons for the Z candidate are chosen as the two same flavor opposite charge leptons whose dilepton mass is closest to the Z pole mass. The dilepton invariant mass distribution in each of the four analysis channels can be found in Figure 6.16. The contribution from $t\bar{t}$ is seen in green in each of the distributions, and can be seen to dominate the side-bands in the $\mu\mu\mu$, $e\mu\mu$, and $ee\mu$ channels. The side-bands in the eee channel are dominated by Z+jets, and thus can not be easily used for $t\bar{t}$ estimation. In addition, the expected $t\bar{t}$ contribution to the eee channel is expected to be small. Therefore, the MC prediction is used for the eee channel rather than the side-band method.

Since the statistics of both the data and MC side-bands are small after all selection, the dilepton invariant mass distribution after the leptons have been selected, but without and isolation cut on the non-Z lepton, is used to check data/MC consistency.

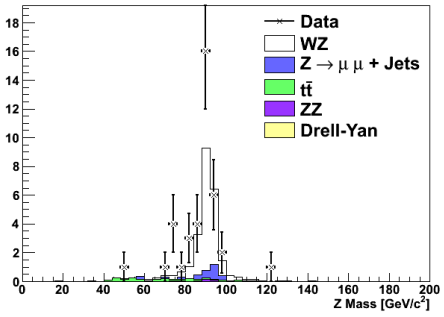

(a) $\mu\mu\mu$

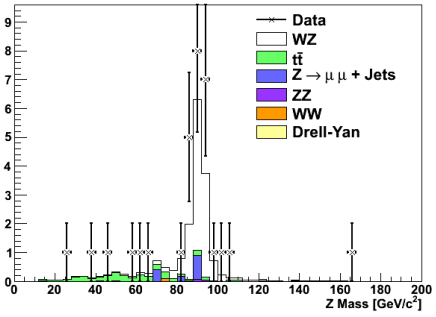

(b) $e\mu\mu$

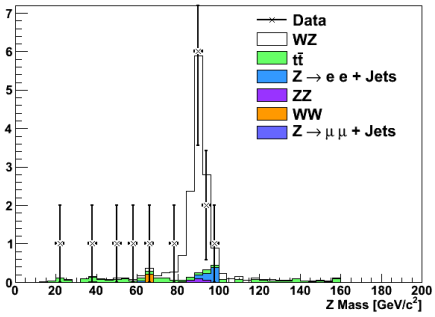

(c) $ee\mu$

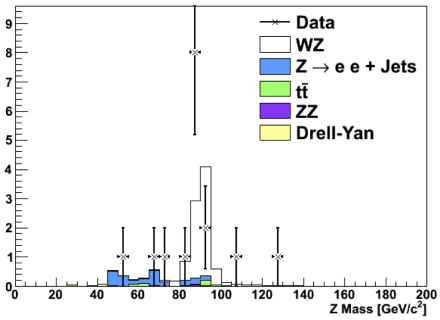

(d) eee

Figure 6.16: The invariant mass of the Z candidate, defined by the two leptons whose invariant mass is closest to the Z mass pole, after all analysis cuts have been applied except the Z mass cut, is shown in each of the four decay channels.

This distribution for the $\mu\mu\mu$, $e\mu\mu$, and $ee\mu$ channels can be found in Figure 6.17. The data and MC agree fairly well in each of these distributions, and the long flat tails of the $t\bar{t}$ distribution in the side-bands can easily be seen.

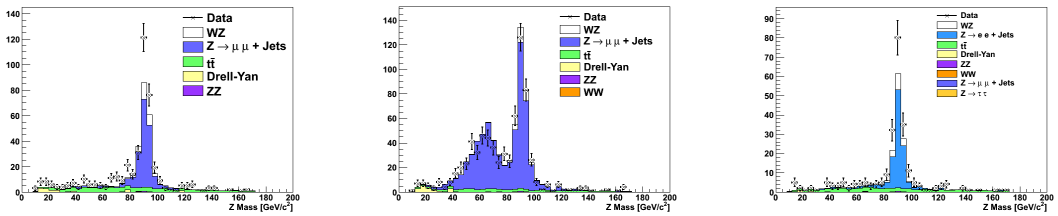

(a) $\mu\mu\mu$ (b) $e\mu\mu$ (c) $ee\mu$

Figure 6.17: The invariant mass of the Z candidate, defined by the two leptons whose invariant mass is closest to the Z mass pole, after the third lepton is selected, but is not required to be isolated, is shown in the $\mu\mu\mu$, $e\mu\mu$, and $ee\mu$ channels.

The estimate of the $t\bar{t}$ background in the signal region of $m_{ll} \in [81, 101]$ is performed with a linear extrapolation from the side bands. More precisely, the density of events in data is calculated in the mass ranges $[40, 70]$ GeV and $[110, 140]$ GeV and the average density of the two mass windows is used as the estimated density of $t\bar{t}$ events in the signal region. These mass ranges in the side-bands are chosen so that $t\bar{t}$ is the dominant source of events, as determined using the MC simulation. The final $t\bar{t}$ estimate is calculated by multiplying the density by the signal mass window size of 20 GeV. It should be noted that the MC predicts small contributions from non-$t\bar{t}$ events in the side-bands, and this MC prediction is subtracted before estimating the $t\bar{t}$ density. For the Z+jets contributions to the side-band, the MC prediction is scaled by the ratio of the Data-Driven Z+jets estimate in the signal region to the MC Z+jets estimate in the signal region. Thus, the $t\bar{t}$ contribution in the signal widow,

$N^{t\bar{t}}_{m_{ll}\in[81,101]}$, is calculated with the equation,

$$\begin{aligned} N^{t\bar{t}}_{m_{ll}\in[81,101]} &= 20 \times \left(\frac{1}{2} \frac{N^{data}_{m_{ll}\in[40,70]} - N^{non-t\bar{t}}_{m_{ll}\in[40,70]}}{30} + \frac{1}{2} \frac{N^{data}_{m_{ll}\in[110,140]} - N^{non-t\bar{t}}_{m_{ll}\in[110,140]}}{30} \right) \\ &= \frac{1}{3} \left(N^{data}_{m_{ll}\in[40,70]} - N^{non-t\bar{t}}_{m_{ll}\in[40,70]} + N^{data}_{m_{ll}\in[110,140]} - N^{non-t\bar{t}}_{m_{ll}\in[110,140]} \right) \end{aligned} \quad (6.15)$$

where $N^{data}_{m_{ll}\in[A,B]}$ is the number of events observed in data with a dilepton mass in the range $[A, B]$, and $N^{non-t\bar{t}}_{m_{ll}\in[A,B]}$ is the predicted number of non-$t\bar{t}$ events in the dilepton mass range $[A, B]$. This linear extrapolation is used, rather than a polynomial or template fit using the MC distributions, because the statistics of both the data and the MC simulation in the side-bands are too small for more sophisticated techniques.

Systematics uncertainties on the $t\bar{t}$ estimate are determined using closure tests in the simulation after several stages of the selection. That is, the side band estimate is calculated using the $t\bar{t}$ MC simulation and compared with the direct estimate from the same MC simulation of the integrated number of predicted events under the Z peak. This closure test is performed after the third lepton is selected but before isolation is imposed, after the third lepton is selected and requiring isolation, after the missing energy cut, and after the full selection. Across all lepton channels and stages of selection, the side-band fit predicts values between 73% to 129% of the direct estimates in the signal region under the Z peak. The majority of fit estimates fall within 20% of the direct estimate, and thus a 20% systematic uncertainty is assigned due to the choice of fit function and fit range.

The final $t\bar{t}$ estimates using the side-band method, calculated from the sample after all selection except the Z mass window criteria, can be found in Table 6.17. Both

the statistical and systematics uncertainties are shown. The estimates are dominated by statistical uncertainty due to the low statistics in the sidebands of the Z mass distribution currently available in the data.

Channel	$\mu\mu\mu$	$e\mu\mu$	$ee\mu$	eee
Expected Events	$0.4 \pm 0.5 \pm 0.1$	$0.9 \pm 0.7 \pm 0.3$	$0.8 \pm 0.6 \pm 0.2$	0.2 ± 0.1

Table 6.17: Top background predictions. Estimates for the $\mu\mu\mu$, $e\mu\mu$, and $ee\mu$ channels are taken from data. The estimate for the eee channel is taken from Monte Carlo. The first uncertainty is statistical; the second is from systematic sources.

6.9.4 $W/Z + \gamma$

Leptonic decays of $W^{\pm}$ and Z bosons produced in association with photons can mimic the tri-lepton signature when a photon undergoes a conversion into an electron-positron pair upon interaction with the material of the detector or when a photon is accidentally matched to a track and mis-identified as an electron. Such a final state is different from those in the data-driven methods for backgrounds containing fake leptons because the photon is not necessarily associated to a jet. While a dedicated study for leptons produced from photons would be ideal, this background is expected to be small and control regions in data with adequate statistics are not available. Thus, the $W/Z + \gamma$ is estimated using MC simulations. The estimated background contributions from this process are shown in Table 6.18.

6.10 Summary of Observed and Expected Events

The number of expected and observed events after applying all selection cuts are shown in Table 6.18. A total of 71 $W^{\pm}Z$ candidates events are observed in data with 50.3 signal and 12.1 background events expected.

Both statistical and systematic uncertainties are given in the table for all four tri-lepton channels. The description of the systematic uncertainties can be found in Section 6.12. For each channel and each process, the fractional systematic uncertainties are calculated by combining different sources (Table 6.23) in quadrature and are then applied to the central value to get the final systematic uncertainty, except for the data driven estimates of the W/Z+jets background and $t\bar{t}$ background. The systematic for $t\bar{t}$ is added linearly over channels, as the systematic comes from the same course (i.e. uncertainty on the closure of the method). The systematics for the W/Z+jets estimates with a $W \to \mu\nu$ are summed linearly since the uncertainties for the muon fakes are correlated in both channels. The same applies to the estimates in the channels with a $W \to e\nu$. The two sets of W/Z+jets systematic uncertainties are then summed in quadrature, since the uncertainties associated with fake electrons and fake muons are uncorrelated. To be conservative, the systematics for the MC estimates in different channels are treated as correlated and are added linearly. To get the total background systematic, the MC uncertainties are summed in quadrature with the systematics from the W/Z+jets and $t\bar{t}$ backgrounds. It should be noted that this summing of the systematics is not used for the uncertainty estimates in the cross section fit. The fit procedure accounts for the full granularity and correlation

of systematic sources across the different channels, as described in Section 6.13.4.

Final State	eee	$ee\mu$	$e\mu\mu$	$\mu\mu\mu$	Combined
Observed	11	9	22	29	71
ZZ	0.4±0.0±0.0	1.0±0.1±0.1	0.8±0.1±0.0	1.7±0.1±0.1	3.9±0.1±0.2
W/Z+jets	$2.0\pm0.5^{+0.7}_{-0.7}$	$0.7\pm0.3^{+1.1}_{-0.4}$	$1.7\pm0.5^{+0.6}_{-0.6}$	$0.4\pm0.3^{+1.6}_{-0.3}$	$4.8\pm0.8^{+4.0}_{-1.9}$
Top	0.2±0.1±0.0	0.8±0.6±0.2	0.9±0.7±0.3	0.4±0.5±0.1	2.3±1.0±0.5
$W/Z+\gamma$	0.5±0.3±0.0	–	0.6±0.4±0.0	–	1.1±0.5±0.1
Bkg (total)	$3.1\pm0.6^{+0.7}_{-0.7}$	$2.5\pm0.7^{+1.2}_{-0.4}$	$3.9\pm0.9^{+0.6}_{-0.6}$	$2.6\pm0.6^{+1.6}_{-0.3}$	$12.1\pm1.4^{+4.1}_{-2.0}$
Expected signal	7.7±0.2±0.8	11.6±0.2±1.0	12.4±0.2±1.1	18.6±0.3±1.5	50.3±0.4±4.3
Expected S/B	2.5	4.7	3.2	7.2	4.2

Table 6.18: Summary of observed events and expected signal and background contributions in the four tri-lepton and combined channels. The W/Z+jets background and top quark background ($ee\mu$,$e\mu\mu$ and $\mu\mu\mu$ channel) are estimated using data-driven methods. The other predictions come from MC events. All the numbers are calculated with 3 but rounded up to 2 decimal places, and the first error is statistical while the second is systematic.

6.11 Signal Sample Distributions

Figure 6.18 shows the dilepton invariant mass of events before the Z mass requirement, as well as the Z rapidity distributions for events passing the 10 GeV Z mass window cut. For selected Z events (within the 10 GeV Z mass window cut) The leading lepton p_T, ϕ, and η are shown in Figure 6.19, while the E_T^{miss}, the number of vertices, and the number of leptons distributions are plotted in Figure 6.20.

The kinematic distributions for inclusive $W^{\pm}Z$ candidate events are plotted in Figure 6.21. The mass of the WZ system is calculated by using the W mass as a constraint. This allows the neutrino p_z to be solved in a quadratic equation. The

lower $|p_z|$ solution to the quadratic equation is chosen, as studies in truth find this to have better resolution that the higher $|p_z|$ solution. In the case the solution is imaginary, only the real part is taken.

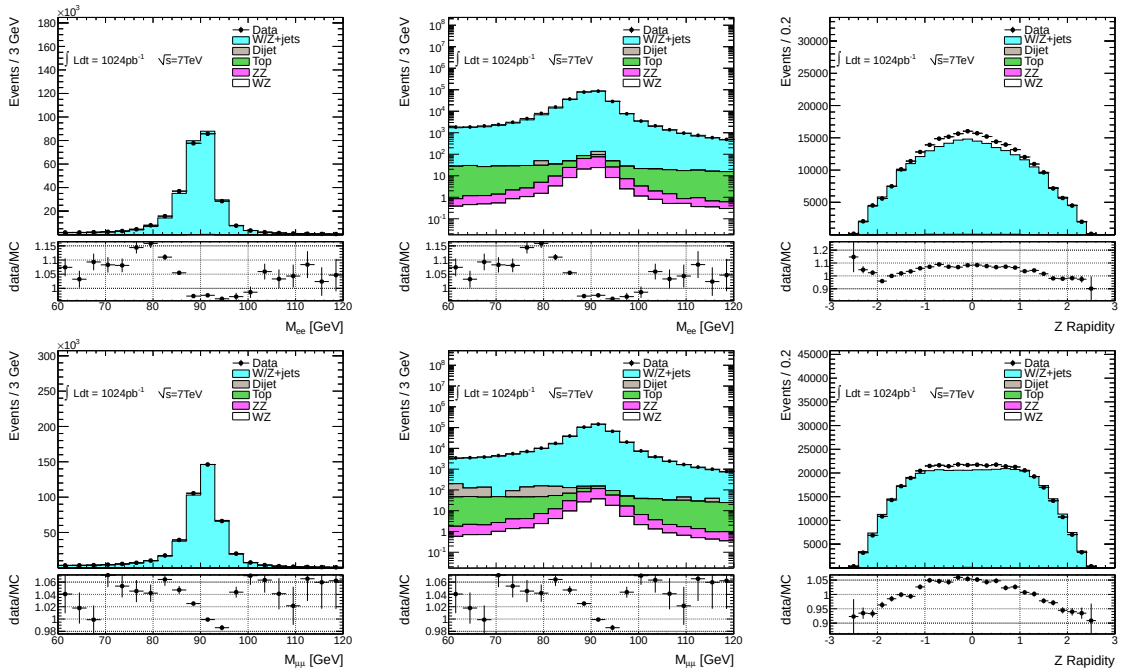

Figure 6.18: Invariant mass of dilepton pairs in linear scale (left) and log scale (middle) before the Z mass cut, as well as the Z rapidity after the Z cut, in the ee (top), $\mu\mu$ (bottom) channels.

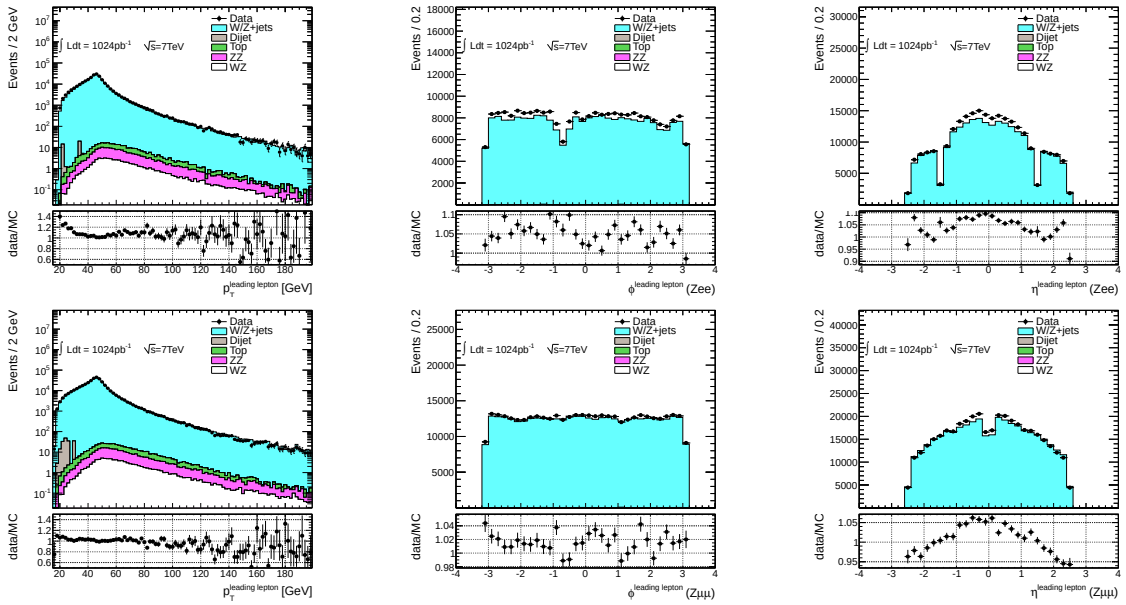

Figure 6.19: Distribution of the p_T (left), ϕ (middle), and η (right) of leading leptons in $Z \to ee$ (top) and $\mu\mu$ (bottom) events passing the 10 GeV mass window cut.

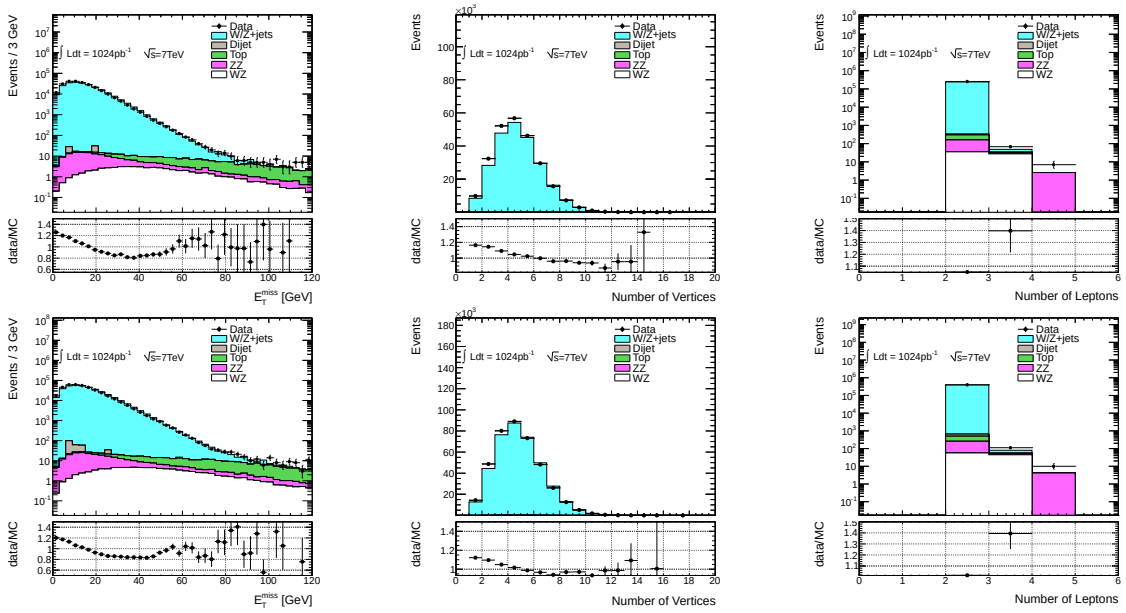

Figure 6.20: Distribution of E_T^{miss} (right), number of vertices (middle), and number of leptons in $Z \to ee$ (top) and $\mu\mu$ (bottom) events passing the 10 GeV mass window cut.

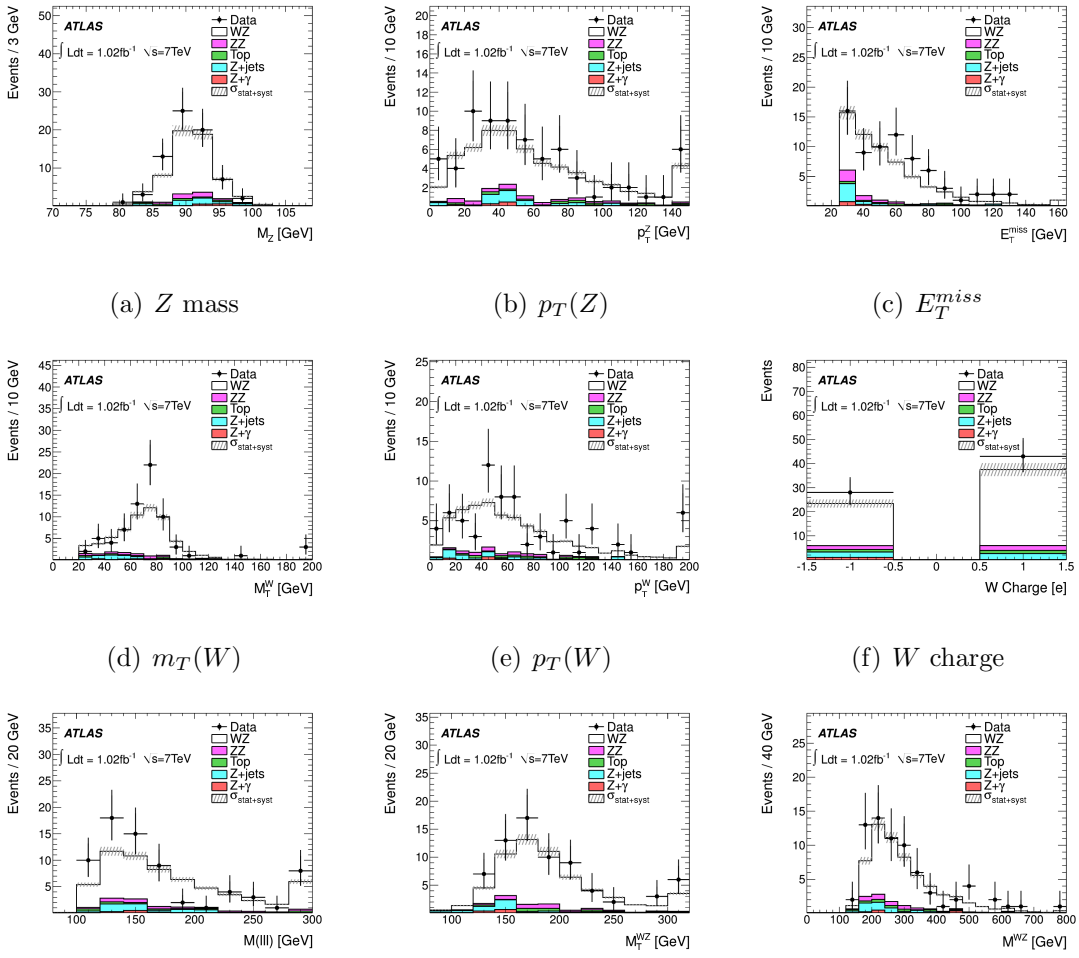

(a) Z mass (b) $p_T(Z)$ (c) E_T^{miss}

(d) $m_T(W)$ (e) $p_T(W)$ (f) W charge

(g) Trilepton invariant mass (h) $W^{\pm}Z$ transverse mass (i) $W^{\pm}Z$ mass

Figure 6.21: Kinematic distributions for inclusive $W^{\pm}Z$ candidate events.

6.12 Systematic Uncertainties

The sources of systematics uncertainties in the analysis come from the uncertainties on the physics object reconstruction efficiencies and resolutions, trigger efficiencies, PDFs, and theoretical cross section normalizations. The systematics for each physics object used in the event reconstruction are calculated separately using the signal samples, but are also used for background uncertainty estimates because sufficient MC background statistics are not available. The effect of the systematic uncertainties on the $W^{\pm}Z$ event predictions are calculated by varying the systematic uncertainty of the underlying source in signal MC and taking the fractional difference between the nominal predicted number of events and predicted number of events with the systematic variation. The only exceptions are the theoretical cross section uncertainty and the PDF/scale uncertainty, for which the calculations are described in the text. For all systematics, the uncertainties of different channels resulting from the same underlying source variation are treated as fully correlated.

The uncertainties from efficiencies and resolutions are used as uncertainties on $W^{\pm}Z$ event selection/reconstruction efficiency (denoted C_{WZ} and described in Section 6.13.1) and on the background normalizations in the cross section extraction. Uncertainties due to PDFs are calculated as uncertainties on the selection efficiency and on the fiducial acceptance, denoted A_{WZ}, which is the fraction of events falling within the acceptance of the detector and selection cuts at the truth level, as described in Section 6.13.2.

Additional systematic uncertainties which are not discussed in detail in this section include the luminosity uncertainty of 3.7%, as described in Section 4.7.3. Uncertainties on the Data-Driven background estimates are discussed in the appropriate parts of Section 6.9. Finally, the uncertainties caused by pileup are accounted for in the electron and muon isolation systematics, and as a systematics in the modeling of the missing energy.

It should be noted that uncertainties from muon and electron scale and resolution uncertainties are discussed in the lepton specific sections and in the E_T^{miss} section. The lepton specific section considers the systematic effect on the selection efficiency, excluding the effect on E_T^{miss}, while the E_T^{miss} section discusses the effect on the missing energy calculation and transverse mass cut. This separation is performed only for technical implementation reasons. Since the underlying source is the same, the uncertainties on lepton scale and resolution from the E_T^{miss} variation are considered fully correlated with the selection efficiency changes. Thus the two uncertainties are added linearly and treated as a single systematic in the likelihood function. While this is a conservative approach, these uncertainties are not dominant and have little effect on the results.

6.12.1 Theoretical Cross Section

The uncertainties on the theoretical total cross section calculations for the signal and background processes can be found in Table 6.19. The uncertainties take into account PDF uncertainties, differences in PDF modeling, renormalization and factorization scale changes, and in some cases experimental measurements. The calculation of

the uncertainty on the $W^{\pm}Z$ cross section can be found in Section 6.3, while the background uncertainty calculations are described in detail in References [35, 43, 47, 9]. These uncertainties are translated into uncertainties on the overall normalizations of MC predictions.

Sample	$W^{\pm}Z$	WW	ZZ	$Z+\gamma$	$t\bar{t}$
Uncertainty [%]	$^{+7.5}_{-4.6}$	$^{+5.5}_{-4.5}$	$^{+5.0}_{-4.1}$	$^{+5.0}_{-5.0}$	$^{+7.0}_{-9.6}$

Table 6.19: Uncertainties on the theoretical cross sections for the signal and background samples used in the analysis [35, 43, 47, 9].

6.12.2 Trigger

The uncertainty on the trigger efficiency is determined by the uncertainties on the trigger scale factors. The uncertainty on the event level trigger scale factors are determined by propagating the uncertainty on the single lepton triggers through the event level scale factor calculation, as described in Section 6.4.1. The uncertainties on the single leptons trigger scale factors are determined by performing the Z tag-and-probe method but varying the lepton selection cuts, the m_{ll} cut, the trigger matching ΔR cut, and by considering uncertainties on the subtracted backgrounds.

The overall uncertainties on the event level scale factors are listed in Table 6.8. The event level scale factor is varied within the uncertainty of $\sim$1% in all channels for each signal MC event, and the fractional change in the predicted number of events from nominal is taken as the trigger systematic. This variation is done for all channels simultaneously in order to be conservative, and thus the trigger uncertainty is considered correlated across all channels.

6.12.3 Muons

The primary sources of uncertainty related to muons come from the reconstruction efficiency and the momentum resolution. A systematic on the muon isolation cut efficiency has also been considered, but is seen to be negligible even when considering the effect of pileup by calculating data/MC isolation efficiency differences as a function of the number of primary vertices in the event.

The differences observed in the muon reconstruction efficiencies between the data and MC are taken into account by weighting the simulation by scale factors. The single lepton reconstruction efficiency scale factor uncertainties are dominated by statistical errors in the Z tag-and-probe method, and are $\sim$1% or less over the full η coverage. The scale factors are varied within their uncertainties and the fractional change in the predicted number of signal MC events from nominal is taken as the systematic uncertainty. The resulting systematic uncertainty per channel can be found in Table 6.20.

The resolution of the muon momentum effects the efficiency for selecting muons as well as the efficiency for passing event selection cuts (such as the Z mass requirement). There is an uncertainty on the muon resolution corrections applied to the MC coming from statistical errors on the Z-pole template smearing method, as well as from uncertainty on the knowledge of the ATLAS material budget and Muon Spectrometer alignment. Therefore, the smearing corrections applied to the ID, MS, and Combined muons are varied within uncertainties, and the fractional change in the predicted number of signal MC events from nominal is taken as the overall system-

atic uncertainty. The resulting systematic uncertainty coming from the ID, MS, and Combined muon resolution uncertainty can be found for each channel in Table 6.20.

The total uncertainty due to muon related systematics is also found in Table 6.20. Each of the systematics are considered independent, and thus the total uncertainty is calculated as the quadrature sum of each of the individual systematics per channel. This total is only provided to give a sense of the overall size of muon related uncertainties, but each systematic is treated separately in the cross section extraction.

Uncertainty per channel (%)		μee	$\mu\mu e$	$\mu\mu\mu$
Rec. efficiency		$^{+0.64}_{-0.64}$	$^{+1.30}_{-1.29}$	$^{+1.95}_{-1.92}$
p_T smearing	ID	0.04	0.35	0.22
	MS	0.17	0.11	0.12
	combination	<0.1	0.2	0.2
Muon isolation		negligible		
Total		0.7	1.4	2.0

Table 6.20: Systematic uncertainties, per channel, coming from muon-related sources.

6.12.4 Electrons

The primary sources of electron related systematics are the uncertainties associated with the electron reconstruction and identification efficiency, energy scale, energy smearing, and calorimeter isolation.

The differences observed in the electron reconstruction and identification efficiencies between the data and MC are taken into account by weighting the simulation by scale factors. The dominant cause of uncertainty of the single electron reconstruction

and identification scale factors is in the background subtraction for the Z tag-and-probe measurements [45], and is 1-2% or less over η range. In addition, there is an uncertainty on the identification efficiency E_T dependent correction, which is on the order of 3% except at very low p_T where it is larger, as seen in Figure 6.9. The scale factors are varied within their quoted uncertainties and the fractional change in the predicted number of signal MC events from nominal is taken as the overall systematic. The signal deviations due to the identification efficiency η-dependent scale-factors and the E_T corrections are added in quadrature to obtain the combined electron identification uncertainty. This is then added in quadrature with the derived uncertainty due to the electron reconstruction efficiency to obtain the total electron efficiency uncertainty, which can be found in Table 6.21.

The electron energy scale is calibrated and checked in data and MC using $Z \to ee$ events by studying the position of the Z mass peak. The dominant uncertainties on the energy scale come from the modeling of the material in ATLAS and the calibration of the EM calorimeter presampler energy scale, as well as several other smaller contributions [45]. The systematic uncertainty on the $W^{\pm}Z$ selection efficiency and background predictions are then determined by varying the electron energy scale within the quoted uncertainties and observing the fractional change in the predicted number of signal MC events from nominal. The resulting uncertainty can be found in Table 6.21.

As in the muon case, the electron resolution is corrected in MC in order to match the observed data. The uncertainty on the electron resolution corrections applied to the

MC are dominated by the uncertainty on the resolution sampling term (which is held fixed in the Z-pole resolution smearing method). The smearing corrections applied to MC are varied within uncertainties, and the fractional change in the predicted number of signal MC events from nominal is taken as the overall systematic uncertainty. The resulting systematic uncertainty can be found for each channel in Table 6.21.

The uncertainty on the efficiency of the electron calorimeter isolation requirement is conservatively estimated by summing three components in quadrature. This includes differences between data and MC when measuring the isolation efficiency using Z tag-and-probe, differences between data and MC in W events, and uncertainties on the isolation pileup correction. The electron isolation efficiency is varied within uncertainties, and the fractional change in the predicted number of signal MC events from nominal is taken as the overall systematic uncertainty. The resulting systematic uncertainty can be found for each channel in Table 6.21.

The total uncertainty due to electron related systematics is also found in Table 6.21. Each of the systematics is considered independent, and thus the total uncertainty is calculated as the quadrature sum of each of the individual systematics per channel. This total is only provided to give a sense of the overall size of uncertainties, but each systematic is treated separately in the cross section extraction.

6.12.5 Missing Transverse Energy

Since the E_T^{miss} in this analysis is built from other reconstructed objects, the uncertainties on those objects can be propagated to the E_T^{miss} in a straightforward way,

Source	eee	$ee\mu$	$e\mu\mu$
Energy scale	0.4	0.3	0.2
Energy smearing	0.2	0.15	0.1
Efficiency	5.2	3.5	1.8
Calorimeter isolation	3.4	2.9	2.4
Total	6.2	4.6	3.0

Table 6.21: Summary of electron reconstruction systematic uncertainties (%).

as described in detail in Reference [34]. For example, the uncertainty due to the jet energy scale on the E_T^{miss} is calculated by varying the energy scale of the jets and recalculating the E_T^{miss}. This recalculation of the missing energy will affect the efficiency of the E_T^{miss} and M_T cuts, and thus contributes to the uncertainty on the signal selection efficiency and the background normalizations. The E_T^{miss} systematics are calculated by varying the uncertainties of the underlying objects in signal MC, and calculating the fractional change in the expected number of events from the nominal. The main sources of E_T^{miss} uncertainty are,

- The uncertainty on the muon energy scale and resolution
- The uncertainty on the electron energy scale and resolution
- The uncertainty on the jet energy scale
- The uncertainty on the topo cluster energy scale in the *Cellout* term.
- The description of pileup in the MC

For the electrons and muons, the method of propagating uncertainty is the same as described in the electron and muon specific systematic uncertainty sections. The jet

energy scale uncertainties are derived from MC and from dijet/Z+jet balance studies, and the jet contributions to the E_T^{miss} are varied within the uncertainty to calculate the effect on the E_T^{miss}.

For the uncertainty on the *CellOut* term, the topo-cluster energy scales are varied within uncertainties as a function of the cluster p_T and η. Specifically, each cluster is multiplied by $1 \pm a \times (1 + b/p_T)$, where is $a = 3\%(10\%)$ for $\eta < (>)3.2$ and $b = 1.2$ [34]. While this may result in a large uncertainty on the *CellOut* term, this term is only a small contribution to the overall E_T^{miss} calculation and thus results in a small overall uncertainty for the $W^{\pm}Z$ analysis.

Pileup introduces additional energy into the calorimeter in each event and thus affects the resolution. Differences in pileup between the MC modeling and the data could lead to difference in the selection efficiency. The modeling of pileup in MC is studied by comparing Z data and MC samples which simulate the pileup conditions. The dominant effect is on the jet, *CellOut*, and tau terms in the E_T^{miss}. The systematic uncertainty on the description of in-time pileup is determined by varying these terms up and down by 3%. The out-of-time pileup uncertainty is determined by smearing the E_T^{miss} by 5 GeV in 33% of the MC events. This is due to the poor simulation of bunches early in the train (corresponding to 33% of the bunches), and a smearing of 5 GeV covers the difference.

Table 6.22 summarizes the E_T^{miss} systematic uncertainties on the $W^{\pm}Z$ selection efficiency and the MC background prediction due to the sources considered.

Source	eee	$ee\mu$	$e\mu\mu$	$\mu\mu\mu$
Topo cluster energy scale	0.76	0.91	0.51	0.20
Electron energy scale	0.23	0.17	0.37	0.0
Electron energy resolution	0.99	0.17	0.46	0.0
Jet energy scale	0.41	0.18	0.23	0.38
Muon energy scale	0.0	0.28	0.11	0.04
Muon smearing uncertainty (ID)	0.0	0.06	0.09	0.11
Muon smearing uncertainty (MS)	0.0	0.21	0.30	0.12
In-time pileup uncertainty	0.48	0.37	0.21	0.25
Out-of-time pileup uncertainty	1.31	0.21	0.54	0.23

Table 6.22: Summary of E_T^{miss} systematic uncertainties (%).

6.12.6 PDF and Scale

The calculation of the total cross section takes into account the fiducial acceptance due to phase-space requirements on the MC simulations, as described in Section 6.13. The central value of the fiducial acceptance, A_{WZ}, is calculated based on events generated with MCFM using the CTEQ 6.6 NLO parton distribution function (PDF) and the corresponding ATLAS MC10 tune. The calculation of the acceptance uncertainties is itemized below:

- The uncertainty within the CTEQ 6.6 PDF set is obtained by varying the PDF within the 44 error eigenvector sets, as described in the CTEQ manual. A symmetric uncertainty is evaluated by averaging positive and negative uncertainties.

$$\sigma^+ = \sigma^- = \frac{\sqrt{\sum_{i=1}^{n}[max(A_i - A_{WZ}, 0)]^2} + \sqrt{\sum_{i=1}^{n}[max(A_{WZ} - A_i, 0)]^2}}{2A_{WZ}}, \quad (6.16)$$

  where A_{WZ} is the WZ acceptance evaluated at the central value of CTEQ 6.6. The acceptance of the other PDF sets is evaluated by applying event-by-event PDF re-weighting to the WZ signal samples.

- The uncertainty between different PDF sets is estimated by comparing CTEQ6.6 to the central MSTW2008 NLO 68% CL PDF set.

The uncertainty calculated from the 44 CTEQ6.6 error eigenvectors is ∼0.8%, and the central value deviation from MSTW2008 NLO is ∼1.1%. The uncertainty due to the statistics of the sample is about 0.6%. The combined systematic uncertainty with quadratic sum is 1.5%, which is taken as the PDF uncertainty for A_{WZ}.

6.12.7 Summary of Systematics

A summary of the systematic uncertainties used as input for the cross section measurement and the aTGC analysis can be found in Table 6.23. These uncertainties have been calculated using the signal MC sample, and the same (relative) uncertainties are assigned to the corresponding MC background processes.

Source	$\mu\mu\mu$	$e\mu\mu$	$ee\mu$	eee
μ reconstruction efficiency	1.9	1.3	0.6	-
μ p_T smearing	0.2	0.2	<0.1	-
e reconstruction efficiency	-	1.8	3.5	5.2
e energy scale	-	0.2	0.3	0.4
e energy smearing	-	0.1	0.15	0.2
calorimeter isolation	-	2.4	2.9	3.4
E_T^{miss}: cluster energy scale	0.20	0.51	0.91	0.76
E_T^{miss}: electron energy scale	0.0	0.37	0.17	0.23
E_T^{miss}: electron energy resolution	0.0	0.46	0.17	0.99
E_T^{miss}: jet energy scale	0.38	0.23	0.18	0.41
E_T^{miss}: muon energy scale	0.04	0.11	0.28	0.0
E_T^{miss}: muon smearing uncertainty (ID)	0.11	0.09	0.06	0.0
E_T^{miss}: muon smearing uncertainty (MS)	0.12	0.30	0.21	0.0
E_T^{miss}: in-time pileup	0.25	0.21	0.37	0.48
E_T^{miss}: out-of-time pileup	0.23	0.54	0.21	1.31
Trigger	1.0	1.0	1.0	1.0
PDF	1.51	1.51	1.51	1.51
Luminosity	3.7	3.7	3.7	3.7

Table 6.23: Summary of all relative acceptance uncertainties (%).

6.13 Cross Section Measurement

The total inclusive cross section is calculated by taking the number of observed events, correcting for the efficiency that an event is reconstructed, and then extrapolating to the full phase space of events which includes events outside of the detector and selection acceptance. The efficiency correction is measured relative to a *fiducial volume*. This fiducial volume requires that the physics objects fell inside the detector acceptance as well as requirements on lepton momentum, the Z mass, and the W transverse mass. Thus the efficiency correction, called the *fiducial efficiency*, corrects the number of observed events to the number of events produced within the fiducial volume. Then the extrapolation to the total phase is performed from the number of events produced within the fiducial volume to the total number of events produced. The reason to perform the extrapolation in this way is that the theoretical uncertainties on the measurement primarily affect the extrapolation from the fiducial volume to the full acceptance. In order to avoid the theoretical errors from the extrapolation to the full phase space, a *fiducial cross section* is also measured only within the fiducial volume.

The fiducial volume, defined using the same cuts on truth level objects in all channels, is,

- $p_T^{\ell} > 15\,\text{GeV}$ for the two charged leptons from the Z decay
- $p_T^{\ell} > 20\,\text{GeV}$ for the charged lepton from the W decay
- $|\eta^{\ell}| < 2.5$ for the three charged leptons

- $p_T^{\nu} > 25\,\text{GeV}$ for the neutrino
- $|m_{\ell\ell} - m_Z| < 10\,\text{GeV}$ for the Z candidate
- $m_T^W > 20\,\text{GeV}$ for the W candidate

The leptons used in the fiducial definition include only muons and electrons produced directly from W and Z decays, and thus decays of taus to electrons and muons are not included. It should be noted that for truth object selection, *dressed* final state leptons (electrons and muons) are used. A dressed final state lepton has all photons within $\Delta R < 0.1$ added to the Lorentz vector of the lepton. This dressing is performed so that the final state leptons are physically well-defined, and so that the dependence on the modeling of soft and collinear photon radiation from the leptons is minimized.

For a given $W^{\pm}Z \to l\nu l'l'$ channel, where $l, l' \in \{e, \mu\}$, the fiducial cross section is calculated as

$$\sigma_{WZ}^{fid} \times BR\{WZ \to l\nu l'l'\} = \sigma_{WZ\to l\nu l'l'}^{fid} = \frac{N_{l\nu l'l'}^{obs} - N_{l\nu l'l'}^{bkg}}{\mathcal{L} \times C_{WZ\to l\nu l'l'}} \tag{6.17}$$

where $N_{l\nu l'l'}^{obs}$ and $N_{l\nu l'l'}^{bkg}$ denote the number of observed and background events respectively, $\mathcal{L}$ is the luminosity and $C_{WZ\to l\nu l'l'}$ is the fiducial efficiency correction factor (discussed in detail in Section 6.13.1), and $BR\{WZ \to l\nu l'l'\}$ is the branching ratio for a W to decay to $l\nu$ and a Z to decay to $l'l'$. Since the fiducial volume is defined by the leptonic kinematics, the fiducial cross section is calculated specifically for leptonic decays of $W^{\pm}Z$ and therefore must include the branching ratio.

The cross section in the total phase space volume in each channel is calculated as,

$$\sigma_{WZ}^{tot} = \frac{N_{l\nu l'l'}^{obs} - N_{l\nu l'l'}^{bkg}}{\mathcal{L} \times BR\{WZ \to l\nu l'l'\} \times A_{WZ\to l\nu l'l'} \times C_{WZ\to l\nu l'l'}} \tag{6.18}$$

where $A_{WZ\to l\nu l'l'}$ is the factor which extrapolates from the fiducial volume to the total phase space, and will be discussed in detail in Section 6.13.2.

In practice, a maximum likelihood (ML) approach is used to calculate both the single channel and combined cross section, as discussed in detail in Section 6.13.4. This approach takes into account the Poisson statistics of the samples, and easily allows the inclusion of the $W^{\pm}Z \to \tau + X$ contribution when either the W or the Z decay includes a tau that subsequently decays to an electron or muon.

It should be noted that the systematic uncertainties in Section 6.12 are calculated by varying an underlying systematic source in the signal MC and calculating the difference in the number of predicted events, ΔN_{WZ}^{MC}, between the prediction with the systematic variation and the nominal prediction of N_{WZ}^{MC}. This fractional change in event predictions due to experimental uncertainties translates into a C_{WZ} uncertainty because,

$$\begin{aligned}\frac{\Delta N_{WZ}^{MC}}{N_{WZ}^{MC}} &= \frac{\Delta\left(\sigma_{WZ}\times A_{WZ}\times C_{WZ}\times\mathcal{L}\right)}{\sigma_{WZ}\times A_{WZ}\times C_{WZ}\times\mathcal{L}} = \frac{(\Delta C_{WZ})\times[\sigma_{WZ}\times A_{WZ}\times\mathcal{L}]}{C_{WZ}\times[\sigma_{WZ}\times A_{WZ}\times\mathcal{L}]} \\ &= \frac{\Delta C_{WZ}}{C_{WZ}}\end{aligned}$$

where the second equality holds because the experimental uncertainties (excluding the luminosity and Data-Driven background uncertainties) only affect the C_{WZ} calculation.

6.13.1 Fiducial Efficiency

The primary purpose of the fiducial efficiency is to correct the reconstructed level event count to a truth level event count defined in a fiducial volume roughly corresponding to the detector and selection acceptance. The reason to only correct to a fiducial volume in this way is that this correction will be less sensitive to theoretical errors (such as PDF uncertainties). This correction essentially gives the probability of reconstructing an event, given that all the objects in the event would have been in the detector and passed the selection level cuts.

The fiducial efficiency correction term is calculated as,

$$C_{WZ\to l\nu l'l'} = \epsilon_{trig} \times \epsilon_{event} \times \epsilon_{lep} \times \alpha_{reco} \tag{6.19}$$

where ϵ_{trig} is the trigger efficiency, ϵ_{event} is the efficiency of the event level cuts (such as the primary vertex cut, etc.), $\epsilon_{lep} = \epsilon_{lep2}\epsilon_{lep2}\epsilon_{lep3}$ is the product of the individual efficiencies for the three leptons to pass the lepton object selection cuts, and finally α_{reco} is the reconstruction to generator level fiducial volume correction which also includes smearing corrections and resolutions. In practice, C_{WZ} can be calculated by applying the necessary corrections to the signal $W^{\pm}Z \to l\nu ll$ MC sample(such as smearing, pileup re-weighting, reconstruction scale factors, etc.) and taking the ratio of the number of events which pass the reconstruction level cuts to the number of events which pass the fiducial volume cuts at the generator level. Thus,

$$C_{WZ\to l\nu l'l'} = \frac{N^{\text{MC Pass All Cuts}}_{\text{Reconstructed } WZ\to l\nu l'l'} \times \text{SF}}{N^{\text{MC Fiducial Volume}}_{\text{Generated } WZ\to l\nu l'l'}} \tag{6.20}$$

where the scale factor is understood to be applied on an event-by-event level. The scale factor (SF) is used to correct for discrepancies in trigger efficiency and recon-

struction efficiency between data and MC, and is defined as

$$SF = \frac{\epsilon_{trig}^{data}}{\epsilon_{trig}^{MC}} \cdot \frac{\epsilon_{reco}^{data}}{\epsilon_{reco}^{MC}} \tag{6.21}$$

with $\epsilon_{reco} = \epsilon_{lep} \cdot \epsilon_{event}$. The fiducial efficiency is calculated for each $W^{\pm}Z \to l\nu l'l'$ decay channel separately, and branching ratios are needed to combine channels and obtain a total cross section.

6.13.2 Total Acceptance

In order to calculate a total inclusive cross section, the reconstruction level cross section must be corrected to the full phase space of possible truth level quantities. This is performed after the fiducial efficiency correction by applying an extrapolation from the truth level fiducial volume to the full phase space of truth. This correction, called the *fiducial acceptance*, is calculated as the ratio of fiducial to total cross section as calculated for a given generator. This cross section ratio is calculated at NLO using MCFM with PDF set CTEQ6.6. However, MCFM only provides calculations at the parton level without showering, photon FSR, and lepton redressing. The MCFM fiducial acceptance is corrected to include these effects using MC@NLO, which can calculate both the parton level and showered level (include photon FSR and lepton redressing) fiducial acceptance. The correction is calculated as the ratio of the fiducial acceptance after showering to the fiducial acceptance at the parton level. In practice, the MC@NLO fiducial acceptance is calculated by taking the ratio of event passing the fiducial volume cuts (which, using the truth information, can be applied at the parton level or after showering/photon radiation/lepton redressing) to the total number of

generated events,

$$A^{MC@NLO}_{WZ\to l\nu l'l'} = \frac{N^{\text{MC Fiducial Volume}}_{\text{Generated } WZ\to l\nu l'l'}}{N^{\text{MC All}}_{\text{Generated } WZ\to l\nu l'l'}} \tag{6.22}$$

The fiducial acceptance, including the MC@NLO correction, is calculated as,

$$A_{WZ\to l\nu l'l'} = A^{MCFM,\ parton}_{WZ\to l\nu l'l'} \frac{A^{MC@NLO,\ showered}_{WZ\to l\nu l'l'}}{A^{MC@NLO,\ parton}_{WZ\to l\nu l'l'}} \tag{6.23}$$

Again, $A_{WZ\to l\nu l'l'}$ is calculated for each channel separately. Using this definition, the fiducial acceptance is calculated at NLO to be 0.342± 0.006, where the uncertainty arises from the statistical error due to the sample size in the MCFM integration (0.6%) and parton distribution function uncertainty (1.5%). Consequently, theoretical uncertainties will primarily affect $A_{WZ\to l\nu l'l'}$ and only lead to small uncertainties on $C_{WZ\to l\nu l'l'}$. The total acceptance correction from reconstruction level to the total phase space is then the product $A_{WZ\to l\nu l'l'} \times C_{WZ\to l\nu l'l'}$.

6.13.3 Acceptance Values

The calculated values of $A_{WZ\to l\nu l'l'}$ and $C_{WZ\to l\nu l'l'}$, are summarized in Table 6.24. The A_{WZ} values have been cross checked with the `POWHEG BOX` generator [93] and differences are found to be $\sim 1\%$.

	$\mu\mu\mu$	$e\mu\mu$	$ee\mu$	eee
C_{WZ}	0.816	0.545	0.502	0.343
A_{WZ}	0.342	0.342	0.342	0.342
$A_{WZ} \times C_{WZ}$	0.279	0.187	0.172	0.117

Table 6.24: Fiducial and total acceptance corrections per channel.

6.13.4 Cross Section Extraction

The cross section is calculated by building a likelihood function and determining the cross section which maximizes the likelihood function. The benefit of this method is that combining estimates from different channels is simple; each channel is treated as a measurement of the cross section and the total likelihood is the product of the individual channel probabilities. In this way, the likelihood function takes into account all channel measurements and ensures that the calculated cross section is the best value that is consistent between channels. Additionally, the likelihood formalism allows systematic uncertainties to be easily incorporated using nuisance parameters. Correlations between channel measurements are incorporated by having the same nuisance parameter control a systematic affect for all correlated channels.

In practice, the likelihood values can be quite small. In addition, several well tested computational minimization packages are available. Thus the negative of the logarithm of the likelihood function is calculated and then minimized. As this transformation is monotonic, negative log-likelihood minimization is equivalent to likelihood maximization.

The negative log-likelihood function for a cross section measurement is calculated as,

$$-\log\, L(\sigma,\{x_k\}) = -\log\left(\prod_{i=1}^{4} \frac{e^{-(N_s^i(\sigma,\{x_k\})+N_b^i(\{x_k\}))} \times (N_s^i(\sigma,\{x_k\})+N_b^i(\{x_k\}))^{N_{obs}^i}}{(N_{obs}^i)!}\right) + \sum_{k=1}^{n} \frac{x_k^2}{2} \tag{6.24}$$

where N_{obs}^i is the number of events observed after full selection in channel i, $x_k \sim N(0,1)$ is a nuisance parameter constrained by a normal distribution with zero mean

and unit variance, and

$$N_b^i(\{x_k\}) = N_b^i \prod_{k=1}^{n}(1 + x_k B_k^i) \tag{6.25}$$

where N_b^i is the number of background events predicted in channel i and B_k^i is the standard deviation representing the k^{th} (fractional) systematic uncertainty for the background in channel i. For the fiducial cross section measurement $\sigma \equiv \sigma^{fid}_{WZ\to l\nu l'l'}$ and

$$N_s^i(\sigma^{fid}_{WZ\to l\nu l'l'}, \{x_k\}) = \frac{\sigma^{fid}_{WZ\to l\nu l'l'}}{\sigma^{tot}_{MC,\ WZ\to l\nu l'l'} \times A_{WZ\to l\nu l'l'}} \times \left(N^{MC}_{WZ\to l\nu l'l'} + N^{MC}_{WZ\to \tau+X}\right) \times \prod_{k=1}^{n}(1+x_k S_k^i) \tag{6.26}$$

While for the total cross section measurement $\sigma \equiv \sigma^{tot}_{WZ}$ and

$$N_s^i(\sigma^{tot}_{WZ}, \{x_k\}) = \frac{\sigma^{tot}_{WZ}}{\sigma^{tot}_{MC,\ WZ}} \times \left(N^{MC}_{WZ\to l\nu l'l'} + N^{MC}_{WZ\to \tau+X}\right) \times \prod_{k=1}^{n}(1 + x_k S_k^i) \tag{6.27}$$

where S_k^i is the standard deviation representing the k^{th} (fractional) systematic uncertainty for the signal in channel i. In equations 6.26 and 6.27, the MC is used to determine the total number of events expected in a given channel. This expectation is then scaled by the ratio of the measured cross section to the MC generator cross section used to produce the MC expectations. In this way, the data is used to drive the measurement to find the best rescaling of the expected signal contributions, and thus allows for the extraction of a cross section.

In equation 6.24, the expression inside the logarithm is essentially the Poisson probability that the expected number of signal and background events produce the observed number of events. The final term in the likelihood equation is the product of the Gaussian constraints on the nuisance parameters x_k. These nuisance parameters account for systematic errors and their effect on the number of expected signal and background events in each channel. Each systematic k is ascribed to an independent

source (if two different systematics are correlated, their linear sum is used here as a single systematic). A single variable x_k is used in all channels and in signal and background as the effect of each systematic is 100% correlated across channels and between signal and background. S_k^i and B_k^i are the fractional sizes of the k^{th} systematic in each channel for signal and background respectively. Note that if systematic k^* only affects a single channel, or only signal and not background, only the $S_{k^*}^i$ and $B_{k^*}^i$ which are effected by systematic k^* are non-zero. Furthermore, it should be noted that, as each parameter x_k has a Gaussian constraint, the number of degrees of freedom of the fit is unchanged from a fit without systematic uncertainties.

To find the most probable value of σ (fiducial or total) the log-likelihood function is minimized simultaneously over σ and all the nuisance parameters x_k. This is called the profile likelihood. The value of σ at the log-likelihood minimum is used as the measurement of σ, i.e.

$$\sigma_{measured} = \arg_{\sigma} \min_{\sigma,\{x_k\}} \; -\log L(\sigma, \{x_k\})$$

The errors are estimated by taking the difference of the cross section at the minimum to the cross section where the log-likelihood is 0.5 units above the minimum along the direction of the parameter σ (while the negative log likelihood is minimized over the nuisance parameters for each σ, i.e. the profile likelihood function). This calculation is performed in the positive and negative directions separately, and thus may yield different positive and negative errors. As the nuisance parameters account for the systematic errors, this error is the combined statistical and systematic uncertainty. The minimization and error calculation is performed with the Minuit package [86].

To calculate the cross section (fiducial or total) in only a single channel i, only the Poisson probability in channel i is used rather than the product over all channels. The Gaussian constraint terms are unchanged.

6.13.5 Likelihood Fit Response

To test the linearity of the likelihood fit method, a large numbers of pseudo experiments are performed with the SM $W^{\pm}Z$ cross section scaled by values between 0.7 to 2.5 as the input cross section for producing pseudo experiments. The predicted event yields for each input cross section are Poisson fluctuated to produce pseudo experiments. The fit cross section σ_{ML} is calculated for each pseudo experiment and the distribution of σ_{ML} versus the input cross section σ_{IN} is shown in Figure 6.22. Plotted in red is the average fit value for each input cross section, with the RMS of the fit cross sections as the error. Finally the black line is the fit to the average σ_{ML} for each input cross section, and this fit line has a slope of 0.99 with a intercept of 0.11 pb. The fit response is linear with a slope of approximately 1.

6.13.6 Cross Section Results

The final results for the fiducial and total cross section measurement in each channel and for the combined measurement are shown in Tables 6.25 and 6.26. The systematic uncertainties include all sources except luminosity, which is listed separately.

The full likelihood function with nuisance parameters will automatically take into account all the systematic errors, and propagate them to the final uncertainty. To

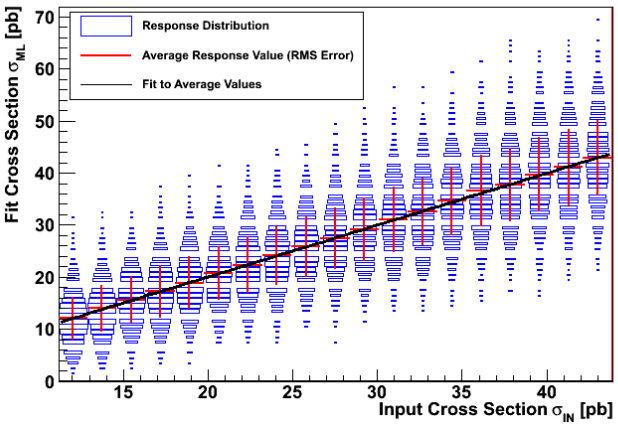

Figure 6.22: Fit cross sections versus the input cross section (blue), average fit cross section for each input cross section with the RMS as the error (red), and a fit to the average fit cross sections (black).

Channel	cross section [fb]
$\mu\mu\mu$	31^{+7}_{-6}(stat) $^{+2}_{-2}$(syst) $^{+1}_{-1}$(lumi)
$e\mu\mu$	31^{+9}_{-7}(stat) $^{+2}_{-2}$(syst) $^{+1}_{-1}$(lumi)
$ee\mu$	12^{+6}_{-5}(stat) $^{+2}_{-2}$(syst) $^{+1}_{0}$(lumi)
eee	22^{+10}_{-8}(stat) $^{+3}_{-3}$(syst) $^{+1}_{-1}$(lumi)
Combined	102^{+15}_{-14}(stat) $^{+7}_{-6}$(syst) $^{+4}_{-4}$(lumi)

Table 6.25: Measured fiducial cross section for each channel and combined.

Channel	cross section [pb]
$\mu\mu\mu$	$24.59^{+5.35}_{-4.64}$(stat) $^{+1.28}_{-1.28}$(syst) $^{+1.00}_{-0.94}$(lumi)
$e\mu\mu$	$25.23^{+6.99}_{-5.92}$(stat) $^{+1.95}_{-1.95}$(syst) $^{+1.04}_{-0.97}$(lumi)
$ee\mu$	$9.73^{+4.93}_{-3.87}$(stat) $^{+1.64}_{-1.62}$(syst) $^{+0.43}_{-0.40}$(lumi)
eee	$17.67^{+8.26}_{-6.57}$(stat) $^{+2.47}_{-2.40}$(syst) $^{+0.78}_{-0.72}$(lumi)
Combined	$20.52^{+3.07}_{-2.77}$(stat) $^{+1.35}_{-1.33}$(syst) $^{+0.85}_{-0.79}$(lumi)

Table 6.26: Measured total cross section for each channel and combined.

understand the contribution from each systematic error separately, each systematic uncertainty is propagated by hand to the acceptance and thus to the final cross section. This is done by adjusting the acceptance of the signal and background in the likelihood function up and down by one sigma, and re-minimizing the likelihood function (without nuisance parameters) to find a new cross section value. Specifically, the following parameters are adjusted: $C_{WZ} \to C_{WZ} \times (1 + \Delta_s)$ where Δ_s is the fractional change in the $W^{\pm}Z \to l\nu l'l'$ estimation, $N_{WZ\to\tau+X} \to N_{WZ\to\tau+X} \times (1 + \Delta_\tau)$ where Δ_τ is the fractional change in the $W^{\pm}Z \to \tau + X$ estimation, and $N_{bkg} \to N_{bkg} \times (1 + \Delta_b)$ where Δ_b is the fractional change in the background estimation. The difference in central cross section value and the cross section obtained after adjusting the acceptance in the likelihood function is taken as the estimate of systematic uncertainty on the cross section.

Systematic uncertainties are determined on the cross section measurement for each source for each channel, and for the combined measurement. The systematic uncertainties on the fiducial and total cross section are summarized in Tables 6.27 and 6.28. All systematic uncertainties are added in quadrature to yield the total uncertainty (denoted "Total (no lumi)"), excluding the luminosity uncertainty.

Source	$\mu\mu\mu$	$e\mu\mu$	$ee\mu$	eee	Combined
μ - reco. efficiency	$^{+2.05}_{-1.99}$	$^{+1.41}_{-1.38}$	$^{+0.69}_{-0.69}$	$^{+0.00}_{0.00}$	$^{+1.32}_{-1.28}$
μ - smear	$^{+0.21}_{-0.21}$	$^{+0.22}_{-0.21}$	$^{+0.11}_{-0.11}$	$^{+0.21}_{-0.21}$	$^{+0.17}_{-0.15}$
e - reco. efficiency	$^{+0.00}_{-0.00}$	$^{+1.97}_{-1.90}$	$^{+4.16}_{-3.87}$	$^{+6.27}_{-5.63}$	$^{+2.11}_{-3.87}$
e - scale	$^{+0.00}_{-0.00}$	$^{+0.22}_{-0.21}$	$^{+0.34}_{-0.34}$	$^{+0.46}_{-0.45}$	$^{+0.19}_{-0.17}$
e - ID	$^{+0.00}_{-0.00}$	$^{+0.11}_{-0.11}$	$^{+0.23}_{-0.23}$	$^{+0.23}_{-0.23}$	$^{+0.11}_{-0.09}$
e - isolation	$^{+0.00}_{-0.00}$	$^{+2.64}_{-2.52}$	$^{+3.43}_{-3.23}$	$^{+4.02}_{-3.75}$	$^{+1.84}_{-1.77}$
E_T^{miss} - cluster	$^{+0.21}_{0.21}$	$^{+0.54}_{-0.53}$	$^{+1.04}_{-1.02}$	$^{+0.92}_{-0.91}$	$^{+0.57}_{-0.54}$
E_T^{miss} - e scale	$^{+0.00}_{-0.00}$	$^{+0.43}_{-0.43}$	$^{+0.23}_{-0.23}$	$^{+0.23}_{-0.23}$	$^{+0.18}_{-0.16}$
E_T^{miss} - e resolution	$^{+0.00}_{-0.00}$	$^{+0.54}_{-0.53}$	$^{+0.23}_{-0.23}$	$^{+1.15}_{-1.13}$	$^{+0.32}_{-0.30}$
E_T^{miss} - μ scale	$^{+0.00}_{-0.00}$	$^{+0.11}_{-0.11}$	$^{+0.34}_{-0.34}$	$^{+0.00}_{-0.00}$	$^{+0.11}_{-0.09}$
E_T^{miss} - μ resolution	$^{+0.21}_{-0.21}$	$^{+0.32}_{-0.32}$	$^{+0.23}_{-0.23}$	$^{+0.00}_{-0.00}$	$^{+0.22}_{-0.20}$
E_T^{miss} - jet	$^{+0.43}_{-0.42}$	$^{+0.22}_{-0.21}$	$^{+0.23}_{-0.23}$	$^{+0.46}_{-0.45}$	$^{+0.34}_{-0.32}$
E_T^{miss} - in pileup	$^{+0.32}_{-0.32}$	$^{+0.22}_{-0.21}$	$^{+0.46}_{-0.46}$	$^{+0.57}_{-0.57}$	$^{+0.37}_{-0.35}$
E_T^{miss} - out pileup	$^{+0.21}_{-0.21}$	$^{+0.54}_{-0.53}$	$^{+0.23}_{-0.23}$	$^{+1.50}_{-1.47}$	$^{+0.45}_{-0.43}$
Trigger	$^{+1.07}_{-1.05}$	$^{+1.08}_{-1.07}$	$^{+1.16}_{-1.14}$	$^{+1.15}_{-1.13}$	$^{+1.10}_{-1.06}$
Bkg cross section	$^{+0.22}_{-0.22}$	$^{+0.27}_{-0.27}$	$^{+0.54}_{-0.54}$	$^{+0.50}_{-0.50}$	$^{+0.31}_{-0.29}$
Data-driven method - Z+jets	$^{+3.45}_{-3.49}$	$^{+3.20}_{-3.21}$	$^{+11.68}_{-11.60}$	$^{+8.50}_{-8.47}$	$^{+4.71}_{-4.66}$
Data-driven method - top	$^{+0.38}_{-0.38}$	$^{+1.43}_{-1.44}$	$^{+2.28}_{-2.29}$	$^{+0.00}_{-0.00}$	$^{+0.85}_{-0.83}$
Signal stat. (MC)	$^{+1.47}_{-1.43}$	$^{+1.80}_{-1.74}$	$^{+1.74}_{-1.68}$	$^{+2.26}_{-2.16}$	$^{+0.85}_{-0.89}$
Bkg stat. (MC)	$^{+0.30}_{-0.30}$	$^{+2.18}_{-2.18}$	$^{+0.91}_{-0.92}$	$^{+3.86}_{-3.85}$	$^{+0.80}_{-0.86}$
Bkg stat. (data-driven)	$^{+2.18}_{-2.20}$	$^{+4.71}_{-4.75}$	$^{+10.14}_{-10.08}$	$^{+6.22}_{-6.21}$	$^{+2.14}_{-2.28}$
Total (no lumi)	$^{+4.99}_{-4.99}$	$^{+7.61}_{-7.56}$	$^{+16.77}_{-16.56}$	$^{+13.90}_{-13.50}$	$^{+6.39}_{-6.34}$

Table 6.27: Relative systematic uncertainties (%) on the fiducial cross section for each channel and combined.

Source	$\mu\mu\mu$	$e\mu\mu$	$ee\mu$	eee	Combined
μ - reco. efficiency	$^{+2.05}_{-1.99}$	$^{+1.41}_{-1.38}$	$^{+0.69}_{-0.68}$	$^{+0.00}_{0.00}$	$^{+1.32}_{-1.28}$
μ - smear	$^{+0.21}_{-0.21}$	$^{+0.22}_{-0.21}$	$^{+0.11}_{-0.11}$	$^{+0.21}_{-0.21}$	$^{+0.17}_{-0.15}$
e - reco. efficiency	$^{+0.00}_{-0.00}$	$^{+1.97}_{-1.90}$	$^{+4.17}_{-3.87}$	$^{+6.27}_{-5.63}$	$^{+2.11}_{-3.87}$
e - scale	$^{+0.00}_{-0.00}$	$^{+0.22}_{-0.21}$	$^{+0.34}_{-0.34}$	$^{+0.46}_{-0.45}$	$^{+0.19}_{-0.17}$
e - ID	$^{+0.00}_{-0.00}$	$^{+0.11}_{-0.11}$	$^{+0.23}_{-0.23}$	$^{+0.23}_{-0.23}$	$^{+0.11}_{-0.09}$
e - isolation	$^{+0.00}_{-0.00}$	$^{+2.64}_{-2.52}$	$^{+3.43}_{-3.23}$	$^{+4.02}_{-3.75}$	$^{+1.84}_{-1.77}$
E_T^{miss} - cluster	$^{+0.21}_{0.21}$	$^{+0.54}_{-0.53}$	$^{+1.04}_{-1.02}$	$^{+0.92}_{-0.91}$	$^{+0.57}_{-0.54}$
E_T^{miss} - e scale	$^{+0.00}_{-0.00}$	$^{+0.43}_{-0.43}$	$^{+0.23}_{-0.23}$	$^{+0.23}_{-0.23}$	$^{+0.18}_{-0.16}$
E_T^{miss} - e resolution	$^{+0.00}_{-0.00}$	$^{+0.54}_{-0.53}$	$^{+0.23}_{-0.23}$	$^{+1.15}_{-1.13}$	$^{+0.32}_{-0.30}$
E_T^{miss} - μ scale	$^{+0.00}_{-0.00}$	$^{+0.11}_{-0.11}$	$^{+0.34}_{-0.34}$	$^{+0.00}_{-0.00}$	$^{+0.11}_{-0.09}$
E_T^{miss} - μ resolution	$^{+0.21}_{-0.21}$	$^{+0.32}_{-0.32}$	$^{+0.23}_{-0.23}$	$^{+0.00}_{-0.00}$	$^{+0.22}_{-0.20}$
E_T^{miss} - jet	$^{+0.43}_{-0.42}$	$^{+0.22}_{-0.21}$	$^{+0.23}_{-0.23}$	$^{+0.46}_{-0.45}$	$^{+0.34}_{-0.32}$
E_T^{miss} - in pileup	$^{+0.32}_{-0.32}$	$^{+0.22}_{-0.21}$	$^{+0.46}_{-0.46}$	$^{+0.57}_{-0.57}$	$^{+0.37}_{-0.34}$
E_T^{miss} - out pileup	$^{+0.21}_{-0.21}$	$^{+0.54}_{-0.53}$	$^{+0.23}_{-0.23}$	$^{+1.50}_{-1.46}$	$^{+0.45}_{-0.43}$
Trigger	$^{+1.07}_{-1.05}$	$^{+1.08}_{-1.07}$	$^{+1.16}_{-1.13}$	$^{+1.15}_{-1.13}$	$^{+1.10}_{-1.06}$
PDF	$^{+1.52}_{-1.48}$	$^{+1.52}_{-1.48}$	$^{+1.51}_{-1.47}$	$^{+1.52}_{-1.48}$	$^{+1.52}_{-1.46}$
Bkg cross section	$^{+0.22}_{-0.22}$	$^{+0.27}_{-0.27}$	$^{+0.54}_{-0.54}$	$^{+0.50}_{-0.50}$	$^{+0.31}_{-0.29}$
Data-driven method - Z+jets	$^{+3.44}_{-3.50}$	$^{+3.19}_{-3.21}$	$^{+11.66}_{-11.60}$	$^{+8.48}_{-8.48}$	$^{+4.71}_{-4.66}$
Data-driven method - top	$^{+0.38}_{-0.38}$	$^{+1.43}_{-1.44}$	$^{+2.28}_{-2.28}$	$^{+0.00}_{-0.00}$	$^{+0.85}_{-0.83}$
Signal stat. (MC)	$^{+1.47}_{-1.43}$	$^{+1.80}_{-1.74}$	$^{+1.74}_{-1.68}$	$^{+2.26}_{-2.16}$	$^{+0.85}_{-0.89}$
Bkg stat. (MC)	$^{+0.30}_{-0.30}$	$^{+2.17}_{-2.18}$	$^{+0.91}_{-0.91}$	$^{+3.86}_{-3.85}$	$^{+0.80}_{-0.86}$
Bkg stat. (data-driven)	$^{+2.18}_{-2.20}$	$^{+4.70}_{-4.76}$	$^{+10.12}_{-10.08}$	$^{+6.22}_{-6.21}$	$^{+2.14}_{-2.28}$
Total (no lumi)	$^{+5.21}_{-5.21}$	$^{+7.75}_{-7.71}$	$^{+16.82}_{-16.63}$	$^{+13.98}_{-13.59}$	$^{+6.56}_{-6.50}$

Table 6.28: Relative systematic uncertainties (%) on the total cross section for each channel and combined.

6.14 Anomalous Triple Gauge Couplings Analysis

A major effect of aTGC is that the number of expected events could vary significantly from the SM prediction. The consistency between the observed data and MC predications including aTGCs is measured by determining the set of aTGC parameters that could reproduce the observed data at the 95% confidence interval. The determination of the confidence interval is performed with a frequentist approach, often called a Neyman-Construction [97] or a Feldman-Cousins method [73].

The charge and parity conserving aTGC model is used (described in Section 2.3.2). This model has three anomalous coupling parameters: Δg_1^Z, $\Delta\kappa^Z$, and λ^Z. In order to determine the confidence interval, a likelihood function that depends on the aTGC parameters must be built. This is done by using the likelihood function from the cross section analysis, but by predicting the number of events as a function of aTGC parameter rather than as a function of cross section. This prediction of the number of events for any anomalous couplings is done smoothly, using the matrix elements and a reweighting procedure.

6.14.1 Likelihood Function for aTGC Analysis

Since the likelihood function in the cross section extraction translates the fit cross section into an expected number of events and then calculates the associated Poisson probabilities, the same likelihood function can be used for the aTGC analysis by replacing only the formula for the expected number of signal events. The new equation

for the expected number of signal events in each channel i is,

$$N_s^i(\Delta g_1^Z, \Delta\kappa^Z, \lambda^Z, \{x_k\}) = \left[N^{MC}_{WZ\to l\nu l'l'}(\Delta g_1^Z, \Delta\kappa^Z, \lambda^Z) + N^{MC}_{WZ\to\tau+X}(\Delta g_1^Z, \Delta\kappa^Z, \lambda^Z)\right] \times \prod_{k=1}^{n}(1 + x_k S_k^i) \quad (6.28)$$

where $N^{MC}_{WZ\to l\nu l'l'}(\Delta g_1^Z, \Delta\kappa^Z, \lambda^Z)$ and $N^{MC}_{WZ\to\tau+X}(\Delta g_1^Z, \Delta\kappa^Z, \lambda^Z)$ are the number of $W^{\pm}Z$ events predicted with aTGC parameters $(\Delta g_1^Z, \Delta\kappa^Z, \lambda^Z)$ for exclusive e/μ decays and decays including taus, respectively. The parameter S_k^i is the standard deviation representing the k^{th} (fractional) systematic uncertainty for the signal in channel i, and x_k is the nuisance parameter determining the impact of the systematic. In order for this equation to be valid, it is required that $N^{MC}_{WZ\to l\nu l'l'}(\Delta g_1^Z, \Delta\kappa^Z, \lambda^Z)$ and $N^{MC}_{WZ\to\tau+X}(\Delta g_1^Z, \Delta\kappa^Z, \lambda^Z)$ can be predicted for any aTGC parameters, and the systematics S_k^i derived using the SM acceptance and efficiency must be valid in the presence of anomalous couplings. The former issue will be discussed in Section 6.14.2 and the latter in Section 6.14.3.

6.14.2 aTGC Reweighting

Given the Lagrangian of the C and P invariant aTGC model, the most general amplitude for the $W^{\pm}Z$ process at LO in anomalous couplings (i.e. no higher order electroweak corrections) can be written as,

$$\mathcal{A} = \mathcal{A}_0 + \Delta g_1^Z \mathcal{A}_{\Delta g_1^Z} + \Delta\kappa^Z \mathcal{A}_{\Delta\kappa^Z} + \lambda^Z \mathcal{A}_{\lambda^Z} \quad (6.29)$$

where $\mathcal{A}_0$ is the SM amplitude and $\mathcal{A}_{\Delta g_1^Z, \Delta\kappa^Z, \lambda^Z}$ are the amplitudes containing the anomalous vertices associated with Δg_1^Z, $\Delta\kappa^Z$, and λ^Z respectively. The amplitudes are calculated from the corresponding Feynman diagrams, except that the anomalous

coupling parameters have been factored out. This factorization is allowed because the Feynman diagrams are linear in the aTGC parameters. In this form, the amplitudes are only functions of the event kinematics and do not depend on the values of the aTGC parameters. This factorization implies that the amplitudes on the right hand side of equation 6.29 can be calculated for each event without any aTGC dependence and thus the total amplitude for each event with any aTGC parameters is a simple linear combination of precomputed amplitudes.

In the process of generating MC simulations, event weights are determined by the cross section, which is in turn calculated using the square amplitudes. Thus the event weight dependence on the anomalous coupling comes from the squared amplitudes. Therefore, the event weights $w(\Delta g_1^Z, \Delta\kappa^Z, \lambda^Z)$ can be written as

$$\begin{aligned} w(\Delta g_1^Z, \Delta\kappa^Z, \lambda^Z) = w_0 \quad &+ \quad (\Delta g_1^Z)^2 w_1 + (\Delta\kappa^Z)^2 w_2 + (\lambda^Z)^2 w_3 \\ &+ \quad 2\Delta g_1^Z w_4 + 2\Delta\kappa^Z w_5 + 2\lambda^Z w_6 \\ &+ \quad 2\Delta g_1^Z \Delta\kappa^Z w_7 + 2\Delta g_1^Z \lambda^Z w_8 + 2\Delta\kappa^Z \lambda^Z w_9. \end{aligned} \quad (6.30)$$

where w_0 is the SM weight while the others come from anomalous vertices. All the weights w_i are independent of the anomalous couplings and depend only on the initial and final particle kinematics. These 10 weights $\{w_0 \ldots w_9\}$ are calculated in MC generators in the process of producing events, and in the case of MC@NLO 4.0 the values for each event are stored. Thus, it is possible to reweight each event to any set of aTGC parameters by taking the stored weights and multiplying them by the appropriate anomalous couplings using equation 6.30. Since all kinematic information is stored per event, any kinematic distribution can be calculated with

any aTGC parameters.

It is also possible to reweight form factors, which are discussed in Section 2.3.4. The events in the MC signal samples with aTGCs are generated with a cutoff scale Λ_{FF}. This cutoff scale can be changed to a new value Λ'_{FF}, by adjusting the the event weights $\{w_0 \dots w_9\}$. More precisely, for each aTGC parameters Δg_1^Z, $\Delta\kappa^Z$, and λ^Z multiplying a weight, the weight must be multiplied by $(1+\hat{s}/\Lambda_{FF}^2)^2$ to remove the old form factor and divided by $(1+\hat{s}/(\Lambda'_{FF})^2)^2$ to add the new form factor. Thus the event weights must be adjusted to,

$$w_i \to \begin{cases} w_i & \text{for } i = 0 \\ w_i(1+\hat{s}/\Lambda^2)^2/(1+\hat{s}/(\Lambda'_{FF})^2)^2 & \text{for } i = 4,5,6 \\ w_i(1+\hat{s}/\Lambda^2)^4/(1+\hat{s}/(\Lambda'_{FF})^2)^4 & \text{for } i = 1,2,3,7,8,9 \end{cases} \tag{6.31}$$

In order to remove the form factor completely, the new cutoff scale is set to infinity, which implies $(1+\hat{s}/(\Lambda'_{FF})^2)^2 \to 1$.

As discussed in the cross section extraction section, it is necessary to apply some additional corrections to the MC samples in order to calculate the expected number of signal events after reconstruction and selection:

- MC generator weights (+1 or −1) from MC@NLO
- Pile-up weights
- Trigger scale factors
- Reconstruction scale factors

After applying these factors, the expected number of signal events N_s^i is the sum of the event weights for the MC signal events that pass the selection. Since, in a given channel, all events and weights are summed, it is useful to first sum each w_j over events such that $W_j^i = \sum_k (w_j^i)_k$ where k is the MC event, j indicates which weight, and $i = \mu\mu\mu$, $e\mu\mu$, μee, and eee is the channel. Then the expected number of signal events N_s^i is calculated as

$$\begin{aligned} N_s^i(\Delta g_1^Z, \Delta\kappa^Z, \lambda^Z) = W_0^i &+ (\Delta g_1^Z)^2 W_1^i + (\Delta\kappa^Z)^2 W_2^i + (\lambda^Z)^2 W_3^i \\ &+ 2\Delta g_1^Z W_4^i + 2\Delta\kappa^Z W_5^i + 2\lambda^Z W_6^i \\ &+ 2\Delta g_1^Z \Delta\kappa^Z W_7^i + 2\Delta g_1^Z \lambda^Z W_8^i + 2\Delta\kappa^Z \lambda^Z W_9^i \end{aligned} \quad (6.32)$$

Once these coefficients $\{W_j^i\}$ are calculated, calculating the number of expected events with any aTGC parameters is simply a matter of multiplication and addition. Notice that N_s^i has a quadratic dependence on the aTGC parameters. This implies that there could be multiple values of aTGC parameters that could predict the same number of expected events. This further implies that there could potentially be two minima of the likelihood function.

6.14.3 Systematics

One potential issue with the limit setting procedure with the likelihood function is the possibility that the systematic errors depend on the aTGCs. If this is the case, then the systematic uncertainties calculated at the SM point may not be valid for setting limits.

Using the reweighting procedure, the expected signal yields are calculated for various anomalous coupling values (the range of values is chosen to be within the ranges still allowed from previous ATLAS studies for conference results [10]). The expected signal yields are seen to vary by up to a factor of 2 as the aTGC values vary. However, the efficiency C_{WZ} remains largely unchanged, with maximum variations of 4%. Since C_{WZ} is relatively unaffected by the aTGC parameters, the experimental systematic uncertainties on C_{WZ} evaluated for the SM can be used in the aTGC limit setting.

The theoretical systematic uncertainties, specifically the PDF uncertainty, are also analyzed in the presence of aTGCs. The total and fiducial cross sections as a function of each aTGC parameter with two different cutoff scales, $\Lambda = 3$ and 1000 TeV, can be found in Figure 6.23. The cross sections are shown for MC@NLO and for MCFM with several different PDF sets. Figure 6.24 shows the same cross sections, but normalized to the SM cross section predicted by that generator and PDF set. Variations due to the generator and to the PDF largely cancel in these plots. The Λ dependence remains, as is expected, and is considerably larger for Δg_1^Z and λ^Z than for $\Delta\kappa^Z$. Finally, the acceptance A_{WZ} as a function of the anomalous couplings is shown in Figure 6.25. As the PDF dependence of the cross section and the acceptance shows little variation as a function of anomalous couplings, the theoretical systematic uncertainties on the cross section normalization and on A_{WZ} evaluated for the SM can be used in the aTGC limit setting.

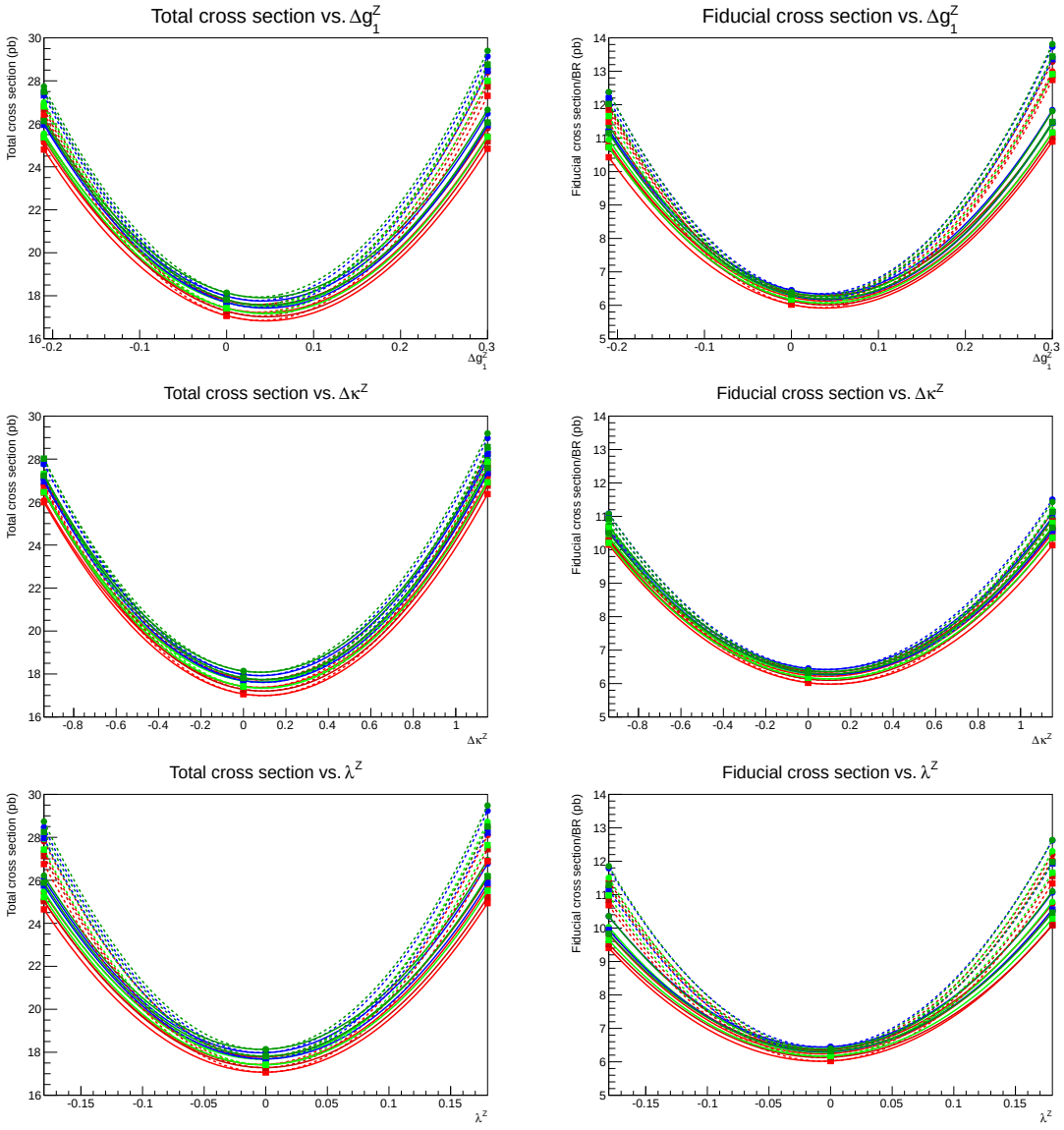

Figure 6.23: Total (left) and fiducial (right) cross section as functions of Δg_1^Z (top), $\Delta\kappa^Z$ (middle), and λ^Z (bottom), computed by MC@NLO (square) and MCFM (circle). The PDF is CTEQ6.6 (red), CT10 (dark red), MSTW2008 (blue), NNPDF2.0 (green), and NNPDF2.1 (dark green). Solid and dashed lines are with $\Lambda = 3$ and 1000 TeV, respectively.

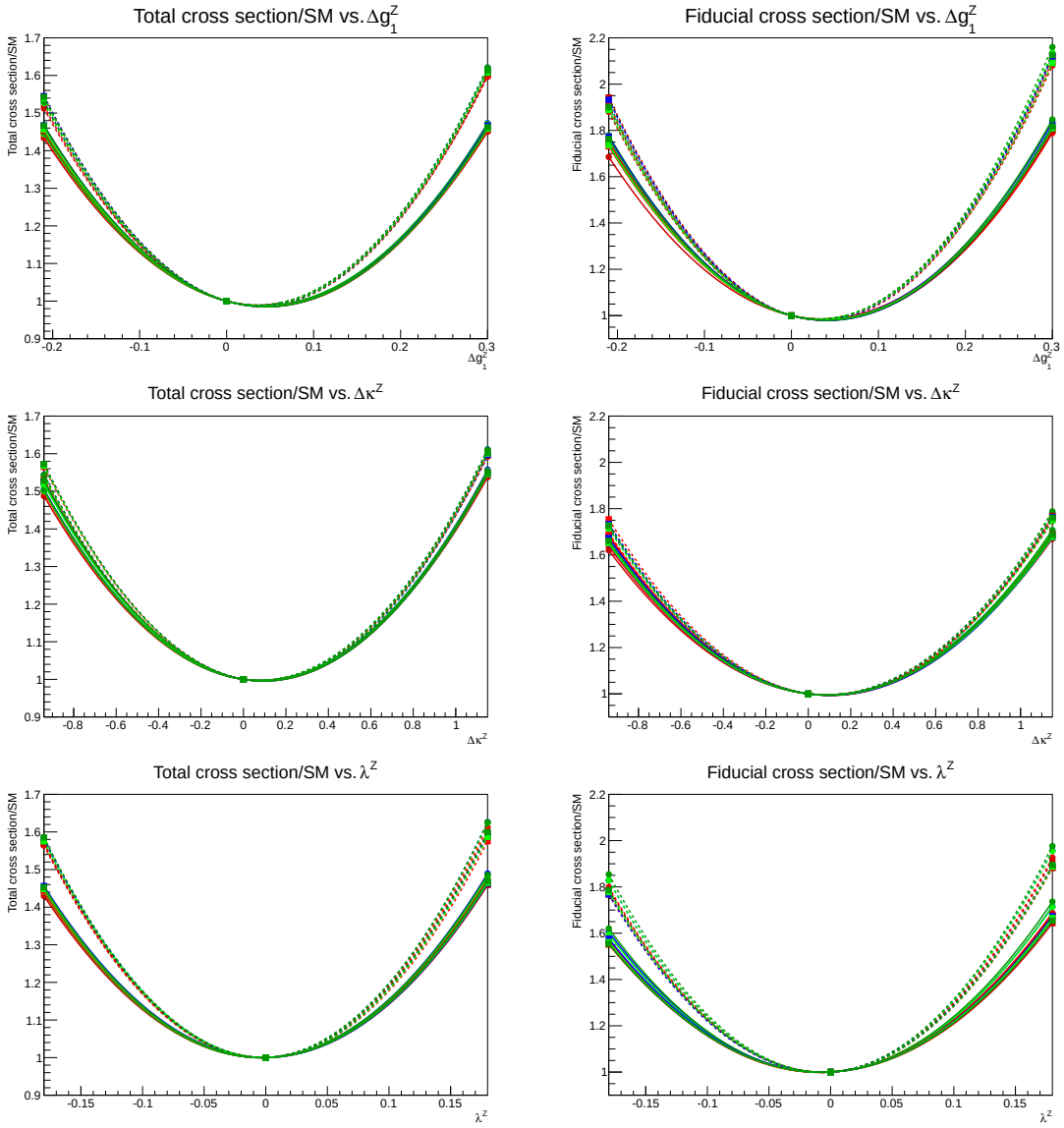

Figure 6.24: Total (left) and fiducial (right) cross section, normalized at the SM point, as functions of Δg_1^Z (top), $\Delta\kappa^Z$ (middle), and λ^Z (bottom), computed by MC@NLO (square) and MCFM (circle). The PDF is CTEQ6.6 (red), CT10 (dark red), MSTW2008 (blue), NNPDF2.0 (green), and NNPDF2.1 (dark green). Solid and dashed lines are with $\Lambda = 3$ and 1000 TeV, respectively.

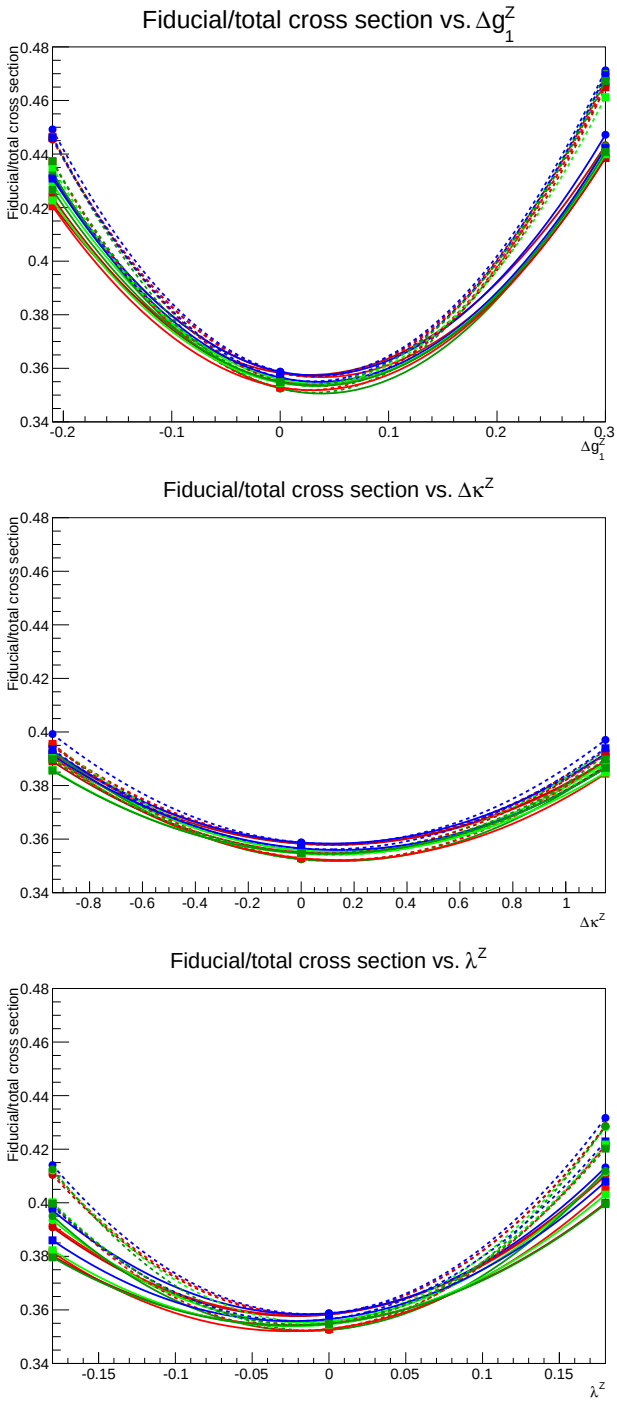

Figure 6.25: Fiducial acceptance A_{WZ} as functions of Δg_1^Z (top), $\Delta\kappa^Z$ (middle), and λ^Z (bottom), computed by MC@NLO (square) and MCFM (circle). The PDF is CTEQ6.6 (red), CT10 (dark red), MSTW2008 (blue), NNPDF2.0 (green), and NNPDF2.1 (dark green). Solid and dashed lines are with $\Lambda = 3$ and 1000 TeV, respectively.

6.14.4 Limit Setting Procedure

To set limits on the aTGC parameters, a frequentist limit approach [61] is adopted. The 95% C.I. for each anomalous coupling is determined separately with the other aTGC parameters set to their SM values of zero. The reweighting procedure described in the previous section allows the expected number of signal events $N_{\rm s}^i$ in channel i to be expressed as a function of aTGC parameters. The set of anomalous couplings for which the observed data is inside of the 95% C.I. of the signal expectation determines the 95% C.I. of the anomalous couplings.

The procedure for determining the 95% C.I. is as follows.

1. The likelihood function $L(n|\sigma,\beta)$ described in Section 6.13.4 is modified by replacing the cross section σ with one of the aTGC parameters $\alpha = \Delta g_1^Z$, $\Delta\kappa^Z$, or λ^Z. The number of signal events N_s^i in channel i is expressed as a quadratic function of α using the reweighting method described in the previous section. The symbol n stands for the observed numbers of data events, and β are the nuisance parameters which represent the Gaussian constrained systematics.

2. A test statistic $q(\alpha)$ is constructed by taking the ratio of the profile maximum likelihood at a test aTGC parameter value α to the full maximum likelihood. That is,

$$q(\sigma) = \frac{L(n|\alpha,\hat{\hat{\beta}})}{L(n|\hat{\alpha},\hat{\beta})} \tag{6.33}$$

where $\hat{\hat{\beta}}$ is the maximum likelihood estimator of β that maximizes the numerator for the fixed test value of α, and $\hat{\alpha}$ and $\hat{\beta}$ are the values of α and β which maximize the denominator.

3. The observed value of the test statistic, $q_{\text{obs}}(\alpha)$, is found using the observed data n_{obs} for each value of the test aTGC parameter. This is done by scanning a range of values of α and determining the value of the test statistic for each α.

4. To determine how often an outcome at least as unlikely as the actual observation is expected, a large number (10,000) of pseudo experiments are generated for each test value of α and the test statistic $q_{\text{pe}}(\alpha)$ is then computed for each pseudo experiment in order to generate a probability distribution of $q(\alpha)$. To generate each pseudo experiment, first, the nuisance parameters β are Gaussian fluctuated around the mean value of $\hat{\hat{\beta}}(\alpha)$. The numbers of "observed" events N^i_{pe} is then drawn randomly from a Poisson distribution whose mean is computed from the value of α and β. The number of pseudo experiments, 10,000, is chosen to ensure that a p-value of 5% can be determined to a reasonable statistical precision of $\pm 0.2\%$.

5. The p-value at each value of α is calculated as the fraction of pseudo experiments whose test statistic $q_{\text{pe}}(\alpha)$ is smaller than the observed value $q_{\text{obs}}(\alpha)$.

6. By scanning α, all values of the aTGC parameter for which $p(\alpha) \geq 5\%$ can be determined and these define the 95% C.I. of α for the observed data.

7. To find the expected sensitivity, the SM expectations for the signal and background are used to generate a large number of toy MC observed data sets, $n^{\text{toy}}_{\text{obs}}$. Using these sets, the distribution of the 95% C.I. for the aTGC parameters can be calculated for each toy data sets.

The expected number of signal events $N_s^i \equiv N_s^i(\alpha)$ is a quadratic function of α and has a minimum near (but not exactly at) the SM point $\alpha = 0$. Thus $N_s^i(\alpha)$ increases in both positive and negative directions away from $\alpha = 0$. As a result, there may be either one or two optimum values of α that best describe the observed data, depending on whether N_{obs} is smaller or larger than the minimum expected value. This results in two possibilities for the 95% C.I. of α: it may be a single continuous region or two disjoint regions.

6.14.5 Expected Limits

To evaluate the expected sensitivity, a larger number of toy MC data sets, $n_{\text{obs}}^{\text{toy}}$, are generated assuming the SM. The left column of Figure 6.26 shows the distributions of the 95% C.I. obtained from the toy experiments, as well as the actual C.I. from the data. In addition, the top-left distribution shows the limits on the fiducial cross section (normalized by the SM cross section) obtained using the likelihood for the cross section fitting, assuming the acceptance for the SM $W^{\pm}Z$ signal, and using the same frequentist procedure to determine limits. The middle column of Figure 6.26 shows the widths of the 95% C.I. If a toy experiment gives two separate C.I., the sum of the two widths is plotted. Although the aTGC parameter limits are not 1-to-1 correlated with the measured cross section, there is still a strong correlation. This is evident in the right column of Figure 6.26, where the fitted fiducial cross section (normalized to the SM) is plotted against the 95% confidence level upper and lower limits of the parameters.

Because of the symmetry of the quadratic aTGC dependence which determines the shape of the likelihood function, there is a strong correlation between the upper and lower limits of the confidence intervals. Therefore, it is unambiguous to define the expected limit as the median of the distribution of upper and lower limits. Using this definition, the 95% C.I. of the expected aTGC limits is shown in Table 6.29.

6.14.6 Observed Limits

Table 6.29 summarizes the observed 68% and 95% C.I. on the anomalous couplings Δg_1^Z, $\Delta\kappa^Z$, and λ^Z. The $1-p$ value as a function of aTGC parameters is shown in Figrue 6.27. Figure 6.28 compares the observed limits with the Tevatron results.

The actual limits observed in the data agree well with what is expected from the value of the fitted cross section. The poorest limits, in terms of the total width of the confidence intervals, are expected when the measured cross section is at the border line between single and double intervals. This happens to be the case with the actual measurement.

	Observed 68% C.I.	Observed 95% C.I.	Expected 95% C.I.
Δg_1^Z	$[-0.13,-0.03]\cup[0.10,0.20]$	$[-0.16,0.24]$	$[-0.12,0.20]$
$\Delta\kappa^Z$	$[-0.6,-0.2]\cup[0.4,0.8]$	$[-0.8,1.0]$	$[-0.6,0.8]$
λ^Z	$[-0.11,-0.04]\cup[0.04,0.11]$	$[-0.14,0.14]$	$[-0.11,0.11]$

Table 6.29: Observed 68% and 95% C.I. and expected 95% C.I. on the anomalous couplings Δg_1^Z, $\Delta\kappa^Z$, and λ^Z.

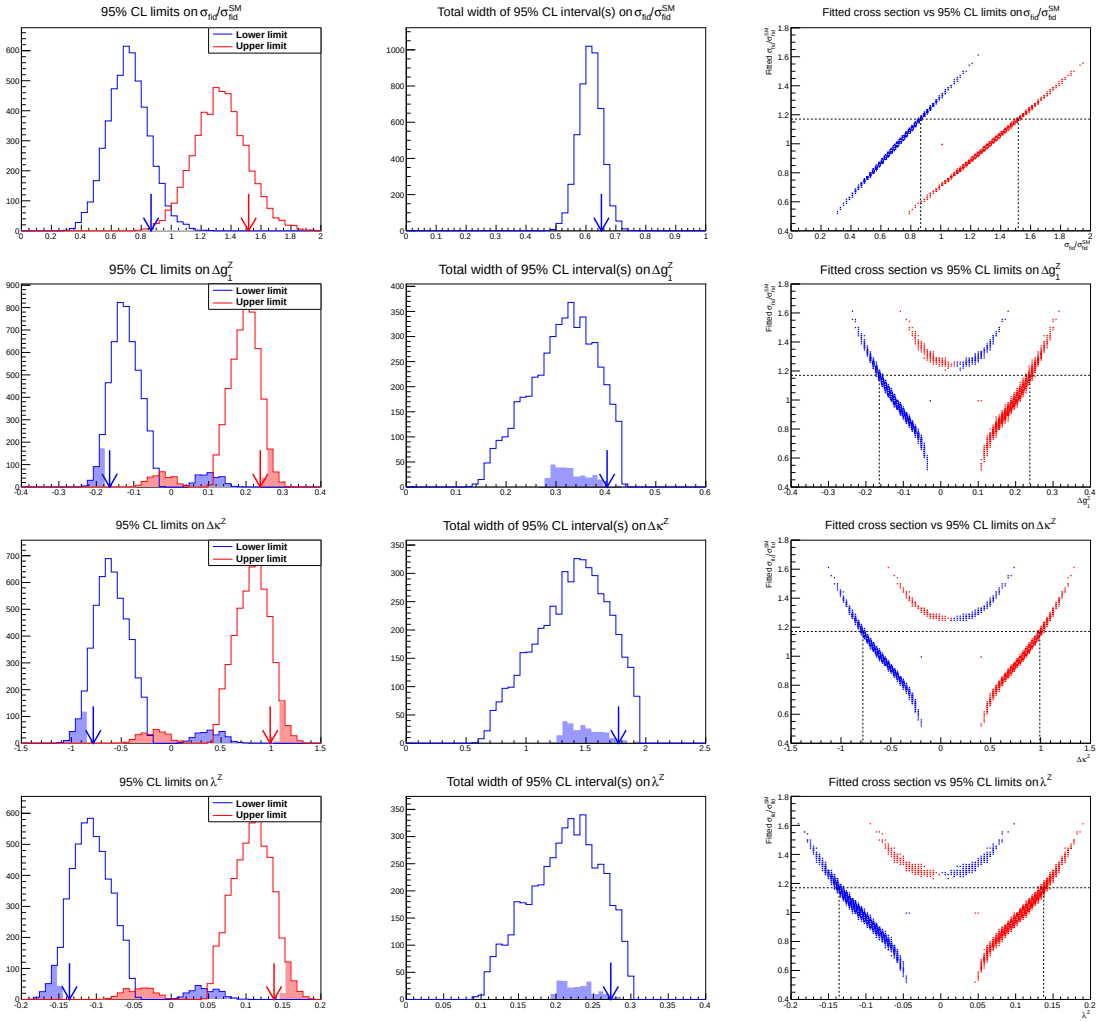

Figure 6.26: The left plots show the upper (red) and lower (blue) limits of the 95% C.I. and the middle plots show the total widths of the 95% C.I. of the fiducial cross section (first row), Δg_1^Z (second row), $\Delta\kappa^Z$ (third row), and λ^Z (fourth row), obtained from toy MC samples. The shaded areas indicate the cases in which two split C.I. were found.The blue and red arrows show the actual limits obtained from data. The right plots show the fitted fiducial cross section v.s. the upper (red) and lower (blue) limits of the 95% C.I. of the fiducial cross section (first row), Δg_1^Z (second row), $\Delta\kappa^Z$ (third row), and λ^Z (fourth row), obtained from toy MC samples. The dashed lines show the observed values from data.

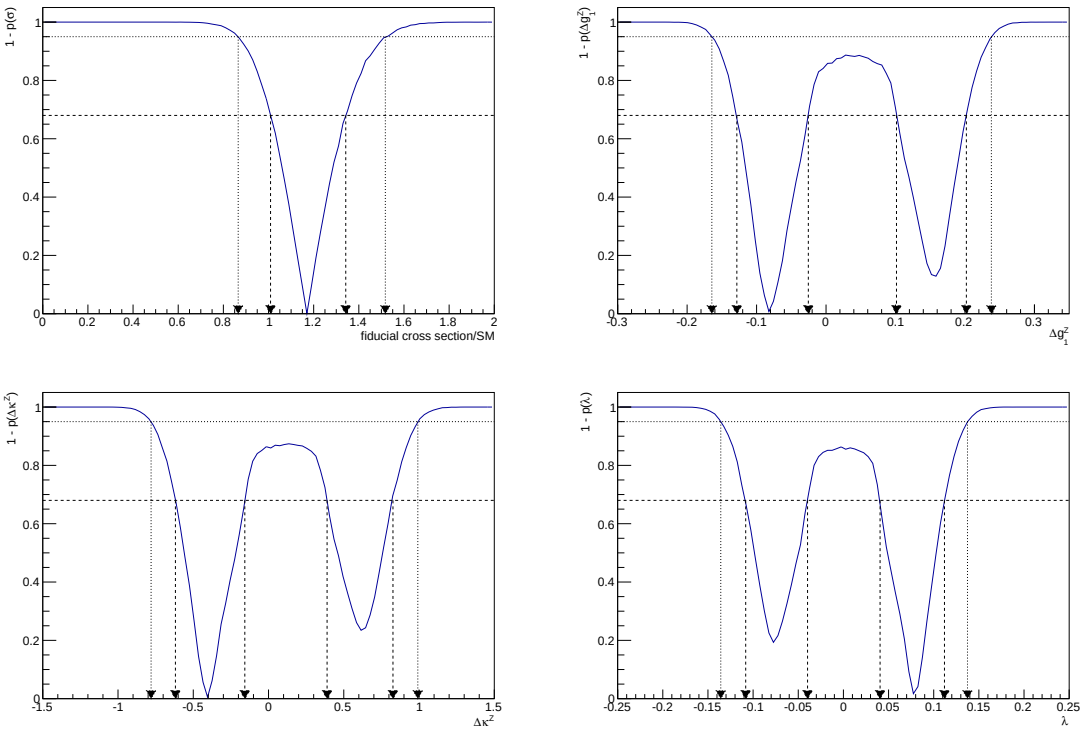

Figure 6.27: $(1-p)$ as a function of the fiducial cross section (top-left), Δg_1^Z (top-right), $\Delta\kappa^Z$ (bottom-left), and λ^Z (bottom-right). Dashed and dotted lines show 68% and 95% C.I., respectively.

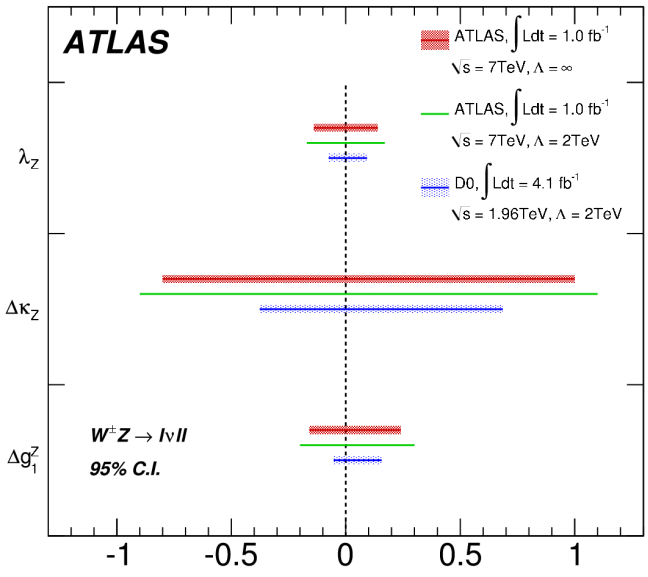

Figure 6.28: aTGC limits from ATLAS and Tevatron experiments. DØ [62] limits are for $W^{\pm}Z$ production with a $p_T(Z)$ shape fit. ATLAS limits are from an event yield fit. Luminosities, center of mass energy and cut-off Λ_{FF} for each experiment are shown and the limits are for 95% C.I.

Chapter 7

Conclusions and Discussion

This thesis has presented a measurement of the $W^{\pm}Z$ production cross section in proton-proton collisions at $\sqrt{s} = 7$ TeV using 1.02 fb^{-1} data acquired by the ATLAS detector in 2011. The cross section is measured using the leptonic decay modes of the W and Z, resulting in final states with electrons, muons, and missing energy. The total inclusive production cross section, as well as the fiducial cross section inside of the fiducial volume of the ATLAS detector and the selection criteria, are measured. These measurements are found to be in good agreement with the Standard Model, but are dominated by statistical uncertainty.

Using the same dataset and event selection, the observed event yields after the $W^{\pm}Z$ signal selection criteria are analyzed within the context of anomalous triple gauge couplings. Limits on the size of the Δg_1^Z, $\Delta\kappa^Z$, and λ^Z anomalous couplings are derived at the 95% confidence interval assuming a cutoff scale of $\Lambda_{FF} = 2$ TeV and $\Lambda_{FF} = \infty$. These limits are compared with limits from the Tevatron, and are

seen to not yet reach the sensitivity of the Tevatron analysis. The primary reason for the lower ATLAS sensitivity is the fact that the event yield is used to derive limits whereas the limits from the Tevatron use the $p_T(Z)$ spectrum which is more sensitive to the $\hat{s}$ dependence of the anomalous cross section.

As the measurement using this data is currently statistically limited, this analysis will benefit greatly from increasing the size of the dataset. This analysis is currently underway using the full 5 fb^{-1} of data collected in 2011. In the full 2011 dataset, preliminary studies of the cross section measurement show that the systematic and statistical uncertainties are approximately the same size. The increased data set will also allow for precise studies of data control regions, thus allowing a reduction in the systematic uncertainties associated to the Data-Driven systematics.

Future studies of anomalous triple gauge couplings will provide much better limits on the couplings and possibly surpass the Tevatron results. An increase in the dataset size will help to reduce the width of the anomalous triple gauge coupling limits. However, as the cross section depends quadratically on the anomalous couplings, the statistical sensitivity of the anomalous coupling analysis will reduce only as $\mathcal{L}^{1/4}$. Looking forward, the major improvement to the anomalous triple gauge coupling analysis will be to set limits using a differential distribution, such as the $p_T(Z)$ spectrum, rather than the event yield. Preliminary studies, using the MC simulation samples, show that setting limit using the $p_T(Z)$ distribution can decrease the width of the 95% confidence intervals by 40-60%.

Bibliography

[1] E. Abat et al. The ATLAS Transition Radiation Tracker (TRT) proportional drift tube: design and performance. *JINST*, 3:P02013, 2008.

[2] E. Accomando and A. Kaiser. Electroweak corrections and anomalous triple gauge-boson couplings in W^+W^- and $W^\pm Z$ production at the LHC. arXiv:0511088 [hep-ph], 2005.

[3] D. Adams et al. Track reconstruction in the ATLAS Muon Spectrometer with MOORE 007. ATLAS Technical Report ATL-SOFT-2003-007, 2003.

[4] S. Agostinelli et al. GEANT4: A simulation toolkit. *Nucl. Instrum. Meth.*, A506:250–303, 2003.

[5] A. Ahmad et al. The silicon microstrip sensors of the ATLAS semiconductor tracker. *NIM A*, 578:98, 2007.

[6] H. Aihara et al. Anomalous Gauge Boson Interactions. arXiv:9503425 [hep-ph], 1995.

[7] ALICE Collaboration. The ALICE Experiment at the CERN Large Hadron Collider. *JINST*, 3:S08002, 2008.

[8] J. Alwall et al. MadGraph/MadEvent v4: The New Web Generation. *JHEP*, 09:028, 2007.

[9] ATLAS and CMS Collaborations and J. Nielsen. W/Z+Jet Cross Section Measurements at the Large Hadron Collider. ATLAS proceedings, ATLCOM-PHYS2009324, 2009.

[10] ATLAS Collaboration. A Measurement of WZ Production in Proton-Proton Collisions at $sqrts = 7$ TeV with the ATLAS Detector. ATLAS Internal Communication **ATL-COM-PHYS-2011-1108** (2011).

[11] ATLAS Collaboration. Athena Computing Framework ATLAS Internal Webpage. `https://twiki.cern.ch/twiki/bin/viewauth/Atlas/AthenaFramework`.

[12] ATLAS Collaboration. ATLAS Detector and Physics Performance Technical Design Report. http://atlas.web.cern.ch/Atlas/GROUPS/PHYSICS/TDR/access.html.

[13] ATLAS Collaboration. ATLAS Electron Trigger Public Results. https://twiki.cern.ch/twiki/bin/view/AtlasPublic/EgammaTriggerPublicResults.

[14] ATLAS Collaboration. ATLAS Good Run List Internal Webpage. https://twiki.cern.ch/twiki/bin/viewauth/Atlas/GoodRunsListsTutoria.

[15] ATLAS Collaboration. ATLAS Muon Combined Performance: Guidelines for Analyses of 2011 Data for EPS. ATLAS Internal Webpage, https://twiki.cern.ch/twiki/bin/viewauth/AtlasProtected/MCPAnalysisGuidelinesEPS2011.

[16] ATLAS Collaboration. ATLAS Muon Performance Public Results. https://twiki.cern.ch/twiki/bin/view/AtlasPublic/MuonPerformancePublicPlots.

[17] ATLAS Collaboration. Atlas muon public performance plots. https://twiki.cern.ch/twiki/bin/view/AtlasPublic/MuonPerformancePublicPlots.

[18] ATLAS Collaboration. ATLAS MuonMomentumCorrections Software Package. ATLAS Internal Webpage, https://svnweb.cern.ch/trac/atlasoff/browser/PhysicsAnalysis/MuonID/MuonIDAnalysis/MuonMomentumCorrections/tags/MuonMomentumCorrections-00-03-05.

[19] ATLAS Collaboration. ATLAS Public ID Tracking Performance Plots. https://twiki.cern.ch/twiki/bin/view/AtlasPublic/InDetTrackingPerformanceApprovedPlots.

[20] ATLAS Collaboration. ATLAS Public Luminosity Plots. https://twiki.cern.ch/twiki/bin/view/AtlasPublic/LuminosityPublicResults.

[21] ATLAS Collaboration. Calibrated $Z \to e^+e^-$ mass. ATLAS note https://atlas.web.cern.ch/Atlas/GROUPS/PHYSICS/EGAMMA/PublicPlots/20101115/CalibratedZee/ATL-COM-PHYS-2010-895/index.html.

[22] ATLAS Collaboration. Electron and photon reconstruction and identification in ATLAS: expected performance at high energy and results at 900 GeV.

ATLAS conference note: ATLAS-CONF-2010-005, https://atlas.web.cern.ch/Atlas/GROUPS/PHYSICS/CONFNOTES/ATLAS-CONF-2010-005/.

[23] ATLAS Collaboration. Electron Efficiencies for EPS Analysis. ATLAS web page https://twiki.cern.ch/twiki/bin/viewauth/AtlasProtected/EfficiencyMeasurements#Electron_efficiencies_for_EPS_an.

[24] ATLAS Collaboration. Expected Performance of the ATLAS Experiment - Detector, Trigger and Physics. arXiv:0901.0512 [hep-ex].

[25] ATLAS Collaboration. How To Clean Jets. https://twiki.cern.ch/twiki/bin/view/AtlasProtected/HowToCleanJets.

[26] ATLAS Collaboration. Jet Energy Resolution Improvement Using Longitudinal Calorimeter Segmentation in ATLAS. ATLAS internal note **ATL-PHYS-INT-2009-051**.

[27] ATLAS Collaboration. Liquid argon calorimeter technical design report. CERN-LHCC-96-041, http://cdsweb.cern.ch/record/33106.

[28] ATLAS Collaboration. Luminosity Determination in pp Collisions at $\sqrt{s} = 7$ TeV using the ATLAS Detector in 2011. ATLAS conference note: ATLAS-CONF-2011-116 https://cdsweb.cern.ch/record/1376384?ln=en.

[29] ATLAS Collaboration. Muon Momentum Resolution in First Pass Reconstruction of pp Collision Data Recorded by ATLAS in 2010. ATLAS Conference Note ATLAS-CONF-2011-046, https://cdsweb.cern.ch/record/1338575?ln=en.

[30] ATLAS Collaboration. Muon reconstruction efficiency in reprocessed 2010 LHC proton-proton collision data recorded with the ATLAS detector. ATLAS Conference Note ATLAS-CONF-2011-063, https://cdsweb.cern.ch/record/1345743.

[31] ATLAS Collaboration. Muon Trigger Efficiencies for EPS. ATLAS internal note https://twiki.cern.ch/twiki/pub/Atlas/MuonTriggerPhysicsTriggerRecommendations2011/trigger.pdf.

[32] ATLAS Collaboration. Performance of primary vertex reconstruction in proton-proton collisions at $\sqrt{s} = 7$ tev in the atlas experiment. ATLAS Conference Note: ATLAS-CONF-2010-069, https://cdsweb.cern.ch/record/1281344?ln=en.

[33] ATLAS Collaboration. Performance of the Electron and Photon Trigger in p-p Collisions at $\sqrt{s} = 7$ TeV with the ATLAS Detector at the LHC. ATLAS note `https://cdsweb.cern.ch/record/1351827`.

[34] ATLAS Collaboration. Reconstruction and Calibration of Missing Transverse Energy and Performance in Z and W events in ATLAS Proton-Proton Collisions at $\sqrt{s} = 7$ TeV. ATLAS conference note **ATLAS-CONF-2011-080** `https://cdsweb.cern.ch/record/1355703?ln=en`.

[35] ATLAS Collaboration. Single Boson and Diboson Production Cross Sections in pp Collisions at $\sqrt{s} = 7$ TeV. ATLAS Internal Communication **ATL-COM-PHYS-2010-695**(2010).

[36] ATLAS Collaboration. Tile calorimeter technical design report. CERN-LHCC-96-042, `http://cdsweb.cern.ch/record/331062`.

[37] ATLAS Collaboration. *ATLAS Muon Spectrometer Technical Design Report*. CERN, Geneva, 1997.

[38] ATLAS Collaboration. ATLAS Pixel Detector Electronics and Sensors. *JINST*, 3(07):P07007, 2008.

[39] ATLAS Collaboration. The ATLAS Experiment at the CERN Large Hadron Collider. *JINST*, 3:S08003, 2008.

[40] ATLAS Collaboration. Jet energy measurement with the ATLAS detector in proton-proton collisions at $\sqrt{s} = 7$ TeV. arXiv:1112.6426 [hep-ex], 2011.

[41] ATLAS Collaboration. Luminosity Determination in pp Collisions at $\sqrt{s} = 7$ TeV using the ATLAS Detector at the LHC. *European Physics Journal C*, 71:1630, 2011.

[42] ATLAS Collaboration. Measurement of the inclusive W+- and Z/gamma cross sections in the electron and muon decay channels in pp collisions at sqrt(s) = 7 TeV with the ATLAS detector. arXiv:1109.5141 [hep-ex], 2011.

[43] ATLAS Collaboration. Measurement of the Top Quark-Pair Production Cross Section with ATLAS in pp collisions at sqrt(s) = 7 TeV. *Eur. Phys. J. C*, 71:1577, 2011.

[44] ATLAS Collaboration. Measurement of the $W^{\pm}Z$ production cross section and limits on anomalous triple gauge couplings in proton-proton collisions at $\sqrt{s} = 7$ TeV with the ATLAS detector. arXiv:1111.5570 [hep-ex], 2011.

[45] ATLAS Collaboration. Electron performance measurements with the ATLAS detector using the 2010 LHC proton-proton collision data. *Eur. Phys. J. C*, 72:1909, 2012.

[46] ATLAS Collaboration. Performance of Missing Transverse Momentum Reconstruction in Proton-Proton Collisions at $\sqrt{s} = 7$ TeV with ATLAS. *Eur.Phys.J.C*, 72:1844, 2012.

[47] ATLAS Collaboration and M. Groll. Associated Production of Weak Bosons at the LHC with the ATLAS Detector. *J. Phys. Conf. Ser.*, 171:012086, 2009.

[48] ATLAS Experiment @ 2011 CERN. ATLAS Photos. `http://www.atlas.ch/photos/index.html`.

[49] D. Belohrad, J.-J. Gras, L.K. Jensen, O.R. Jones, M. Lud-wig, P. Odier, J.J. Savioz, and S. Thoulet. Commissioning and first performance of the LHC beam current measurement systems. `http://accelconf.web.cern.ch/AccelConf/IPAC10/papers/mope059.pdf`.

[50] M. Benedikt and others (eds.). The LHC design report v.3 : the LHC Injector Chain. **CERN-2004-003-V-3**, `http://cdsweb.cern.ch/record/823808`.

[51] J.P. Blewett. 200 gev intersecting storage accelerators. Proceedings of the 8th International Conference on High-Energy Accelerators, CERN, Geneva Switzerland (1971).

[52] O.S. Bruning and others (eds.). The LHC design report v.1 : the LHC Main Ring. **CERN-2004-003-V-1**, `http://cdsweb.cern.ch/record/782076`.

[53] O.S. Bruning and others (eds.). The LHC design report v.2 : the LHC Infrastructure and General Services. **CERN-2004-003-V-2**, `http://cdsweb.cern.ch/record/815187`.

[54] M. Cacciari, G. P. Salam, and G. Soyez. The anti-kt jet clustering algorithm. *JHEP*, 04:063, 2008.

[55] J.M. Campbell et al. Next-to-leading order QCD predictions for W + 2jet and Z + 2jet production at the CERN LHC. *Phys. Rev.*, D68:094021, 2003.

[56] CDF Collaboration. Measurement of the WZ Production Cross Section in $p\bar{p}$ Collisions at $\sqrt{s} = 1.96$ TeV using 7.1 fb^{-1} of CDF Run II Data. `http://www-cdf.fnal.gov/physics/ewk/2011/wz/PublicPages/WZwebpage.html`.

[57] CDF Collaboration. WZ Anomalous Triple Gauge Couplings in 7.1 fb^{-1} of $p\bar{p}$ Collisions at $\sqrt{s} = 1.96$ TeV. `http://www-cdf.fnal.gov/physics/ewk/2011/WZatgc71/`.

[58] CMS Collaboration. The CMS Experiment at the CERN Large Hadron Collider. *JINST*, 3:S08004, 2008.

[59] G. Corcella et al. HERWIG 6: an event generator for Hadron Emission Reactions With Interfering Gluons. *JHEP*, 010:0101, 2001.

[60] T Cornelissen et al. Concepts, design and implementation of the atlas new tracking (newt). ATLAS Technical Report ATL-SOFT-PUB-2007-007, `https://cdsweb.cern.ch/record/1020106`, 2007.

[61] G. Cowan, K. Cranmer, E. Gross, and O. Vitells. Asymptotic Formulae for Likelihood-Based Tests of New Physics. *Eur. Phys. J. C*, 71:1554, 2011.

[62] D0 Collaboration. Measurement of the $WZ \to l\nu ll$ Cross Section and Limits on Anomalous Triple Gauge Couplings in $p\bar{p}$ Collisions at $\sqrt{s} = 1.96$ TeV. *Phys. Lett. B*, 695:67, 2011.

[63] D0 Collaboration. A Measurement of the WZ and ZZ Production Cross Sections using Leptonic Final States in $p\bar{p}$ Collisions. arXiv:1201.5652 [hep-ex], 2012.

[64] R. Decker, S. Jadach, J. Kuhn, and Z. Was. The Tau Decay Library Tauola: Version 2.4. *Comput. Phys. Commun.*, 76:361, 1993.

[65] S. D. Drell and T. Yan. Partons and their applications at high energies. *Ann. Phys.*, 66:578623, 1971.

[66] R. Duda and P. Hart. Use of the Hough Transformation to Detect Lines and Curves in Pictures. *Comm. ACM*, 15, 1972.

[67] O. Eboli, J. Gonzaled-Fraile, and M. C. Gonzalez-Garcia. Scrutinizing the ZW^+W^- vertex at the Large Hadron Collider at 7 TeV. arXiv:1006.3562 [hep-ph], 2010.

[68] R. K. Ellis, W. J. Stirling, and B. R. Webber. *QCD and Collider Physics*. Cambridge University Press, 1996.

[69] S.D. Ellis, J. Huston, K. Hatakeyama, P. Loch, and M. Tonnesmann. Jets in hadronhadron collisions. *Progress in Particle and Nuclear Physics*, 60(2):484–551, 2008.

[70] J. Ellison and J. Wudka. Study of Trilinear Gauge Boson Couplings at the Tevatron Collider. arXiv:9804322 [hep-ph], 1998.

[71] L. Evans and P. Bryant. LHC Machine. *JINST*, 3:S08001, 2008.

[72] E. Farhi and L. Susskind. Technicolour. *Phys. Rept.*, 74:277, 1981.

[73] Gary J. Feldman and Robert D. Cousins. A Unified Approach to the Classical Statistical Analysis of Small Signals. *Phys. Rev. D*, 57:3873–3889, 1998.

[74] R.P. Feynman. Space-time approach to quantum electrodynamics. *Phys. Rev.*, 76(6):769789, 1949.

[75] R.P. Feynman. Mathematical formulation of the quantum theory of electromagnetic interaction. *Phys. Rev.*, 80(3):440457, 1950.

[76] S. Frixione and B.R. Webber. Matching NLO QCD computations and parton shower simulations. *JHEP*, 06:029, 2002.

[77] R. Fruhwirth et al. Application of Kalman Filtering to Track and Vertex Fitting. *Nucl. Inst. Meth. A*, 262, 1987.

[78] R. Fruhwirth, W. Waltenberger, and P. Vanlaer. Adaptive vertex fitting. *J. Phys. G*, 34, 2007.

[79] G.Belanger and F. Boudjema. Probing quartic couplings of weak bosons through three vector production at a 500 GeV NLC. *Phys. Lett. B*, 288:201, 1992.

[80] Sheldon L. Glashow. Partial-symmetries of weak interactions. *Nuclear Physics*, 22(4):579–588, 1961.

[81] Y. A. Golfand and E. P. Likhtman. Extension of the Algebra of Poincare Group Generators and Violation of P invariance. *JETP Lett.*, 13:323, 1971.

[82] P. Golonka and Z. Was. PHOTOS Monte Carlo: a precision tool for QED corrections in Z and W decays. *Eur. Phys. J. C*, page 97, 2006.

[83] D. Griffiths. *Introduction to Elementary Particles*. Wiley-VCH, 2008.

[84] K. Hagiwara, R.D. Peccie, and D. Zeppenfeld. Probing the weak boson sector in $e^+e^- \to W^+W^-$. *Phys. Lett. B*, 282:253–307, 1987.

[85] D. Hanneke, S. Fogwell, and G. Gabrielse. New Measurement of the Electron Magnetic Moment and the Fine Structure Constant. *Phys.Rev.Lett.*, 100:120801, 2008.

[86] F. James. MINUIT - Function Minimization and Error Analysis. CERN Program Library entry D506, Geneva, 1998.

[87] P. Langacker. The physics of heavy Z′ gauge bosons. *Rev. Mod. Phys.*, 81:1199, 2009.

[88] D. Levin. Muonrecpedia. `https://twiki.cern.ch/twiki/bin/view/AtlasProtected/MuonRecoPedia`.

[89] LHC EW Working Group. Working Group on Electroweak precision measurements at the LHC, 11/28/2011 - 11/30/2011. `https://indico.cern.ch/conferenceDisplay.py?confId=145744`.

[90] LHCb Collaboration. The LHCb Detector at the LHC. *JINST*, 3:S08005, 2008.

[91] LHCf Collaboration. The LHCf detector at the CERN Large Hadron Collider. *JINST*, 3:S08006, 2008.

[92] M.L. Mangano et al. ALPGEN, a generator for hard multiparton processes in hadronic collisions. *JHEP*, 07:001, 2003.

[93] T. Melia, P. Nason, R. Rontsch, and G. Zanderighi. W+W-, WZ and ZZ production in the POWHEG BOX. arXiv:1107.5051 [hep-ph].

[94] MoEDAL Collaboration. The MoEDAL Technical Design Report. `http://moedal.web.cern.ch/content/moedal-technical-design-report-tdr`.

[95] K. Nakamura et al. Review of Particle Physics. *Journal of Physics G*, 37, 2010.

[96] A. Neveu and J. H. Schwarz. Quark Model of Dual Pions. *Phys. Rev. D*, 4:1109, 1971.

[97] J. Neyman. Outline of a Theory of Statistical Estimation Based on the Classical Theory of Probability. *Philosophical Transactions of the Royal Society of London A*, 236:333–380, 1937.

[98] R Nicolaidou, L Chevalier, S Hassani, J F Laporte, E Le Menedeu, and A Ouraou. Muon identification procedure for the ATLAS detector at the LHC using Muonboy reconstruction package and tests of its performance using cosmic rays and single beam data. *Journal of Physics: Conference Series*, 219(3):032052, 2010.

[99] M.E. Peskin and D. V. Schroeder. *An Introduction to Quantum Field Theory*. Westview Press, 1995.

[100] J. Pumplin, D.R. Stump, J. Huston, H.L. Lai, P. Nadolsky, and W.K. Tung. New Generation of Parton Distributions with Uncertainties from Global QCD Analysis. arXiv:0201195 [hep-ph], 2008.

[101] P. Ramond. Dual Theory for Free Fermions. *Phys. Rev. D*, 3:2415, 1971.

[102] A. Salam. Elementary particle theory: Relativistic groups and analyticity (Nobel Symposium No. 8), 1968.

[103] J. Schwinger. On quantum-electrodynamics and the magnetic moment of the electron. *Phys. Rev.*, 73(4):416417, 1948.

[104] Maria Smizanska. PythiaB: interface to Pythia6 dedicated to simulation of beauty events.
`http://phys-ds.physics.lsa.umich.edu/docushare/dsweb/Get/Document-2010/g6.ps`, 2003.

[105] Olaf Steinkamp. Lecture on Experimental Methods of Particle Physics: Track Reconstruction.
`http://www.ipp.phys.ethz.ch/education/lectures/empp/contents/`.

[106] The LEP Collaborations: ALEPH and DELPHI and L3 and OPAL and the LEP TGC Working Group. A Combination of Charged Triple Gauge Boson Couplings Measured by the LEP Experiments.
`http://lepewwg.web.cern.ch/LEPEWWG/lepww/tgc/`.

[107] The ROOT team. The ROOT Users Guide.
http://root.cern.ch/drupal/content/users-guide.

[108] S. Torbjorn et al. PYTHIA 6.4 Physics and Manual. *JHEP*, 05:026, 2006.

[109] TOTEM Collaboration. The TOTEM Experiment at the CERN Large Hadron Collider. *JINST*, 3:S08007, 2008.

[110] S. van der Meer. Calibration of the effective beam height in the ISR. CERN note: CERN-ISR-PO-68-31, `https://cdsweb.cern.ch/record/296752`, 1968.

[111] D. V. Volkov and V. P. Akulov. Possible Universal Neutrino Interaction. *JETP Lett.*, 16:438, 1972.

[112] S. Weinberg. What is Quantum Field Theory, and What Did We Think It Is? In *Conference on Historical and Philosophical Reflections on the Foundation of Quantum Field Theory*, Boston, MA, Mar. 13. arXiv:9702027 [hep-th], 1996.

[113] Steven Weinberg. A model of leptons. *Phys. Rev. Lett.*, 19(21):12641266, 1967.

[114] J. Wess and B. Zumino. Supergauge transformations in four dimensions. *Nucl. Phys. B*, 70:39, 1974.

[115] Wikimedia Commons. Standard Model of Elementary Particles. `http://en.wikipedia.org/wiki/File:Standard_Model_of_Elementary_Particles.svg`.

[116] J. Wudka. A short course in effective Lagrangians. arXiv:0002180 [hep-ph], 2000.

[117] A. Yamamoto et al. Progress in ATLAS central solenoid magnet. *IEEE T. Appl. Supercond.*, 10:353, 2000.